

Stony Brook University



OFFICIAL COPY

The official electronic file of this thesis or dissertation is maintained by the University Libraries on behalf of The Graduate School at Stony Brook University.

© All Rights Reserved by Author.

**Aqueous Alteration of Glass on the Martian Surface: A Comparison of Remotely-Acquired
and Experimental Data Sets**

A Dissertation Presented

by

Marcella Roth (Yant)

to

The Graduate School

in Partial Fulfillment of the

Requirements

for the Degree of

Doctor of Philosophy

in

Geosciences

Stony Brook University

December 2017

Copyright by
Marcella Roth
2017

Stony Brook University

The Graduate School

Marcella Roth (Yant)

We, the dissertation committee for the above candidate for the

Doctor of Philosophy degree, hereby recommend

acceptance of this dissertation.

Dr. Deanne Rogers – Dissertation Advisor
Associate Professor, Department of Geosciences

Dr. Hanna Nekvasil - Chairperson of Defense
Professor, Department of Geosciences

Dr. Timothy Glotch
Associate Professor, Department of Geosciences

Dr. Brian Phillips
Professor, Department of Geosciences

Dr. Briony Horgan
Assistant Professor, Department of Earth, Atmospheric, and Planetary Science
Purdue University, USA

This dissertation is accepted by the Graduate School

Charles Taber
Dean of the Graduate School

Aqueous Alteration of Glass on the Martian Surface: A Comparison of Remotely-Acquired and Experimental Data Sets

by

Marcella Roth (Yant)

Doctor of Philosophy

in

Geoscience

Stony Brook University

2017

Abstract

The abundance and species of chemical alteration products on planetary surfaces are related to the starting composition of unaltered protolith, the style and duration of alteration processes, the fluid composition, and fluid-to-rock ratio, and ultimately, the preservation of those products in rocks and soils. Thus, detection and interpretation of alteration mineral assemblages on Mars is critical to deciphering the history of the Martian surface. This dissertation reports investigations into the characterization of altered synthetic Martian materials and natural analogs followed by the comparison of their spectral properties with remotely-sensed data.

For the first time, direct infrared spectral analyses of glasses with Martian compositions, altered under controlled conditions, are presented in order to assess surface weathering and regolith development on Mars. Basaltic glass with rover analyzed compositions (Irvine, Backstay, and Pathfinder) were synthesized and altered under controlled, cation-conservative, acid-sulfate conditions. These experiments provided constraints on how infrared spectral features vary as a function of pH and composition for Martian surface material. A volatile-containing Irvine

composition was also included to observe how chlorine and water affect the spectral and chemical characteristics of unaltered/altered basaltic glass. Furthermore, hydrothermally-altered basalt from Hawaii was spectrally characterized here in order to provide a better understanding of the properties of open-system alteration relative to closed-system. Combined, these data sets provide a spectral library that includes mixtures of unaltered and altered material, poorly crystalline phases, combinations of various grain sizes, and alteration coatings that are difficult to capture with a standard mineral library.

The generated libraries were compared with remotely-sensed data sets (TES and CRISM) which allowed for assessment of alteration at both global and local scales on Mars. Both TES and OMEGA data sets exhibit strong evidence for acid weathered glass in the northern lowlands of Mars, with additional potential detections in Terra Meridiani, Vallis Marineris, and Mawrth Vallis. Because lander/rover measurements have observed isochemically altered, acid-sulfate weathering at disparate locations, the lack of previous orbital detections is in conflict with the rover data. This is attributed primarily to later reworking of soils, which would redistribute the alteration products and dilute their surface abundance. The fine-grained nature of alteration materials may also contribute to their spectral obscuration. The ubiquitous spectral signatures of acid weathering in the northern lowlands suggest a more recent, ongoing process to maintain concentrated alteration materials at the surface.

This work is dedicated to my brilliant, supportive husband, Eric Roth.

I am infinitely grateful for his commitment, his effort, and his patience, both during this Ph.D. and beyond. In addition to pursuing his Ph.D. and M.D., he helped fuel my passion in science and has been an inspiration throughout my graduate career.

“Traveler there is no path. The path forms itself as you walk it.” - Antonio Machado

This work is also dedicated to the memory of my father, Jack Yant Jr., who always supported me, wherever my path led.

Futhermore, I dedicate this work and give thanks to my family who has offered me endless encouragement during this process. I would like to express a sincere gratitude to my grandma – Barbara Hoffman, mother – Becky Yant, sister – Christa Stephenson, and brother – Jack Yant III. I will always appreciate all they have done for me throughout my life. I would also like to recognize my in-laws, Mary Jane and Ed Roth, for their unconditional support and kindness.

Table of Contents

List of Figures.....	ix
List of Tables.....	xii
Chapter 1: Introduction.....	1
1.1 Overview.....	1
1.2 References.....	8
Chapter 2: Background.....	12
2.1 Glass on Mars.....	12
2.2 Alteration Trends on Mars vs. Earth.....	15
2.3 Sulfate Formation.....	17
2.4 Alteration Detection on Mars.....	23
2.5 References.....	27
Chapter 3: Spectral Characterization of Acid Weathering Products on Martian Basaltic Glass.....	47
3.1 Introduction.....	47
3.2 Derivation of Basaltic Compositions.....	51
3.3 Experimental and Analytical Methods.....	52
3.3.1 Overview.....	52
3.3.2 Glass Synthesis Methods.....	54
3.3.3 Alteration Batch Experiments.....	55
3.3.4 Analytical Methods.....	56
3.4 Irvine Glass Alteration Results.....	59
3.4.1 Irvine Glass Chemical and Mineralogical Analyses.....	60
3.4.2 Irvine Glass Infrared Results.....	61
3.4.2.1 Irvine Glass Visible Near-Infrared.....	61
3.4.2.2 Irvine Glass Mid-Infrared.....	62
3.5 Backstay Glass Alteration Results.....	63
3.5.1 Backstay Glass Chemical and Mineralogical Analyses.....	64
3.5.2 Backstay Glass Infrared Results.....	65
3.5.2.1 Backstay Glass Visible Near-Infrared.....	65
3.5.2.2 Backstay Glass Mid-Infrared.....	66
3.6 Pathfinder Soil Glass Infrared Results.....	67
3.6.1 Pathfinder Soil Glass Visible Near-Infrared.....	67
3.6.2 Pathfinder Soil Glass Mid-Infrared.....	68
3.7 Pathfinder Rock Glass Infrared Results.....	68
3.7.1 Pathfinder Rock Glass Visible Near-Infrared.....	68
3.7.2 Pathfinder Rock Glass Mid-Infrared.....	69
3.8 Discussion.....	69
3.8.1 Effects of Composition on Spectral Signatures.....	69
3.8.2 Effects of Composition on Chemical Alteration Assemblages.....	71
3.8.3 Comparison of Spectral and Chemical Data.....	73
3.8.4 Applicability to Mars.....	76
3.9 Conclusions.....	80

3.10 References	82
Chapter 4: Spectral Characterization and Effects of Volatiles on Synthetic Irvine Basaltic Glass	
4.1 Introduction	113
4.2 Experimental and Analytical Methods	115
4.2.1 <i>Glass Synthesis Methods</i>	115
4.2.2 <i>Alteration Batch Experiments</i>	116
4.2.3 <i>Analytical Methods</i>	117
4.3 Glass Alteration Results	120
4.3.1 <i>Chemical and Mineralogical Analyses</i>	121
4.3.2 <i>Infrared Spectral Results</i>	123
4.3.2.1 <i>Visible Near-Infrared</i>	123
4.3.2.2 <i>Glass Mid-Infrared</i>	123
4.4 Discussion.....	125
4.4.1 <i>Effects of pH</i>	125
4.4.2 <i>Effects of Volatiles on Glass Spectral Signatures and Chemical Alteration Assemblages</i>	127
4.4.3 <i>Trends in Volatile-Containing and Volatile-Free Material</i>	129
4.5 Conclusions	130
4.6 References	130
Chapter 5: Visible, Near-Infrared and Mid-Infrared Spectral Characterization of Hawaiian Fumarolic Alteration near Kilauea’s December 1974 Flow: Implications for Spectral Discrimination of Alteration Environments on Mars	
5.1 Introduction	147
5.2 Methods	151
5.2.1 <i>Sample Collection</i>	151
5.2.2 <i>Analytical Techniques</i>	152
5.3 Results	155
5.3.1 <i>Infrared Spectroscopy</i>	155
5.3.2 <i>Chemical and Mineralogical Analyses</i>	159
5.4 Discussion.....	161
5.4.1 <i>Spectral Detectability</i>	161
5.4.2 <i>Hydrothermal Alteration on Mars</i>	165
5.5 Implications	169
5.6 References	170
Chapter 6: Aqueous Alteration of Glass on the Martian Surface: A Comparison of Remotely-Acquired and Experimental Data Sets	
6.1 Introduction	194
6.2 Spectral Library Description	197
6.2.1 <i>Synthetic Analog Materials</i>	197
6.2.2 <i>Terrestrial Analog Materials</i>	199
6.3 Data and Methods	200
6.3.1 <i>General Approach</i>	200

6.3.2 Thermal Emission Spectrometer (TES).....	201
6.3.3 Observatoire pour la Minéralogie, l'Eau, les Glaces et l'Activité (OMEGA). ..	202
6.4 Results	203
6.4.1 Acidalia Planitia	205
6.4.2 Terra Meridiani.....	206
6.4.3 Mawrth Vallis.....	207
6.4.4 Valles Marineris.....	208
6.4.5 Terra Sirenum	209
6.5 Discussion.....	210
6.5.1 Isochemical Acid Alteration on the Martian Surface.....	210
6.5.2 Spectral Detectability in the MIR and VNIR.....	211
6.5.3 On the Possible Sulfate Detection in Acidalia Planitia	212
6.5.4 Evidence for Geologically Recent Acid Weathering in the Northern Plains ..	214
6.6 Conclusions	215
6.7 References	215
Chapter 7: Concluding Remarks.....	242
Appendix.....	245
Table A1: Linear least squares modeled abundances for Irvine and Backstay glass thermal infrared spectra	245
Table A2: Linear least squares modeled abundances for Pathfinder Soil and Rock glass thermal infrared spectra	248
Table A3: Linear least squares modeled abundances for pressed pellet Irvine and Backstay glass thermal infrared spectra	251
Table A4: Linear least squares modeled abundances for Irvine volatile-containing glass particulate thermal infrared spectra	254
Table A5: Linear least squares modeled abundances for the averaged thermal emission spectra for each group of Hawaiian material	257
Figure A1: One pixel per degree binned global TES maps showing the abundances ranging from 20-50% for the Individual Altered and Unaltered Irvine material.....	261
Figure A2: One pixel per degree binned global TES maps showing the abundances ranging from 20-50% for the Individual Altered and Unaltered Backstay material	262
Figure A3: One pixel per degree binned global TES maps showing the abundances ranging from 20-50% for the Individual Altered and Unaltered Pathfinder Soil material	263
Figure A4: One pixel per degree binned global TES maps showing the abundances ranging from 20-50% for the Individual Altered and Unaltered Pathfinder Rock material	264
Figure A5: One pixel per degree binned global TES maps showing the abundances ranging from 20-50% for the Individual Altered BAS101 and BSB101 materials	265

List of Figures

Figure 2-1. Diagram from Hurowitz and McLennan [2007) comparing the weathering trends for Earth and Mars.....	43
Figure 2-2: Diagram from Hurowitz et al. [2006] showing A) log activity of Al^{+3} vs. pH with speciation of Al in respect to kaolinite precipitation and B) log activity of Fe^{+3} vs. pH with speciation of Fe in respect to goethite precipitation.....	44
Figure 2-3: Diagram adapted from Hurowitz et al. [2006] showing a mechanism for alteration of rock surfaces.....	45
Figure 2-4: Diagram from Chemtob et al. [2014] showing a mechanism for silica coating formation on Hawaiian basalts.....	46
Figure 3-1: Overview of alteration material observed for Irvine, Backstay, Pathfinder Soil, and Pathfinder Rock material	96
Figure 3-2: Scanning electron micrograph of the Irvine material altered in pH0.....	97
Figure 3-3: Raman spectra acquired with a 532 nm laser on the unpolished surfaces of the Irvine material altered in pH0-1	98
Figure 3-4: X-ray diffractograms for the Irvine and Backstay material altered in pH0 ...	99
Figure 3-5: Scanning electron micrograph of the Irvine material altered in pH1.....	100
Figure 3-6: A) Reflectance spectra of unaltered and altered (pH0-1) Irvine glass samples plotted with B) the best fit library spectra.....	101
Figure 3-7: Modeled thermal emission spectra of Irvine glass and pellet material altered in pH0, pH1, and pH3	102
Figure 3-8: Scanning electron micrograph of the Backstay material altered in pH0.....	103
Figure 3-9: Raman spectra acquired with a 532 nm laser on the unpolished surfaces of the Backstay material altered in pH0-1.....	104
Figure 3-10: Scanning electron micrograph of the Backstay material altered in pH1....	105
Figure 3-11: A) Reflectance spectra of unaltered and altered (pH0-1) Backstay glass samples plotted with B) the best fit library spectra	106
Figure 3-12: Modeled thermal emission spectra of Backstay glass and pellet material altered in pH0, pH1, and pH3	107
Figure 3-13: A) Reflectance spectra of unaltered and altered (pH0-1) Pathfinder soil glass samples plotted with B) the best fit library spectra.....	108
Figure 3-14: Modeled thermal emission spectra of Pathfinder soil glass material altered in pH0-4	109
Figure 3-15: A) Reflectance spectra of unaltered and altered (pH0-1) Pathfinder rock glass samples.....	110
Figure 3-16: Modeled thermal emission spectra of Pathfinder rock glass material altered in pH0-4.....	111
Figure 3-17: Comparison of the A) reflectance signatures and B) thermal emission signatures of the unaltered and altered material from the four compositions; Irvine, Backstay, Pathfinder soil, and Pathfinder rock.....	112
Figure 4-1: Diagram displaying the effects of Cl (0.7 wt. %) and H ₂ O (0.8 wt. %) on the liquidus of a Humphrey like basalt from Filiberto and Treiman [2009]	136
Figure 4-2: Overview of alteration material observed for Irvine, Backstay, Pathfinder Soil, and Pathfinder Rock material.....	137

Figure 4-3: Scanning electron micrograph of the Irvine volatile-containing material altered in pH0	138
Figure 4-4: Scanning electron micrograph of the Irvine volatile-containing material altered in pH2	139
Figure 4-5: Scanning electron micrograph of the Irvine volatile-containing glass rock chunk altered in pH0.....	140
Figure 4-6: A) Reflectance spectra of unaltered and altered (pH0-2) Irvine volatile-containing glass samples plotted with B) the best fit library spectra.....	141
Figure 4-7: Comparison of thermal emission signatures for A) IRVG-VC particulate material, B) IRVG-VC pellet material, and C) IRVG-VC powder material	142
Figure 4-8: Modeled thermal emission spectra of Irvine volatile-containing sand-sized glass samples and pellet glass samples altered in pH 0, 2, and 4	143
Figure 4-9: Modeled thermal emission spectra of the Irvine volatile-containing glass rock chunk altered in pH0.....	144
Figure 4-10: Comparison of the A) VNIR reflectance signatures and B) MIR emission signatures for unaltered glass material with Irvine volatile-free (IRVG-VF) and volatile-containing (IRVG-VC) compositions	145
Figure 4-11: Comparison of the infrared signatures for the unaltered and altered material with Irvine volatile-free and volatile-containing compositions.....	146
Figure 5-1: Image of the volcanic vent from which the samples were collected and close-up images of the samples in situ and ex situ.....	186
Figure 5-2: Thermal emission signatures of the collected samples grouped based on similarities of dominant spectral features	187
Figure 5-3: Linear least squares analysis models for the average thermal emission spectrum for each group.....	189
Figure 5-4: Secondary electron images of HI_15_MHY samples.....	190
Figure 5-5: XRD patterns for the three samples that exhibited amorphous humps consistent with more Si-rich material than basaltic glass	191
Figure 5-6: Handheld XRF data separated into groups determined using a minimum distance clustering algorithm on chemical data for each sample. Plots of Al vs. Si contents and Fe vs. Si contents for the natural fumarolic materials	192
Figure 5-7: Comparison of the infrared spectral signatures for the laboratory isochemically altered materials (sulfate-dominated) with the natural fumarolic altered materials (silica-dominated)	193
Figure 6-1: Overview of the A) reflectance signatures and B) thermal emission signatures of the unaltered and altered (pH0-2) material from the four Yant <i>et al.</i> [2016] compositions	233
Figure 6-2: Overview of the A) reflectance signatures and B) thermal emission signatures of the unaltered and altered material from the two Horgan <i>et al.</i> [2017] compositions	234
Figure 6-3: One pixel per degree binned global TES maps showing combined abundances and RMS differences for all of the unaltered and altered material from the four Yant <i>et al.</i> [2016] and two Horgan <i>et al.</i> [2017] compositions and sulfate/glass abundances from the original library [Rogers and Hamilton, 2015]	235
Figure 6-4: One pixel per degree binned global TES maps showing abundances and RMS differences for the altered material from the four Yant <i>et al.</i> [2016] compositions	236
Figure 6-5: One pixel per degree binned global TES maps showing abundances and RMS differences for the altered material from the two Horgan <i>et al.</i> [2017] compositions....	237

Figure 6-6: Reflectance spectra for each of the regions of interest from the green areas shown in Figure 6-8..... 238

Figure 6-7: Linear least squares models using the Backstay library for TES pixels that overlap with OMEGA sulfate detections in Acidalia 239

Figure 6-8: Images of stamps showing the overlap of Irvine TES pixels with OMEGA sulfate features for Meridiani Planum, Mawrth Vallis, and Valles Marineris 240

Figure 6-9: TES signature from Acidalia plotted along with model using Backstay Library. Shown for comparison are the spectra for average northern and southern Acidalia signatures along with the Backstay material altered under pH0 241

List of Tables

Table 3-1. Previous studies of basalt and tephra alteration	94
Table 3-2. Synthetic Pathfinder, Irvine, and Backstay glass bulk compositions	95
Table 3-3. Acid Solutions used in batch alteration experiments	95
Table 4-1. Synthetic Irvine Glass Bulk Compositions for the Volatile-Free and Volatile-Containing material.....	135
Table 5-1. Previous studies of Hawaiian basalt and tephra in situ alteration from a planetary perspective	183
Table 5-2: Overview of alteration material observed for all of the samples analyzed in this study	184
Table 5-3: Quantitative elemental abundances as determined by hXRF	185
Table 6-1: Library spectra.....	231
Table 6-2: Synthetic Pathfinder, Irvine, Backstay and terrestrial Bas101, Bsb101 glass bulk compositions	232
Table 6-3: Spectral parameters utilized for the detection of sulfates.....	232

A work of science always includes taking from previous researchers and teachers, then adding information to give back to the whole community. I wish to thank my advisor Dr. Deanne Rogers as well as Dr. Timothy Glotch and Dr. Hanna Nekvasil. None of this work would have been possible without the guidance and support of these incredible mentors.

Chapter 1:

Introduction

1.1 Overview

One of the fundamental questions about the geological history of Mars is, what were the style(s), duration, and timing of chemical alteration on the surface/near-surface? One way to help address this question is through analysis of the abundance and distribution of secondary minerals on the surface. Locating regions consistent with alteration phases can provide insight on the aqueous history of Mars and regions for potential habitability. The identity of various secondary minerals (sulfates, chlorides, oxides, and phyllosilicates) has been inferred from chemical and mineralogical analyses of Martian rocks and soils by instruments on the *Pathfinder* [e.g., *Foley et al.*, 2003], *Spirit* [e.g., *Morris et al.*, 2006], *Opportunity* [e.g., *Clark et al.*, 2005], and *Curiosity* [e.g., *Vaniman et al.*, 2014] landers/rovers. These minerals are indicators of aqueous alteration environments at widely separated geographical locations. From orbit, however, evidence of widespread alteration is lacking. The infrared (IR) spectrometers onboard Mars Express (MEx), Mars Reconnaissance Orbiter (MRO), and Mars Global Surveyor (MGS) have observed and mapped some secondary minerals (sulfates, chlorides, carbonates, oxides, phyllosilicates, and zeolites) in numerous, but relatively small-scale, isolated locations [e.g., *Bibring et al.*, 2005; *Gendrin et al.*, 2005; *Langevin et al.*, 2005; *Poulet et al.*, 2005; *Osterloo et al.*, 2008; *Ehlmann et al.*, 2011; *Wray*, 2012]. Spectrally, much of the Martian surface is consistent with unaltered or minimally-altered material [e.g., *Ody et al.*, 2012]. Thus, there is a difference in the picture of Martian surface materials provided by the lander/rover and orbiter data.

From orbit, regolith compositions and alteration are assessed primarily from IR spectroscopy, which is sensitive to mineralogy. Thus, to assess styles and abundance of chemical

alteration, the IR spectral properties of analog materials must be known. Although laboratory alteration experiments have been carried out to understand the chemical and mineralogical end products of basaltic weathering, these end products have been traditionally assessed quantitatively by using rock, fluid, and precipitate geochemistry. Alteration assemblages from these previous experimental studies are not easily translated to expected IR spectral signatures for two reasons. First, experimental studies do not typically report mineral abundance, only the presence of mineral species, making it difficult to assess the influence of alteration products on IR spectral characteristics. Second, weathered surfaces can be difficult to analyze quantitatively with spectroscopy [*Kraft et al.*, 2003; *Michalski et al.*, 2006; *Kraft et al.*, 2007; *Hamilton et al.*, 2008; *Rampe et al.*, 2009]. Because alteration products often form as a thin coating/fracture fill, or are fine-grained and poorly consolidated, inaccuracies can arise due to non-linear spectral mixing from coating and rind geometry [e.g., *Ramsey and Christensen*, 1998]. The problems associated with non-linear mixing cannot be avoided, but insight would be provided from the direct comparison of remotely-sensed data with a library consisting of spectra collected for laboratory unaltered/altered glass materials.

In order to more reliably interpret remote spectra of altered terrains, this work focuses on collecting spectral data of synthetic Martian basaltic glasses from controlled weathering experiments and in-situ hydrothermally-altered Hawaiian basalt and comparing the spectral shapes of the experimental and in-situ materials to orbital data. Currently, most libraries contain spectra of pure, coarse-grained materials; the spectral data obtained here provides spectral libraries that include mixtures of unaltered and altered material, poorly crystalline phases, combinations of various grain sizes, and alteration coatings that are difficult to capture with a standard mineral library. Furthermore, by linking geochemical experiments with IR spectral measurements, we can

assess the degree to which starting pH, composition, and particle size influence the spectral signature of acid-altered Martian materials as well as provide insight on the detectability of alteration phases and distinction of sulfate vs. silica dominated assemblages.

This dissertation includes four science chapters, with relevant background information for glass occurrence, alteration trends on Mars, sulfate formation, and detection of alteration on the surface of Mars provided in *Chapter 2*. The major chapters focused on (1) simulating and spectrally characterizing acid weathering of Martian surface materials (*Chapter 3*), (2) exploring the role of magmatic volatiles on the spectral properties of unaltered and acid-weathered Martian glasses (*Chapter 4*), (3) investigating the spectral and mineralogical differences associated with open- and closed-system weathering on basaltic materials (*Chapter 5*), and (4) using the laboratory spectral measurements of the altered synthetic materials to interpret IR data sets acquired from orbit at Mars (*Chapter 6*). A brief description of the major conclusions is provided in *Chapter 7*. Additional details about each science chapter are provided below.

In *Chapter 3* of this dissertation, isochemical, closed system weathering of synthetic Martian glass particulates was simulated with a low fluid-to-rock ratio and low starting pH range (<4). Based on a number of chemical and mineralogical measurements made by landed missions [*Clark et al., 1993; Haskin et al., 2005; Ming et al., 2006; Clark et al., 2005; Morris et al., 2006*], this type of environment has been proposed as a common and persistent alteration setting on the Martian surface [*Hurowitz and McLennan, 2007; Hurowitz and Fischer, 2014*]. These experiments were performed to address the following questions: 1) Under what conditions does glass alteration result in detectable alteration products? 2) What are the spectral characteristics of the altered samples--do they appear dominated by sulfate, silica, or a mixture of these products? and 3) How does starting composition affect the spectral signatures of altered materials in both the mid-infrared

(MIR) and the visible/near-infrared (VNIR)? For the first time, direct IR spectral analyses of glasses with Martian compositions, altered under controlled conditions, are presented in order to assess surface weathering and regolith development on Mars. Basaltic glasses of Irvine and Backstay composition were synthesized and altered using H₂SO₄-HCl acid solutions (pH0-4). Scanning electron microscopy (SEM), x-ray diffraction (XRD), Raman, and IR spectral measurements were acquired for each reaction product. IR spectra were also acquired from previously synthesized and altered glasses with Pathfinder measured compositions. Acid alteration of glass in the most acidic solutions (pH \leq 1) yielded sulfate-dominated VNIR and MIR spectra. Spectral differences between alteration products from each starting material were present, reflecting strong sensitivity to changes in mineral assemblage. In the MIR, alteration features were preserved after reworking and consolidation. In the VNIR, hydrated sulfate features were present along with strong negative spectral slopes. These glass spectra allow for the direct comparison of laboratory acquired signatures to TES and OMEGA data, which is described in *Chapter 6*.

In *Chapter 4*, the effects of Cl and H₂O on the spectral properties of unaltered and altered synthetic glasses were investigated in order to address whether volatile-containing materials can be spectrally distinguished from volatile-free materials. Volcanic glasses preserve primary melt compositions, along with volatile species that can be used to infer mantle reservoirs and accretionary processes [e.g., *Saal et al.*, 2008]. The availability of both crustal and magmatic volatiles is key for producing significant amounts of glass from volcanism [*Bouška and Bell*, 1993]. The volatile budget of the silicate Earth is dominated by the C-O-H system (O₂, H₂O, H₂, CO₂, CO, and CH₄) and the effects of magmatic volatiles (H₂O, F, Cl, C-species, and S-species) on Earth are well understood. It has been suggested that the C-species are less significant in Martian magmatic systems. Due to this difference, the abundances as well as the roles of magmatic

volatile elements may vary between Mars and Earth. It is important to understand how chlorine and water affect surface mineralogy because both play a crucial role in the surface alteration of Mars as well as during magmatic and degassing processes. Furthermore, volatile contents and species would likely affect the atomic bond length/structures and spectral shapes of glasses, but presently, the effects of volatiles on Martian glass spectra have not been assessed.

A “volatile-containing” (1 wt. % Cl and H₂O added) synthetic Irvine glass was compared with previously studied “volatile-free” (0 wt. % Cl and H₂O added) synthetic Irvine glass. The samples were subjected to low temperature aqueous alteration with various acidic solutions in an identical method to the volatile-free samples. Unaltered and altered samples were characterized using SEM and VNIR, MIR, and Raman spectroscopy. The volatile-free and volatile-containing Irvine glass materials had alteration assemblages which included Ca-, Fe-, Mg-Al-, Al-, and Mg-sulfates. The volatile-free glass assemblage also included Na-Mg-(Fe) and Mn-sulfates, whereas Fe-Al-sulfates were only observed in the volatile-containing glass assemblage. Acid alteration on particles in the most acidic solutions (pH \leq 1) yielded sulfate-dominated VNIR and MIR spectra whereas particles altered in pH \geq 2 were dominated by unaltered glass. Spectral differences were observed between the altered volatile-free and volatile-containing glass material in the MIR and VNIR indicating the importance of including volatile-bearing glasses in spectral libraries used to interpret signatures on the Martian surface.

The previous chapters focused on cation-conservative weathering because it is suggested as the most recent weathering process. However, early Martian history (Noachian to mid-Hesperian) may have been warmer and wetter which would be better represented by an open-system environment. Groundwater systems could also be simulated using this type of environment. In *Chapter 5*, naturally-altered samples were collected from an active fumarolic vent on Kilauea

and analyzed in order to investigate how the chemical and spectral properties of naturally-altered Hawaiian fumarolic deposits compare with those of alteration assemblages formed in other Mars-relevant environments. This work addressed the following questions: 1) What are the VNIR and MIR spectral characteristics of fumarolic alteration from basaltic starting materials? 2) How do the IR spectral signatures relate to chemical and physical variations among samples? 3) How do MIR spectral signatures compare with VNIR signatures? and 4) How do the spectral properties of fumarolic deposits compare with those of alteration assemblages formed in other Mars-relevant environments?

The focus of this chapter is on a solfatara site that consists of hydrothermally-altered basalt and alteration products deposited in and around a passively degassing volcanic vent situated directly adjacent to the December 1974 flow on its northwest side. Reflectance spectra were acquired in the VNIR region and emission spectra in the MIR range in order to better understand the spectral properties of hydrothermally altered materials. The VNIR signatures were consistent with silica, Fe-oxides, and sulfates (Ca, Fe). Primarily silica-dominated spectral signatures were observed in the MIR and changes in spectral features between samples appear to be driven by grain size effects in this wavelength range. The nature of the sample coating and the MIR emission signatures exhibit variations that may be correlated with distance from the vent. Chemical analyses indicate that most surfaces were characterized by silica-rich material, Fe-oxides, and sulfates (Ca, Fe). The silica and Fe-oxide-dominated IR spectral signatures exhibited by the hydrothermally-altered material in this study were distinct from the sulfate-dominated spectral signatures exhibited by previously studied low-temperature aqueous acid-sulfate weathered basaltic glass. This likely reflects a difference in open vs. closed system weathering, where mobile cations are removed from the altered surfaces in the fumarolic setting. The Martian surface has a complex history that

includes volcanic activity and widespread aqueous alteration, likely including hydrothermal environments. Hydrothermal environments are of particular interest as they potentially indicate habitable conditions, due to their ability to provide microbial communities with water and energy in an otherwise cold/arid environment.

In *Chapter 6*, the laboratory acquired IR spectral signatures of altered synthetic Martian basaltic glasses [*Chapter 3, Yant et al., 2016*] and altered terrestrial analog basaltic glasses [*Horgan et al., 2017*] were compared with TES and OMEGA data sets between 70°N and 70°S latitude. This work addressed the following questions: 1) To what degree do Martian surface materials exhibit spectral signatures consistent with alteration via open-system and/or cation-conservative weathering processes? 2) Are there locations spectrally consistent with acidic, low fluid-to-rock ratios, and cation-conservative weathering beyond the rover-investigated sites? and 3) What alteration conditions are represented on Mars currently (at landing sites and globally)? Both TES and OMEGA data sets exhibit strong evidence for acid weathered glass in the northern lowlands of Mars, with additional potential detections in Terra Meridiani, Vallis Marineris, and Mawrth Vallis. Because lander/rover measurements have observed isochemically altered, acid-sulfate weathering at disparate locations, the lack of orbital detections is seemingly in conflict with the rover data. This is primarily attributed to later reworking of soils, which would redistribute the alteration products and dilute their surface abundance. The fine-grained nature of alteration materials may also contribute to their spectral obscuration. The ubiquitous spectral signatures of acid weathering in the northern lowlands suggest a more recent, ongoing process to maintain concentrated alteration materials at the surface. One potential mechanism for this process in the northern lowlands is melting of seasonal water frost, which could release trapped aerosols deposited by previous volcanic eruptions.

1.2 References:

- Bibring, J.-P., Y. Langevin, A. Gendrin, et al., (2005), Mars surface diversity as revealed by the OMEGA/Mars Express observations, *Science* 307, 1576–81.
- Bigham, J. M., and D. K. Nordstrom (2000), Iron and aluminum hydroxysulfates from acid sulfate waters, in *Sulfate Minerals: Crystallography, Geochemistry and Environmental Significance*, edited by C. N. Alpers, J. L. Jambor, and D. K. Nordstrom, pp. 351 – 403, Mineral. Soc. Of Am., Washington, D. C.
- Bouška, V., and J. F. Bell III (1993), Assumptions about the presence of natural glasses on Mars, *J. Geophys. Res.*, 98, 18,719–18,725, doi:10.1029/93JE01959.
- Burns R.D. and D.S. Fisher (1990), Iron–sulfur mineralogy of Mars: magmatic evolution and chemical weathering products, *J. Geophys. Res.*, 95 pp., 14415–14421.
- Clark, B. C. (1993), Geochemical components in Martian soil. *Geochim. Cosmochim. Acta* 57, 4575–4581.
- Clark, B.C., R.V. Morris, S.M. McLennan, R. Gellert, B. Jolliff, A.H. Knoll, S.W. Squyres, T.K. Lowenstein, D.W. Ming, N.J. Tosca, A. Yen, P.R. Christensen, S.P. Gorevan, J. Brückner, W.M. Calvin, G. Dreibus, W.H. Farrand, G. Klingelhöfer, H. Waenke, J. Zipfel, J.F. Bell III, J.P. Grotzinger, H.Y. McSween Jr., R. Rieder (2005), Chemistry and mineralogy of outcrops at Meridiani Planum, *EPSL*. 240, 73-94.
- Ehlmann, B.L., J.F. Mustard, S.L. Murchie, J-P. Bibring, A. Meunier, A.A. Fraeman, and Y. Langevin, (2011), Subsurface water and clay mineral formation during the early history of Mars. *Nature*. 479, 53.
- Foley, C. N., T. Economou, and R. N. Clayton (2003), Final chemical results from the Mars Pathfinder alpha proton X-ray spectrometer, *JGR.*, 108, 8096, E12.

- Gendrin, A., N. Mangold, J.-P. Bibring, et al., (2005), Sulfates in Martian layered terrains: the OMEGA/Mars Express view, *Science* 307, 1587–91.
- Golden, D. C., D. W. Ming, R. V. Morris, and S. A. Mertzman (2005), Laboratory-simulated acid-sulfate weathering of basaltic materials: Implications for formation of sulfates at Meridiani Planum and Gusev crater, Mars, *J. Geophys. Res.*, 110, E12S07.
- Golombek, M. P., et al. (2005), Assessment of Mars Exploration Rover landing site predictions, *Nature*, 436, 44–48, doi:10.1038/nature03600.
- Hamilton, V. E., R. V. Morris, J. E. Gruener, and S. A. Mertzman (2008), Visible, near-infrared, and middle infrared spectroscopy of altered basaltic tephras: Spectral signatures of phyllosilicates, sulfates, and other aqueous alteration products with application to the mineralogy of the Columbia Hills of Gusev Crater, Mars: *JGR-Planets*, v. 113, p. E12S43.
- Haskin, L. A., A. Wang, B. L. Jolliff, H. Y. McSween, B. C. Clark, D. J. Des Marais, S. M. McLennan, N. J. Tosca, J. A. Hurowitz, et al., (2005), Water alteration of rocks and soils from the Spirit rover site, Gusev crater, Mars, *Nature*, 436, 66-69.
- Horgan, B. H. N., R. J. Smith, E. A. Cloutis, P. Mann, and P. R. Christensen (2017), Acidic weathering of basalt and basaltic glass: 1. Near-infrared spectra, thermal infrared spectra, and implications for Mars, *J. Geophys. Res. Planets*, 122, 172–202, doi:10.1002/2016JE005111.
- Hurowitz, J.A., S.M. McLennan (2007), A ~3.5 Ga record of water-limited, acidic weathering conditions on Mars: *EPSL*, v. 260, p. 432-443.
- Hurowitz, J. A., and W. W. Fischer (2014), Contrasting styles of water–rock interaction 862 at the Mars Exploration Rover landing sites, *Geochimica et Cosmochimica Acta*, 127, 863 25-38.

- Kraft, M. D., J. R. Michalski, and T. G. Sharp (2003), Effects of pure silica coatings on thermal emission spectra of basaltic rocks: Considerations for Martian surface mineralogy: *Geophysical Research Letters*, v. 30.
- Kraft, M. D., T. G. Sharp, J. R. Michalski, and E. B. Rampe (2007), Combined Thermal and Near Infrared Spectra of Hydrous Silica Coatings: Implications for Surface Type 2 Mineralogy and Recent Liquid Water on Mars: *Lunar Planet. Sci. XXXVIII*.
- Langevin, Y., F. Poulet, J.-P. Bibring, and B. Gondet (2005), Sulfates in the North Polar region of Mars detected by OMEGA/Mars Express, *Science* 307, 1584–6.
- Madden M. E., R. J. Bodnar and J. D. Rimstidt (2004), Jarosite as an indicator of water-limited chemical weathering on Mars. *Nature* 431, 821–823.
- Michalski, J. R., M. D. Kraft, T. G. Sharp, and P. R. Christensen (2006), Effects of chemical weathering on infrared spectra of Columbia River Basalt and spectral interpretations of martian alteration: *Earth and Planetary Science Letters*, v. 248, p. 822-829.
- Ming D. W., D. W. Mittlefehldt, R. V. Morris, D. C. Golden, R. Gellert, A. Yen, B.C. Clark, S. W. Squyres, W. H. Farrand, S. W. Ruff, R. E. Arvidson, G. Klingelhöfer, H. Y. McSween, D. S. Rodionov, C. Schröder, P. A. de Souza, and A. Wang (2006), Geochemical and mineralogical indicators for aqueous processes in the Columbia Hills of Gusev crater, Mars. *J. Geophys. Res.* 111, E02S12.
- Morris, R. V., G. Klingelhöfer, C. Schröder, D. S. Rodionov, A. Yen, D. W. Ming, P. A. de Souza Jr., I. Fleische, et al. (2006), Mössbauer mineralogy of rock, soil, and dust at Gusev Crater, Mars: Spirit's journey through weakly altered olivine basalt on the plains and pervasively altered basalt in the Columbia Hills. *J. Geophys. Res.*, 111, E02S13, doi:10.1029/2005JE002584.

- Ody, A., F. Poulet, Y. Langevin, J-P. Bibring, G. Bellucci, F. Altieri, B. Gondet, M. Vincendon, J. Carter, and N. Manaud (2012), Global maps of anhydrous minerals at the surface of Mars from OMEGA/MEx, *JGR.*, 117, E00J14.
- Osterloo, M. M., V. E. Hamilton, J. L. Bandfield, T. D. Glotch, A. M. Baldrige, P. R. Christensen, L. L. Tornabene, and F. S. Anderson (2008), Chloride-bearing materials in the southern highlands of Mars, *Science*, 319, 1651–1654, doi:10.1126/science.1150690.
- Poulet, F., J-P. Bibring, J. F. Mustard, et al., (2005), Phyllosilicates on Mars and implications for early martian climate, *Nature* 438, 623–7.
- Rampe, E. B., M. D. Kraft, and T. G. Sharp (2009), Chemical Weathering Trends from TIR Spectral Models: Implications for Deriving Weathering Trends From Martian Spectral Data, *LPSC XL*, Abs. 2132.
- Ramsey, M.S. and P.R. Christensen (1998), Mineral abundance determination: Quantitative deconvolution of thermal emission spectra. *J. Geophys. Res.* 103 (B1), 577–597.
- Saal, A. E., E. H. Hauri, M. L. Cascio, J. A. Van Orman, M. C. Rutherford, and R. F. Cooper (2008), Volatile content of lunar volcanic glasses and the presence of water in the Moon's interior, *Nature*, 454, 192–195, doi:10.1038/nature07047.
- Vaniman, D. T., et al., (2014), Mineralogy of a mudstone on Mars, *Science*, 343.
- Wray, J.J. (2012), The Scientific Necessity of Landing at Diverse Sites on Mars. Concepts and Approaches for Mars Exploration, abstract 4380.
- Yant, M., A. D. Rogers, H. Nekvasil, Y.-Y. S. Zhao, and T. Bristow (2016), Spectral characterization of acid weathering products on Martian basaltic glass, *Journal of Geophysical Research - Planets*, 121, doi:10.1002/2015JE004969.

Chapter 2:

Background

This chapter provides additional background on the major aspects of this dissertation which includes relevant information for glass occurrence, alteration trends on Mars, sulfate formation, and detection of alteration on the surface of Mars.

2.1 Glass on Mars:

Silicate glasses can be formed naturally through volcanism and hypervelocity impacts. The nature and distribution of these materials provide insight into the volcanic and impact processes that form them, and allow interpretation of how planetary bodies evolve [e.g., *Saal et al.*, 2008; *Tompkins and Pieters*, 2010]. Volcanic glasses also preserve primary melt compositions, along with volatile species that can be used to infer mantle reservoirs and accretionary processes [e.g., *Saal et al.*, 2008]. The lower gravity and atmospheric density of Mars create conditions that are more conducive to explosive basaltic eruptions than Earth [*Wilson and Head*, 1994]. Observations of Martian geology have identified numerous deposits suggested to form from explosive volcanic processes that suggestive of degassing volatiles [e.g., *Greeley et al.*, 2000; *Hynek et al.*, 2003; *Grant et al.*, 2010; *Michalski and Bleacher*, 2013] and would be expected to yield glassy deposits. Given the low temperature, humidity, and oxygen partial pressure, glasses formed under the present climatic conditions may have survived to the present time. Additionally, oxidative weathering is extremely slow in the current Martian climate [e.g., *Burns and Fisher*, 1993], and thus glasses predicted to be thermodynamically unstable may exist metastably on the surface [*Gooding*, 1978; *Gooding and Keil*, 1978]. For Mars missions, glass is a crucial material to explore because it can preserve chemical and textural biosignatures [*Howard et al.*, 2013].

High silica amorphous material has been detected as a prevalent component (~10-40 %) across many regions of Mars by the Thermal Emission Spectrometer (TES) [Bandfield *et al.*, 2000; Rogers and Christensen, 2007]. This high silica material ($\text{Si/O} > 0.35$) has been observed with abundances of 15-20% in low-albedo regions and at abundances greater than 30% in Acidalia Planitia and Solis Planum [Bandfield, 2002; Bandfield *et al.*, 2002]. This material has been interpreted as an unweathered volcanic product, potentially glass within a basaltic andesite [Bandfield *et al.*, 2000; Hamilton *et al.*, 2001] or as an alteration product (e.g., smectite clays [Wyatt and McSween, 2002], palagonite [Morris *et al.*, 2003; Morris *et al.*, 2008], silica-rich alteration products [Kraft *et al.*, 2003; Michalski *et al.*, 2005], zeolites [Ruff, 2004; Minitti and Hamilton, 2010], altered basaltic glass [Minitti *et al.*, 2007], and/or oxidative weathering products [Salvatore *et al.*, 2013]). A primary or secondary origin of this high silica material is important as an andesitic basalt would imply magmatic evolution from the typical basalt, subduction and continental crust formation, whereas a silica-rich alteration product would imply widespread alteration on the Martian surface. High silica phases are structurally and compositionally complex; thus, it is difficult to determine the high-silica spectral component of Martian MIR signatures. The regions where this material is observed are typified by Acidalia Planitia (Surface Type 2, ST2) and exhibit spectral signatures consistent with andesite or altered basalt [Bandfield *et al.*, 2000]. Based on observations in the northern lowlands where ST2 signatures are detected, the high-silica phases have been interpreted as altered glasses via interpretation of OMEGA data in the VNIR [Horgan and Bell, 2012]. Glasses have been detected in Hesperian aged materials (e.g., Columbia Hills, Nili Patera), suggesting that glasses are capable of surviving surface weathering on Mars and could be contributing to the high-silica phase detections.

The spectral character of unaltered glass is dependent on composition, polymerization, and its disordered nature. A typical glass signature in the MIR has a broad spectral absorption without internal spectral structure, due to the disordered nature of the glass [Parke, 1974; Johnson *et al.*, 2002]. The position of the emissivity minimum for the broad absorption is controlled by the composition and polymerization of the tetrahedral framework. Divalent cations (e.g., Fe, Mg, Ca) lengthen the average Si-O bond distance resulting in a shift of the Si-O features near 1000cm^{-1} (silicate stretching vibrations) and 500cm^{-1} (silicate bending vibrations) to lower wavenumbers [e.g., King *et al.*, 2004]. Glasses with relatively lower silica contents will have MIR features that are less intense and broader because of the larger distribution of energies due to the lengthening of the Si-O bond distance [Hamilton *et al.*, 2008]. Natural Fe-bearing glass exhibits an absorption band between 1.07 and $1.20\mu\text{m}$ [e.g., Adams, 1974; Minitti *et al.*, 2002], and sometimes exhibits a second absorption centered between 1.90 and $2.05\mu\text{m}$ [e.g., Horgan *et al.*, 2014]. The spectral character of volcanic glass can be distinguished from impact glass [e.g., Farrand *et al.*, 2016]. The Si-O bending feature is observed to be broader in volcanic glass relative to impact glass. Furthermore, partially/fully devitrified glass exhibits unique spectral signatures when compared with pristine glass [e.g., Crisp *et al.*, 1990; Farrand *et al.*, 2016]. Changes in the features are observed for the devitrified glass as disordered silica tetrahedra become ordered into chains/sheets of silica tetrahedra.

When volcanic glass is exposed to an acidic fluid, dissolution initiates with the removal of the network modifying cations in the order of the relative rates for breaking their corresponding metal–oxygen bonds. Dissolution continues with successive removal of cations in the order of the relative rates for breaking their corresponding metal–oxygen bonds until the glass is destroyed or the reaction is halted (e.g., evaporation). For the basaltic glasses utilized in this study, the network

modifying cations are more soluble in the acidic solutions than the network forming cations, Si and Al; this results in the formation of a Si and Al-rich surface layer [e.g., *Oelkers et al.*, 2009]. The Si-O bonds are the slowest breaking bonds resulting in increased resistance to weathering for glasses with higher silica contents [e.g., *Wolff-Boenisch et al.*, 2004].

2.2 Alteration Trends on Mars vs. Earth

Experimental work on the acid-sulfate alteration of synthetic Martian material by *Tosca et al.*, [2004] provided significant background for the work presented here. [Tosca *et al.*, 2004] observed that the difference in bulk chemistry between terrestrial and Martian basalt compositions significantly affects the secondary mineralogy of the alteration material. Synthetic rock and soils (based on compositions measured by the Mars Pathfinder Rover mission) were exposed to acidic solutions (pH ~0-4) with fluid to rock ratios of 1:1 and 10:1, under ambient temperature and pressure conditions. The secondary mineral assemblages formed from these Pathfinder experiments indicated the significant impact of primary mineralogy on Martian aqueous alteration, as well as placed constraints on the reactivity of primary lithologies and the alteration assemblages that occur on the surface of Mars.

On Earth, alteration products are usually enriched in the less soluble elements Al and Fe⁺³, because the more soluble elements, Ca, Na, Mg, and K are leached from the primary material (**Figure 2-1**). This is a consequence of the pH range of the typical groundwater under terrestrial conditions, which falls within a range of approximately 5 (Hawaiian rain forest soils) - 9 (sparsely vegetated regions of Iceland), as well as the fluid-to-rock ratio [*Hurowtiz et al.*, 2006]. This results in an assemblage dominated by clay minerals, Al-hydroxides, and Fe-oxides that formed under moderate pH and high fluid-to-rock ratios. However, the weathering profile on Mars (**Figure 2-1**) is dictated by more acidic conditions and low fluid-to-rock ratios. Acidic conditions have been

identified in Hesperian terrains at landing sites (e.g., Meridiani Planum, Gusev Crater) and are hypothesized to have been common during this time period based on widespread detection of Hesperian sulfates from orbit and geochemical models of Hesperian climatic conditions [e.g., *Hurowitz and McLennan, 2007*]. Utilizing previous experimental studies by *Tosca et al. [2004]* and *Hurowitz et al. [2005]*, *Hurowitz et al. [2006]* observed that, under the more acidic conditions suggested for Mars, Fe^{+3} and Al are more soluble (**Figure 2-2A-B**) resulting in a unique weathering profile. In addition, the rate of Fe^{+2} oxidation to Fe^{+3} is orders of magnitude lower under more acidic conditions, which allows Fe^{+2} to remain in solution for a longer time period. This results in an alteration assemblage dominated by sulfates (Mg, Fe, +/- Ca), and silica that formed under low pH and lower fluid-to-rock ratios [*Hurowitz et al., 2006*].

Sulfate and silica are commonly identified as alteration products from Martian analog studies (**Table 2-1**). Sulfate and silica present on the surface of substrates each contribute uniquely to the visual appearance and IR spectral signatures observed for the material. *Hurowitz et al. [2006]* suggests a model for the formation of the sulfate-dominated alteration observed at Gusev crater (**Figure 2-3**). Small volumes of acidic fluid react with the surface of the material resulting in a fluid enriched in the most soluble elements (in the case of glass) or elements contained in the primary minerals undergoing the most rapid alteration (in the case of crystalline) (**Figure 2-3A**). An alteration rind, depleted in the most soluble elements, is left behind (**Figure 2-3B**), and the fluid subsequently undergoes evaporation and deposits alteration minerals (**Figure 2-3C**). Si^{+4} is relatively insoluble in low pH conditions ($\text{pH} < 2-3$) and basaltic cations are relatively mobile [*El-Shamy et al., 1972*; *Minitti et al., 2007*]. This can result in basalt leaching or dissolution that could form a silica-enriched layer beneath the fluid containing the mobile cations. When the fluid is evaporated, in a closed system, salts containing the more mobile cations can precipitate on top of

the silica-enriched layer. The formation of the sulfates overlying the silica layer results in a larger spectral signal from the sulfates relative to the silica. In order to form a sulfate-dominated assemblage, the fluid-to-rock ratio needs to be small enough that the soluble elements are not mobilized and are allowed to evaporate on top of the leached surface in a closed system.

If the system is open and the fluid can migrate, a silica-dominated assemblage can be formed. Silica rich coatings have been observed to form on basalt surfaces over longer periods of time in neutral pH conditions [Dorn, 2012] and in shorter periods of time in acid pH conditions [Chemtob and Rossman, 2014]. Chemtob and Rossman [2014] suggest that silica coatings on glassy basalts from Hawaii are formed by reaction of acidic fluids in an open system (**Figure 2-4**). The liquid becomes acidified by volcanically derived fluids (**Figure 2-4A-B**). Reaction of this low pH fluid dissolves the basalt. The basaltic cations are more soluble than the silica and the cations remain dissolved at low pH and the silica is precipitated in place. The fluid is mobilized carrying away the more soluble cations, leaving behind Ti and Fe⁺³, which have lower mobility and are deposited as Fe-Ti-oxides, in addition to the silica (**Figure 2-4C**). Silica can also be transported to the surface by fluids that penetrate to the interior of the basalt (**Figure 2-4D-E**). As alteration continues over a period of years, episodes of dissolution-reprecipitation can result in the thickening of the silica layer and the remobilization of Fe and Ti to the surface (**Figure 2-4F**).

2.3 Sulfate Formation

Sulfates can be formed on Mars through a variety of mechanisms including 1) surface weathering of volcanic material [e.g., Bibring *et al.*, 2005], 2) oxidation of sulfides [Dehouck *et al.*, 2012], or 3) evaporation of standing bodies of water [e.g., Tosca *et al.*, 2005]. Some sulfates indicate acidic conditions (e.g., jarosite), and can provide insight into the aqueous fluid history of Mars. In this study, we focus on the surface weathering of volcanic rocks which can form sulfates

through a variety of mechanisms including, 1) formation in dirty (aerosol containing) ice [Niles and Michalski, 2009], 2) condensation of acid fog [e.g., Banin et al., 1997; Tosca et al., 2004], 3) seasonal melting of ice or snow [Kite et al., 2013], and 4) exposure to hydrothermal systems [e.g., McCollum and Hynek, 2005; Ruff et al., 2011]. The first two mechanisms typically occur in low temperature conditions while the third and fourth potentially occur at higher fluid-to-rock ratios. Here, IR spectral properties of volcanic surfaces altered under cation conservative conditions (possible analog for dirty ice and acid fog) and open system conditions (possible analog for seasonal melting and hydrothermal alteration) are analyzed.

Acid weathering inside the dirty ice has been hypothesized to occur when thin films of water, formed through radiant heating, enable the reaction between silicate material and sulfate-rich aerosols deposited from the atmosphere during previous volcanic outgassing as described by Niles and Michalski et al. [2009]. Mars had extreme amounts of outgassing occurring earlier in its history that could produce ice deposits with significant sulfur contents. This weathering mechanism is a closed-system, low fluid-to-rock environment that occurs at low temperatures and can produce sulfates along with poorly crystalline aluminosilicates and oxides/oxyhydroxides. Additionally, seasonal melting of snow or ice due to changes in obliquity can provide a source of water for acidic alteration, which can occur on a greater spatial scale [Kite et al., 2013]

Acid fog involves the interaction of volcanically derived acidic volatiles with crustal material resulting in mineral/glass dissolution under low fluid to rock ratios and low temperatures. The basalt-fluid reaction durations are short, which limits the contribution of elements to the fluid during dissolution restricting the formation of large crystals. The timescale for acid fog alteration is on the order of years, Settle [1979] suggests that during periods of persistent volcanism SO₂ gas could become globally distributed on short timescales (days), be oxidized to form sulfuric acid

aerosol droplets ($\text{H}_2\text{SO}_4 \cdot n\text{H}_2\text{O}$) within a few months or years, and then gravitationally settle onto the surface within a similar time period (months to a few years). The acid fog model also involves little transport of fluid, resulting in isochemical weathering [Golden *et al.*, 2005] with spectral signatures dominated by hydrated sulfates [Yant *et al.*, 2016]. The bulk chemistry of the volcanic material being weathered significantly affects the secondary mineralogy of the alteration material [Tosca *et al.*, 2004; Yant *et al.*, 2016].

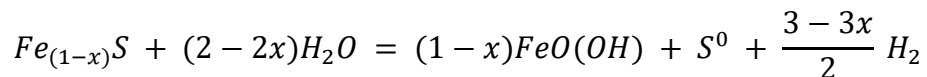
Fumarolic alteration, specifically at a solfatara, involves hydrothermal modification of the volcanic material resulting in silica and Fe-oxide dominated spectral features. Silica formation may be due to aerosol fallout from the fumarole or due to leaching caused by acid rain/acid fog interactions [Schiffman *et al.*, 2006; Minitti *et al.*, 2007]. In this environment, volcanically derived acidic fluids can interact with basaltic materials and result in dissolution. The basaltic cations are more soluble than the silica and the cations remain dissolved at low pH and the silica is precipitated in place. The fluid is mobilized carrying away the more soluble cations, leaving behind Ti and Fe^{+3} , which have lower mobility and are deposited as Fe-Ti-oxides, in addition to the silica. This mobilization is facilitated by liquid water, possibly sourced from rainwater and condensed water vapor from nearby plumes [Chemtob and Rossman, 2014]. Consequently, this can result in silica or Fe-oxide-dominated spectral signatures at the source and sulfate signatures away from source.

Sulfates can also be formed through the oxidation of sulfides. Results from Dehouck *et al.* [2012] indicated that the reaction of sulfides, specifically pyrrhotite, with basaltic silicates under neutral conditions, can produce sulfates. This provides a mechanism for sulfate formation without low pH conditions and could possibly provide unique spectral features. The weathering of pyrrhotite can produce elemental sulfur and Fe-oxyhydroxides. The sulfur can be further oxidized to produce sulfuric acid. The formation of Ca- and Mg-sulfates in these experiments indicates that

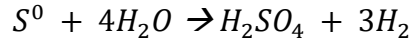
silicates were altered along with pyrrhotite, because silicates were the only source of these cations in the closed chemical system. The acidification induced by the weathering of pyrrhotite promoted the weathering of silicates and formation of sulfates.

The third mechanism for forming sulfates on Mars is from the evaporation of standing bodies of water. This requires vastly more fluid than the previous two mechanisms, which can produce more crystalline sulfates, which are well observed in spectral signatures. Evaporation in a closed system produces an evaporite sequence that reflects the chemistry of host rock. This is a common weathering mechanism on Earth; however, the evaporite sequence will be distinct for Mars given its basaltic composition and relatively lower pH fluids [Hurowitz *et al.*, 2006]. Martian fluids are enriched in Mg, SiO₂, Ca, and under acidic conditions, Fe [Tosca and McLennan, 2006]. Chemical reactions will generally be driven by acidic fluids and subsequent increase in pH from interaction with mafic minerals. These acidic fluids have a high buffering capacity that can require more rock interactions to reach relative higher pH fluids [e.g., Hurowitz *et al.*, 2006].

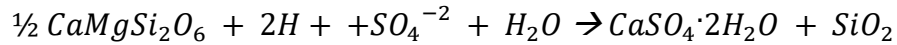
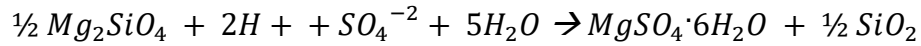
The source of acidity and sulfur involved in these mechanisms include the initial bulk composition of the rock (e.g., sulfides) [Dehouck *et al.*, 2012], volcanic emissions [e.g., Bibring *et al.*, 2006], impact recycling [e.g., McLennan *et al.*, 2006] and/or hydrolysis associated with iron oxidation [e.g., Hurowitz *et al.*, 2010]. Reaction of sulfides (e.g., pyrrhotite) with basaltic silicates (e.g., olivine, pyroxene) under neutral conditions can produce sulfates as described previously [Dehouck *et al.*, 2012]. The weathering of pyrrhotite can produce elemental sulfur and Fe-oxyhydroxides through the following equation:



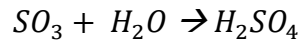
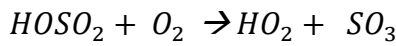
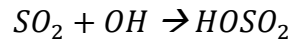
In order to produce sulfates, further oxidation of sulfur and dissolution of silicates is needed to form sulfuric acid:



The sulfuric acid can interact with silicate minerals to form sulfates:



Settle [1979] suggested that sulfates on Mars would form in the atmosphere from volcanic emissions. Sulfur isotopes in Martian meteorites confirmed this hypothesis. This provides a means for sulfates being detected across the planet. Formation of sulfuric acid in the gas phase can be explained by the following equations:



Gas-particle conversion occurs when the saturation vapor pressure of H₂SO₄ is exceeded. This is likely to occur over conversion to elemental sulfur as shown by previous work in a CO₂ atmosphere. Relative to terrestrial volcanic systems, Tharsis has a sulfur content increased by a factor of 4 to 7 [*Gaillard and Scaillet, 2009*]. This could be due to the higher iron content observed for Martian magmas as sulfur preferentially partitions with iron. An oxidizing environment would produce the H₂S and SO₂ gasses necessary to form sulfates. In a reducing environment, sulfides would be formed from Tharsis which also provide the necessary components for sulfates [*Gaillard and Scaillet, 2009*]. Evidence for volcanic activity as recent as the Late Amazonian is provided by crystallization ages of the Martian meteorites and crater counts as young as a few million years.

Impact processes could also be associated with the generation of sulfur-rich acidic fluids through the recycling of sulfate bearing soils/sedimentary rocks [e.g., *McLennan et al.*, 2006; *Zolotov*, 2007]. This phenomenon has been studied on Earth through the Chicxulub impact which released several orders of magnitude more sulfur gas relative to a volcanic eruption [*Pope et al.*, 1997; *Pierazzo et al.*, 1998]. Similar processes could have taken place on Mars producing acids in the cooling plumes from impact into the sulfur-rich Martian regolith. Impact generated fine particles and glasses could be altered along with surrounding surface materials and potentially alteration could reach the subsurface. This mechanism would allow for the generation of acidic fluids with or without a warm/wet climate, although a warm/wet climate would have diluted acids and reduced the amount of acid weathering. Impacts were most prevalent during the Noachian and the impact-generated rainfalls could have provided a source for the formation of valley networks and acidic fluids without invoking a prolonged warm/wet climate [*Segura et al.*, 2002]. Noachian clay deposits could have persisted through acid weathering due to their massive nature and low permeability.

The oxidation of ferrous iron to form ferric sulfates and iron oxides is another potential source for acidity [*Hurowitz et al.*, 2010]. *Hurowitz et al.* [2010] provide a mechanism in which near neutral pH subsurface waters that are rich in ferrous iron were oxidized from exposure to dissolved molecular O₂ or by ultraviolet radiation. This oxidation would result in the formation of schwertmannite (Fe³⁺₁₆O₁₆(OH,SO₄)₁₂₋₁₃·10-12H₂O) which could then dissolve and reprecipitate to form jarosite (KFe³⁺₃(OH)₆(SO₄)₂) and goethite (FeO(OH)); the goethite can dehydrate and form hematite (Fe₂O₃) [*Glotch et al.*, 2004; *Glotch et al.*, 2006]. Acid is generated during the Fe oxidation and formation of the previously mentioned secondary minerals. This

mechanism only accounts for acid produced from Fe oxidation, the oxidation of reduced sulfur could also produce acid [Halevy *et al.*, 2007].

2.4 Alteration Detection on Mars

The sulfates detected on Mars are predominantly consistent with the major components of altered mafic igneous rocks (Mg, Fe Ca, Al and Na). The sequence of sulfate precipitation is determined by the solubility of specific sulfate phase, with solubility increasing from Mg-, Ca-, Fe-, to Al-sulfates where Mg-sulfates are the first to precipitate and Al-sulfates are the last. Mg-sulfates were observed in Chryse Planitia and Utopia Planitia duricrusts by the Viking X-ray Fluorescence Spectrometer (XRFS) onboard Pathfinder [Clark *et al.*, 1991]. Mg-, Ca-, and Fe-sulfates have been observed for rocks and soils at Gusev crater by the Alpha Particle X-ray Spectrometer (APXS) [Haskin *et al.*, 2005; Ming *et al.*, 2006; Wang *et al.*, 2006] and Mossbauer instruments [Morris *et al.*, 2006] onboard the Mars Exploration Rover (MER), *Spirit*. Furthermore, the Miniature Thermal Emission Spectrometer (Mini-TES) detected sulfates in several classes of Gusev crater rocks, Clovis (10-25% sulfate, gypsum and epsomite), Wishstone (10% sulfate, anhydrite), Watchtower (5-15% sulfate, gypsum) [Ruff *et al.*, 2006]. Silica was also observed by APXS for Gusev soils [Ming *et al.*, 2006; Haskin *et al.*, 2005]. Mg-, Ca-, and Fe-sulfates were detected in Meridiani Planum outcrops by the APXS [Clark *et al.*, 2005] and Mossbauer [Klingelhofer *et al.*, 2004] instruments onboard the MER, *Opportunity*. Sulfates (Mg, Ca, Fe) and Fe-oxide (hematite) were also detected by the Mini-TES at Meridiani Planum within Eagle crater and across the plains between Eagle and Endurance craters (10-35% sulfate) [Christensen *et al.*, 2004a; Glotch *et al.*, 2006]. Cl/Br salts were observed by the APXS instrument in Meridiani Planum soils, rock, and outcrops [Rieder *et al.*, 2004; Clark *et al.*, 2005]. Chemin onboard

Curiosity detected calcium sulfates, iron oxide or hydroxides, iron sulfides, amorphous material, and trioctahedral smectites at Yellowknife Bay in Gale Crater [Vaniman *et al.*, 2014].

In general, the MER missions observed secondary assemblages dominated by Fe-oxides and Mg-, Fe-, and Ca-sulfates and the Pathfinder mission observed Mg-sulfate. These assemblages are consistent with olivine weathering in basalts under low pH and low fluid-to-rock ratios [Hurowitz *et al.*, 2006]. Although there are some cases where the altered material was enriched in Al, which suggests non-isochemical alteration [Ming *et al.*, 2006], most of the altered materials observed by the MERs still have a basaltic chemical composition indicating isochemical alteration and/or low fluid-to-rock ratios [Bell, 2008]. The most recent rover mission, however, observed a different alteration assemblage in rocks that included phyllosilicates and minor amounts of sulfates [Vaniman *et al.*, 2014]. Interaction of basalt under moderate to alkaline pH and high fluid-to-rock ratios is suggested by this unique assemblage [Bridges *et al.*, 2015]. In any case, all of the landing sites exhibit evidence for chemical alteration, both on the surface and in rock interiors [e.g., Hurowitz and McLennan., 2007; Bridges *et al.*, 2015].

From orbit, however, evidence of widespread alteration is lacking. The VNIR spectrometers OMEGA [e.g., Gendrin *et al.*, 2005; Carter *et al.*, 2013] and CRISM [e.g., Bishop *et al.*, 2008; Mustard *et al.*, 2008; Ehlmann *et al.*, 2011] have observed and mapped some hydrated secondary minerals in numerous, but relatively small-scale, isolated locations [e.g., Bibring *et al.*, 2005; Gendrin *et al.*, 2005; Langevin *et al.*, 2005; Poulet *et al.*, 2005; Ehlmann *et al.*, 2011; Ehlmann and Edwards, 2014]. Most orbital sulfate detections have been observed in the VNIR wavelength range using CRISM and/or OMEGA data sets [e.g., Murchie *et al.*, 2009; Milliken *et al.*, 2010; Ackiss and Wray, 2012; Carter *et al.*, 2013; Ehlmann and Edwards, 2014]. CRISM is a hyperspectral imager on the Mars Reconnaissance Orbiter spacecraft that collects data spanning

the VNIR and MIR wavelengths from 0.4-5.1 μm . The spatial resolution ranges from 200m/pixel to 18m/pixel [Murchie *et al.*, 2007]. OMEGA is a VNIR hyperspectral imager (0.35 to 5.1 μm) onboard Mars Express. The spatial resolution of this instrument is lower than CRISM and ranges from 4.8km/pixel to 300m/pixel [Bibring *et al.*, 2004]. Alteration mineral features can be observed in VNIR wavelength region of OMEGA and CRISM data because this range is sensitive to the crystal field transitions, charge transfers, and vibrational features of iron-bearing and hydrated minerals [Burns, 1993; Clark, 1999]. Hydrated phases are detected by combinations and overtones of vibration transitions in the 1.1 – 2.65 μm range, while most of the fundamental vibrations lie outside of this range, between 2.7 and 15 μm [e.g., Clark *et al.*, 1990; Cloutis *et al.*, 2002, 2006; Bishop *et al.*, 2008]. OH induces stretching overtones in the 1.35–1.55 μm region and vibration transitions in the 2.14-2.65 μm range that vary based on the cation involved. H₂O combination features are generally observed in the 1.9 μm range. S–O bending overtones are also observed in this range, usually occurring between 2.2 and 2.5 μm [Cloutis *et al.*, 2006]. In general, the primary and secondary indicators of polyhydrated sulfates occur near 1.4 (OH), 1.9 (H₂O), and 2.4 (S-O) μm and the indicators for a monohydrated sulfate occur near 2.1 (shifted H₂O) and 2.4 (S-O) μm [Lichtenberg *et al.*, 2010].

The MIR spectrometers TES [e.g., Christensen *et al.*, 2000] and THEMIS [e.g., Viviano and Moersch, 2012] have observed very limited secondary minerals (e.g., oxides and phyllosilicates). TES is a spectrometer onboard Mars Global Surveyor that collects MIR data from 6-50 μm at a spatial resolution of 3km [Christensen *et al.*, 1992]. THEMIS is a camera onboard the Mars Odyssey orbiter that is meant to be used in conjunction with TES as it provides increased spatial resolution (100m), but decreased spectral resolution (10 bands between 6 and 15 micrometers) relative to TES [Christensen *et al.*, 2003]. In the MIR sulfates produce unique spectral signatures

that are dependent on the cations involved as well as the hydration state. However, in general the MIR spectra of sulfates have internal vibrational features near 1050-1250 (ν_3 asymmetric stretch), 1000 (ν_1 symmetric stretch), 500-700 (ν_4 asymmetric bend), and 400-500 (ν_2 symmetric bend) cm^{-1} [e.g., *Herzberg*, 1945; *Nakamoto*, 1986; *Vassallo and Finnie*, 1992; *Bishop and Murad*, 2005], and at $<550\text{cm}^{-1}$ due to lattice vibrations [e.g., *Serna et al.*, 1986; *Clark*, 1999]. Spectrally, much of the Martian surface is consistent with unaltered or minimally-altered material [e.g., *Ody et al.*, 2012]. Thus, there is a difference in the picture of Martian surface materials provided by the lander/rover and orbiter data.

There are a few potential reasons for this. First, alteration durations and conditions were likely spatially variable across the planet; perhaps not all regions experienced the alteration style or durations as those inferred from the landing sites. Second are the disparate spatial scales; perhaps unaltered and altered materials are mixing in the field of view [e.g., *Viviano*, 2012]. For example, basaltic grains capable of saltation typically contain the lowest abundances of alteration products at Gusev crater [e.g., *Bandfield et al.*, 2011]; perhaps basaltic sands mix with altered rocks in the spectrometer fields of view and reduce the detectability of alteration. Third is the idea that alteration assemblage mineral abundances measured through in-situ chemical and Mössbauer measurements (or from laboratory alteration experiments) are not easily translated into IR spectral signatures due to non-linear mixing, making it difficult to project the influence of alteration products on the spectral characteristics measured from orbit. Spectral characteristics and detectability of alteration depends greatly on the presence of mixtures, particle size, and areal coverage within the field of view [e.g., *Michalski et al.*, 2006]. Thus, the limited detections could be a result of the difficulties in translating chemically-measured alteration to spectral characteristics. We can address this third possibility by directly comparing laboratory alteration

signatures of Martian surface material from this study with TES and OMEGA data. Instead of interpreting surfaces as basalt plus alteration products, where the secondary phases are not distinguished from one another [e.g., *Rogers and Christensen, 2007*], we can possibly infer the type of weathering environment, primary lithology, and/or the spatial variability by direct comparison of spectral shape.

2.5 References:

- Ackiss S, Wray J. (2012), Hydrated sulfates in the southern high latitudes of Mars. *Lunar Planet. Sci. Conf. Abstr.* 43:2434.
- Adams, J. B., C. Pieters, and T. B. McCord (1974), Orange glass - Evidence for regional deposits of pyroclastic origin on the moon, In: *Lunar Science Conference*, 5, 171–186.
- Bandfield, J. L., V. E. Hamilton, and P. R. Christensen (2000), A global view of Martian surface compositions from MGS-TES, *Science*, 287, 1626– 1630.
- Bandfield, J. L. (2002), Global mineral distributions on Mars, *J. Geophys. Res.*, 107(E6), 5043, doi:10.1029/2001JE001802.
- Bandfield, J. L., K. S. Edgett, and P. R. Christensen (2002), Spectroscopic study of the Moses Lake dune field, Washington: Determination of compositional distributions and source lithologies, *J. Geophys. Res.*, 107(E11), 5092, doi:10.1029/2000JE001469.
- Bandfield, J.L., A.D. Rogers, C.S. Edwards (2011), The Role of Aqueous Alteration in the Formation of Martian Soils, *Icarus*, 211, 157–171.
- Banin, A., F. X. Han, I. Kan, and A. Cicelsky (1997), Acidic volatiles and the Mars soil: *J. Geophys. Res.-Planets*, v. 102, p. 13341-13356.
- Bell, J. F. (2008), *The Martian Surface. Composition, Mineralogy and Physical Properties*, Cambridge Univ. Press, Cambridge, U. K., ISBN-13 978-0- 521-86698-9.

- Bibring, J. -P., et al. (2004), OMEGA: Observatoire pour la Minéralogie, l'Eau, les Glaces et l'Activité, in Mars Express: The Scientific Payload, edited by A. Wilson and A. Chicarro, 37–49, pp., volume 1240 of ESA Special Publication, August, Noordwijk, The Netherlands.
- Bibring, J.-P., Y. Langevin, A. Gendrin, et al., (2005), Mars surface diversity as revealed by the OMEGA/Mars Express observations, *Science* 307, 1576–81.
- Bibring, J.-P., Y. Langevin, J. F. Mustard, F. Poulet, R. Arvidson, A. Gendrin, B. Gondet, N. Mangold, P. Pinet, and F. Forget (2006), Global mineralogical and aqueous Mars history derived from OMEGA/Mars express data, *Science*, 312, 400–404, doi:10.1126/science.1122659.
- Bishop, J.L. and Murad, E. (2005) The visible and infrared spectral properties of jarosite and alunite. *American Mineralogist*, 90, 1100.1107.
- Bishop et al., (2008), Phyllosilicate diversity and past aqueous activity revealed at Mawrth Vallis, Mars. *Science* 321:830–833.
- Bridges, J. C., S. P. Schwenzer, R. Leveille, F. Westall, R. C. Wiens, N. Mangold, T. Bristow, P. Edwards, and G. Berger (2015), Diagenesis and clay mineral formation at Gale Crater, Mars, *J. Geophys. Res. Planets*, 120, 1–19, doi:10.1002/2014JE004757.
- Burns, R.G. and D.S. Fisher (1993), Rates of oxidative weathering on the surface of Mars, *J. Geophys. Res.*, 98, 3365-3372.
- Burns, R. (1993), *Mineralogical Applications of Crystal Field Theory*, Second Edition, Cambridge University Press, Cambridge, 551p.
- Carter et al., (2013), Hydrous minerals on Mars as seen by the CRISM and OMEGA imaging spectrometers: Updated global view. *JGR*, 118:831–858.

- Chemtob, S.M, G.R. Rossman, (2014), Timescales and mechanisms of formation of amorphous silica coatings on fresh basalts at Kīlauea Volcano, Hawai'i, *Journal of Volcanology and Geothermal Research*, Volume 286, 1 October 2014, Pages 41-54, ISSN 0377-0273.
- Christensen, P. R., et al. (1992), Thermal Emission Spectrometer experiment: The Mars Observer mission, *J. Geophys. Res.*, *97*, 7719–7734.
- Christensen, et al., (2000), Detection of crystalline hematite mineralization on Mars by the Thermal Emission Spectrometer: Evidence for near-surface water. *JGR*, *105*:9623–9642.
- Christensen, P.R., Bandfield, J.L., Bell, J.F., III, Hamilton, V.E., Ivanov, M.A., Jakosky, B.M., Kieffer, H.H., Lane, M.D., Malin, M.C., McConnochie, T., McEwen, A.S., McSween, H.Y., Jr., Moersch, J.E., Neelson, K.H., Rice, J.W., Jr., Richardson, M., Ruff, S.W., Smith, M.D., and Titus, T.N. (2003), Morphology and composition of the surface of Mars: Mars Odyssey THEMIS results: *Science*, v. 300, p. 2056–2061, doi: 10.1126/ science.1080885.
- Christensen, P.R., Wyatt, M.B. Glotch, T.D., Rogers, A.D., Anwar, S., Arvidson, R.E., Bandfield, J.L., Blaney, D.L., Budney, C., Calvin, W.M., Fallacaro, A., Fergason, R.L., Gorelick, N., Graff, T.G., Hamilton, V.E., Hayes, A.G., Johnson, J.R., Knudson, A.T., McSween Jr., H.Y., Mehall, G.L., Mehall, L.K., Moersch, J.E., Morris, R.V., Smith, M.D., Squyres, S.W., Ruff, S.W., and Wolf, M.J. (2004a) Mineralogy at Meridiani Planum from the Mini-TES experiment on the Opportunity rover. *Science*, *306*, 1733-1739.
- Christensen, P.R., S. W. Ruff, R. L. Fergason, A.T. Knudson, R. E. Arvidson, J. L. Bandfield, D.L. Blaney, C. Budney, W. M. Calvin, T. D. Glotch, M. P. Golombek, T.G. Graff, V.E. Hamilton, A. Hayes, J.R. Johnson, H. Y. McSween, Jr., G. L. Mehall, L. K. Mehall, J.E. Moersch, R.V. Morris, A. D. Rogers, M. D. Smith, S.W. Squyres, M.J. Wolff, and M.B. Wyatt. (2004b) Initial

results from the Mini-TES experiment in Gusev crater from the Spirit Rover, *Science*, 305, 837-842.

Clark, R.N., T.V.V. King, M. Klejwa, G. Swayze, and N. Vergo (1990), High Spectral Resolution Reflectance Spectroscopy of Minerals, *J. Geophys Res.* **95**, 12653-12680.

Clark, B.C., R.V. Morris, S.M. McLennan, R. Gellert, B. Jolliff, A.H. Knoll, S.W. Squyres, T.K. Lowenstein, D.W. Ming, N.J. Tosca, A. Yen, P.R. Christensen, S.P. Gorevan, J. Brückner, W.M. Calvin, G. Dreibus, W.H. Farrand, G. Klingelhöfer, H. Waenke, J. Zipfel, J.F. Bell III, J.P. Grotzinger, H.Y. McSween Jr., R. Rieder (2005), Chemistry and mineralogy of outcrops at Meridiani Planum, *EPSL.* 240, 73-94.

Clark, R.N., G.A Swayze, A.J Gallagher, N Gorelick, F.A Kruse (1991), Mapping with imaging spectrometer data using the complete band shape least-squares fit to multiple spectral features from multiple materials. *Proceedings of the Third AVIRIS Workshop*, JPL Publication, vol. 91-28, Jet Propul. Lab, Pasadena, CA, pp. 2–3.

Clark, R.N. (1999) Chapter 1: Spectroscopy of Rocks and Minerals, and Principles of Spectroscopy. In A.N. Rencz, Ed., *Manual of Remote Sensing, Remote Sensing for the Earth Sciences*, 3, p. 3.58. John Wiley and Sons, New York.

Cloutis, E. A., P. M. Asher, and S. A. Mertzman (2002), Spectral reflectance properties of zeolites and remote sensing implications, *J. Geophys. Res.*, 107(E9), 5067.

Cloutis, E. A., F.C. Hawthorne, S.A. Mertzman, K. Krenn, M.A. Craig, D. Marcino, M. Methot, J. Strong, J.F. Mustard, D.L. Blaney, J.F. Bell III, and F. Vilas (2006), Detection and discrimination of sulfate minerals using reflectance spectroscopy, *Icarus*, 184, 121 – 157.

- Dehouck, E., V. Chevrier, A. Gaudin, N. Mangold, P.-E. MathZ, P. Rochette (2012), Evaluating the role of sulfide-weathering in the formation of sulfates or carbonates on Mars, *Geochim. Cosmochim. Acta*, 90, 47-63, doi:10.1016/j.gca.2012.04.057.
- Dorn, R.I. (2012), Formation of silica glaze rock coatings through water vapor interactions. *Phys. Geogr.* 33 (1), 21–31.
- Ehlmann, B.L. and C.S. Edwards (2014), Mineralogy of the martian surface. *Annual Reviews of Earth and Planetary Sciences*, 42, 291–315.
- Ehlmann, B.L., J.F. Mustard, S.L. Murchie, J-P. Bibring, A. Meunier, A.A. Fraeman, and Y. Langevin, (2011), Subsurface water and clay mineral formation during the early history of Mars. *Nature*. 479, 53.
- El-Shamy, T. M., J. Lewins, and R. W. Douglas (1972), The dependence of the pH on the decomposition of glasses by aqueous solutions, *J. Soc. Glass Technol.*, 13(3), 81 – 87.
- Farrand, W. H., S. P. Wright, A. D. Rogers, and T. D. Glotch (2016), Basaltic glass formed from hydrovolcanism and impact processes: Characterization and clues for detection of mode of origin from VNIR through MWIR reflectance and emission spectroscopy, *Icarus*, 275, 1–13, doi:10.1016/j.icarus.2016.03.027.
- Gaillard, F. and B. Scaillet (2009) The sulfur content of volcanic gases on Mars. *Earth and Planetary Science Letters*, Elsevier, 279 (1-2), pp.34-43.
- Gellert, R., R. Rieder, R.C. Anderson, J. Bruckner, B.C. Clark, G. Dreibus, T. Economou, G. Klingelhofer, G.W. Lugmair, D.W. Ming, S.W. Squyres, C. d'Uston, H. Wanke, A. Yen, J. Zipfel (2004), Chemistry of rocks and soils in Gusev Crater from the Alpha Particle X-ray spectrometer. *Science* 305, 829–832.

- Gellert, R., R. Rieder, J. Brückner, B. Clark, G. Dreibus, G. Klingelhöfer, G. Lugmair, D. Ming, H. Wänke, A. Yen, J. Zipfel, and S. Squyres (2006), Alpha Particle X-Ray Spectrometer (APXS): Results from Gusev crater and calibration report. *J. Geophys. Res.*, 111, E02S05, doi:10.1029/2005JE002555.
- Gendrin, A., N. Mangold, J.-P. Bibring, et al., (2005), Sulfates in Martian layered terrains: the OMEGA/Mars Express view, *Science* 307, 1587–91.
- Glotch, T.D., R.V. Morris, P.R. Christensen, T.G. Sharp (2004), Effect of precursor mineralogy on the thermal infrared emission spectra of hematite: application to Martian hematite mineralization. *J. Geophys. Res.*, 109.
- Glotch, T. D., J. L. Bandfield, P. R. Christensen, W. M. Calvin, S. M. McLennan, B. C. Clark, A. D. Rogers, and S. W. Squyres (2006), The mineralogy of the light-toned outcrop at Meridiani Planum as seen by the Miniature Thermal Emission Spectrometer and implications for its formation, *J. Geophys. Res.*, 111, E12S03, doi:10.1029/ 2005JE002672.
- Golden, D. C., D. W. Ming, R. V. Morris, and S. A. Mertzman (2005), Laboratory-simulated acid-sulfate weathering of basaltic materials: Implications for formation of sulfates at Meridiani Planum and Gusev crater, Mars, *J. Geophys. Res.*, 110, E12S07.
- Gooding, J.L., and K. Keil (1978), Alteration of glass as a possible source of clay minerals on Mars, *Geophys. Res. Lett.*, 5, 727-730.
- Gooding, J.L. (1978), Chemical weathering on Mars, *Icarus*, 33, 483-513.
- Grant, J. A., S. A. Wilson, E. Noe Dobrea, R. L. Fergason, J. L. Griffes, J. M. Moore, A. D. Howard, (2010), HiRISE views enigmatic deposits in the Sirenum Fossae region of Mars, *Icarus*, Volume 205, Issue 1, Pages 53-63, ISSN 0019-1035, <http://dx.doi.org/10.1016/j.icarus.2009.04.009>.

- Greeley, R., Bridges, N.T., Crown, D.A., Crumpler, L., Fagents, S.A., Mouginis-Mark, P.J., Zimbleman, J.R., (2000) *Volcanism on the Red Planet: Mars*. In: Zimbleman J.R., Gregg T.K.P. (eds) *Environmental Effects on Volcanic Eruptions*. Springer, Boston.
- Halevy, I., Zuber, M. T. & Schrag, D. P. (2007), A sulfur dioxide climate feedback on early Mars. *Science* 318, 1903–1907.
- Hamilton, V. E., R. V. Morris, J. E. Gruener, and S. A. Mertzman (2008), Visible, near-infrared, and middle infrared spectroscopy of altered basaltic tephra: Spectral signatures of phyllosilicates, sulfates, and other aqueous alteration products with application to the mineralogy of the Columbia Hills of Gusev Crater, Mars: *J. Geophys. Res.-Planets*, v. 113, p. E12S43.
- Hamilton, V.E., Wyatt, M.B., McSween Jr., H.Y., Christensen, P.R. (2001), Analysis of terrestrial and martian volcanic compositions using thermal emission spectroscopy: II. Application to martian surface spectra from the Mars Global Surveyor Thermal Emission Spectrometer. *J. Geophys. Res.* 106, 14733–14746.
- Horgan, B., and J. F. Bell III (2012), Widespread weathered glass on the surface of Mars, *Geology*, 40(5), 391–394.
- Horgan, B. H. N., E. A. Cloutis, P. Mann, and J. F. Bell (2014), Near-infrared spectra of ferrous mineral mixtures and methods for their identification in planetary surface spectra, *Icarus*, 234, 132–154, doi:10.1016/j.icarus.2014.02.031.
- Haskin, L. A., A. Wang, B. L. Jolliff, H. Y. McSween, B. C. Clark, D. J. Des Marais, S. M. McLennan, N. J. Tosca, J. A. Hurowitz, J. D. Farmer, A. Yen, S. W. Squyres, R. E. Arvidson, G. Klingelhöfer, C. Schröder, P. de Souza, D. W. Ming, R. Gellert, J. Zipfel, J. Brückner, J. F. Bell, III, K. Herkenhoff, P. R. Christensen, S. Ruff, D. Blaney, S. Gorevan, N. A. Cabrol, L.

- Crumpler, J. Grant, and L. Soderblom, (2005), Water alteration of rocks and soils from the Spirit rover site, Gusev crater, Mars, *Nature*, 436, 66-69.
- Herzberg, G. (1945) *Infrared and Raman Spectra of Polyatomic Molecules*. Van Nostrand, New York.
- Howard, K. T., et al. (2013), Biomass preservation in impact melt ejecta, *Nat. Geosci.*, 6, 1018–1022, doi:10.1038/ngeo1996.
- Hurowitz, J. A., S. M. McLennan, D. H. Lindsley, and M. A. A. Schoonen (2005), Experimental epithermal alteration of synthetic Los Angeles meteorite: Implications for the origin of Martian soils and identification of hydrothermal sites on Mars, *J. Geophys. Res.*, 110, E07002, doi:10.1029/2004JE002391.
- Hurowitz, J. A., S. M. McLennan, N. J. Tosca, R. E. Arvidson, J. R. Michalski, D. W. Ming, C. Schröder, and S. W. Squyres (2006), In situ and experimental evidence for acidic weathering of rocks and soils on Mars, *J. Geophys. Res.*, 111, E02S19.
- Hurowitz, J.A., S.M. McLennan (2007), A ~3.5 Ga record of water-limited, acidic weathering conditions on Mars: *EPSL*, v. 260, p. 432-443.
- Hurowitz, J. et al. (2010), Origin of acidic surface waters and the evolution of atmospheric chemistry on early Mars. *Nature Geosci.* 3, 323–326.
- Hynek, B.M., Phillips, R.J., Arvidson, R.E. (2003) Explosive volcanism in the Tharsis region: Global evidence in the martian geologic record. *J. Geophys. Res.* 108. doi:10.1029/2003JE002062.
- Johnson, J. R., P. R. Christensen, and P. G. Lucey (2002), Dust coatings on basaltic rocks and implications for thermal infrared spectroscopy of Mars, *J. Geophys. Res.*, 107(E6), 5035.

- King, P. L., P. F. McMillan, and G. M. Moore (2004), Infrared spectroscopy of silicate glasses with application to natural systems, in *Infrared Spectroscopy in Geochemistry, Exploration Geochemistry, and Remote Sensing*, Mineral. Assoc. of Can. Short Course Ser., vol. 33, edited by P. L. King, M. S. Ramsey, and G. A. Swayze, pp. 93 – 133, Mineral. Assoc. of Can., Ottawa.
- Kite, E.S., Halevy, I., Kahre, M.A., Wolff, M.J., and Manga, M. (2013), Seasonal melting and the formation of sedimentary rocks on Mars, with predictions for the Gale Crater mound: *Icarus*, v. 223, p. 181–210, doi:10.1016/j.icarus. 2012.11.034.
- Klingelhöfer, G., R. V. Morris, B. Bernhardt, C. Schröder, D. S. Rodionov, P.A. de Souza, Jr., A. Yen, R. Gellert, E. N. Evlanov, B. Zubkov, J. Foh, U. Bonnes, E. Kankeleit, P. Gütllich, D. W. Ming, F. Renz, T. Wdowiak, S. W. Squyres, R. E. Arvidson (2004), Jarosite and hematite at Meridiani Planum from the Mössbauer Spectrometer on the Opportunity Rover, *Science*, 306, 1740-1745.
- Kraft, M. D., J. R. Michalski, and T. G. Sharp (2003), Effects of pure silica coatings on thermal emission spectra of basaltic rocks: Considerations for Martian surface mineralogy: *Geophysical Research Letters*, v. 30.
- Langevin, Y., F. Poulet, J.-P. Bibring, and B. Gondet (2005), Sulfates in the North Polar region of Mars detected by OMEGA/Mars Express, *Science* 307, 1584–6.
- Lichtenberg, K. A., R.E. Arvidson, R.V. Morris, S.L. Murchie, J.L. Bishop, D.F. Remolar, T.D. Glotch, E.N. Dobreá, J.F. Mustard, J. Andrews-Hanna, and L.H. Roach (2010), Stratigraphy of hydrated sulfates in the sedimentary deposits of Aram Chaos, Mars, *J. Geophys. Res.*, 115, E00D17.
- McCollom, T. M. and B. M. Hynek (2005), A volcanic environment for bedrock diagenesis at Meridiani Planum on Mars, *Nature* 438, 1129–31.

- McLennan, S. M., Taylor, S. R. and Hemming, S. R. (2006), Composition, differentiation, and evolution of continental crust: Constraints from sedimentary rocks and heat flow. In: M. Brown and T. Rushmer, eds. *Evolution and Differentiation of the Continental Crust*. Cambridge Univ. Press, pp. 92-134.
- Michalski, J. R. and Bleacher, J. E. (2013), Supervolcanoes within an ancient volcanic province in Arabia Terra, Mars, *Nature* 502, 47–52.
- Michalski J.R., M.D. Kraft, T.G. Sharp, L.B. Williams, and P.R. Christensen (2005), Mineralogical constraints on the high-silica martian surface component observed by TES. *Icarus* 174: 161-177.
- Michalski, J. R., M. D. Kraft, T. G. Sharp, and P. R. Christensen (2006), Effects of chemical weathering on infrared spectra of Columbia River Basalt and spectral interpretations of martian alteration: *Earth and Planetary Science Letters*, v. 248, p. 822-829.
- Milliken, R.E., Grotzinger, J.P., Thomson, B.J. (2010), Paleoclimate of Mars as captured by the stratigraphic record in Gale Crater. *Geophys. Res. Lett.* 37, L04201. doi:10.1029/2009GL041870.
- Ming D. W., D. W. Mittlefehldt, R. V. Morris, D. C. Golden, R. Gellert, A. Yen, B.C. Clark, S. W. Squyres, W. H. Farrand, S. W. Ruff, R. E. Arvidson, G. Klingelhöfer, H. Y. McSween, D. S. Rodionov, C. Schröder, P. A. de Souza, and A. Wang (2006), Geochemical and mineralogical indicators for aqueous processes in the Columbia Hills of Gusev crater, Mars. *J. Geophys. Res.* 111, E02S12.
- Minitti, M.E. and Hamilton, V.E. (2010). A search for basaltic-to-intermediate glasses on Mars: Assessing martian crustal mineralogy. *Icarus* 210, 135–149.

- Minitti, M. E., J. F. Mustard, and M. J. Rutherford (2002), Effects of glass content and oxidation on the spectra of SNC-like basalts: Applications to Mars remote sensing, *107(E5)*, 5030, doi:10.1029/2001JE001518.
- Minitti, M. E., C. M. Weitz, M. D. Lane, and J. L. Bishop (2007), Morphology, chemistry, and spectral properties of Hawaiian rock coatings and implications for Mars, *J. Geophys. Res.*, *112*, E05015, doi:10.1029/2006JE002839.
- Morris, R.V., Graff, T.G., Mertzman, S.A., Lane, M.D., Christensen, P.R. (2003), Palagonitic (not andesitic) Mars: evidence from the thermal emission and VNIR spectra of palagonitic alteration rinds on basaltic rocks. In: *Proceeding from the International Conference on Mars*, vol. 6, abstract 3211.
- Morris, R. V., G. Klingelhöfer, B. Bernhardt, C. Schröder, D. S. Rodionov, P. A. de Souza Jr., A. Yen, R. Gellert, E. N. Evlanov, D. W. Ming, F. Renz, T. Wdowiak, S. W. Squyres, R. E. Arvidson, and the Athena Science Team (2004), Mössbauer mineralogy on Mars: First results from the Spirit landing site in Gusev crater, *Science*, *305*, 833-836.
- Morris, R. V., G. Klingelhöfer, C. Schröder, D. S. Rodionov, A. Yen, D. W. Ming, P. A. de Souza Jr., I. Fleische, T. Wdowiak, R. Gellert, B. Bernhardt, E. N. Evlanov, B. Zubkov, J. Foh, U. Bonnes, E. Kankeleit, P. Gütlich, F. Renz, S. W. Squyres, and R. E. Arvidson (2006), Mössbauer mineralogy of rock, soil, and dust at Gusev Crater, Mars: Spirit's journey through weakly altered olivine basalt on the plains and pervasively altered basalt in the Columbia Hills. *J. Geophys. Res.*, *111*, E02S13, doi:10.1029/2005JE002584.
- Morris, R.V., Hamilton, V.E., Gruener, J.E., Ming, D.W., Mertzman, S. (2008), Visible and near-IR spectra for aqueous alteration products (palagonite, phyllosilicates, sulfates) of basaltic

- tephra on Mauna Kea volcano, Hawaii. In: Proceedings from the Workshop on Martian Phyllosilicates: Recorders of Aqueous Processes, abstract 1441.
- Murchie, S. et al. (2007), Compact Reconnaissance Imaging Spectrometer for Mars (CRISM) on Mars Reconnaissance Orbiter (MRO). *Journal of Geophysical Research* 112, E05S03. doi:10.1029/2006JE002682.
- Murchie, S. L., et al. (2009), A synthesis of Martian aqueous mineralogy after 1 Mars year of observations from the Mars Reconnaissance Orbiter, *J. Geophys. Res.*, 114, E00D06, doi:10.1029/2009JE003342.
- Mustard J. F., Murchie S. L., Pelkey S. M., Ehlmann B. L., Milliken R. E., Grant J. A., Bibring J.-P., Poulet F., Bishop, J. L., et al. (2008), Hydrated silicate minerals on Mars observed by the CRISM instrument on MRO. *Nature* 454:305–309.
- Nakamoto, K. (1986) *Infrared and Raman Spectra of Inorganic and Coordination Compounds*. Wiley and Sons, New York.
- Niles P. B. and Michalski J. (2009), Meridiani Planum sediments on Mars formed through weathering in massive ice deposits. *Nat. Geosci.* 2, 215–220.
- Ody, A., F. Poulet, Y. Langevin, J.-P. Bibring, G. Bellucci, F. Altieri, B. Gondet, M. Vincendon, J. Carter, and N. Manaud (2012), Global maps of anhydrous minerals at the surface of Mars from OMEGA/MEx, *JGR.*, 117, E00J14.
- Oelkers, E.H. Golubev, S.V., Char'rat, C., Pokrovsky, O.S. and Schott, J. (2009). The surface chemistry of multi-oxide silicates. *Geochimica et Cosmochimica Acta*, 73, 46174634.
- Parke, S. (1974), Glasses, in *The Infrared Spectra of Minerals*, edited by V. C. Farmer, pp. 483-514, Mineralogical Society of London, London.

- Pierazzo, E., D. A. Kring, and H. J. Melosh (1998), Hydrocode simulation of the Chicxulub impact event and the production of climatically active gases, *J. Geophys. Res.*, 103(E12), 28607–28625, doi:10.1029/98JE02496.
- Pope, K. O., K. H. Baines, A. C. Ocampo, B. A. Ivanov, Energy, volatile production, and climatic effects of the Chicxulub Cretaceous/Tertiary impact, *J. Geophys. Res.*, 102, 21645–21664, 1997.
- Poulet, F., J.-P. Bibring, J. F. Mustard, et al., (2005), Phyllosilicates on Mars and implications for early martian climate, *Nature* 438, 623–7.
- Rieder, R., et al. (2004), Chemistry of rocks and soils at Meridiani Planum from the alpha particle x-ray spectrometer, *Science*, 306, 1746–1749, doi:10.1126/science.1104358.
- Rogers, A.D. and P.R. Christensen (2007), Surface mineralogy of Martian low-albedo regions from MGS-TES data: Implications for upper crustal evolution and surface alteration, *JGR.*, 112, E01003.
- Ruff, S.W. (2004), Spectral evidence for zeolite in the dust on Mars. *Icarus* 168, 131–143.
- Ruff, S. W., P. R. Christensen, D. L. Blaney, W. H. Farrand, J. R. Johnson, J. R. Michalski, J. E. Moersch, S. P. Wright, and S. W. Squyres (2006), The rocks of Gusev Crater as viewed by the Mini-TES instrument, *J. Geophys. Res.*, 111, E12S18, doi:10.1029/2006JE002747.
- Ruff, S. W., J.D. Farmer, W.M. Calvin, K.E. Herkenhoff, J.R. Johnson, R.V. Morris, M.S. Rice, R.E. Arvidson, J.F. Bell III, P.R. Christensen, and S.W. Squyres (2011), Characteristics, distribution, origin, and significance of opaline silica observed by the Spirit rover in Gusev crater, Mars, *J. Geophys. Res.*, 116, E00F23.

- Saal, A. E., E. H. Hauri, M. L. Cascio, J. A. Van Orman, M. C. Rutherford, and R. F. Cooper (2008), Volatile content of lunar volcanic glasses and the presence of water in the Moon's interior, *Nature*, 454, 192–195, doi:10.1038/nature07047.
- Salvatore, M. R., J. F. Mustard, J. W. Head, R. F. Cooper, D. R. Marchant, and M. B. Wyatt (2013), Development of alteration rinds by oxidative weathering processes in Beacon Valley, Antarctica, and implications for Mars, *Geochim. Cosmochim. Acta*, 115, 137–161, doi:10.1016/j.gca.2013.04.002.
- Schiffman, P., R. Zierenberg, N. Marks, J. L. Bishop, and M. D. Dyar (2006), Acid-fog deposition at Kilauea volcano: A possible mechanism for the formation of siliceous-sulfate rock coatings on Mars, *Geology*, 34(11), 921–924, doi:10.1130/G22620A.1.
- Segura, T. L., O. B. Toon, A. Colaprete, and K. Zahnle (2002), Environmental effect of large impacts on Mars, *Science*, 290, 1976–1980.
- Serna, C.J., Cortina, C.P., and Ramos, J.V.G. (1986), Infrared and Ramen study of alunite-jarosite compounds. *Spectrochimica Acta*, 42A, 729.834.
- Settle, M. (1979), Formation and deposition of volcanic sulfate aerosols on Mars, *J. Geophys. Res.*, 84, 8343 – 8354
- Tompkins, S. and Pieters, C. M. (2010), Spectral characteristics of lunar impact melts and inferred mineralogy. *Meteoritics & Planetary Science*, 45: 1152–1169. doi:10.1111/j.1945-5100.2010.01074.x
- Tosca, N.J. et al. (2004), Acid-sulfate weathering of synthetic Martian basalt: The acid fog model revisited, *J. Geophys. Res.*, 109, E05003.
- Tosca, N. J. and McLennan, S. M. (2006) Chemical divides and evaporite assemblages on Mars. *Earth Planet. Sci. Lett.* 241, 21-31.

- Tosca, N. J., McLennan, S. M. et al. (2005) Geochemical modeling of evaporation processes on Mars: Insight from the sedimentary record at Meridiani Planum. *Earth Planet. Sci. Lett.* 240, 122-148.
- Vaniman, D. T., et al., (2014), Mineralogy of a mudstone on Mars, *Science*, 343.
- Vassallo, A.M. and Finnie, K.S. (1992) Infrared emission spectroscopy of some sulfate minerals. *Applied Spectroscopy*, 46, 1477-1482.
- Viviano, C. E., (2012) Characterizing phyllosilicate distribution, abundance, and origin on Mars, PhD diss., University of Tennessee, 2012. http://trace.tennessee.edu/utk_graddiss/1366.
- Viviano and Moersch (2012), A technique for mapping Fe/Mg-rich phyllosilicates on Mars using THEMIS multispectral thermal infrared images. *JGR*, 117:E07007.
- Wang, A., L. A. Haskin, S. W. Squyres, B. L. Jolliff, L. Crumpler, R. Gellert, C. Schröder, K. Herkenhoff, J. Hurowitz, N.J. Tosca, W.H. Farrand, R. Anderson, and A.T. Knudson (2006) Sulfate deposition in subsurface regolith in Gusev crater, Mars. *J. Geophys. Res.*, 111, E02S17, doi:10.1029/2005JE002513.
- Wilson, L., Head, J.W. (1994), Mars: Review and analysis of volcanic eruption theory and relationships to observed landforms. *Rev. Geophys.* 32, 221–263.
- Wolff-Boenisch D., S. R. Gislason, E. H. Oelkers, and C. V. Putnis (2004), The dissolution rates of natural glasses as a function of their composition at pH 4 and 10.6, and temperatures from 35 to 74C, *Geochim. Cosmochim. Acta*, 68, 4843-4858.
- Wray, J.J. (2012), The Scientific Necessity of Landing at Diverse Sites on Mars. Concepts and Approaches for Mars Exploration, abstract 4380.
- Wyatt, M. B., and H. Y. McSween (2002), Spectral evidence for weathered basalt as an alternative to andesite in the northern lowlands of Mars. *Nature*, 417, 263– 266.

Yant, M., A. D. Rogers, H. Nekvasil, Y.-Y. S. Zhao, and T. Bristow (2016), Spectral characterization of acid weathering products on Martian basaltic glass, *Journal of Geophysical Research - Planets*, 121, doi:10.1002/2015JE004969.

Zolotov, M. Y., and M. V. Mironenko (2007), Timing of acid weathering on Mars: A kinetic-thermodynamic assessment, *J. Geophys. Res.*, 112, E07006.

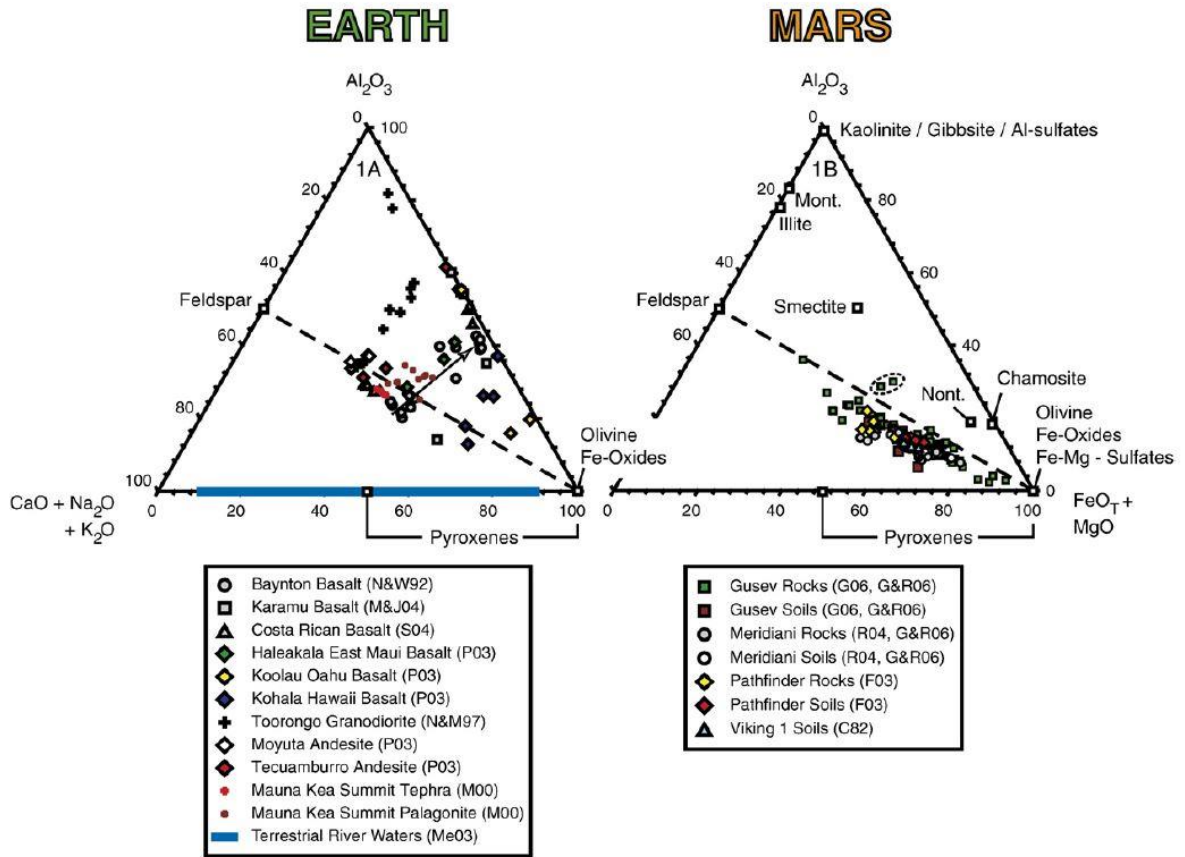


Figure 2-1: Diagram from *Hurowitz and McLennan* [2007) comparing the weathering trends for Earth and Mars.

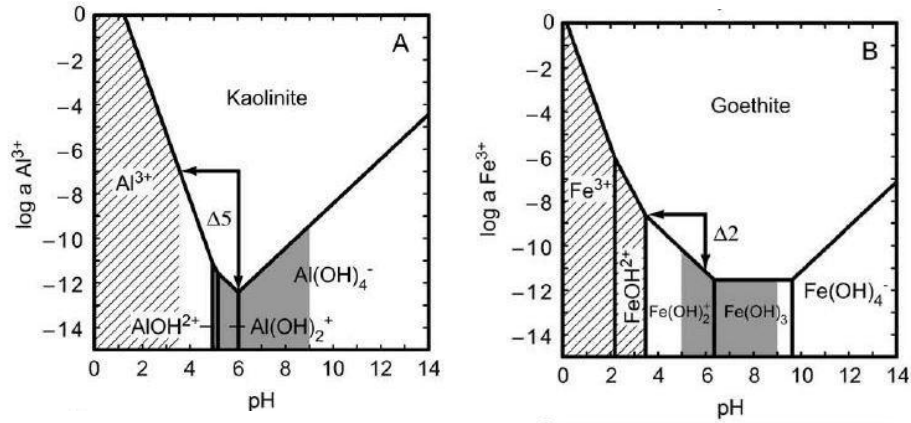


Figure 2-2: Diagram from *Hurowitz et al.* [2006] showing A) log activity of Al^{3+} vs. pH with speciation of Al in respect to kaolinite precipitation and B) log activity of Fe^{3+} vs. pH with speciation of Fe in respect to goethite precipitation. Cross hatched field represents experimental Martian pH range utilized by *Hurowitz et al.* [2005] and *Tosca et al.* [2004] and shaded area represents the pH range of most natural terrestrial waters.

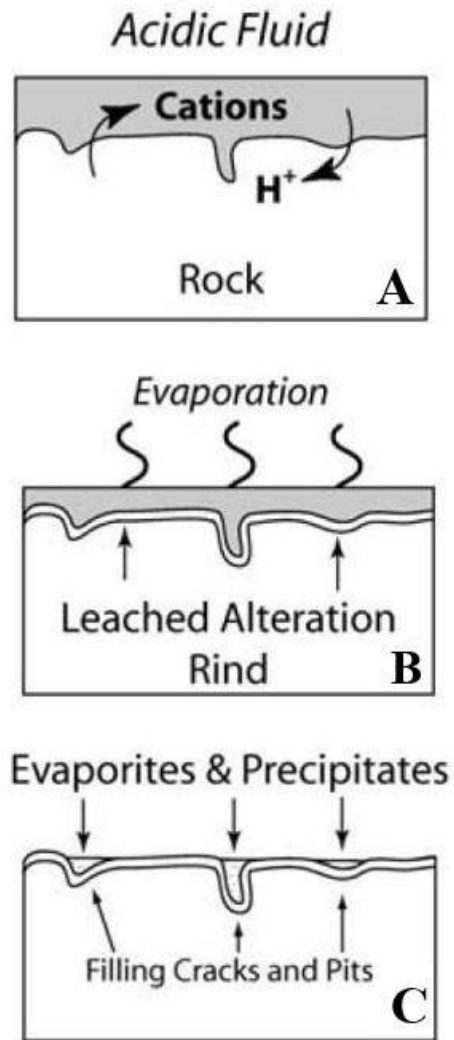


Figure 2-3: Diagram adapted from *Hurowitz et al.* [2006] showing a mechanism for alteration of rock surfaces. A) Small volumes of acidic fluid react with the surface of the material, then B) leached alteration rind, depleted in the most soluble elements, is left behind, and C) the fluid subsequently undergoes evaporation and deposits alteration minerals on the surface.

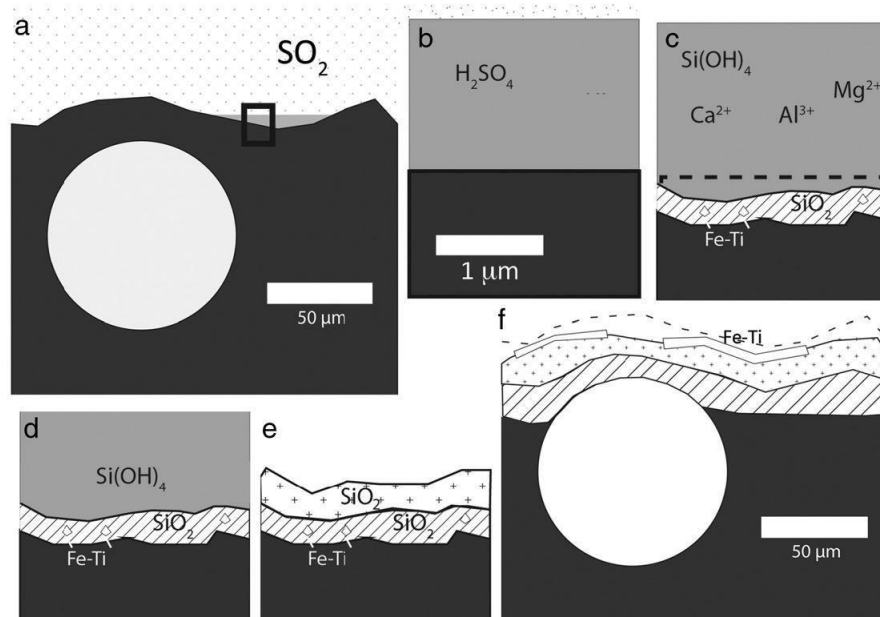


Figure 2-4: Diagram from *Chemtob and Rossman* [2014] showing a mechanism for silica coating formation on Hawaiian basalts. A) Unaltered basaltic surface is contacted with fluid in the presence of acidic vapors B) Liquid becomes acidified by volcanically derived fluids, C) basaltic cations are dissolved in the acidic fluid and the silica is precipitated in place, D) Silica can also be transported to the surface by fluids that penetrate to the interior of the basalt, E) Silica-bearing fluids derived from the subsurface evaporate precipitating silica, and F) episodes of dissolution-reprecipitation can result in the thickening of the silica layer and the remobilization of Fe and Ti to the surface.

Chapter 3:

Spectral Characterization of Acid Weathering Products on Martian Basaltic Glass

This chapter was published in the Journal of Geophysical Research – Planets
Yant, M., A. D. Rogers, H. Nekvasil, Y.-Y. S. Zhao, and T. Bristow (2016), Spectral
characterization of acid weathering products on Martian basaltic glass, J. Geophys. Res.
Planets, 121, doi:10.1002/2015JE004969

3.1 Introduction

The abundance and species of chemical alteration products on planetary surfaces are related to the starting composition of unaltered protolith, the style and duration of alteration processes, the fluid composition, the fluid-to-rock ratio [e.g., *Tosca et al.*, 2004; *Golden et al.*, 2005; *Ming et al.*, 2006], and ultimately, to the preservation of those products in rocks and soils. Thus, detection and interpretation of alteration mineral assemblages on Mars is critical to deciphering the history of the Martian surface. Among the techniques available to detect mineral assemblages on Mars, visible and infrared (IR) spectroscopic remote sensing provides the greatest areal coverage at the highest spatial resolution, allowing for assessment of spatial and/or temporal variability in weathering environment. Multiple instruments provide IR data of Mars; these include the Compact Reconnaissance Imaging Spectrometer for Mars (CRISM) and Observatoire pour la Minéralogie, l'Eau, les Glaces et l'Activité (OMEGA) which operate in the visible/near-infrared (VNIR) spectral range and the Thermal Emission Spectrometer (TES), Miniature Thermal Emission Spectrometer (Mini-TES), and Thermal Emission Imaging System (THEMIS) which operate in the mid-infrared (MIR) spectral range [e.g., *Christensen et al.*, 1992; *Christensen et al.*, 2003; *Bibring et al.*, 2005; *Murchie et al.*, 2007].

Numerous experimental and natural analog alteration studies have provided constraints on the minerals formed during alteration of basaltic materials under a variety of pH, fluid-to-rock ratio, and temperature conditions, as summarized in **Table 3-1** [e.g., *Banin et al.*, 1997; *Morris et al.*, 2000a; *Morris et al.*, 2000b; *Baker et al.*, 2000; *Tosca et al.*, 2004; *Fernandez-Remolar et al.*, 2005; *Schiffman et al.*, 2006; *Minitti et al.*, 2007; *Hamilton et al.*, 2008; *Seelos et al.*, 2010; *Ehlmann et al.*, 2012; *Hynek et al.*, 2013; *Marcucci et al.*, 2013; *Marcucci and Hynek*, 2014; *Chemtob and Rossman*, 2014; *McCanta et al.*, 2014]. However, for a variety of reasons, it is difficult to predict the spectral character of these alteration assemblages. These include non-reporting of phase abundance, and/or difficulty in detecting amorphous phases. In addition, because alteration products often form as a thin coating/fracture fill, or are fine-grained and poorly consolidated, non-linear IR spectral mixing can arise. This can make it difficult to detect certain alteration phases [*Michalski et al.*, 2006; *Kraft et al.*, 2007] and obtain quantitative abundances [*Kraft et al.*, 2003; *Michalski et al.*, 2006; *Hamilton et al.*, 2008; *Rampe et al.*, 2009] of alteration phases using spectroscopy.

The problem of non-linear mixing cannot be avoided, but direct comparison of spectral shape between different weathered surfaces may be useful. Indeed, some previous studies have provided spectral characterizations of naturally-altered surfaces [*Morris et al.*, 2000a; *Morris et al.*, 2000b; *Schiffman et al.*, 2006; *Minitti et al.*, 2007; *Hamilton et al.*, 2008; *Seelos et al.*, 2010; *Ehlmann et al.*, 2012; *Hynek et al.*, 2013; *Marcucci et al.*, 2013] (**Table 2-1**). However, because natural samples can be exposed to a variety of processes, and because differences in bulk chemistry can significantly affect the secondary mineralogy of the alteration product [e.g., *Tosca et al.*, 2004], there is a need to assess alteration assemblages from laboratory experiments on materials matching measured Martian compositions. Here, we link experimental weathering and spectral

studies by first conducting geochemical alteration experiments on synthetic Martian glass under varying pH conditions, and then characterizing the VNIR and MIR spectral properties of the weathered surfaces. This will enhance the understanding of the spectral properties of altered glasses with Martian surface compositions.

In this work, we focus on simulating one type of environment predicted to be common on Mars, primarily based on lander measurements: acid sulfate weathering under low fluid-to-rock ratios and nearly isochemical conditions [*Burns and Fisher, 1990; Bigham and Nordstrom, 2000; Madden et al., 2004; Golden et al., 2005; Ming et al., 2006*]. Based on the presence of Ca- and Mg-sulfates and the formation of coatings/rinds on Gusev rocks, *Golden et al.* [2005] suggested that the Gusev Crater surface materials were derived from acid sulfate alteration of an originally basaltic composition under low fluid-to-rock ratios and/or nearly isochemical conditions. The observation of ferric sulfates, which form exclusively under low-pH conditions, combined with the absence of Al-phyllsilicates in altered materials also suggests an acidic and low fluid-to-rock ratio weathering environment [*Ming et al., 2006*]. These conditions can likely be extended to other areas of Mars including the Opportunity, Pathfinder, and Viking 1 landing sites because the elemental measurements and soil chemistry are consistent with low pH and low water-to-rock ratios [*Hurowitz et al., 2006*]. Results from *Hurowitz and Fischer* [2014] indicate that the chemistry of soils at Gusev crater and Meridiani Planum and rinds at Gusev crater suggest a water limited environment with chemical alteration dominated by sulfur-rich fluids; this resulted in the formation of secondary phases without physical separation from the primary substrate, also referred to as “cation-conservative” [*Niles and Michalski, 2009*] conditions. The cation-conservative chemical weathering characteristics displayed by the undisturbed soils from Gusev crater and Meridiani Planum indicate similar weathering processes for the alteration rinds on rocks

and the regolith on Mars [Hurowitz and Fischer, 2014]. Hurowitz and McLennan [2007] suggest that this low fluid-to-rock ratio and low pH alteration environment has been dominant since approximately 3.5 Ga.

However, from orbit, evidence of widespread alteration is lacking. The MIR spectrometers TES [Christensen *et al.*, 2000] and THEMIS [Milam *et al.*, 2010; Viviano and Moersch, 2012] and the VNIR spectrometers OMEGA [e.g., Gendrin *et al.*, 2005; Carter *et al.*, 2013] and CRISM [e.g., Bishop *et al.*, 2008; Mustard *et al.*, 2008; Ehlmann *et al.*, 2011] have observed and mapped some secondary minerals (sulfates, chlorides, carbonates, oxides, phyllosilicates, and zeolites) in numerous, but small-scale, point locations [e.g., Bibring *et al.*, 2005; Gendrin *et al.*, 2005; Langevin *et al.*, 2005; Poulet *et al.*, 2005; Ehlmann *et al.*, 2011]. Yet, much of the Martian surface is spectrally consistent with unaltered or minimally-altered material [e.g., Bandfield, 2002; Rogers and Christensen, 2007; Ody *et al.*, 2012]. Thus, there is a difference in the picture of Martian surface materials provided by the lander/rover and orbiter data.

In order to more reliably interpret remote spectra of altered terrains, we focused on obtaining spectral data of synthetic Martian basaltic glasses, from controlled weathering experiments. By linking geochemical experiments with IR spectral measurements, we can provide insight on the detectability of alteration phases and assess the degree to which starting pH and composition influence the spectral signature of acid-altered Martian materials. For example, under what conditions does glass alteration result in detectable alteration products? What are the spectral characteristics of the altered samples; do they appear dominated by sulfate, silica, or a mixture of these products? How does starting composition affect the spectral signature of altered materials in both the MIR and the VNIR? This study also allows for the direct comparison of laboratory spectral

data to TES and OMEGA data, which expands the assessment of the extent of acidic alteration beyond the landing sites to other regions on Mars (*Chapter 6*).

3.2 Derivation of Basalt Compositions

Since the analogs underwent chemical alteration, the ideal composition for this study is one that is relatively unaltered. Gusev crater contains several basalts that are considered to be the least altered Martian rocks. In order to provide the best representation of the Martian surface a range of compositions was utilized. Irvine, Adirondack, and Backstay are among the least altered rocks in Columbia Hills when using nanophase oxides, hematite, and sulfates as an alteration index. Irvine and Backstay are both aphanitic and can be readily analyzed for bulk composition. Backstay and Irvine have small pits that could possibly be eroded vesicles which would be problematic as a part of the original composition would be missing from the analysis. However, these vesicles could be due to three different reasons. First, the pits could be from weathering, but looking at the rest of the rock there is not a lot of alteration so it is unlikely that this is the cause. Second, the pits could be from turbulence, but this is also unlikely. Third, the pits could have resulted from volatiles like CO₂, H₂O, F, and Cl which wouldn't have been trapped in the mineral assemblage anyways. The third case is the most likely and would indicate that Backstay and Irvine are similar to average basalt on earth and would be good candidates for compositions to use for this project.

The Irvine analysis was done on an unbrushed surface which could affect the composition determined by the APXS. Dust covering the surface of the rock could increase the amount of sulfate that is shown by the chemical analysis which would be a disadvantage for this project. However, analysis was done on both a brushed and unbrushed surface of Backstay and the results showed that there was little difference in the chemical composition. Since Irvine and Backstay

were both found on Husband Hill, it can be assumed that there would have been little difference between the analysis of an unbrushed and brushed surface of Irvine as well. The Mini-TES spectra of the natural surfaces of both Backstay and Irvine do not show any obvious spectral features of dust, which also suggests that the surfaces are relatively unaffected by dust [McSween *et al.*, 2006].

Adirondack contains large dark crystals that are suggested to be olivine. Because of the phaneritic nature of this composition, the melt composition may not be accurate and it was not included in this study. Irvine and Backstay were both synthesized because of the difference in composition between the two; Backstay contains a higher abundance of alkalis. The Pathfinder rock and soil samples, synthesized and analyzed by *Tosca et al.*, [2004], were also included in this study for spectral characterization. Together these compositions allowed for the assessment of the changes in secondary mineralogy with respect to changes in bulk composition, on the surface of Mars.

3.3 Experimental and Analytical Methods

3.3.1 Overview

In this work, we spectrally analyzed the unaltered and acid-altered surfaces of synthetic Martian basaltic glass with Irvine, Backstay, Pathfinder rock (PFR), and Pathfinder soil (PFS) compositions (**Table 3-2**). Irvine and Backstay were measured by the Mars Exploration Rover (MER) *Spirit* at Gusev Crater [McSween *et al.*, 2006]. These two compositions were chosen because they best fit the characteristics of relatively unaltered, aphanitic, basaltic rocks [McSween *et al.*, 2006]. Aphanitic rocks are desired because they can be readily analyzed for bulk composition. The other two compositions (Pathfinder rock/soil) were synthesized and altered by *Tosca et al.* [2004]. Together, this range of compositions (tholeiitic basaltic, alkalic basaltic, and basaltic andesitic) provides useful information on how bulk composition can affect the secondary

mineralogy and spectral characteristics for Martian surface material.

The samples underwent alteration in pH0-4 solutions with low fluid-to-rock ratios (1:1 for Irvine and Backstay, 10:1 for Pathfinder compositions [Tosca *et al.*, 2004]). The higher fluid to rock ratio implemented by Tosca *et al.* [2004] could result in the formation of a larger abundance of alteration material. However, in lower pH systems (pH<3.4) fluid to rock ratio has little effect on the neutralization of the solution [Hurowitz *et al.*, 2006], so considerable differences between the two experiments are not expected. The range of acidic solutions allows for a better understanding of the environmental conditions associated with certain IR spectral features and corresponding alteration assemblages. Also, it should be noted the pH is not held constant in the Irvine, Backstay, or Pathfinder experiments. It is expected that the pH increases after interaction with the basaltic material. This is due to an increase in alkalinity as cations are released during dissolution of the starting material. In nature, it is expected that the pH of the solution would increase during reaction with a sample without replenishment of fresh acidic solution, thus our experiments do not control pH.

Figure 3-1 provides an overview of the samples used, alteration conditions, and analytical measurements made. Following spectral analysis of the particulate surfaces of the altered Irvine and Backstay material, the samples were ground into powder and pressed into pellets; MIR characteristics were measured for the samples in pellet form. Spectral models from the pressed pellet samples provide the best constraints on volumetric mineral abundance, because surface alteration products are mixed homogeneously with unaltered material and because volume scattering is minimized in pressed pellet form [e.g., Salisbury and Wald, 1992]. However, we recognize that the particulate samples, rather than pressed pellets, are likely more representative of Martian soils, and therefore provide the best direct spectral comparison.

3.3.2 Glass Synthesis Methods

Major oxides for Irvine and Backstay were measured directly by APXS [McSween *et al.*, 2006]. The compositions (**Table 3-2**) were synthesized by a mixture of oxides, silicates, phosphate, chloride, and sulfate. An initial Fe³⁺/Fe²⁺ ratio of 80:20 was used to minimize the change induced by the graphite capsule. All components were added in ascending wt. % order to an automatic agate mortar/pestle and mixed under ethanol after the addition of each new aliquot. The exception to this order was the Fe sponge (used in combination with hematite to attain the desired FeO content), which was added last because it oxidizes easily and absorbs moisture when it comes in contact with air.

After drying, approximately 0.25g of powdered mixture was packed into a graphite capsule. The graphite capsule induces an oxygen fugacity along a displaced GCO buffer in the absence of a fluid phase, yielding an f_{O_2} at approximately FMQ-2 for the conditions of the experiment [Whitaker *et al.*, 2007]. A capsule was inserted into a talc assemblage, which was loaded into a piston cylinder press. The press was pressurized to 5kbar and heated to 1400°C and held at these conditions for 3 hours. After 3 hours at 1400°C, the power was shut off and the melt quenched into a basaltic glass.

The electron microprobe analyses of the unaltered Irvine and Backstay glass indicated that the major oxide abundances of the analyzed sample are near the target abundances, except for sodium and potassium for the Backstay composition (**Table 3-2**). The low sodium and potassium amounts are likely artifacts of the measurement technique; the mobile nature of these two elements combined with prolonged exposure to the electron beam can result in apparent depletions [Vassamillet and Caldwell, 1969]. Several points were analyzed on each glass sample in order to

determine the chemical heterogeneity of the material. The chemical gradient of the glass compositions were minimal, indicating homogeneous samples.

3.3.3 Alteration Batch Experiments

The samples were removed from the graphite capsule and then ultrasonically rinsed in water. Each sample was crushed and sieved to a particle size between 300 and 63 μ m (medium to very fine sand). After sieving, the sand was ultrasonically rinsed and then further rinsed in ethanol to remove any fine particulates that may have still been attached to the sand surfaces. Rinses were performed on samples until no fine particulates were visible. The samples were left to dry for 2 days at room temperature.

Acidic solutions (pH0, 1, 2, 3, and 4) were prepared using deionized water, sulfuric acid, and hydrochloric acid (**Table 3-3**). A S:Cl molar ratio of 5 was used for every acidic solution as an approximation of the 4.7 ± 0.3 value observed in Gusev soils [*Gellert et al.*, 2004]. The ratio from the soil was used because the amounts of S and Cl for rock surfaces in Gusev crater are highly variable, but the soil values are consistent. Also, because this experiment is utilizing multiple Gusev crater rock compositions the soil ratio will be used for consistency between the different materials. The pH range used in the experiments here is meant to simulate fluids derived from the mixing of variable amounts of water with volcanic outgassing. The more acidic pH conditions may represent fluids located close to the volcanic source and may become less acidic with movement farther away from the source.

For each reaction, approximately 0.25g of basaltic glass was added to a Savillex™ Teflon® beaker. The diluted mixtures of sulfuric acid and hydrochloric acid were used to react with the samples at room temperature and pressure with a fluid to rock ratio of 1:1. Both Irvine and Backstay synthesized material were altered in solutions that ranged from pH0-4 (Irvine samples,

[pH values of 0 (IRVG-pH0), 1 (IRVG-pH1), 2 (IRVG-pH2), 3 (IRVG-pH3) and 4 (IRVG-pH4)]; Backstay samples, [pH values of 0 (BKSG-pH0), 1 (BKSG-pH1), 2 (BKSG-pH2), 3 (BKSG-pH3) and 4 (BKSG-pH4)]. The duration of each reaction was 14 days in order to stay consistent with the Pathfinder experiments [Tosca *et al.*, 2004].

Following the reaction period, the samples were air dried at room temperature for 2 days. After the evaporation period, the samples were analyzed with MIR emission spectroscopy in the MIR, VNIR, Raman spectroscopy, scanning electron microscopy/energy dispersive spectroscopy (SEM/EDS) and x-ray diffraction (XRD). MIR spectral characterization was also performed on the Irvine and Backstay synthesized samples after the material was powdered and pressed into pellets.

For the Pathfinder samples, the synthesis, alteration, and chemical analyses were performed by Tosca *et al.* [2004] and here we provide IR spectral characterization. Two different compositions, a Pathfinder basaltic rock and a Pathfinder basaltic soil, were utilized to demonstrate the effect of bulk composition on the formation of alteration minerals. The PFRG (Pathfinder rock glass) and PFSG (Pathfinder soil glass) materials were crushed into coarse to very fine sand particles and underwent aqueous alteration in ~pH0-4 solutions with a fluid to rock ratio of 10:1. After an alteration period of 14 days the samples were evaporated for 2 days at 45-55°C. Before alteration the samples were analyzed by electron microprobe, during alteration DCP-AES was used for fluid analysis, and after the alteration period the materials were analyzed using XRD and SEM/EDS [Tosca *et al.*, 2004].

3.3.4 Analytical Methods

Chemical analyses of polished pieces of unaltered synthetic samples were performed using a Cameca SX-100 electron microprobe at the American Museum of Natural History. An

accelerating voltage of 15kV and a nominal beam current of 10nA were used during all analyses. Chemical and morphological analyses of secondary phases were obtained using a LEO 1550 SFEG scanning electron microscope (SEM) equipped with an EDAX energy dispersive x-ray spectrometer (EDS). Analyses were performed using an accelerating voltage of 20kV. The EDS system is capable of quantitative elemental analysis, but only for relatively flat surfaces. All of the EDS analyses discussed here are semi-quantitative because the analyses were performed on samples with variable surface angles. EDS analysis provides the elemental composition of the mineral phase, but does not allow for exact element ratios. With the ratios provided by EDS, a comparison between elements present in the spectra can be done. Combining the elemental makeup and the morphology of a grain can allow for mineral identification. The other analytical techniques (XRD, Raman) can also be utilized to properly identify phases.

The altered material was characterized by x-ray diffraction (XRD) with a Rigaku Smartlab x-ray diffractometer using Cu K α radiation generated at 40kV and 40mA. The powders were pressed flat into the well of a glass sample holder. A 0.5-degree divergent slit was used in conjunction with a D/tex Ultra 250 1D silicon strip detector during analysis, with a scan step of 0.01 degree at a rate of 2 degrees a minute. Phase identification was done using Rigaku's PDXL 2 software and MDI's Jade software in conjunction with the ICDD PDF-2 database. Semi-quantitative abundance of minerals was assessed by Rietveld refinement using PDXL 2. Due to the considerable Fe content of these samples there could be some Fe fluorescence present in the XRD patterns. This results in a high intensity background, but the major peaks are discernible.

The unaltered synthetic samples were spectrally characterized using MIR and VNIR spectroscopy, while the spectral analysis of the altered samples also included Raman. VNIR (350-2500nm) bidirectional reflectance spectra were acquired using an ASD FieldSpec3 Max

spectrometer at Stony Brook University. The measurements were collected with incidence and emergence angles of 30° and 0°, respectively. VNIR spectra were compared with library spectra of well-characterized samples available from RELAB (<http://www.planetary.brown.edu/relab/>). Hydrated materials (clay, sulfates, silica) often exhibit similar features in the VNIR with absorptions near 1.40 and 1.90 μm which can create difficulty in ascertaining the phases responsible for the spectral signature. Due to the similarity of the library spectra, the alteration assemblages of the VNIR data are grouped into polyhydrated sulfates (PHS) or monohydrated sulfates (MHS) \pm silica in **Figure 3-1**. Also, negative slopes were observed in the VNIR signatures of several altered samples that were not present in the unaltered material, which is indicated by “slope change” or “no change” in **Figure 3-1**.

Raman analyses were conducted at Stony Brook University using a WiTEC alpha300R confocal Raman microscope system equipped with a double frequency 532nm Nd: YAG excitation laser with a nominal laser power of 50mW at this wavelength. The system is also equipped with multiple object lenses ranging from 4 to 100X magnification, allowing spatial resolutions between several microns and 250nm/pixel. The spectra acquired for this study were in the range of 40-1200 cm^{-1} . Raman spectra were compared with library spectra available from the RRUFF database [Downs, 2006], which are well characterized using XRD and electron microprobe.

MIR emissivity spectra were acquired between 225-2000 cm^{-1} on Stony Brook University’s Nicolet 6700 FTIR spectrometer equipped with a CsI beamsplitter and deuterated triglycine sulfate cesium iodide (DTGS CsI) detector. The atmosphere was purged of H₂O and CO₂. Each sample was put into an aluminum sample cup painted with Krylon Ultra Flat Black paint. Because the altered samples were expected to contain sulfate minerals, which could dehydrate upon heating, emission measurements of altered samples were made by cooling the samples well below the

detector temperature [Baldridge and Christensen, 2009]. A thermo-electric cooling apparatus was used to actively cool the samples during spectral measurement. The samples were actively cooled to approximately -15°C within the chamber and maintained at that temperature for the duration of 256 scans (~9 minutes).

MIR spectra of altered samples were analyzed using linear least squares analysis [e.g., Ramsey and Christensen, 1998; Rogers and Aharonson, 2008] with a library of sulfate, silica, iron oxide and sulfur spectra, over the spectral range of 400-1400cm⁻¹. Most of the library spectra and samples used in this study are described in [Lane et al., 2007; Ruff et al., 2011; Lane et al., 2015, Sklute, 2015; see **Appendix Tables A1, A2, A3**]. The library also included the spectra of the unaltered samples, so that the altered samples could be modeled as a simple mixture of unaltered material plus alteration products. Last, a quasi-linear slope spectrum was also included to account for slopes present in the altered samples, due to spatial and/or temporal non-isothermality within the sample or sample collection process. Although linear spectral mixing cannot be assumed for some of these mixtures, the models allow us to characterize the spectrally dominant phases for descriptive purposes (e.g., sulfate- or silica-dominated assemblages, vs. assemblages dominated by unaltered material), and provides a comparison to what would be observed in models of spectra acquired at Mars.

3.4 Irvine Glass Alteration Results

The following section describes the alteration results for the Irvine glass composition. Upon evaporation of the fluid, the sample altered in the lowest pH (IRVG-pH0), formed a pellet. The alteration material was white and powdery. The sample still appeared “wet” after the evaporation period, which could be due to sulfuric acid as it has a very low vapor pressure and can remain on the sample after the evaporation period [Tosca, 2003]. An extended evaporation period

of 10 days was used for this sample, but a thin coating of liquid remained. IRVG-pH1 exhibited a very fine-grained coating of white alteration. The samples altered in the pH 2-4 solutions underwent the least alteration, and are predominantly unaltered basaltic glass. An overview of the alteration material observed for all materials from the chemical and spectral analyses is displayed in **Figure 3-1**.

3.4.1 Irvine Glass Chemical and Mineralogical Analyses

Interaction with the pH0 solution produced a variety of secondary mineral phases and the surface was dominated by a sulfur-rich coating overlying sulfate phases (**Figure 3-2A**). Mg-sulfate phases with an encrusting habit were also observed along with slender Ca-sulfate grains (**Figure 3-2B**). Fe-Al-sulfate phases that appear as plates are also observed (**Figure 3-2C**). This sample also exhibited Na-Mg-sulfates that occurred in tabular aggregates (**Figure 3-2D**). Due to the uneven sample surface as well as the sulfur rich coating observed on this sample, it is difficult to obtain diagnostic Raman spectra over much of the sample, and only two signatures were observed for IRVG-pH0 (**Figure 3-3A-B**). The first signature is most consistent with Al-sulfate (alunogen) and/or Mg-Al-sulfate (pickeringite) and the second signature is most consistent with Ca-sulfate (anhydrite). XRD confirmed the presence of the Mg- (hexahydrite), Ca- (anhydrite, gypsum), Fe-Al- (voltaite), and Al-sulfates (tamarugite) (**Figure 3-4A**) observed through SEM and Raman.

The secondary mineral assemblage for the material altered in pH1 also included a variety of phases and morphologies, but was dominated by spherical aggregates of tabular Na-Mg-Fe-sulfates and large (~400 μ m) Ca-sulfate crystals (**Figure 3-5A**). Another Na-Mg-Fe-sulfate phase was observed, but with a different morphology than the previous phase, forming a more tabular aggregate (**Figure 3-5B**). The alteration phases observed through SEM/EDS also included

encrusting Mg-sulfates, similar to the Mg-sulfate phase observed for the previous sample (**Figure 3-5C**). Al-sulfate was also identified and it occurred in relatively large plates (**Figure 2-5D**). Acicular grains of Mg-Al-sulfate were also present (**Figure 3-3E**). Much of the alteration on IRVG-pH1 was very fine grained and powdery, making it difficult to obtain diagnostic Raman spectra on the largest portions of the coating. There were elongated Ca-sulfate grains that could be observed without any magnification. Raman indicated the presence of Ca-sulfate (anhydrite) and Mn-sulfate (ilesite) (**Figure 3-3C-D**). These features are not representative of the majority of the secondary assemblage because of the difficulty obtaining diagnostic spectra of the powder coating. No alteration phases were observed through XRD for this sample.

The surface of the altered material from the pH2 solution had a porous characteristic, indicating some dissolution. The only alteration phase observed for this sample was Ca-sulfate via SEM. Interaction with pH3-4 solutions did not produce any secondary phases detectable by SEM, Raman, or XRD. There are a few dissolution pockets observed through SEM for the samples altered in pH3-4, but these materials appear to have undergone less dissolution.

3.4.2 Irvine Glass Infrared Results

3.4.2.1 Irvine Glass Visible Near-Infrared

The unaltered Irvine glass material and glass samples altered in pH2-4 exhibit very shallow features in the VNIR. The shallow character of the spectra can be attributed to their dark surfaces and lack of alteration material. Only the Irvine glass samples subjected to pH0-1 conditions have spectral features that deviate from the unaltered material in the VNIR. The reflectance spectra for IRVG-pH0 and IRVG-pH1 have similar spectral features, but different spectral shapes (**Figure 3-6A**), both exhibiting additional features near 0.97, 1.95, 2.08, 2.23 and 2.41 μm . IRVG-pH0 also exhibits features near 0.61 and 1.45 μm and IRVG-pH1 has an additional feature near 1.34 μm . The

broad band near $0.97\mu\text{m}$ is attributed to ferrous iron for both IRVG-pH0 and IRVG-pH1. The $1.45\mu\text{m}$ feature is likely due to OH stretching overtones or H_2O overtones/combination bands while the feature near $1.95\mu\text{m}$ is due to H_2O combinations. The 2.08 and $2.41\mu\text{m}$ absorptions can be attributed to combinations of OH or H_2O bending, stretching, and rotational fundamentals or S–O bending overtones [Cloutis *et al.*, 2006]. Silica has bands at 1.40 and $1.90\mu\text{m}$, with a broader band at $\sim 2.25\mu\text{m}$ [Marcucci *et al.*, 2013] and could be contributing to features near $2.23\mu\text{m}$ for IRVG-pH0-1, however we note that the strong ~ 1.90 and $1.40\mu\text{m}$ bands are absent. Although the exact phases are difficult to determine, the IRVG-pH0 sample exhibits the primary and secondary indicators of polyhydrated sulfates (near 1.95 , 2.40 , and $1.45\mu\text{m}$) [Lichtenberg *et al.*, 2010]. Influences can be observed from Na-Mg-sulfate (blödite) near 1.95 , 2.08 , and $2.41\mu\text{m}$, (Mg, Fe^{+2})-Al-sulfate (pickeringite, halotrichite) near 0.97 and $1.45\mu\text{m}$, and silica ($2.23\mu\text{m}$) (**Figure 3-6B**). The VNIR reflectance spectrum for IRVG-pH1 contains the primary indicators for a monohydrated sulfate (2.10 and $2.40\mu\text{m}$), which is consistent with the best library match, monohydrated Fe^{+2} -sulfate (szomolnokite). Silica may also be contributing to the feature near $2.23\mu\text{m}$ and Na-Mg-sulfate (blödite) may be influencing the spectrum near 1.45 , 1.95 , and $2.08\mu\text{m}$. Fe^{+2} -Al-sulfate (halotrichite) and/or Mg-Al-sulfate (pickeringite) may be influencing the slope of the overall spectrum. Only the library spectrum for pickeringite is shown due to the similarity of the halotrichite features.

3.4.2.2 Irvine Glass Mid-Infrared

The MIR emission spectral features of the unaltered glass samples are all consistent with each other, exhibiting distinct absorptions at 1015 , 870 , 665 , and 460cm^{-1} , as indicated for example, in **Figure 3-7C**. The MIR emission features for the glasses altered in pH0-1 vary from the unaltered material (**Figure 3-7A-B**) and have distinct spectral shapes. IRVG-pH0 exhibits new

absorptions near 1170, 1050, and 575 cm^{-1} that are most consistent with Fe^{+3} -sulfate with influences from amorphous Fe^{+3} -sulfate, Fe-oxides, Ca- sulfate, (Zn, Fe^{+2} ,Mn)-Al-sulfate, Mg-sulfate, and K- $\text{Fe}^{+2/3}$ -Al-sulfate. IRVG-pH1 retains a hint of the unaltered glass spectral character, with a feature near 460 cm^{-1} , but has additional absorptions near 1180, 1095, and 575 cm^{-1} . The additional absorptions present for IRVG-pH1 are most consistent with Fe^{+3} -sulfate with influences from silica, Fe-oxides, and Al-, Ca-, Mg-, Fe^{+2} -sulfates. The spectral signatures for the samples altered in pH 2-4 are similar to the unaltered material suggesting they have undergone little alteration in the MIR. Due to the similarity of the spectral features of these three samples one representative spectrum is shown, IRVG-pH3 (**Figure 3-7C**). Based on the modeled abundances there are ~17-20% alteration phases in the IRVG-pH2-4 samples and the spectra are most consistent with unaltered material with lesser amounts of Fe^{+3} -sulfate. The modeled assemblages for IRVG-pH2 and IRVG-pH3 also include Fe-oxides and IRVG-pH4 includes amorphous Fe^{+3} -sulfate.

Similar to the particulate surface, the pressed pellet model of IRVG-pH0 (**Figure 3-7D**) includes a variety of sulfates, but with a dominance of (Mg, Mn, Fe^{+2})-Al-bearing sulfates. The pressed pellet model also includes ~13% amorphous silica, which is absent in the assemblage of the particulate surface. The pressed pellet spectrum of IRVG-pH1 (**Figure 3-7E**) exhibits features most consistent with unaltered material with influence from various sulfates, Fe-oxide, and silica. The models for the pressed pellet samples for IRVG-pH2-4 indicate little to no alteration (<~5-17%) (**Figure 3-7F**), comparable to MIR emission signatures of the particulate samples.

3.5 Backstay Glass Alteration Results

After the evaporation period, the Backstay glass sample subjected to pH0 conditions was cemented into a single pellet, similar to the Irvine pH0 sample. The surface facing the bottom of

the container was coated in solid white material, whereas the surface facing the lid of the container was coated in powdery white alteration material. BKSG-pH1 was coated with white powdery material. The samples altered in the pH2-4 solutions underwent the least alteration, and visibly appear as unaltered basaltic glass.

3.5.1 Backstay Glass Chemical and Mineralogical Analyses

SEM observations of BKSG-pH0 determined that the top and bottom surfaces have the same secondary assemblage. This sample had a considerable amount and variety of secondary mineral phases, with an assemblage of Ca-, Fe-, Mg-, and Na-Al-sulfates. Fe-Mg-sulfates with tabular forms are present (**Figure 3-8A, cross**). This sample exhibits prismatic Ca-sulfate phases (**Figure 3-8B**). BKSG-pH0 also displays Fe-sulfates with a globular habit (**Figure 3-8C**) and plates of Na-Al-sulfate (**Figure 3-8D**). Where crystals or coating phases are absent, a cracked surface is observed by SEM (**Figure 3-8A, square**). This surface is rich in S and Mg with some Fe and Na contribution based on EDS ratios. This could be the cement that is responsible for adhering the glass grains into a pellet following evaporation of the solution. Due to the uneven sample surface as well as the coating observed on this sample, it is difficult to obtain diagnostic Raman spectra over much of the surface; only one sulfate signature was observed for BKSG-pH0 and is most consistent with Mg-sulfate (epsomite) and Fe⁺²-sulfate (rozenite) (**Figure 3-9A**). Only Na-Mg-sulfate (blödite) and Ca-sulfate (gypsum) were observed in the XRD data (**Figure 3-4B**).

Compared to BKSG-pH0, alteration products on BKSG-pH1 were finer grained. However, like BKSG-pH0, BKSG-pH1 also exhibited Ca-, Fe-, Mg-, and Na-Al-sulfates. SEM/EDS analyses indicated that this sample has aggregates of platy Na-Al-sulfates (**Figure 3-10A, square**). Ca-sulfate was observed in an elongated form (**Figure 3-10B**). This sample also exhibits Fe-Mg-sulfates (**Figure 3-10C**). A cement or coating was also observed for BKSG-pH1 (**Figure 3-10A,**

cross), though it appears to be different from BKSG-pH0. This feature is rich in S, Si, and Al with some Na, Fe, and Mg and tends to form in a fibrous manner. Ca-sulfate (gypsum), Na-Al-sulfate (Na-Alum, tamarugite), and/or Fe⁺²-sulfate (rozenite) were also observed through Raman techniques (**Figure 3-9B-C**). No alteration was observed in the XRD data.

The sample altered in the intermediate acidic environment (pH2) had much less alteration material when observed with SEM. The only secondary phase identified was Fe-sulfate. This phase was also observed by Raman as Fe⁺²-sulfate (rozenite, szomolnokite) (**Figure 3-9D**). This sample also exhibited a Si-rich coating with some Al, Mg, Ca, and Fe contribution. Ca-sulfate was the only phase observed in the sample altered in pH3 via SEM. There were no secondary phases observed for BKSG-pH4 by any analytical technique.

3.5.2 Backstay Glass Infrared Results

3.5.2.1 Backstay Glass Visible Near-Infrared

The VNIR reflectance spectrum for the unaltered Backstay glass exhibits shallow features and additional absorptions were observed only for the material altered in pH0 and pH1 (**Figure 3-11A**). The unaltered material exhibits broad absorptions near 1.10, 1.95, and 2.22 μ m. BKSG-pH0 and BKSG-pH1 both display features near 0.43, 0.88, 1.21, 1.46, 1.78, 1.95, 2.22, and 2.41 μ m, due to Fe, H₂O and OH/H₂O vibrational combinations, S-O overtones, and/or Si-OH stretching, and exhibit strong negative spectral slopes. These samples also exhibit strong concave-up slopes, as described by *Horgan and Bell* [2012]. In the BKSG-pH1 sample, the features described above are greatly shallowed compared to those in BKSG-pH0, and the negative slope is more evident. Although the exact phases are difficult to determine, the altered glass samples exhibit the primary and secondary indicators of polyhydrated sulfates (near 1.90, 2.40, and 1.40 μ m), which can be indistinguishable in the VNIR [*Lichtenberg et al.*, 2010] (**Figure 3-11B**). The spectral features for

BKSG-pH0 and BKSG-pH1 are most consistent with Fe⁺²-sulfate (melanterite) with influence from (Mg, Fe⁺²)Al-sulfate (pickeringite, halotrichite) and/or Mg-sulfate (hexahydrite). Silica may be influencing the feature near 2.22μm for BKSG-pH0-1. The overall spectral shape for these two samples is most comparable to pickeringite and hexahydrite. The spectral characteristics of BKSG-pH 2-4, are not discernible from the unaltered material.

3.5.2.2 Backstay Glass Mid-Infrared

The unaltered glass emissivity spectra all exhibit absorptions near 1005, 860, 660, 580, and 455cm⁻¹, as indicated for example, in **Figure 3-12C**. The only glass samples with spectral characteristics that deviate significantly from the unaltered material are BKSG-pH0 and BKSG-pH1. For the glass sample altered in the most acidic environment, pH0, all of the unaltered absorptions are lost and new features are present near 1110, 760, and 610cm⁻¹ (**Figure 3-12A**). These new features are most consistent with Fe⁺²-sulfate with influence from Ca-sulfate and minor amounts of Mg-, Na-, Fe⁺³-, Al-, and Fe⁺²-Al-sulfate. In the MIR emission spectrum for BKSG-pH1 (**Figure 3-12B**), most of the features are shallow. The weak absorptions could be due to the fine grained (<1μm) surface alteration material as observed via SEM (**Figure 3-8**). The combination of the new and original absorptions indicates that the spectrum of the sample surface is now influenced by the presence of sulfate(s), but the new material does not completely dominate the spectrum. Unaltered material is dominant in the MIR models, but there is some influence from Ca-sulfate, silica, and minor amounts of Fe⁺²-sulfate, Fe⁺³-sulfate, and Fe-oxide. The glass samples subjected to the weaker acids, pH2-4, do not display significant differences from the unaltered material in the MIR for the particulate surfaces, and because of the similarity of the spectral features of these three samples one representative spectrum is shown, BKSG-pH3 (**Figure 3-12C**). The MIR models indicate that these samples are mainly unaltered material (~77%), but suggest an

alteration assemblage including (Zn, Fe⁺², Mn)-Al-sulfate, Ca-sulfate +/- silica, sulfur, and Fe-oxides.

Unlike the particulate surface, the pressed pellet spectrum for BKSG-pH0 has features most consistent with unaltered material with some influence from various sulfates, silica, and Fe-oxide (**Figure 3-12D**). Although, both the particulate and pellet modeled spectra show that BKSG-pH1 is dominated by unaltered material, the pellet model indicates less influence from alteration phases (**Figure 3-12E**). The models for the pressed pellet samples for BKSG-pH2-4 indicate little to no alteration (~86% unaltered material) (**Figure 3-7F**), comparable to MIR emission signatures of the particulate samples.

3.6 Pathfinder Soil Glass Infrared Results

3.6.1 Pathfinder Soil Glass Visible Near-Infrared

The unaltered and altered glass materials from *Tosca et al.* [2004] were analyzed with VNIR reflectance and MIR emission spectroscopy in this study. The synthesis, alteration, SEM/EDS, and XRD analyses of these samples were performed by Nick Tosca during the 2004 study and are reported in **Figure 3-1**. Only the VNIR reflectance signatures for PFSG-A (pH0) and PFSG-B (pH1) deviate considerably from the unaltered PFSG sample spectrum (**Figure 3-13A**). Both samples exhibit features near 0.43, 0.91, 1.17, 1.34, 1.45, 1.75, 1.95, 2.22, and 2.41 μm, due to Fe, H₂O and OH/H₂O vibrational combinations, S-O overtones, and/or Si-OH stretching. These features are consistent with polyhydrated sulfates and the best spectral match was Fe^{+2,3}-sulfate (copiapite), with possible influence from (Mg, Fe⁺²)Al-sulfate (pickeringite, halotrichite) and/or Mg-sulfate (hexahydrate) (**Figure 3-13B**). Silica may be influencing the feature near 2.22 μm. Although the spectral characteristics of PFSG-A and PFSG-B are very similar, the

features for PFSG-B are much shallower. The feature near $0.91\mu\text{m}$ is broadened for PFSG-B and not as much distinction can be made between this absorption and the absorption near $1.17\mu\text{m}$.

3.6.2 Pathfinder Soil Glass Mid-Infrared

The unaltered PFSG material exhibits features near 990 , 685 , and 450cm^{-1} in the MIR range, as indicated for example, in **Figure 3-14E**. The only spectral signature that was dominated by alteration material was from the sample altered under the most acidic conditions (PFSG-A, pH0). The features were flat with uniformly high emissivity, which can be attributed to the small grain size of the alteration material. The modeled abundances indicate $\sim 77\%$ total alteration, dominated by Al-sulfate with influences from (Zn, Fe^{+2} , Mn)-Al-sulfate and minor amounts of (K) Fe^{+3} -sulfate, Fe-oxide, and Ca-sulfate (**Figure 3-14A**). In the sample altered in a pH1 (PFSG-B), the deepest unaltered glass feature at 990cm^{-1} is broadened and an additional absorption appears near 1100cm^{-1} , most likely due to the formation of sulfate(s) (**Figure 3-14B**). The features are most consistent with unaltered material ($\sim 46\%$), but Al-sulfate, silica, Fe^{+3} -sulfate, Fe-oxide, Ca-sulfate, and minor amounts of Fe^{+2} -Al-, Mg-, and Fe^{+2} -sulfate are contributing to the spectral signature. The same broadening of the original glass features and the addition of an absorption near 1090cm^{-1} are observed in the spectrum of PFSG-C (pH2) (**Figure 3-14C**). Again, the features are most consistent with unaltered material ($\sim 71\%$), but there is some influence suggested from Fe^{+3} -sulfate, Al-sulfate, Fe-oxide, and Ca-sulfate. The MIR spectra suggest little alteration for PFSG-D (pH3) and PFSG-E (pH4) (**Figure 3-14D-E**).

3.7 Pathfinder Rock Glass Infrared Results

3.7.1 Pathfinder Rock Glass Visible Near-Infrared

All of the altered PFRG material exhibited VNIR reflectance signatures similar to the unaltered sample with features near 1.10 , 1.95 , and $2.22\mu\text{m}$ (**Figure 3-15**). However, there is a

more distinct hump in the broad feature near 1.10 μm for the altered materials. Also, there is an additional feature near 1.35 μm for the material altered in pH1 (PFRG-B) that is not exhibited by any of the library spectra. Unlike the previously discussed altered samples, no negative spectral slope was observed.

3.7.2 Pathfinder Rock Glass Mid-Infrared

The unaltered PFRG material displays MIR spectral features near 1040, 690, and 455 cm^{-1} . All of the altered PFRG spectra (pH0-4) exhibit features similar to the unaltered PFRG material, indicating <12% total alteration (**Figure 3-16A-E**). Although there are only minor amounts of secondary phases, the spectral signatures for PFRG-A (pH0) (**Figure 3-16A**), PFRG-B (pH1) (**Figure 3-16B**), and PFRG-D (pH3) (**Figure 3-16D**) indicate some influence from Fe-oxide, and Al, (K)Fe⁺³, and Ca-sulfate. The modeled abundances for PFRG-C (pH2) (**Figure 3-16C**) indicate small amounts of Fe-oxide and Ca-sulfates and the alteration assemblage for PFRG-E (pH4) (**Figure 3-16E**) includes Fe-oxide, Ca-sulfate, Fe⁺³-sulfate, (Zn,Fe⁺²,Mn)-Al-sulfate, and minor sulfur.

3.8 Discussion

3.8.1 Effects of Composition on Spectral Signatures

In the VNIR range, spectral differences can be observed between the four unaltered compositions (Irvine, Backstay, Pathfinder soil, and Pathfinder rock) as well as between altered samples from each starting material (**Figure 3-17A**), reflecting changes in the mineral assemblage. Influence from secondary phases are observed for Irvine, Backstay, and PFSG material altered in pH \leq 1, however, all of the PFRG spectra are consistent with unaltered material. The absorptions associated with alteration material are most consistent with hydrated sulfates, though the exact phases differ for the individual sample samples.

Strong negative slopes are observed in the VNIR reflectance signatures for the altered Irvine, Backstay, and Pathfinder Soil glass samples. In addition, the altered Backstay samples also exhibit strong concave-up slopes, as described by *Horgan and Bell* [2012]. This illustrates the effect that primary glass composition can have on the spectral character of altered samples in the VNIR range. For example, the magnitude and shape of spectral slopes the VNIR was observed to vary greatly with starting composition (**Figure 3-17A**). Strong negative [e.g., *Poulet et al.*, 2007] and concave-up slopes [*Horgan and Bell*, 2012] observed in VNIR data of the Martian lowlands been attributed to thin varnishes of ferric oxide-bearing rinds, impact melts [e.g., *Poulet et al.*, 2007], or acidic leaching of silicate glasses [*Horgan and Bell*, 2012]. *Horgan and Bell* [2012] suggest that these shapes are formed from the interaction of silicate glass with small volumes acidic fluids [e.g., *Minitti et al.*, 2007], resulting in a concave-up shape produced by thin (3-10 μ m) silica-enriched leached glass rinds and a negative slope due to a thin coating of leached Fe⁺² overlying the Si-rich rind. In the northern lowlands of Mars, the negative slope varies in its concavity, which has been attributed to variable degrees of Fe-coating removal to expose the Si-rich, leached glass rind underneath [*Horgan and Bell*, 2012]. In this work, only the Backstay glass exhibited the negative, concave spectral slopes in the VNIR, despite alteration under similar conditions as the other glasses. Our work demonstrates that the magnitude and concavity of the negative slope associated with coated glass is also affected by primary glass composition, and thus inferences about leached/coated surfaces from VNIR spectra may be complicated by this factor.

In the MIR, spectral differences can be also observed between the unaltered and altered material from the four starting compositions (**Figure 3-17B**). Alteration features dominate the spectral signatures for the Irvine material altered in pH \leq 1, Backstay and Pathfinder soil material altered in pH=0, and for none of the Pathfinder rock spectra. This suggests relatively more

alteration in the Irvine composition relative to the other three starting compositions. Minimal (<20%) alteration was observed in the Pathfinder rock glass from low pH conditions. This may be associated with the silica content of the starting glass material as the Irvine composition had the lowest silica content and the Pathfinder rock glass composition had the highest silica content (**Table 3-1**). Glass dissolution rates have been shown to decrease exponentially with increasing SiO₂ content [e.g., *Wolff-Boenisch et al.*, 2004]. Although the alteration assemblages for each composition are similar in that they contain a variety of sulfates and silica the spectral signatures from the lowest pH solutions vary considerably. This is likely largely due to differences in mineral/phase abundance, but additional possible reasons for this are discussed in **Section 3.8.3**.

Linking geochemical alteration experiments of the four different compositions (Irvine, Backstay Pathfinder soil, and Pathfinder rock) with spectral measurements provides constraints on how IR features vary as a function of pH (0-4) and composition (tholeiitic basaltic glass, alkali basaltic glass, basaltic andesite glass) for Martian surface material. Direct comparison of the MIR and VNIR spectral analyses with Raman, SEM/EDS, and XRD bridges the gap between mineral composition/abundance and spectral signal in the IR. This can be applied to the spectral data obtained from Mars in order to better constrain variability of weathering on a global scale.

3.8.2 Effects of Composition on Chemical Alteration Assemblages

The Irvine and Backstay compositions are most similar to the Pathfinder soil composition which has significantly lower silica and a higher overall fraction of network-modifying elements such as Fe and Mg, while other cations are of lower abundance than the Pathfinder rock composition. This suggests that the degree of polymerization of the silicate framework of the Irvine, Backstay, and Pathfinder soil glasses is less than that of the Pathfinder rock glass [*Tosca et al.*, 2004]. There is a difference in reactivity between compositions with lower silica versus higher

silica abundances [e.g., *Wolff-Boenisch et al.*, 2004]. Through experimental work on glasses with silica contents of 46.09-72.62 wt.%, *Wolff-Boenisch et al.* [2004] indicated that glass dissolution rates increase exponentially with decreasing SiO₂ content. During the dissolution of glass, ions will be removed from the glass structure in the order of the relative rates for breaking their corresponding metal–oxygen bonds. For silicate glasses, alkali and alkaline-earth metals near the glass surface will be preferentially released. The Si-O bonds are the slowest breaking bonds and will be the most resistant to weathering [e.g., *Perret et al.*, 2003; *Wolff-Boenisch et al.*, 2004; *Declercq et al.*, 2012]. The higher silica content of the Pathfinder rock glass will result in an increased resistance to chemical alteration processes. This resistance can be observed in the MIR and VNIR spectral signatures as the Pathfinder rock glasses exhibit little alteration relative to the other compositions.

Irvine, Backstay, and Pathfinder soil glass compositions have similar alteration assemblages based on chemical analyses, including silica and Ca-, (Na)Al-, Mg-, and (Al)Fe-sulfates. However, there are several distinctions between the assemblages. For the Irvine alteration assemblage, Fe-Al-sulfate (pH0) and Mg-Al-sulfate (pH1) are present, but are absent in the other three compositions. This could be due to the very high Mg, increased Fe, and increased Al content for the starting Irvine composition, relative to the other compositions. Also, no pure Fe-sulfate is observed for the Irvine material, potentially due to the considerable amount of Fe-Al-sulfate present. Irvine and Backstay both display Na-Mg-(Fe)-sulfates which are not observed for either Pathfinder composition. This could be attributed to the increased Mg-content of Irvine and Backstay relative to Pathfinder soil composition as the Na contents are similar. Na-Al sulfate is present in the alteration assemblages for Backstay and Pathfinder soil, but not present in the Irvine assemblage. This could be due to the slightly higher Na content of the Backstay and Pathfinder

soil starting compositions or due to the formation of considerable (Fe,Mg)Al-sulfate for Irvine. The alteration phases observed for the Pathfinder rock glass material are limited to three phases, Ca-sulfate, Fe-oxide, and silica. The difference in reactivity can be a result of the increased abundance of silica in the starting composition for Pathfinder rock relative to Irvine, Backstay, and Pathfinder soil.

3.8.3 Comparison of Spectral and Chemical Data

The MIR spectral characteristics and models generally exhibit the major trends observed with the other analytical techniques. The glass materials follow the chemically-observed trend of increasing alteration with decreasing pH as well as the trend of a larger variety of phases being present in lower pH conditions and limited number of phases in high pH conditions (**Figure 3-1**). However there are some discrepancies observed between the MIR and analytical data such as the presence of Fe-oxides and (Zn, Fe⁺²,Mn)-Al-sulfates in MIR models when these phases are absent in the chemical analyses as well as the observation of minor phases and silica through surface chemical analyses (SEM, Raman) that are not observed by IR and/or XRD techniques. These differences may arise for a variety of reasons, described in subsequent paragraphs.

First, non-linear spectral mixing may be occurring in some of the samples. Although minerals are relatively strongly absorbing throughout much of the MIR spectral range, small particles (<~63µm) are optically thin in some portions of the MIR range, resulting in increased transmission in these regions and non-linear spectral mixing [*Ramsey and Christensen, 1998*]. Transmission features can be observed in the MIR emission signature of PFSG-A (pH0) (**Figure 3-14A**). Alteration products often form as thin coating/fracture fill, or are fine grained or poorly consolidated (**Figure 3-2, 3-5, 3-8, 3-10**), which could cause changes in spectral band morphology or locations leading to incorrect modeled abundances. Fine particles can also lead to a reduction

in spectral contrast due to multiple surface scattering [Salisbury, 1993], making it difficult to resolve spectral features.

A second reason relates to difficulties in detecting amorphous silica with XRD or Raman. Although amorphous material is observed in the XRD patterns, we were not able to distinguish secondary amorphous silica from the glass itself. However, amorphous silica is distinct from basaltic glass in the MIR, and contributed to the spectral shape of some of our samples (**Figure 3-7B,D,E; Figure 3-12B,D; Figure 3-14B**). Some poorly crystalline, silica rich material was observed during SEM/EDS for some of these samples and could be responsible for the silica signatures in the MIR (**Figure 3-10A**).

Third, the spectral detectability of some phases may be reduced simply due to the order in which they were deposited. This, combined with the various penetration depths of the analytical techniques (Raman (surface), SEM (surface), MIR (10-100's μm), VNIR (10's μm), and XRD (bulk composition)), could result in discrepancies between reported results from each technique. This is most apparent in the pressed pellet data. Both the particulate and pellet MIR spectra for IRVG-pH0 had features influenced by a variety of sulfates, but the pellet exhibited dominance of (Mg, Mn, Fe^{+2})-Al-bearing sulfates instead of the Fe^{+3} -sulfate observed for the particulate surface. The pressed pellet model also includes ~13% amorphous silica, which is absent in the assemblage of the particulate surface (**Figure 3-7A,D**). For the IRVG-pH1 (**Figure 3-7B,E**), BKSG-pH0 (**Figure 3-12A,D**), and BKSG-pH1 (**Figure 3-12B,E**) samples, unaltered material contributes more to the pellet spectral signature than the respective particulate spectral signatures. When the samples are powdered and pressed into pellets, buried phases can contribute more to the spectral signatures with less contribution from the surface phases.

A fourth possible reason may relate to incomplete spectral libraries and/or non-pure library spectra, for the Raman, MIR, and VNIR. For example, available Raman and emissivity library spectra for Mn-Al-sulfate (apjohnite), (Zn, Fe⁺², Mn)-Al-sulfate (dietrichite), Fe⁺²-Al-sulfate (halotrichite), and Mg-Al-sulfate (pickeringite) are very similar to each other, but given the lack of Zn and low abundance of Mn in the starting composition it is unlikely that dietrichite and apjohnite are present in any of the assemblages.

A fifth possible reason (particularly for the least altered samples) relates to slight inaccuracies in the spectral calibration. When modeling the mixed spectra, the unaltered spectrum was used as an end-member in the spectral models. Any slight inaccuracies in the spectral calibration between the altered and unaltered samples will result in small abundances of other phases being used to account for the mismatch. In a few cases, spectral slopes imposed on the spectra, which arise from changing temperatures during spectral acquisition may not be fully accounted for with a slope end-member, as observed for the Pathfinder Soil Glass samples (**Figure 3-14**). Fe-oxides and (Zn, Fe⁺², Mn)-Al-sulfate, which both have shallow spectral features across most of the spectrum and a subtle negative slope towards long wavelengths, may have been used in small to moderate abundances to fit the MIR spectra. (Zn, Fe⁺², Mn)-Al-sulfate is modeled at >10% abundance for IRVG-pH0, BKSG-pH3, and PFSG-A. Given the absence of (Zn, Fe⁺², Mn)-Al-sulfate in any of the other analytical techniques and the lack of Zn in the starting composition this phase is not likely present in any of these samples and is observed in the modeled abundances due to inaccuracies in spectral calibration.

In the VNIR range, low absorption coefficients result in non-linear mixing, making it difficult to detect minerals that are not the spectrally dominant phase. For example, the only material that exhibited alteration features in the VNIR were the Irvine, Backstay, and Pathfinder

Soil Glass samples altered in $\text{pH} \leq 1$ (**Figures 3-6, 3-11, 3-13, 3-15**). Also, some of the samples that appear unaltered in the VNIR exhibit some alteration phases in the MIR, Raman, SEM, and/or XRD measurements. Furthermore, hydrated materials (clay, sulfates, silica) often exhibit similar features in the VNIR with absorptions near 1.40 and 1.90 μm which can create difficulty in ascertaining the phases responsible for the spectral signature. This can result in identification of only one phase when several are present. The VNIR reflectance features exhibited by the samples altered in $\text{pH} \leq 1$ conditions were often most consistent with a single sulfate phase even though numerous sulfate phases, Fe-oxides, and/or amorphous material were observed for these samples in the MIR and other analytical techniques (**Figure 3-1**). There could also be differences in the IR data due to the slightly smaller penetration depth of VNIR when compared to MIR, resulting in higher sensitivity to the upper few microns of the surface. Despite these issues, we can generally observe signatures consistent with poly- and monohydrated sulfates (PHS, MHS, **Figure 3-1**) in particulate materials altered in $\text{pH} \leq 1$.

3.8.4 Applicability to Mars

We simulated isochemical, closed system weathering of synthetic Martian glass particulates with a low fluid-to-rock ratio and low starting pH range (<4). Based on a number of chemical and mineralogical measurements made by landed missions [*Clark, 1993; Haskin et al., 2005; Ming et al., 2006; Clark et al., 2005; Morris et al., 2006*], this type of environment has been proposed as a common and persistent alteration setting on the Martian surface [*Hurowitz and McLennan, 2007; Hurowitz and Fischer, 2014*]. Numerous laboratory studies have determined that sulfates and amorphous silica are common alteration products under this scenario (**Table 3-1**), however, to date, sulfates and silica have only been identified in isolated regions by high-resolution orbiting spectrometers [e.g., *Bibring et al., 2006*].

In general, acid alteration on particles resulted in sulfate-dominated spectral signatures in the most acidic solutions ($\text{pH} \leq 1$), though amorphous silica was present based on chemical analyses. Silicon is relatively insoluble in low pH conditions ($\text{pH} < 2-3$) and basaltic cations are relatively mobile [El-Shamy *et al.*, 1972; Minitti *et al.*, 2007]. This can result in basalt leaching or dissolution that could form a silica-enriched layer beneath the fluid containing the mobile cations. When the fluid is evaporated, in a closed system as simulated here, salts containing the more mobile cations can precipitate on top of the silica-enriched layer. The formation of the sulfates overlying the silica layer results in a larger spectral signal from the sulfates relative to the silica. When the samples are powdered and pressed into pellets, buried silica can contribute more to the spectral signature as observed for IRVG-pH0 and BKSG-pH0 (**Figure 3-7A, D; Figure 3-12A, D**). For all of the materials, alteration was only visible after the evaporation period. It is possible that the secondary phases formed from leaching during the reaction period. However, no mineral formation was observed until after the evaporation period, suggesting that the majority of the alteration material was formed from dissolution and precipitation upon evaporation.

A second finding relates to spectral detectability. Several possibilities may have contributed to the lack of widespread sulfate detection in the orbital data, 1) acid alteration at $\text{pH} \geq 2$, 2) mixing of small amounts of sulfates with unaltered material, 3) prevalence of intermediate-to-high silica glass in Martian starting materials (more resistant to acid alteration than low silica glass), 4) a lack of sulfur, 5) alteration features obscured by dust, and/or 6) a lack of pervasive acid-sulfate weathering. In the MIR, our experimental alteration results in well-developed spectral features that are consistent with sulfate and mask the glass signature only at $\text{pH} \leq 1$ (**Figure 3-7A-B; Figure 3-12A-B; Figure 3-14A-B**). This signature is preserved even when reworked and consolidated as observed in the pellet material (**Figure 3-7D; Figure 3-12D**).

However, unaltered material contributes more to the pellet spectral signatures for all of the samples except IRVG-pH0. Repeated mixing events could result in spectral signatures dominated by unaltered material. In the VNIR, spectra would be expected to have high reflectance and well-developed 1.45, 1.95, and 2.40 μm features due to polyhydrated sulfate(s) (**Figures 3-5, 3-10, 3-12, 3-14**). If acidic conditions, involving alteration fluids of initial $\text{pH} \leq 1$, persisted regionally into more recent times, sulfate-dominated signatures in TES and CRISM spectra would be expected to be more common than they are because sulfates produced in more recent times may be less likely to be reworked and mixed with unaltered material. TES models do suggest low levels of sulfate in Martian soils [e.g., *Cooper and Mustard, 2001; Bandfield, 2002; Cooper and Mustard, 2002; Gendrin and Mustard, 2004; Rogers and Christensen, 2007*], thus perhaps these were produced in more ancient times in large amounts on regional scales but have since been redistributed throughout Martian soils and diluted by other materials. This would suggest that acid-sulfate weathering has not resulted in abundant sulfates being formed in more recent times over regions large enough to be detected. However, small amounts of acid sulfate alteration could be widespread in recent times but not intense enough in any specific large location to result in a concentration of sulfates high enough to be detectable with IR techniques (e.g., minor interactions with acid aerosols). Additionally, small scale and subsurface alteration via brines could persist into recent times and lead to large amounts of sulfates but on local scales difficult to observe with orbital spectral observations [e.g., *Chevrier and Altheide, 2008; Tosca et al., 2008*].

The lack of detection for alteration material could also be related to the silica content of the starting composition. Based on the results shown here, little to no alteration material was detected in the IR signatures of the altered (pH0-4) samples with the highest silica content (PFRG). TES data are consistent with a high silica amorphous phase as a prevalent component (~10-40 %)

across many regions of Mars [Bandfield *et al.*, 2000; Rogers and Christensen, 2007]. Though the primary vs. secondary alteration nature of that phase has been debated [Bandfield *et al.*, 2000; Hamilton *et al.*, 2001; Wyatt and McSween, 2002; Kraft *et al.*, 2003; Michalski *et al.*, 2005; Salvatore *et al.*, 2014], a silica-rich volcanic glass remains as one of the viable explanations. As described in **Section 3.8.2**, silica-rich glasses would be most resistant to alteration. In this scenario, water-limited, isochemical acidic weathering conditions could be largely similar across much of Mars, but glassy surfaces with higher silica contents would be less affected.

Another possibility for a lack of sulfate detection, that is not demonstrated here, is variations in primary sulfur content [Dehouck *et al.*, 2012] or sulfur added to the system [Hurowitz and Fischer, 2014]. Results from Dehouck *et al.* [2012] indicated that the reaction of sulfides, specifically pyrrhotite, with basaltic silicates under neutral conditions, can produce sulfates. They suggest that differences in sulfate detection on Mars could be due to variation in the initial sulfide content of the bedrock. Based on the consistent values of basaltic cations and inconsistent sulfur values between Gusev crater rocks (Adirondack), Gusev crater soils, and Meridiani soils, Hurowitz and Fischer [2014] suggest that the deviations observed in the chemistries of these materials are due to differences in the amount of sulfur added to the system without considerable mobilization of cations. This could be a result of a water limited environment with chemical alteration dominated by S-rich fluids resulting in secondary phases forming without physical separation from the primary substrate under cation-conservative conditions. Areas where sulfate phases are not detected could also be due simply to a lack of acid weathering with S-rich fluids in that particular region, suggesting that any acid-sulfate weathering has been temporally limited or restricted to patchy, isolated locations on rocks and soils. IR Spectral identifications of Martian surfaces can also be obscured by thin coatings (10-20 μ m) of atmospherically deposited dust [e.g., Johnson *et*

al., 2002]. The dust can cause difficulty in discriminating spectral features attributable to fine-particle coatings from those of the rock surface, which could result in the masking of alteration features. Future work will focus on detailed, regional comparisons of Mars TES and OMEGA data with laboratory data (**Chapter 6**).

Last, this study illustrates the effect that primary glass composition can have on the spectral character of altered samples in both the MIR and VNIR range (**Figure 3-17A-B**). For example, the magnitude and shape of spectral slopes in the VNIR was observed to vary greatly with starting composition (**Figure 3-17A**). Strong negative [e.g., *Poulet et al.*, 2007] and concave-up slopes [*Horgan and Bell*, 2012] observed in VNIR data of the Martian lowlands have been attributed to thin varnishes of ferric oxide-bearing rinds, impact melts [e.g., *Poulet et al.*, 2007], or acidic leaching of silicate glasses [*Horgan and Bell*, 2012]. *Horgan and Bell* [2012] suggest that these shapes are formed from the interaction of silicate glass with small volumes of acidic fluids [e.g., *Minitti et al.*, 2007], resulting in a concave-up shape produced by thin (3-10 μ m) silica-enriched leached glass rinds and a negative slope due to a thin coating of leached Fe⁺³ overlying the Si-rich rind. In the northern lowlands of Mars, the negative slope varies in its concavity, which has been attributed to variable degrees of Fe-coating removal to expose the Si-rich, leached glass rind underneath [*Horgan and Bell*, 2012]. In this work, only the Backstay glass exhibited the negative, concave spectral slopes in the VNIR, despite alteration under similar conditions as the other glasses. Our work demonstrates that the magnitude and concavity of the negative slope associated with coated glass is also affected by primary glass composition, and thus inferences about leached/coated surfaces from VNIR spectra may be complicated by this factor.

3.9 Conclusions

From our work, we can make the following conclusions:

1. A distinction in alteration extent and products was observed for glass substrates having differing compositions, with more alteration in the lowest silica glass (Irvine) and less alteration in the highest silica glass (Pathfinder Rock). Spectral differences between alteration products from each starting material were also present, reflecting changes in the alteration mineral assemblage.
2. The MIR spectral characteristics and models generally exhibit the major trends observed with the chemical analyses. However there also some discrepancies observed between the MIR and analytical data such as the presence of amorphous silica, Fe-oxides, and (Zn, Fe⁺²,Mn)-Al-sulfates in MIR models when these phases are absent in the chemical analyses. The features exhibited in the VNIR often resulted in the identification of only one phase when several are present.
3. Acid alteration on particles resulted in sulfate-dominated assemblages in the most acidic solutions ($\text{pH} \leq 1$) that exhibited well-developed sulfate features, in the TIR, that are preserved after reworking and consolidation, and strong 1.45, 1.95, and 2.40 μm features in the VNIR.
4. From orbit, evidence of widespread surface alteration is lacking. Our results demonstrate that continued or repeated exposure to acid sulfate weathering environments should have a discernible spectral signature in existing datasets (sulfate-dominated spectral assemblages in the MIR, and sulfate-dominated signatures or slope changes in the VNIR). Although such signatures are found in a few isolated locations on Mars with high resolution spectrometers, much of the Martian surface lacks these characteristics, suggesting that either: 1) most acid alteration occurred at $\text{pH} \geq 2$, 2) small amounts of sulfates were reworked with unaltered material, 3) there is a prevalence of intermediate-to-high silica

glass in Martian starting materials (more resistant to acid alteration than low silica glass), 4) primary or added sulfur were lacking, 5) alteration features are obscured by dust, and/or 6) large-scale, pervasive, acid-sulfate weathering of the Martian surface did not occur. However, detailed comparisons between our lab data and existing TES, Mini-TES, CRISM and OMEGA data are needed to further test this assertion, and will be the subject of future work.

3.10 References:

- Baker, L. L., D. J. Aгенbroad, and S. A. Wood (2000), Experimental hydrothermal alteration of a Martian analog basalt: Implications for Martian meteorites, *Meteorit. Planet. Sci.*, 35, 31– 38.
- Baldridge, A. M. (2008), Thermal Infrared Spectral Studies of Sulfates and Chlorides; Applications to Salts on the Martian Surface, Ph.D. Dissertation thesis, 204 pp., Arizona State University, Tempe, AZ.
- Baldridge, A.M., P.R. Christensen (2009), Laboratory Technique for Thermal Emission Measurement of Hydrated Minerals: *Applied Spectroscopy*, v. 63, p. 678-688.
- Bandfield, J. L., V. E. Hamilton, and P. R. Christensen (2000), A global view of Martian surface compositions from MGS-TES, *Science*, 287, 1626– 1630.
- Bandfield, J.L. (2002), Global mineral distribution on Mars. *J. Geophys. Res.* 107 (E6), doi:10.1029/2001JE001510.
- Banin, A., F. X. Han, I. Kan, and A. Cicelsky (1997), Acidic volatiles and the Mars soil: *J. Geophys. Res.-Planets*, v. 102, p. 13341-13356.
- Bibring, J.-P., Y. Langevin, A. Gendrin, et al., (2005), Mars surface diversity as revealed by the OMEGA/Mars Express observations, *Science* 307, 1576–81.

- Bibring, J.-P., Y. Langevin, J. F. Mustard, F. Poulet, R. Arvidson, A. Gendrin, B. Gondet, N. Mangold, P. Pinet, and F. Forget (2006), Global mineralogical and aqueous Mars history derived from OMEGA/Mars express data, *Science*, 312, 400–404, doi:10.1126/science.1122659.
- Bigham, J. M., and D. K. Nordstrom (2000), Iron and aluminum hydroxysulfates from acid sulfate waters, in *Sulfate Minerals: Crystallography, Geochemistry and Environmental Significance*, edited by C. N. Alpers, J. L. Jambor, and D. K. Nordstrom, pp. 351 – 403, Mineral. Soc. Of Am., Washington, D. C.
- Bishop et al., (2008), Phyllosilicate diversity and past aqueous activity revealed at Mawrth Vallis, Mars. *Science* 321:830–833.
- Burns R.D., D.S. Fisher (1990), Iron–sulfur mineralogy of Mars: magmatic evolution and chemical weathering products, *J. Geophys. Res.*, 95 pp., 14415–14421.
- Carter et al., (2013), Hydrous minerals on Mars as seen by the CRISM and OMEGA imaging spectrometers: Updated global view. *JGR*, 118:831–858.
- Chemtob, S.M, G.R. Rossman (2014), Timescales and mechanisms of formation of amorphous silica coatings on fresh basalts at Kīlauea Volcano, Hawai'i, *Journal of Volcanology and Geothermal Research*, Volume 286, 1 October 2014, Pages 41-54, ISSN 0377-0273.
- Chevrier, V. F., and T. S. Altheide (2008), Low temperature aqueous ferric sulfate solutions on the surface of Mars, *Geophys. Res. Lett.*, 35, L22101, doi:10.1029/2008GL035489.
- Christensen, P. R., et al. (1992), Thermal Emission Spectrometer experiment: The Mars Observer mission, *J. Geophys. Res.*, 97, 7719–7734, 1992.
- Christensen, P.R., J. L. Bandfield, R. N. Clark, K. S. Edgett, V. E. Hamilton, T. Hoefen, H. H. Kieffer, R. O. Kuzmin, M. D. Lane, M. C. Malin, R. V. Morris, J. C. Pearl, R. Pearson, T. L.

- Roush, S. W. Ruff, and M. D. Smith (2000), Detection of crystalline hematite mineralization on Mars by the Thermal Emission Spectrometer: Evidence for near-surface water. *J. Geophys. Res.*, 105:9623–9642.
- Christensen, P. R., et al. (2003), Miniature Thermal Emission Spectrometer for the Mars Exploration Rovers, *J. Geophys. Res.*, 108(E12), 8064, doi:10.1029/2003JE002117, 2003.
- Clark, B. C. (1993), Geochemical components in Martian soil. *Geochim. Cosmochim. Acta* 57, 4575–4581.
- Clark, B.C., R.V. Morris, S.M. McLennan, R. Gellert, B. Jolliff, A.H. Knoll, S.W. Squyres, T.K. Lowenstein, D.W. Ming, N.J. Tosca, A. Yen, P.R. Christensen, S.P. Gorevan, J. Brückner, W.M. Calvin, G. Dreibus, W.H. Farrand, G. Klingelhöfer, H. Waenke, J. Zipfel, J.F. Bell III, J.P. Grotzinger, H.Y. McSween Jr., R. Rieder (2005), Chemistry and mineralogy of outcrops at Meridiani Planum, *EPSL*. 240, 73-94.
- Cloutis, E. A., F.C. Hawthorne, S.A. Mertzman, K. Krenn, M.A. Craig, D. Marcino, M. Methot, J. Strong, J.F. Mustard, D.L. Blaney, J.F. Bell III, and F. Vilas (2006), Detection and discrimination of sulfate minerals using reflectance spectroscopy, *Icarus*, 184, 121 – 157.
- Cooper, C. D. and J. F. Mustard (2001), TES observations of the global distribution of sulfate on Mars, *Lunar Planet. Sci.* XXXII, Abs# 2048.
- Cooper, C. D. and J. F. Mustard (2002), Sulfates on Mars: Comparing TES and ISM Results, *Lunar Planet. Sci.* XXXIII, Abs# 1997.
- Declercq, T. Diedrich, M. Perrot, S.R. Gislason, E.H. Oelkers (2012), Experimental determination of rhyolitic glass dissolution rates at 40–200 °C and $2 < \text{pH} < 10.1$. *Geochim. Cosmochim. Acta*, 100, pp. 251–263.

- Dehouck, E., V. Chevrier, A. Gaudin, N. Mangold, P.-E. MathZ, P. Rochette (2012), Evaluating the role of sulfide-weathering in the formation of sulfates or carbonates on Mars, *Geochim. Cosmochim. Acta*, 90, 47-63, doi:10.1016/j.gca.2012.04.057.
- Downs, R. T. (2006), The RRUFF Project: an integrated study of the chemistry, crystallography, Raman and infrared spectroscopy of minerals. Program and Abstracts of the 19th General Meeting of the International Mineralogical Association in Kobe, Japan. O03-13
- Ehlmann, B.L., J.F. Mustard, S.L. Murchie, J-P. Bibring, A. Meunier, A.A. Fraeman, and Y. Langevin, (2011), Subsurface water and clay mineral formation during the early history of Mars. *Nature*. 479, 53.
- Ehlmann, B. L., D. L. Bish, S. W. Ruff, and J. F. Mustard (2012), Mineralogy and chemistry of altered Icelandic basalts: Application to clay mineral detection and understanding aqueous environments on Mars, *J. Geophys. Res.*, 117, E00J16, doi:10.1029/2012JE004156.
- El-Shamy, T. M., J. Lewins, and R. W. Douglas (1972), The dependence of the pH on the decomposition of glasses by aqueous solutions, *J. Soc. Glass Technol.*, 13(3), 81 – 87.
- Fernández-Remolar, D. C., R. V. Morris, J. E. Gruener, R. Amils, and A. H. Knoll (2005), The Río Tinto Basin, Spain: Mineralogy, sedimentary geobiology, and implications for interpretation of outcrop rocks at Meridiani Planum, Mars, *Earth Planet. Sci. Lett.*, 240(1), 149–167, doi:10.1016/j.epsl.2005.09.043.
- Gellert, R., R. Rieder, R.C. Anderson, J. Bruckner, B.C. Clark, G. Dreibus, T. Economou, G. Klingelhofer, G.W. Lugmair, D.W. Ming, S.W. Squyres, C. d'Uston, H. Wanke, A. Yen, J. Zipfel (2004), Chemistry of rocks and soils in Gusev Crater from the Alpha Particle X-ray spectrometer. *Science* 305, 829–832.

- Gellert, R., R. Rieder, R.C. Anderson, J. Bruckner, B.C. Clark, G. Dreibus, T. Economou, G. Klingelhofer, G.W. Lugmair, D.W. Ming, S.W. Squyres, C. d'Uston, H. Wanke, A. Yen, J. Zipfel (2004), Chemistry of rocks and soils in Gusev Crater from the Alpha Particle X-ray spectrometer. *Science* 305, 829–832.
- Gendrin, A. and J.F. Mustard (2004), Sulfate-cemented soils detected in TES data through the application of an automatic band detection algorithm. LPSC XXXV, Abs #1205.
- Gendrin, A., N. Mangold, J.-P. Bibring, et al., (2005), Sulfates in Martian layered terrains: the OMEGA/Mars Express view, *Science* 307, 1587–91.
- Glotch, T.D., R.V. Morris, P.R. Christensen, T.G. Sharp (2004), Effect of precursor mineralogy on the thermal infrared emission spectra of hematite: application to Martian hematite mineralization. *J. Geophys. Res.*, 109.
- Glotch, T. D., and M. D. Kraft (2008), Thermal transformations of akaganéite and lepidocrocite to hematite: Assessment of possible precursors to Martian crystalline hematite, *Phys. Chem. Min.*, 35, 569-581.
- Golden, D. C., D. W. Ming, R. V. Morris, and S. A. Mertzman (2005), Laboratory-simulated acid-sulfate weathering of basaltic materials: Implications for formation of sulfates at Meridiani Planum and Gusev crater, Mars, *J. Geophys. Res.*, 110, E12S07.
- Hamilton, V. E., M. B. Wyatt, H. Y. McSween, and P. R. Christensen (2001), Analysis of terrestrial and Martian volcanic compositions using thermal emission spectroscopy: II. Application to Martian surface spectra from MGS TES, *J. Geophys. Res.*, 106, 14,733–14,746.
- Hamilton, V. E., R. V. Morris, J. E. Gruener, and S. A. Mertzman (2008), Visible, near-infrared, and middle infrared spectroscopy of altered basaltic tephra: Spectral signatures of phyllosilicates, sulfates, and other aqueous alteration products with application to the

- mineralogy of the Columbia Hills of Gusev Crater, Mars: *J. Geophys. Res.-Planets*, v. 113, p. E12S43.
- Haskin L.A., et al. (2005), Water alteration of rocks and soils on Mars at the Spirit rover site in Gusev crater. *Nature* 436, 66-69.
- Horgan, B., and J. F. Bell III (2012), Widespread weathered glass on the surface of Mars, *Geology*, 40(5), 391–394, doi:10.1130/g32755.1
- Hurowitz, J. A., S. M. McLennan, N. J. Tosca, R. E. Arvidson, J. R. Michalski, D. W. Ming, C. Schröder, and S. W. Squyres (2006), In situ and experimental evidence for acidic weathering of rocks and soils on Mars, *J. Geophys. Res.*, 111, E02S19.
- Hurowitz, J.A and S.M. McLennan (2007), A ~ 3.5 Ga record of water-limited, acidic weathering conditions on Mars, *Earth and Planetary Science Letters*, Volume 260, Issues 3–4, 30 August 2007, Pages 432-443, ISSN 0012-821X.
- Hurowitz, J. A., and W. W. Fischer (2014), Contrasting styles of water–rock interaction 862 at the Mars Exploration Rover landing sites, *Geochimica et Cosmochimica Acta*, 127, 863 25-38.
- Hynek, B. M., T. M. McCollom, E. C. Marcucci, K. Brugman, and K. L. Rogers (2013), Assessment of environmental controls on acid-sulfate alteration at active volcanoes in Nicaragua: Applications to relic hydrothermal systems on Mars, *J. Geophys. Res. Planets*, 118, 2083–2104, 43 doi:10.1002/jgre.20140.
- Johnson, J. R., P. R. Christensen, and P. G. Lucey (2002), Dust coatings on basaltic rocks and implications for thermal infrared spectroscopy of Mars, *J. Geophys. Res.*, 107(E6), 5035.
- Kraft, M. D., J. R. Michalski, and T. G. Sharp (2003), Effects of pure silica coatings on thermal emission spectra of basaltic rocks: Considerations for Martian surface mineralogy: *Geophysical Research Letters*, v. 30.

- Kraft, M. D., T. G. Sharp, J. R. Michalski, and E. B. Rampe (2007), Combined Thermal and Near Infrared Spectra of Hydrous Silica Coatings: Implications for Surface Type 2 Mineralogy and Recent Liquid Water on Mars: *Lunar Planet. Sci.* XXXVIII.
- Lane, M.D. (2007), Mid-infrared emission spectroscopy of sulfate and sulfate-bearing minerals. *Am. Mineral.*, 92, pp. 1–18
- Lane, M.D., J.L. Bishop, M.D. Dyar, T.H. Hiroi, S.A. Mertzman, D.L. Bish, P.L. King, and A.D. Rogers (2015), Mid-infrared emission spectroscopy and visible/near-infrared reflectance spectroscopy of Fe-sulfate minerals. *Am. Mineral.*, 100, pp. 66-82.
- Langevin, Y., F. Poulet, J.-P. Bibring, and B. Gondet (2005), Sulfates in the north polar region of Mars detected by OMEGA/Mars Express, *Science*, 307, 1584 – 1586.
- Lichtenberg, K. A., R.E. Arvidson, R.V. Morris, S.L. Murchie, J.L. Bishop, D.F. Remolar, T.D. Glotch, E.N. Dobre, J.F. Mustard, J. Andrews-Hanna, and L.H. Roach (2010), Stratigraphy of hydrated sulfates in the sedimentary deposits of Aram Chaos, Mars, *J. Geophys. Res.*, 115, E00D17.
- Lichtenberg, K. A., R.E. Arvidson, R.V. Morris, S.L. Murchie, J.L. Bishop, D.F. Remolar, T.D. Glotch, E.N. Dobre, J.F. Mustard, J. Andrews-Hanna, and L.H. Roach (2010), Stratigraphy of hydrated sulfates in the sedimentary deposits of Aram Chaos, Mars, *J. Geophys. Res.*, 115, E00D17.
- Madden M. E., R. J. Bodnar and J. D. Rimstidt (2004), Jarosite as an indicator of water-limited chemical weathering on Mars. *Nature* 431, 821–823.
- Marcucci, E. C., and B. M. Hynek (2014), Laboratory simulations of acid-sulfate weathering in volcanic hydrothermal conditions: Implications for early Mars, *J. Geophys. Res.*

- Marcucci, E. C., B. M. Hynek, K. S. Kierein-Young, and K. L. Rogers (2013), Visible-near-infrared reflectance spectroscopy of volcanic acid-sulfate alteration in Nicaragua: Analogs for early Mars, *J. Geophys. Res. Planets*, 118, 2213–2233, doi:10.1002/jgre.20159.
- McCanta, M.C., M.D. Dyar, and A.H. Treiman (2014), Alteration of Hawaiian basalts under sulfur-rich conditions: Applications to understanding surface–atmosphere interactions on Mars and Venus. *Am. Min.*, 99, pp. 291–302.
- McSween, H.Y., S. W. Ruff, R. V. Morris, J. F. Bell III, K. Herkenhoff, R. Gellert, K. R. Stockstill, L. L. Tornabene, S. W. Squyres, J. A. Crisp, P. R. Christensen, T. J. McCoy, D. W. Mittlefehldt, and M. Schmidt (2006), Alkaline volcanic rocks from the Columbia Hills, Gusev crater, Mars. *J. Geophys. Res.*, 111 (E9), E09S91.
- Michalski J.R., M.D. Kraft, T.G. Sharp, L.B. Williams, and P.R. Christensen (2005), Mineralogical constraints on the high-silica martian surface component observed by TES. *Icarus* 174: 161-177.
- Michalski, J. R., M. D. Kraft, T. G. Sharp, and P. R. Christensen (2006), Effects of chemical weathering on infrared spectra of Columbia River Basalt and spectral interpretations of martian alteration: *Earth and Planetary Science Letters*, v. 248, p. 822-829.
- Milam, K.A., H.Y. McSween Jr., J. Moersch, and P.R. Christensen (2010), Distribution and variation of plagioclase compositions on Mars. *JGR*, 115, E09004.
- Ming D. W., D. W. Mittlefehldt, R. V. Morris, D. C. Golden, R. Gellert, A. Yen, B.C. Clark, S. W. Squyres, W. H. Farrand, S. W. Ruff, R. E. Arvidson, G. Klingelhöfer, H. Y. McSween, D. S. Rodionov, C. Schröder, P. A. de Souza, and A. Wang (2006), Geochemical and mineralogical indicators for aqueous processes in the Columbia Hills of Gusev crater, Mars. *J. Geophys. Res.* 111, E02S12.

- Minitti, M. E., C. M. Weitz, M. D. Lane, and J. L. Bishop (2007), Morphology, chemistry, and spectral properties of Hawaiian rock coatings and implications for Mars, *J. Geophys. Res.*, 112, E05015, doi:10.1029/2006JE002839.
- Morris, R. V., D.C. Golden, J.F. Bell III, T.D. Shelfer, A.C. Scheinost, N.W. Hinman, G. Furniss, S.A. Mertzman, J.L. Bishop, D.W. Ming, C.C. Allen, D.T. Britt (2000a), Mineralogy, composition and alteration of Mars Pathfinder rocks and soils: Evidence from multispectral, elemental and magnetic data on terrestrial analogue, SNC meteorite and Pathfinder samples, *J. Geophys. Res.*, 105, 1757–1817.
- Morris, R. V., T. Graff, M. D. Lane, D. C. Golden, C. S. Schwandt, D.W. Ming, T.D. Shelfer, S. A. Mertzman, J. F. Bell, J. Crisp, and P. R. Christensen (2000b), Acid sulfate alteration products of a tholeiitic basalt: Implications for interpretation of Martian thermal emission spectra, *Lunar Planet. Sci.*, XXXI, Abs. 2014.
- Morris, R. V., et al. (2006), Mössbauer mineralogy of rock, soil, and dust at Gusev crater, Mars: Spirit's journey through weakly altered olivine basalt on the plains and pervasively altered basalt in the Columbia Hills, *J. Geophys. Res.*, 111, E02S13, doi:10.1029/2005JE002584.
- Murchie, S., et al. (2007), Compact Reconnaissance Imaging Spectrometer for Mars (CRISM) on Mars Reconnaissance Orbiter (MRO), *J. Geophys. Res.*, 112, E05S03, doi:10.1029/2006JE002682.
- Mustard J. F., Murchie S. L., Pelkey S. M., Ehlmann B. L., Milliken R. E., Grant J. A., Bibring J.-P., Poulet F., Bishop, J. L., et al. (2008), Hydrated silicate minerals on Mars observed by the CRISM instrument on MRO. *Nature* 454:305–309.
- Niles P. B. and Michalski J. (2009), Meridiani Planum sediments on Mars formed through weathering in massive ice deposits. *Nat. Geosci.* 2, 215–220.

- Ody, A., F. Poulet, Y. Langevin, J.-P. Bibring, G. Bellucci, F. Altieri, B. Gondet, M. Vincendon, J. Carter, and N. Manaud (2012), Global maps of anhydrous minerals at the surface of Mars from OMEGA/MEx, *JGR.*, 117, E00J14.
- Perret, J.L. Crovisier, P. Stille, G. Shields, U. Mäder, T. Advocat, K. Schenk, M. Chardonnens (2003), Thermodynamic stability of waste glasses compared to leaching behavior. *Appl. Geochem.*, 18, pp. 1165–1184.
- Poulet, F., J.-P. Bibring, J. F. Mustard, et al., (2005), Phyllosilicates on Mars and implications for early martian climate, *Nature* 438, 623–7.
- Poulet, F., C. Gomez, J.-P. Bibring, Y. Langevin, B. Gondet, P. Pinet, G. Bellucci, and J. Mustard (2007), Martian surface mineralogy from Observatoire pour la Mineralogie, l'Eau, les Glaces et l'Activite' on board the Mars Express spacecraft (OMEGA/ MEx): Global mineral maps, *J. Geophys. Res.*, 112, E08S02, doi:10.1029/2006JE002840.
- Rampe, E. B., M. D. Kraft, and T. G. Sharp (2009), Chemical Weathering Trends From TIR Spectral Models: Implications For Deriving Weathering Trends From Martian Spectral Data, *LPSC XL*, Abs. 2132.
- Ramsey, M.S. and P.R. Christensen (1998), Mineral abundance determination: Quantitative deconvolution of thermal emission spectra. *J. Geophys. Res.* 103 (B1), 577–597.
- Rogers, A.D. and O. Aharonson (2008), Mineralogical composition of sands in Meridiani Planum determined from MER data and comparison to orbital measurements. *J. Geophys. Res. Planets* 113, E06S14.
- Rogers, A.D. and P.R. Christensen (2007), Surface mineralogy of Martian low-albedo regions from MGS-TES data: Implications for upper crustal evolution and surface alteration, *JGR.*, 112, E01003.

- Ruff, S. W., J.D. Farmer, W.M. Calvin, K.E. Herkenhoff, J.R. Johnson, R.V. Morris, M.S. Rice, R.E. Arvidson, J.F. Bell III, P.R. Christensen, and S.W. Squyres (2011), Characteristics, distribution, origin, and significance of opaline silica observed by the Spirit rover in Gusev crater, Mars, *J. Geophys. Res.*, 116, E00F23.
- Salisbury, J. W., and A. Wald (1992), The role of volume scattering in reducing spectral contrast of Reststrahlen bands in spectra of powdered minerals, *Icarus*, 96, 121-128.
- Salisbury, J. W. (1993), Mid-Infrared Spectroscopy: Laboratory Data, in *Remote Geochemical Analysis: Elemental and Mineralogical Composition*, Pieters. C. M., Englert, P. A., Ed., Cambridge University Press, Cambridge, UK.
- Salvatore, M.R., J.F. Mustard, J.W. Head III, A.D. Rogers, and R.F. Cooper (2014), The dominance of cold and dry alteration processes on recent Mars, as revealed through pan-spectral orbital analyses. *Earth Planet. Sci. Lett.*, 404 (2014), pp. 261-272.
- Schiffman, P., R. Zierenberg, N. Marks, J. L. Bishop, and M. D. Dyar (2006), Acid-fog deposition at Kilauea volcano: A possible mechanism for the formation of siliceous-sulfate rock coatings on Mars, *Geology*, 34(11), 921–924, doi:10.1130/G22620A.1.
- Seelos, K. D., R. E. Arvidson, B. L. Jolliff, S. M. Chemtob, R. V. Morris, D. W. Ming, and G. A. Swayze (2010), Silica in a Mars analog environment: Ka'u Desert, Kilauea Volcano, Hawaii, *J. Geophys. Res.*, 115, E00D15, doi:10.1029/2009JE003347.
- Sklute, E., (2015), On the Subject of Analyzing Iron and Sulfur Bearing Minerals from Three Extreme Environments: Geological Carbon Sequestration, Acid Mine Drainage, and Mars. Ph.D. Dissertation thesis, 433 pp., Stony Brook University, Stony Brook, NY.
- Tosca, N.J., (2003), Acid-Sulfate Weathering of Synthetic Martian Basalt: The Acid Fog Model Revisited. Master's Thesis, 97 pp., Stony Brook University, Stony Brook, NY.

- Tosca, et al., (2004), Acid-sulfate weathering of synthetic Martian basalt: The acid fog model revisited, *J. Geophys. Res.*, 109, E05003.
- Tosca, N.J., A.H. Knoll, and S.M. McLennan (2008), Water activity and the challenge for life on early Mars: *Science*, v. 320, p. 1204–1207, doi: 10.1126/science.1155432.
- Vassamillet, L. F. and Caldwell, V. E. (1969), Electron-probe microanalysis of alkali metals in glasses. *Journal of Applied physics*, 40, 1637-1640.
- Viviano, C.E. and J.E. Moersch (2012), A technique for mapping Fe/Mg-rich phyllosilicates on Mars using THEMIS multispectral thermal infrared images. *JGR*, 117:E07007.
- Whitaker, M.L., Nekvasil, H., Lindsley, D.H., and DiFrancesco, N.J. (2007), The Role of Pressure in Producing Compositional Diversity in Intraplate Basaltic Magmas, *J. Petrol.*, vol. 48, no. 2, pp. 365–393.
- Wolff-Boenisch D., S. R. Gislason, E. H. Oelkers, and C. V. Putnis (2004), The dissolution rates of natural glasses as a function of their composition at pH 4 and 10.6, and temperatures from 35 to 74C, *Geochim. Cosmochim. Acta*, 68, 4843-4858.
- Wyatt, M. B., V. E. Hamilton, H. Y. McSween Jr., P. R. Christensen, and L. A. Taylor (2001), Analysis of terrestrial and Martian volcanic compositions using thermal emission spectroscopy: 1. Determination of mineralogy, chemistry, and classification strategies, *J. Geophys. Res.*, 106(E7), 14711–14732.
- Wyatt, M. B., and H. Y. McSween (2002), Spectral evidence for weathered basalt as an alternative to andesite in the northern lowlands of Mars. *Nature*, 417, 263– 266.

Table 3-1. Previous studies of basalt and tephra alteration.

	Material	Conditions*	Analytical techniques ^A	Secondary phases
<i>Banin et al., 1997</i>	Partly palagonitized Hawaiian tephra	*Laboratory weathering in various acidic (pH~2.5-7.75) solutions, ambient temperature	XRD	Al-sulfate, Ca-sulfate
<i>Morris et al., 2000a</i>	unaltered, palagonitic, and sulfatetic tephra from Mauna Kea Volcano, steam vent material from Kilauea Volcano	In situ, hydrolytic and acid-sulfate alteration	Diffuse reflectance, XRD, MB, XRF	Nanophase-oxides, glass, silica, Fe-sulfate, Al-sulfate, smectite, Fe-oxides
<i>Morris et al., 2000b</i>	Tholeiitic basalt from Sulfur Bank, Hawaii	In situ, acidic alteration (pH~4-5)	XRD, TIR	Anatase, nanophase silica, Na-Al-sulfate, Ca-sulfate
<i>Baker et al., 2000</i>	High-Fe basalt, Columbia River Basalt Group	*Laboratory, low and high temperature (23-400°C) alteration through aqueous solutions and vapors	XRD, SEM, ICP-AES	Carbonates, free silica phases, zeolites, phyllosilicates
<i>Tosca et al., 2004</i>	Synthetic Pathfinder glass and basalt	*Laboratory, low pH, ambient temperature	SEM, XRD, EMP, ICP-AES	Mg, Fe, Ca, Al-sulfate, Fe-oxides, amorphous silica
<i>Fernandez-Remolar et al., 2005</i>	Rio Tinto river system deposits, Spain	In situ low pH, ambient temperature alteration	XRD, MB, ICP-MS, TXRF	Mg, Al, Fe, Ba, Ca-sulfate, Fe-oxides
<i>Schiffman et al., 2006</i>	Siliceous-sulfate basalt coatings, Ka'u Desert, Hawaii	In situ, low pH alteration	XRD, SEM, VNIR, EMP, MB	Amorphous silica, jarosite, hydrated iron oxides
<i>Miniti et al., 2007</i>	Glass-rich basalts, Hawaii	In situ, low pH alteration	EMP, VNIR, TIR	Hydrated silica with minor Fe, Ti, and S-bearing materials, ferric oxides/oxyhydroxides
<i>Hamilton et al., 2008</i>	Basaltic tephra, Mauna Kea Volcano, Hawaii	In situ, low – neutral- high pH, ambient – high temperature	XRD, VNIR, TIR	Phyllosilicates, Fe-oxides, kaolinite, smectite, cristobalite, palagonite, Na-(Fe,Al)-sulfate
<i>Seelos et al., 2010</i>	Lava, ash, and solfatara deposits, Ka'u Desert, Hawaii	In situ, low pH alteration	VNIR, Raman, EMP	Amorphous silica and Fe-oxides
<i>Ehlmann et al., 2012</i>	Iceland basaltic lava flows	In situ, low-high temperature, low – high sulfur	VNIR, TIR, XRD	Al and Fe/Mg smectites, hematite, hydrous silica phases
<i>Hynek et al., 2013</i>	Nicaraguan volcanic systems	In situ, low – neutral pH (-1-6), ambient – high temperature	XRD, XRF, SEM, EMP, VNIR	Sulfur, silica, Ca, Al, Fe, Mg, Mg-sulfates, phyllosilicates
<i>Marcucci et al., 2013</i>	Freshly exposed basalt, Nicaragua	In situ, acidic steam-driven alteration	VNIR	Ca, Al, Fe, Mg-sulfates, oxides/hydroxides, and phyllosilicates
<i>Marcucci and Hynek, 2014</i>	Basalt, Cerro Negro Volcano, Nicaragua	*Laboratory, low pH, high temperature (65-200°C)	SEM, XRD, ICP-AES	Ca-sulfate, Na-Al-sulfate, Fe-oxide, amorphous Al-Si gel
<i>Chemtob and Rossman, 2014</i>	Surface coatings on basalts, Kilauea Volcano, Hawaii	In situ, low pH alteration	SEM, EMP, Raman	Amorphous silica, Fe-Ti-oxides
<i>McCanta et al., 2014</i>	Solfatara deposits, Halemaumau crater	In situ, low pH (<~2) alteration	SEM, MB, XRD	Amorphous silica overlain by sulfates (Ca, Na-Al, Na-Fe)

^AXRD = X-ray diffraction, MB = Mossbauer, XRF= X-ray fluorescence, TIR = thermal infrared, SEM = scanning electron microscopy, ICP-AES = inductively coupled plasma – atomic emission spectroscopy, VNIR = visible near infrared, EMP = electron microprobe, ICP-MS = inductively coupled plasma – mass spectroscopy, TXRF= total X-ray fluorescence

* Indicates laboratory experiments.

Table 3-2. Synthetic Pathfinder, Irvine, and Backstay glass bulk compositions.

Oxide	Pathfinder Rock Average	Pathfinder Soil Average	Irvine Target	Irvine Average (Synthesized Comp.) ^a	Backstay Target	Backstay Average (Synthesized Comp.) ^a
SiO ₂	57.87	48.68	47.17	48.39	50.00	49.14
TiO ₂	0.51	1.16	1.06	1.08	0.94	0.97
Al ₂ O ₃	10.36	10.29	10.62	10.93	13.41	13.87
FeO ^b	13.73	19.23	19.27	17.83	13.80	15.00
MnO	0.46	0.49	0.36	0.39	0.24	0.23
MgO	2.47	7.66	10.62	10.69	8.39	8.43
CaO	8.68	7.07	6.05	5.87	6.10	6.04
Na ₂ O	4.28	3.56	2.69	2.63	4.19	3.69
K ₂ O	1.11	0.67	0.68	0.67	1.08	0.78
P ₂ O ₅	0.54	1.19	0.97	0.92	1.40	1.37
Cr ₂ O ₃	0.00	0.00	0.20	0.19	0.15	0.14
S	0.00	0.00	0.31	0.33	0.30	0.33
Cl	0.00	0.00	0.00	0.08	0.00	0.01
Total	100.01	100.00	100.00	100.00	100.00	100.00
H ₂ O	0.00	0.00	0.00	2.00 ^c	0.00	2.00 ^c

Source: Irvine and Backstay: McSween *et al.*, 2008 normalized to 100, Pathfinder Rock and Pathfinder Soil: Tosca *et al.*, 2004.

^aAverage of 20 electron microprobe analyses, normalized to 100.00 wt. %.

^bIrvine and Backstay Fe₂O₃ and FeO values have been converted into an 80:20 ratio.

^c2.00 wt. % H₂O from talc dehydration during synthesis.

Table 3-3. Acid Solutions used in batch alteration experiments.

Acid Solution pH	H ₂ SO ₄ (mol/L)	HCl (mol/L)
0	1.0 x 10 ⁰	2.0 x 10 ⁻¹
1	1.0 x 10 ⁻¹	2.0 x 10 ⁻²
2	1.0 x 10 ⁻²	2.0 x 10 ⁻³
3	1.0 x 10 ⁻³	2.0 x 10 ⁻⁴
4	1.0 x 10 ⁻⁴	2.0 x 10 ⁻⁵

Irvine Glass					
	pH0	pH1	pH2	pH3	pH4
TIR ^A					
VNIR ^B	PHS ± silica slope change	MHS ± PHS, silica slope change	No change	No change	No change
SEM/Raman/XRD ^C	Ca, Al, Mg, Fe-Al, Na-Mg-sulfates S-rich coating	Ca, Al, Mg, Mg-Al, Na-Mg-Fe, Mn-sulfates	Ca-sulfate	None	None
Backstay Glass					
	pH0	pH1	pH2	pH3	pH4
TIR ^A					
VNIR ^B	PHS ± silica slope change	PHS ± silica slope change	No change	No change	No change
SEM/Raman/XRD ^C	Ca, Fe, Na-Mg, Na-Al-sulfates S-Mg-rich coating	Ca, Fe, Mg, Na-Al-sulfates S-Si-Al-rich coating	Fe-sulfate Si-rich coating	Ca-sulfate	None
Pathfinder Soil Glass					
	A (pH0)	B (pH1)	C (pH2)	D (pH3)	E (pH4)
TIR ^A					
VNIR ^B	PHS ± silica slope change	PHS slope change	No change	No change	No change
SEM/XRD ^{C,D}	Al, Na-Al, Mg, Fe, Ca-sulfate silica	Al, Mg, Fe, Ca-sulfate silica	Fe, Ca-sulfate silica	Ca-sulfate Fe-oxide, silica	Na-sulfate Fe-oxide
Pathfinder Rock Glass					
	A (pH0)	B (pH1)	C (pH2)	D (pH3)	E (pH4)
TIR ^A					
VNIR ^B	No change	No change	No change	No change	No change
SEM/XRD ^{C,D}	Ca-sulfate, Ca-Na-sulfate cements silica	Ca-sulfate, Ca-Na-sulfate cements	Ca-Na-sulfate cements	unaltered	Fe-oxide, halite

^A TIR pie chart color key: = unaltered material, = Fe⁺³-sulfate, = Fe⁺²-sulfate, = Al-sulfate, = Ca-sulfate, = Mg-sulfate, = Fe-oxides, = amorphous silica, = amorphous Fe⁺³-sulfate, = sulfur, = (Zn, Fe⁺², Mn)Al-sulfate, = Na-sulfate, = Fe⁺²-Al-sulfate.

^B PHS = polyhydrated sulfates, MHS = monohydrated sulfates.

^C All XRD measurements indicated amorphous material which could be glass, silica, or other amorphous materials.

^D All SEM and XRD measurements for the Pathfinder samples were performed by *Tosca et al.* [2004].

Figure 3-1: Overview of alteration material observed for Irvine, Backstay, Pathfinder Soil, and Pathfinder Rock material.

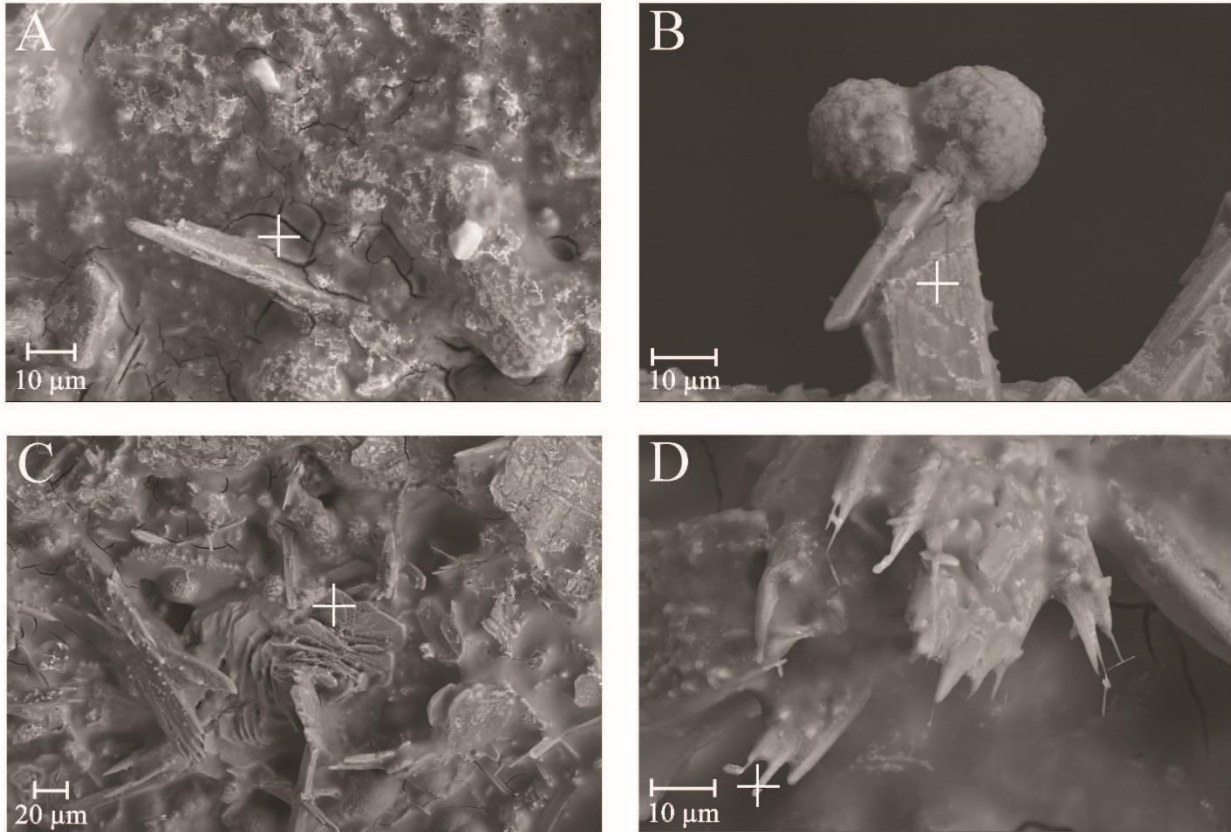


Figure 3-2: Scanning electron micrograph of IRVG-pH0 displaying A) cracked sulfur-rich surface coating, B) B) encrusting Mg-sulfate phase with a slender Ca-sulfate grain, C) platy Fe-Al -sulfate phase, and D) tabular aggregates of Na-Mg-sulfate.

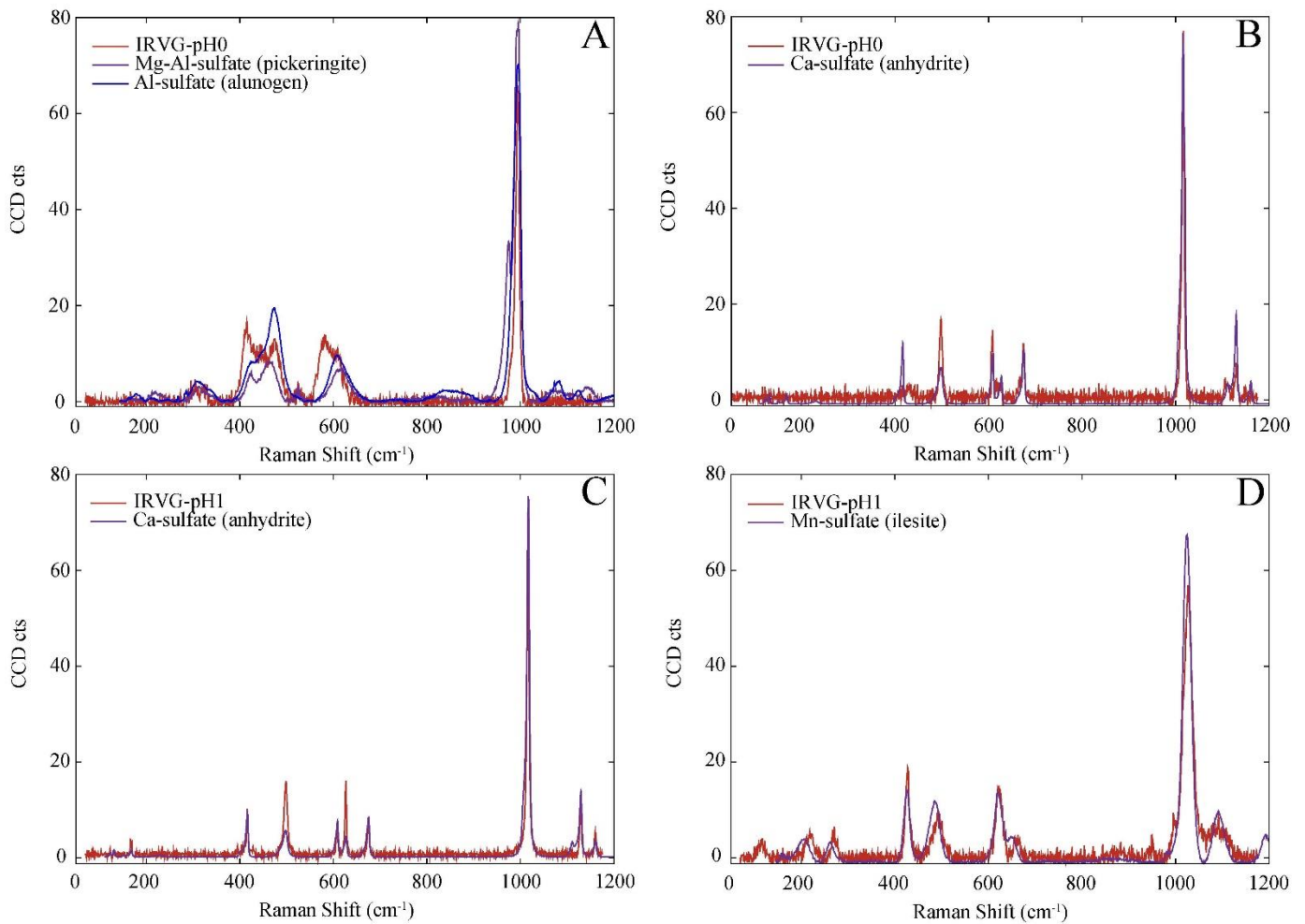


Figure 3-3: Raman spectra acquired with a 532nm laser on the unpolished surfaces of IRVG-pH0 and IRVG-pH1. IRVG-pH0 exhibits two distinct alteration signatures, A) Mg-Al-sulfate (pickeringite) and Al-sulfate (alunogen) and B) Ca-sulfate (anhydrite). IRVG-pH1 exhibits two distinct alteration signatures, C) Ca-sulfate (anhydrite) and D) Mn-sulfate (ilesite).

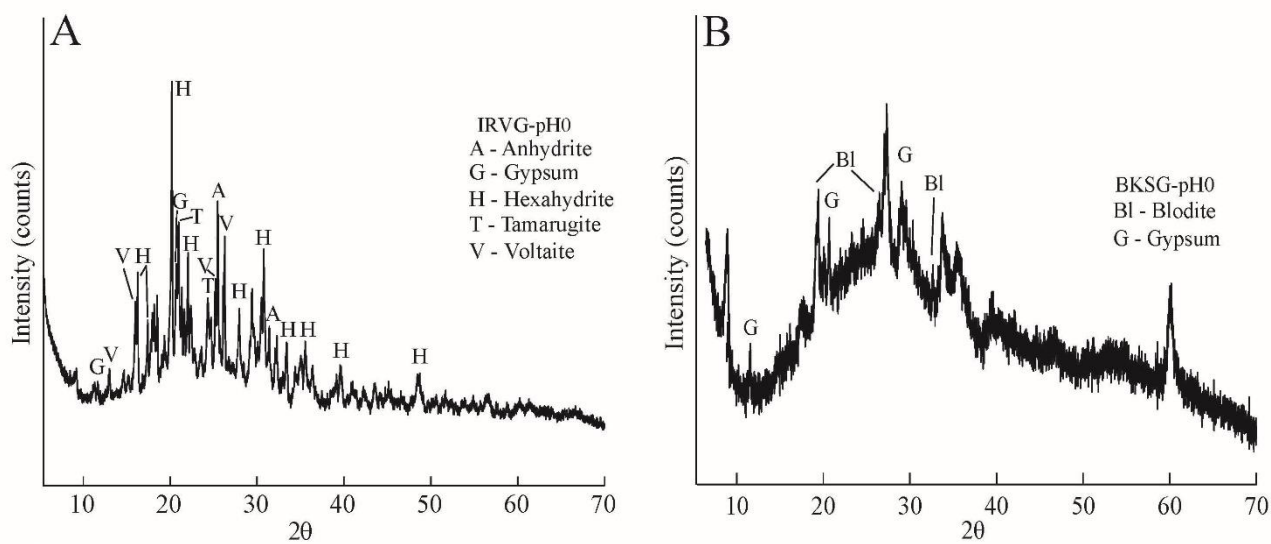


Figure 3-4: X-ray diffractograms showing the secondary phases observed for A) the Irvine glass material altered in pH0 (IRVG-pH0) and B) the Backstay glass material altered in pH0 (BKSG-pH0).

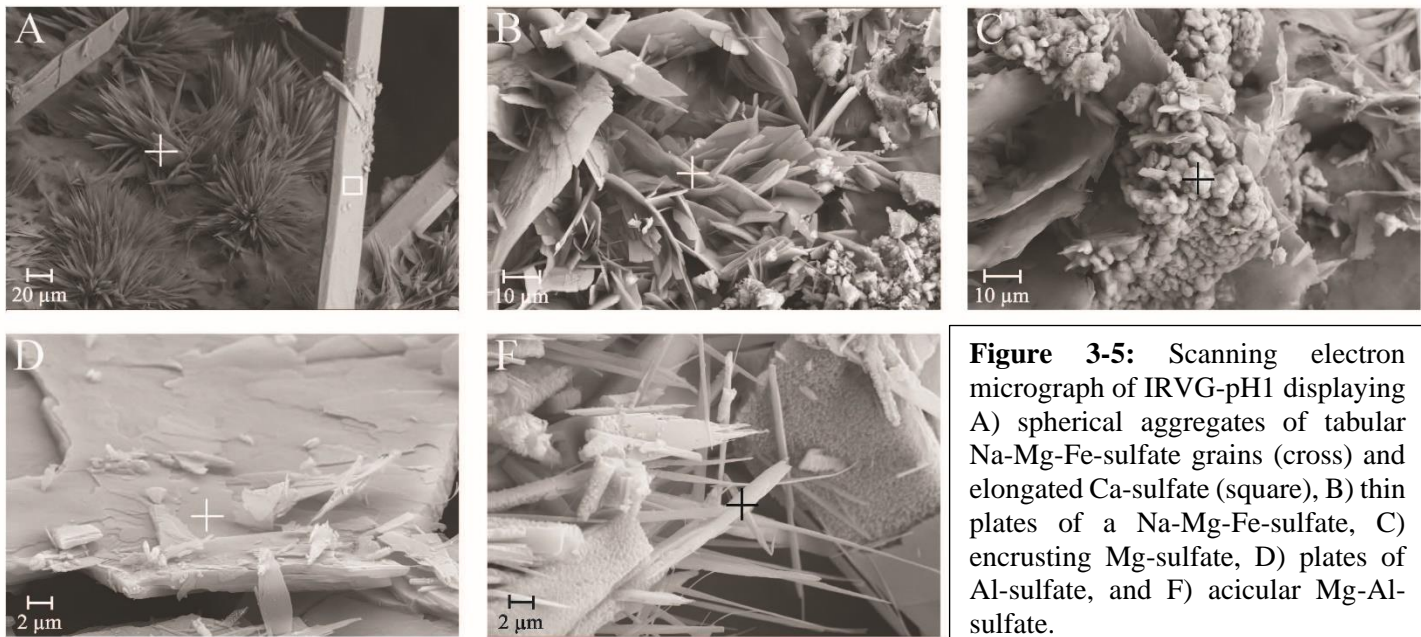


Figure 3-5: Scanning electron micrograph of IRVG-pH1 displaying A) spherical aggregates of tabular Na-Mg-Fe-sulfate grains (cross) and elongated Ca-sulfate (square), B) thin plates of a Na-Mg-Fe-sulfate, C) encrusting Mg-sulfate, D) plates of Al-sulfate, and F) acicular Mg-Al-sulfate.

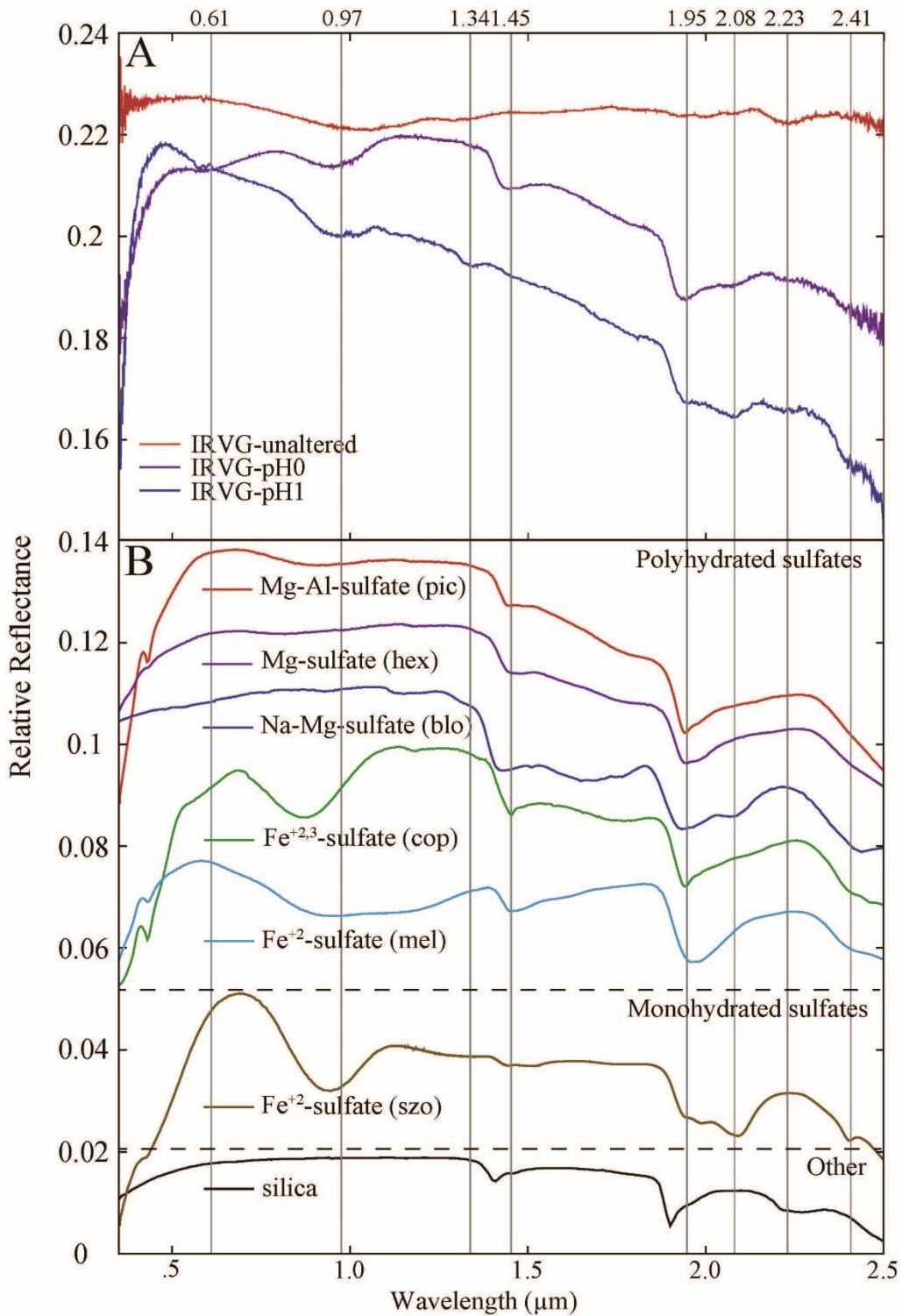


Figure 3-6: A) VNIR reflectance spectra of unaltered and altered (pH0-1) Irvine glass samples plotted with B) the best fit library spectra. Vertical lines indicate features discussed in text. The y-axis has been offset for clarity. Pic = pickeringite, hex = hexahydrate, blo = blödite, cop = copiapite, mel = melanterite, szo = szomolnokite.

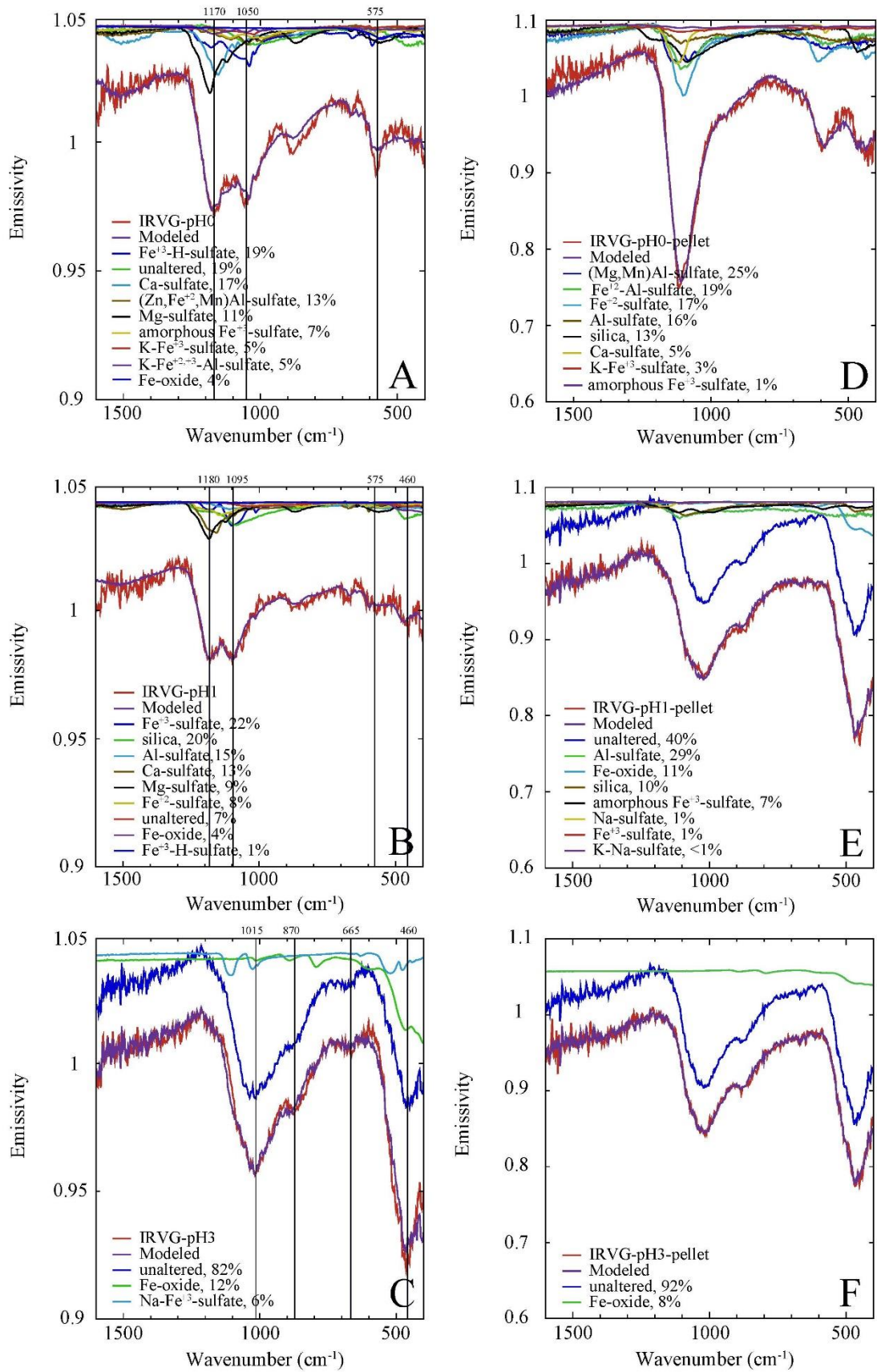


Figure 3-7: Modeled MIR emission spectra of Irvine glass material altered in A) pH0, B) pH1, C) pH3 and the modeled MIR emission spectra of the Irvine pellet material altered in D) pH0, E) pH1, and F) pH3. Vertical lines indicate features discussed in text.

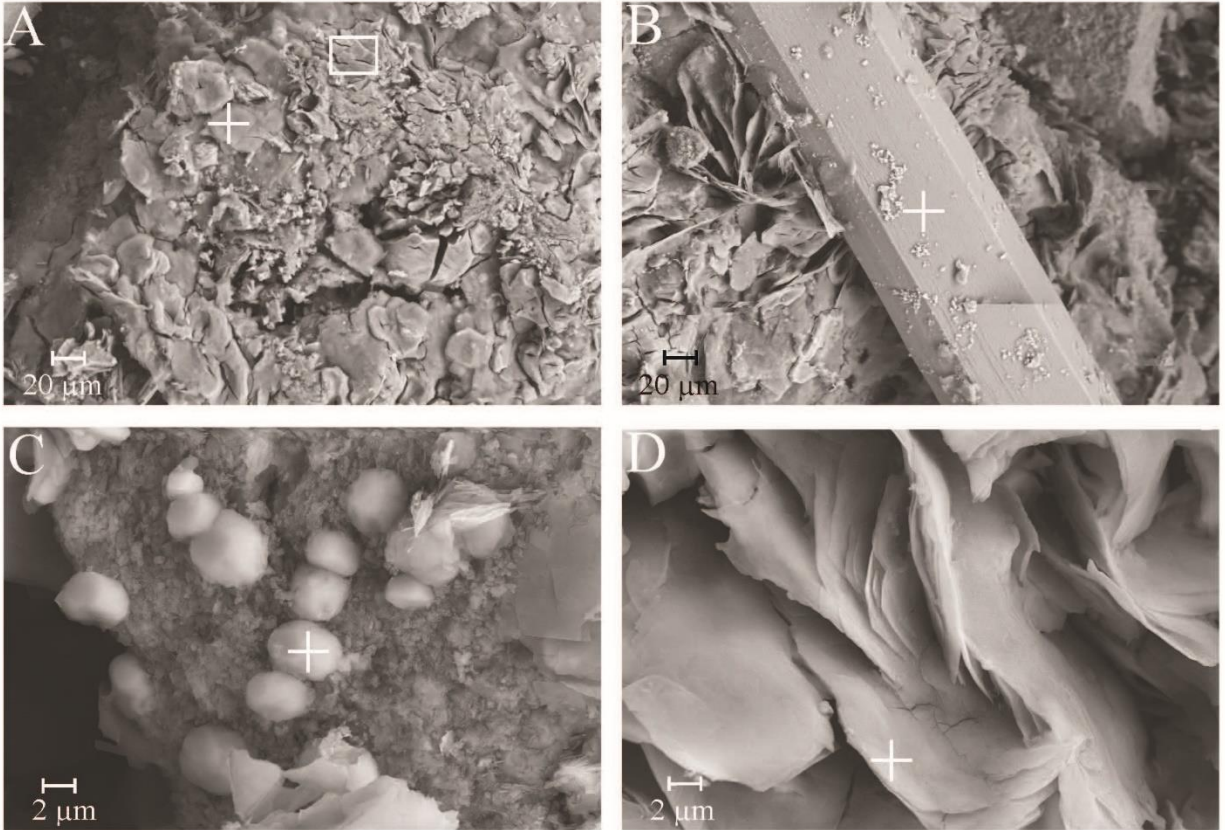


Figure 3-8: Scanning electron micrograph of BKSG-pH0 displaying A) tabular Fe-Mg-sulfate (cross) and cracked surface coating rich in Mg, Al, Fe, Na, and S (square), B) prismatic Ca-sulfate phases, C) globular Fe-sulfate, and D) plates of Na-Al-sulfate.

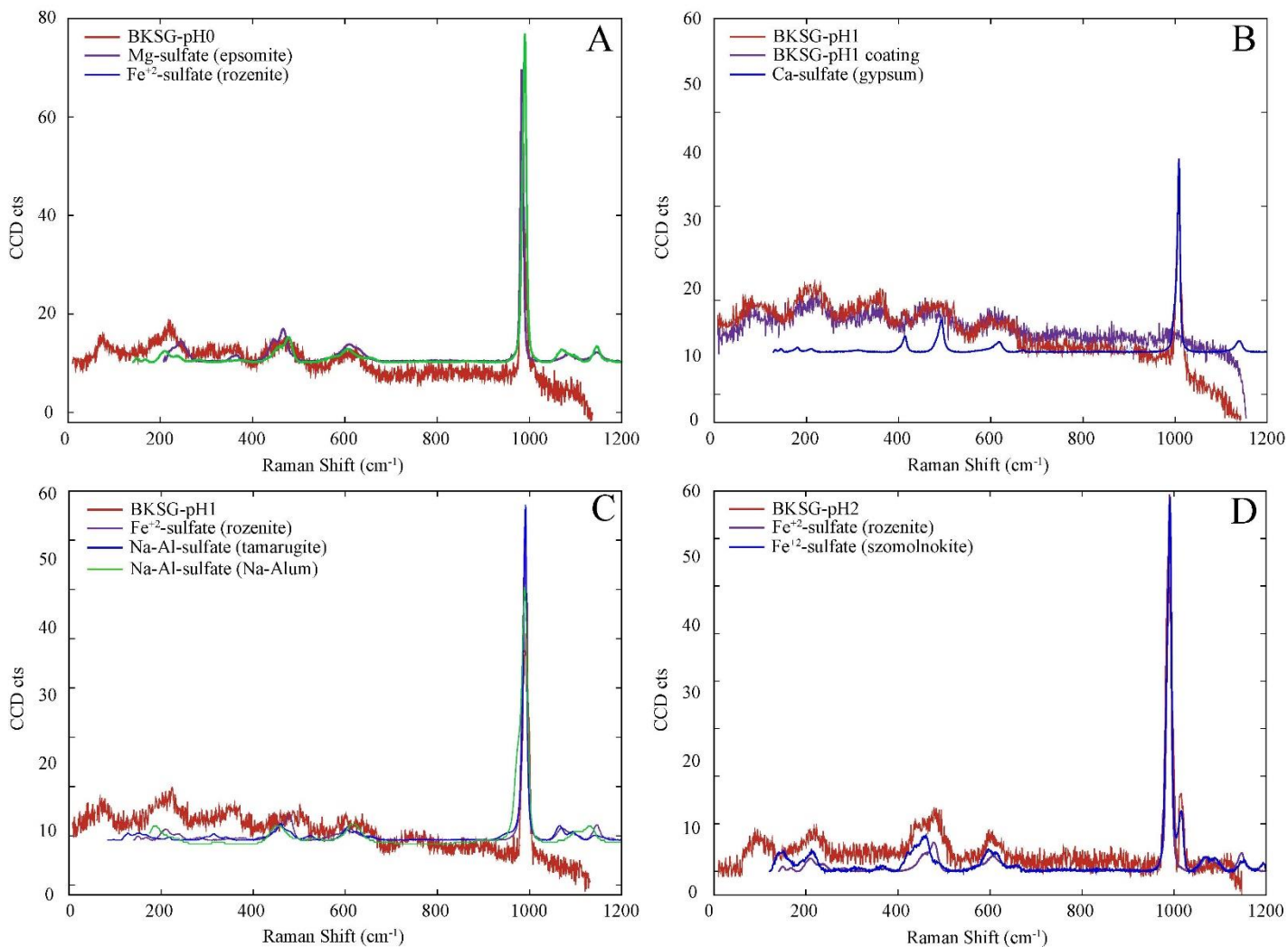


Figure 3-9: Raman spectra acquired with a 532nm laser on the unpolished surfaces of BKSG-pH0, BKSG-pH1, and BKSG-pH2. BKSG-pH0 exhibits one distinct alteration signature, A) Mg-sulfate (epsomite) and Fe²⁺-sulfate (rozenite). BKSG-pH1 exhibits two distinct alteration signatures, B) Ca-sulfate (gypsum) and C) Fe²⁺-sulfate (rozenite) and Na-Al-sulfate (tamarugite, Na-Alum). BKSG-pH2 exhibits one distinct alteration signature, D) Fe²⁺-sulfate (rozenite, szomolnokite).



Figure 3-10: Scanning electron micrograph of BKSG-pH1 displaying A) cement rich in S, Si and Al (cross) and plates of Na-Al-sulfate (square), B) elongated Ca-sulfate, and C) Fe-Mg-sulfate.

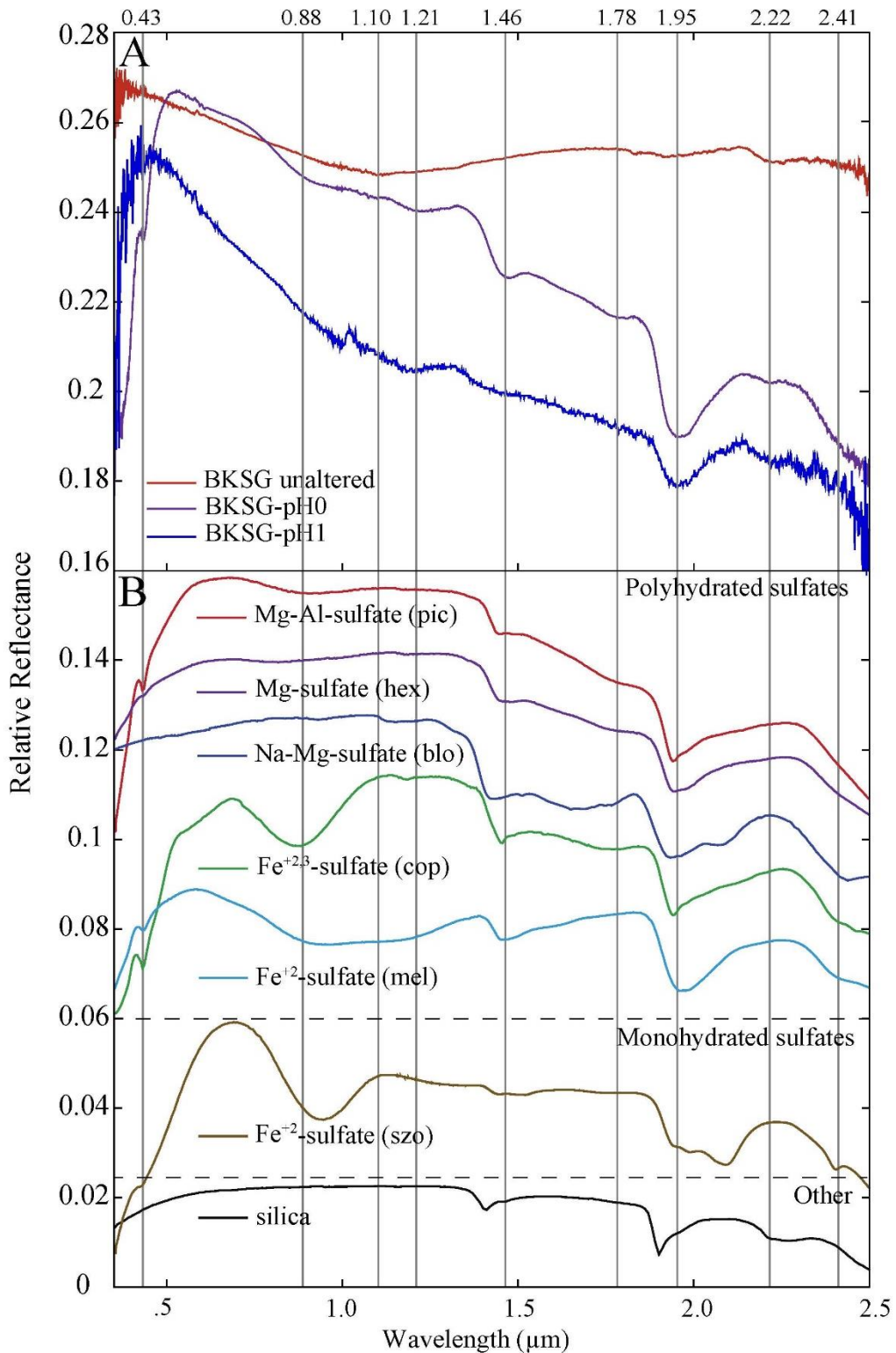


Figure 3-11: A) VNIR reflectance spectra of unaltered and altered (pH0-1) Backstay glass samples plotted with B) the best fit library spectra. BKSG-pH1 is scaled by a factor of 5. Vertical lines indicate features discussed in text. The y-axis has been offset for clarity. Pic = pickeringite, hex = hexahydrite, blo = blödite, cop = copiapite, mel = melanterite, szo = szomolnokite.

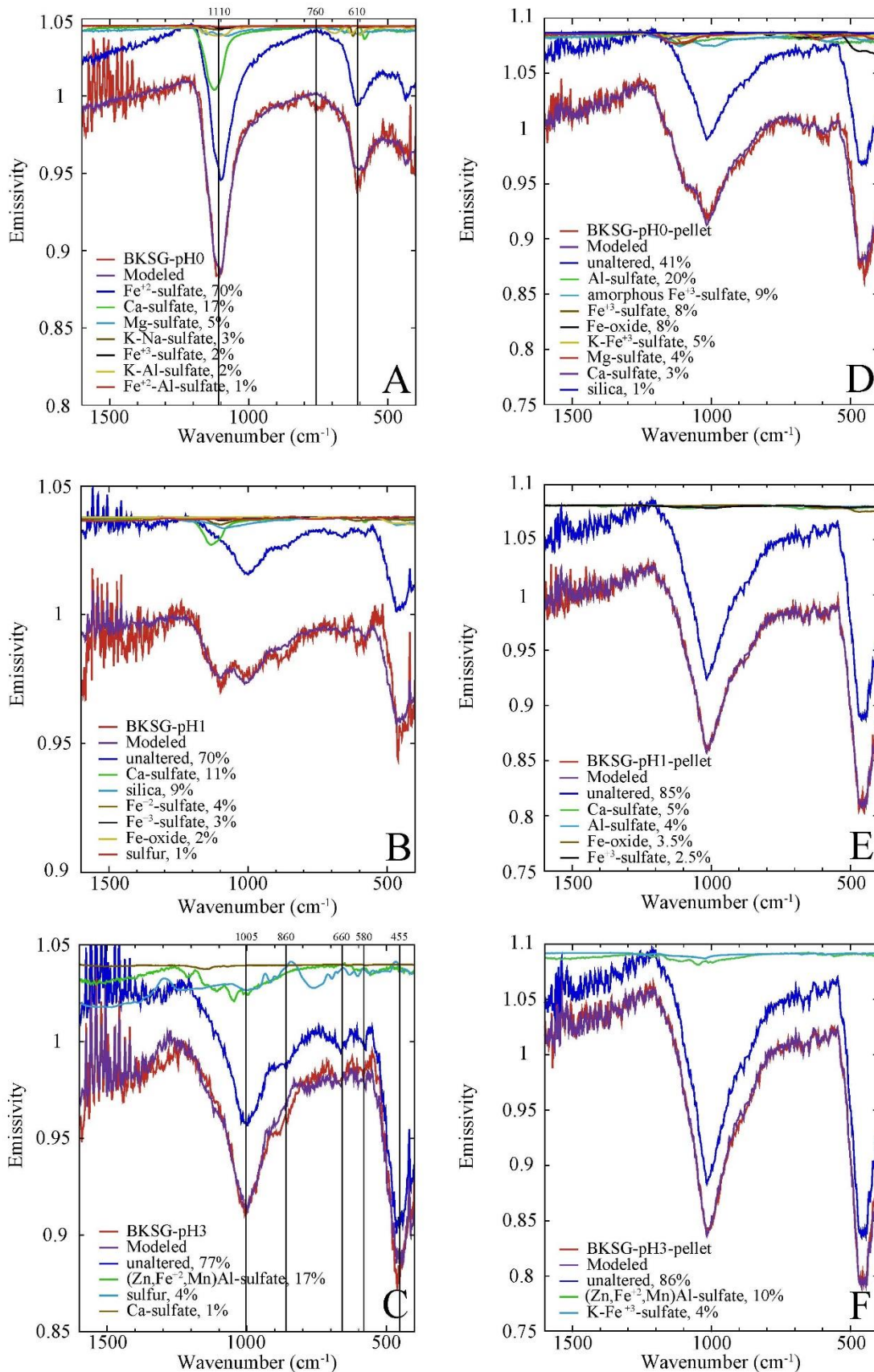


Figure 3-12: Modeled MIR emission spectra of Backstay glass material altered in A) pH0, B) pH1, C) pH3 and the modeled MIR emission spectra of the Backstay pellet material altered in D) pH0, E) pH1, and F) pH3. Vertical lines indicate features discussed in text.

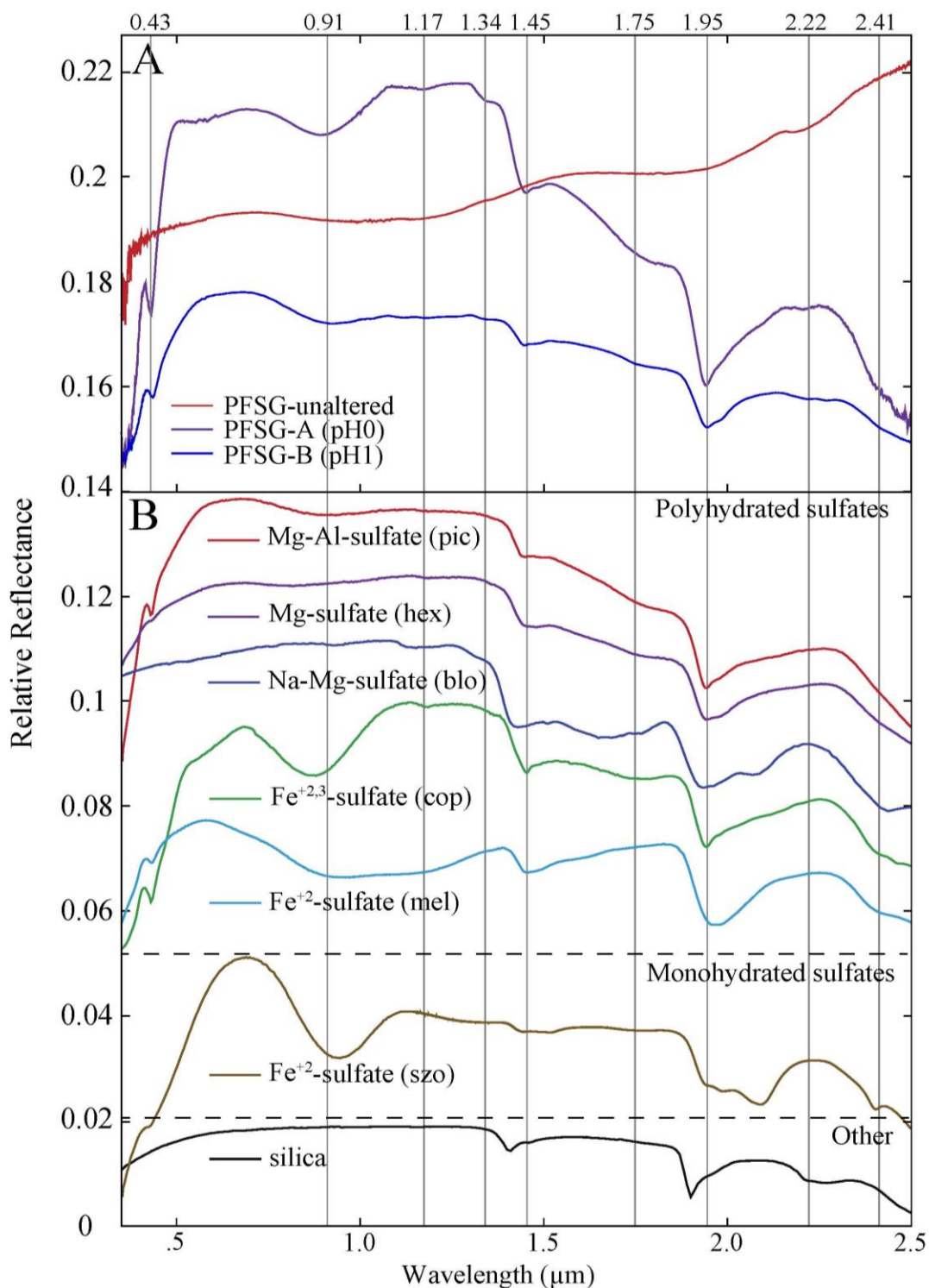


Figure 3-13: A) VNIR reflectance spectra of unaltered and altered (pH0-1) Pathfinder soil glass samples plotted with B) the best fit library spectra. PFSG-unaltered is scaled by a factor of 5. Vertical lines indicate features discussed in text. The y-axis has been offset for clarity. Pic = pickeringite, hex = hexahydrite, blo = blödite, cop = copiapite, mel = melanterite, szo = szomolnokite.

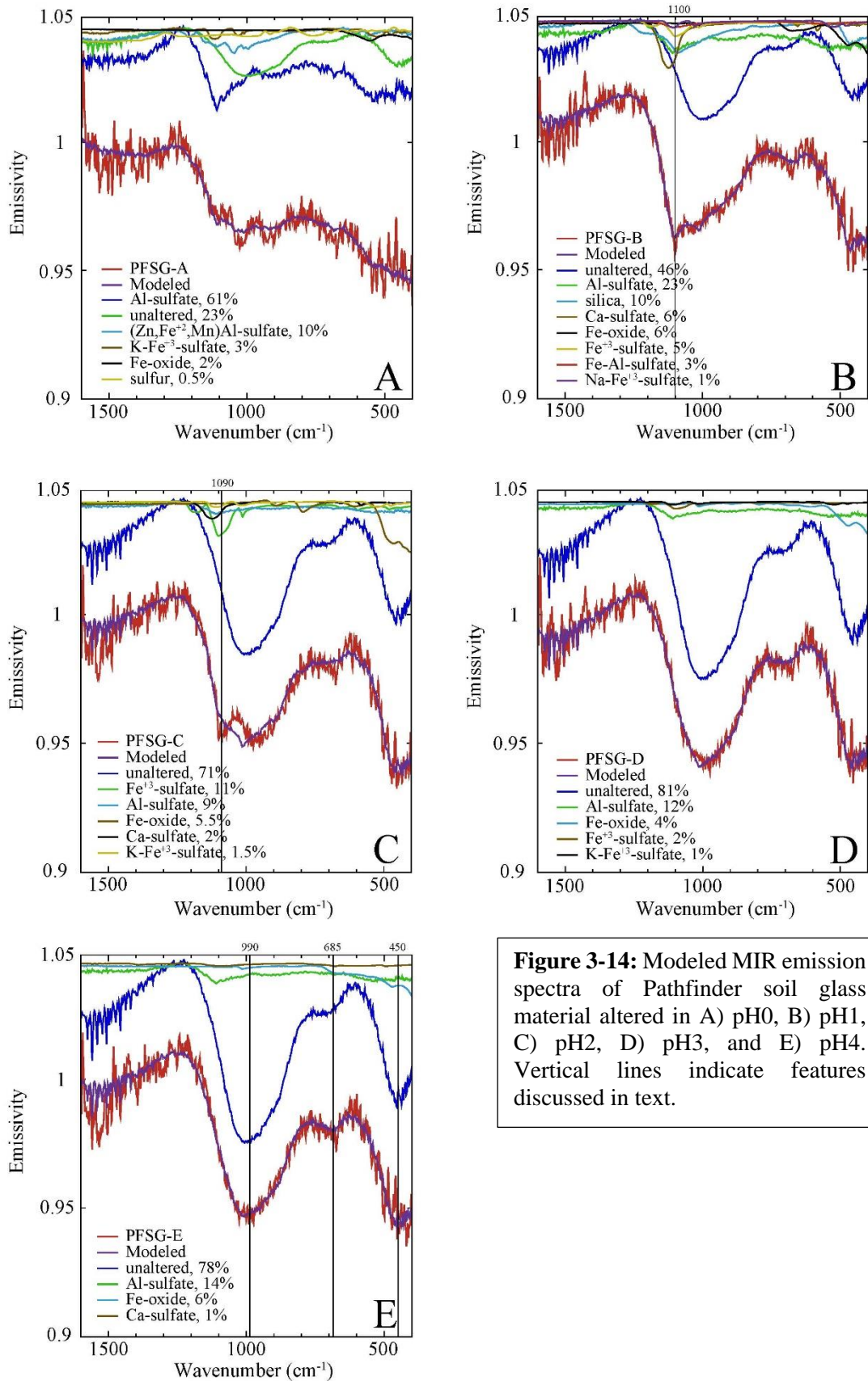


Figure 3-14: Modeled MIR emission spectra of Pathfinder soil glass material altered in A) pH0, B) pH1, C) pH2, D) pH3, and E) pH4. Vertical lines indicate features discussed in text.

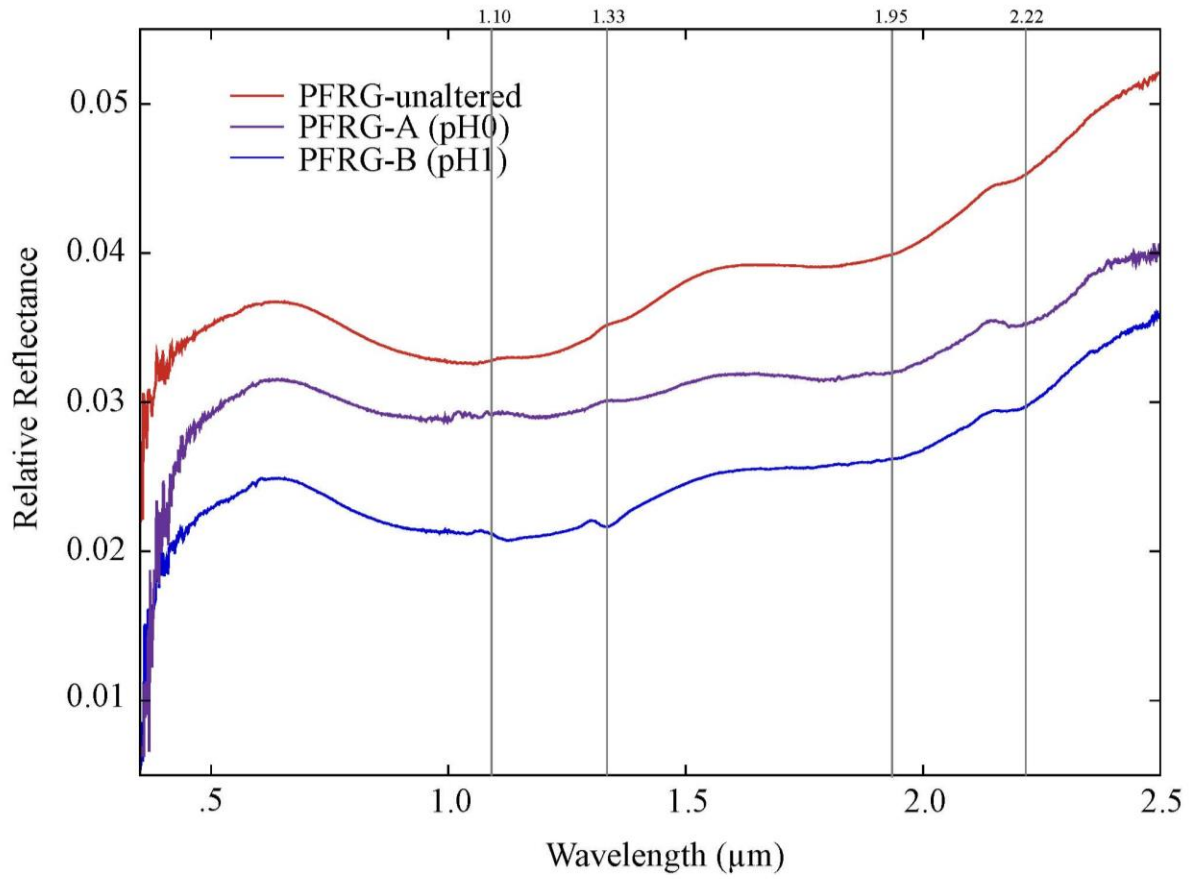


Figure 3-15: A) VNIR reflectance spectra of unaltered and altered (pH0-1) Pathfinder rock glass samples. Vertical lines indicate features discussed in text.

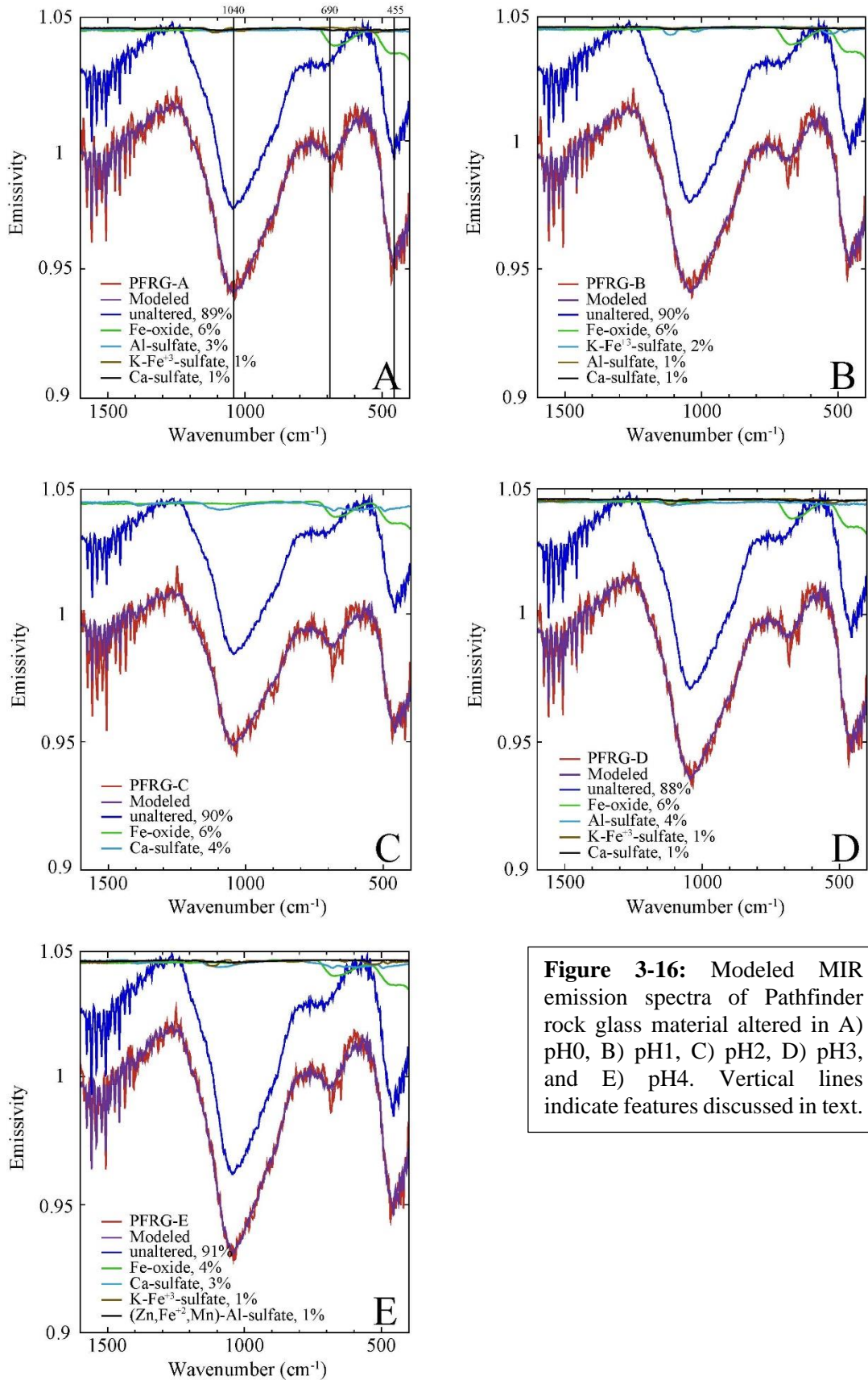


Figure 3-16: Modeled MIR emission spectra of Pathfinder rock glass material altered in A) pH0, B) pH1, C) pH2, D) pH3, and E) pH4. Vertical lines indicate features discussed in text.

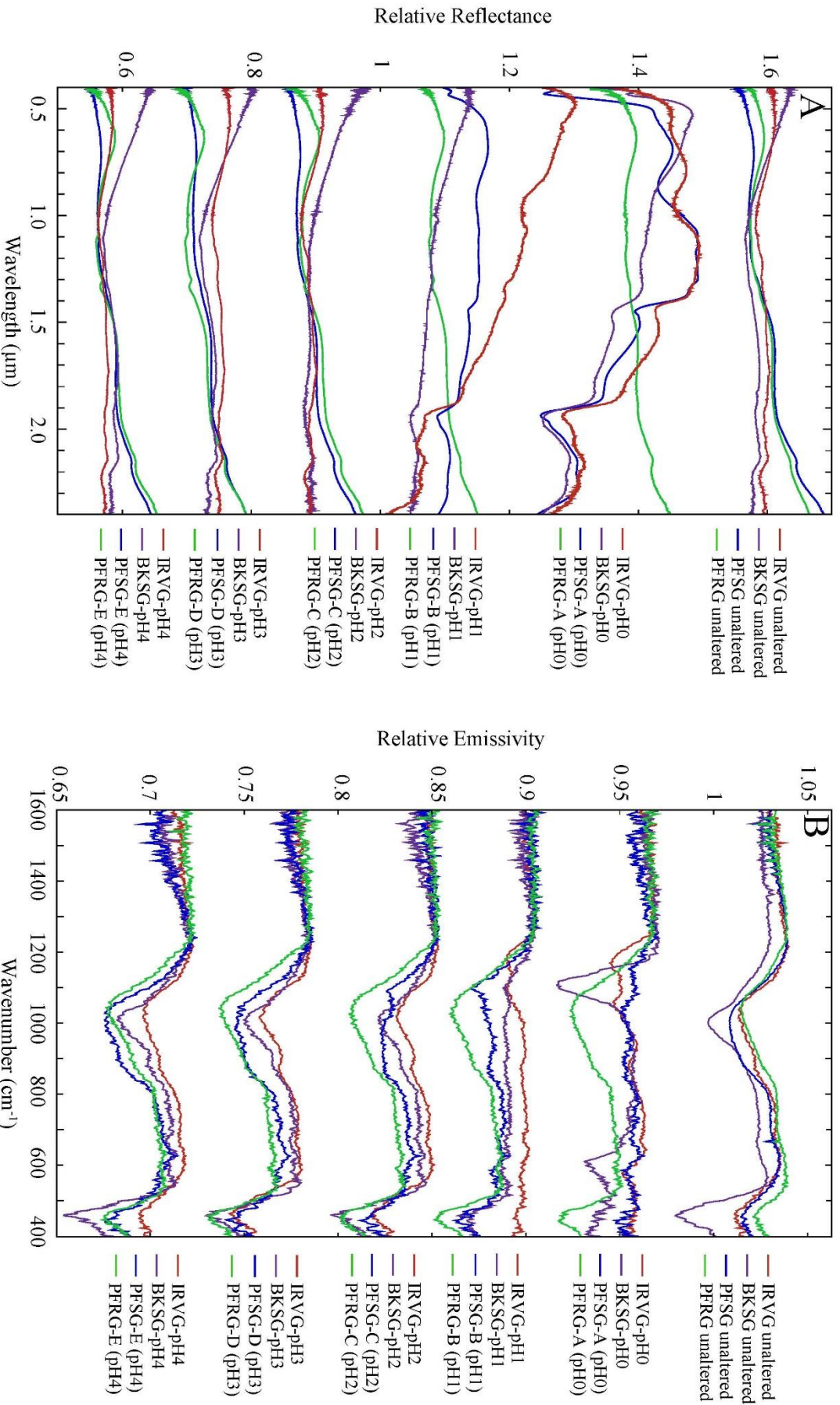


Figure 3-17: Comparison of the A) VNIR reflectance signatures and B) MIR emission signatures of the unaltered and altered material from the four compositions: Irvine (red), Backstay (purple), Pathfinder soil (blue), and Pathfinder rock (green).

Chapter 4

Spectral Characterization and Effects of Volatiles on Synthetic Irvine Basaltic Glass

This chapter is being prepared for submission to the Journal of Geophysical Research – Planets

Yant, M., A. D. Rogers, H. Nekvasil, and T. Bristow

4.1 Introduction:

Magmatic volatiles play a crucial role during magmatic and degassing processes as well as in the surface alteration of Mars. Earlier studies have examined the effect of chlorine and water on the primary mineralogy of Martian rocks [*Filiberto and Treiman, 2009; Médard and Grove, 2008; Mysen and Cody, 2004; Stebbins and Du, 2002; Zeng et al., 1999; Zimova and Webb, 2006*]. However, this study is unique in that it examines how chlorine and water influence the alteration mineralogy and infrared (IR) signatures of Martian surface glass materials. It is vital to add a spectral analysis component because it can be applied to the entirety of Mars instead of limiting the comparison to rover sites. For Mars missions, glass is a crucial material to explore because it can preserve chemical and textural biosignatures [*Howard et al., 2013*]. Understanding the IR signatures associated with hydrated/chlorinated glass materials is important in the search for life on the Martian surface.

Magmatic volatiles (H₂O, F, Cl, C-species, and S-species) influence the physiochemical processes that control the thermal stabilities of minerals and melts, magma eruptive processes, and transportation of economically important metals. The volatile budget of the silicate Earth is dominated by the C-O-H system (O₂, H₂O, H₂, CO₂, CO, and CH₄) [*Jambon 1994; Mysen et al., 2009*], but it is suggested that the C-species are less significant in Martian magmatic systems. Due to this difference, the abundances as well as the roles of magmatic volatile elements in melt stabilities, eruptive processes, and metal transport may vary between Mars and Earth.

For example, *Filiberto and Treiman* [2009] argue that Cl is the dominant volatile species in Martian basalts due to the average Cl:F:OH in apatite and the abundance of chlor-amphiboles over chlor-fluor-amphiboles and oxy-amphiboles in Martian meteorites. They constrain Cl abundances to >0.3 wt. % in parental magmas for Martian meteorites. It is expected that Martian basalts contain more chlorine than terrestrial basalts because the Cl/La of Mars is approximately 2.5 times the average for terrestrial basalts and mantle rocks. This is consistent with the overall enrichment of Mars in cosmochemically volatile elements when compared to Earth [*Dreibus and Wänke*, 1987]. Cl is also observed at rover landing sites; the Gusev crater basalts/soils have between 0.2 and 2 wt. % Cl [*Gellert et al.*, 2006].

Natural glasses generally have aluminosilicate compositions that contain different amounts of network modifier cations. They can also contain considerable quantities of water in the form of OH groups and/or molecular water. The degree of polymerization of the silicate framework is reduced as the glass modifiers/water increase, due to the formation of non-bridging oxygens. There have been several experimental studies evaluating the water content of Martian basaltic magmas using SNC meteorite compositions. *Johnson et al.* [1991], *Dann et al.* [2001], *Nekvasil et al.* [2007], *Dalton et al.* [2007], and *Draper et al.* [2007] inferred that parental magmas of various SNC's contained between 0.5 and 2.0 wt.% water. Volcanically outgassed water may have contributed significantly to the inventory that formed the variety of aqueous minerals [e.g., *Bell et al.*, 2008] and geomorphic features [e.g., *Carr*, 1996] on the surface.

Previous experiments by *Filiberto and Treiman* [2009] examined the effects of volatiles on crystallization temperatures and products for a crystalline Martian basalt. They observed that the addition of Cl (0.7 wt. %) and H₂O (0.8 wt. %) have similar effects on crystallization temperatures and mineral compositions for a Humphrey basalt (**Figure 4-1**). Both Cl and H₂O

cause a comparable depression in the liquidus, however they differ in their solubility mechanisms and effects on melt structure. Water causes a liquidus depression by depolymerizing the melt by attacking bridging oxygens in the melt structure [Mysen and Cody, 2004; Zeng *et al.*, 1999]. Phase boundaries are relatively unaffected by this process [Médard and Grove, 2008]. Chlorine, however, complexes in the melt with network-modifying cations (Mg, Fe, Ca, Na), which will decrease cation activity, increase silica activity, and increase melt polymerization [Stebbins and Du, 2002; Zimova and Webb, 2006]. This results in a liquidus depression, increased pyroxene stability with respect to olivine, and a multiple saturation point depression.

Based on the above discussion, we hypothesize that volatile contents and species are likely to affect the atomic bond length/structures and spectral shapes of glasses. Here “volatile-containing” (1 wt. % Cl and H₂O added) synthetic Irvine glasses are compared with the “volatile-free” (0 wt. % Cl and H₂O added) synthetic Irvine glasses from **Chapter 3**. The samples are subjected to low temperature aqueous alteration with various acidic solutions in an identical method to the volatile-containing samples. Altered samples are characterized using a variety of spectral (visible/near-infrared - VNIR, mid-infrared - MIR), chemical (scanning electron microscopy - SEM), and mineralogical techniques (Raman, x-ray diffraction - XRD) that are comparable to orbiter and rover analyses.

4.2 Experimental and Analytical Methods

4.3.1 Glass Synthesis Methods

The same procedures used for the Irvine volatile-free glass (IRVG-VF) are used for the Irvine volatile-containing glass (IRVG-VC) material and are outlined in **Section 3.3.2**. Major oxides for Irvine were measured directly by APXS on board the MER, *Spirit*. However, Cl and H₂O were also added to the Irvine composition in sufficient quantity for detection and for

comparison with the volatile-free Irvine material. The composition of Irvine (**Table 4-1**) was synthesized by a mixture of oxides, silicates, phosphate, chloride, and sulfate. The volatile components (chlorine, added as MgCl₂ and water, added as Mg(OH)₂) had fixed values of 1.0 wt. %. An initial Fe³⁺/Fe²⁺ ratio of 80:20 was used to minimize the change induced by the graphite capsule. All components were added in ascending wt. % order to an automatic agate mortar/pestle and mixed under ethanol after the addition of each new aliquot. The exceptions to this order were the Fe sponge (used in combination with hematite to attain the desired FeO content) and MgCl₂, both of which were added last because Fe sponge oxidizes easily and absorbs moisture when it comes in contact with air, and the MgCl₂ is soluble in ethanol.

The electron microprobe analyses of the unaltered Irvine volatile-containing glass indicate that the major oxide abundances of the analyzed sample are near the target abundances, except for sodium and potassium (**Table 4-1**). The low sodium and potassium amounts are a result of the mobile nature of these two elements combined with prolonged exposure to the electron beam [Vassamillet and Caldwell, 1969]. Several points were analyzed on each glass sample in order to determine the chemical heterogeneity of the basalt. The chemical gradient of the glass composition was minimal indicating that the glass is homogenous.

4.3.2 Alteration Batch Experiments

Again, the same procedures used for the Irvine volatile-free glass are used for the Irvine volatile-containing glass material and are outlined in **Section 3.3.3**. The material was crushed and sieved to ensure a particle size of medium to very fine sand. Acidic solutions (pH 0, 2, and 4) were prepared using deionized water, sulfuric acid, and hydrochloric acid with a S: Cl molar ratio of 5:1. Approximately 0.25g of material was added to a Savillex™ Teflon® beaker for each reaction. There was a shortage of fully glass material, so only three samples were available for alteration;

they were assigned solutions of pH0 (IRVG-VC-pH0), 2 (IRVG-VC-pH2) and 4 (IRVG-VC-pH4). The solutions were used to react with the samples at ambient temperature and pressure for 14 days followed by an evaporation period of 2 days. Again, a fluid-to-rock ratio of 1:1 was utilized. After the evaporation period the samples were analyzed with SEM/EDS, and MIR, VNIR, and Raman spectroscopy. MIR spectral characterization was also performed on the powdered samples after XRD analysis. The powders were then pressed into pellets for additional MIR emission measurements.

A separate experiment was set up with a “glass chunk” of ~4mm size. The rock chunk was altered in a solution of pH 0. Due to a limited amount of starting material, only one rock chunk was able to be produced. A pH of 0 was chosen because it is the most acidic pH used in the particulate experiments and produces the highest abundance and variety of alteration material. The acidic solution was prepared as described above. A 24-week reaction period was implemented for the rock chunk in order to provide an adequate reaction period for alteration materials to form on a larger surface. The sample was analyzed weekly with MIR emission spectroscopy, and then placed back into the fluid. After the 24-week alteration period the fluid was allowed to evaporate for 2 days at room temperature and then analyzed with VNIR, Raman, and SEM/EDS. It should be noted that it is expected that the pH did not stay constant in any of these experiments and that the pH increases after interaction with the basaltic material. This is due to an increase in alkalinity as cations are released during dissolution of the starting material. In nature, it is expected that the pH of the solution would increase during reaction with a sample. Because the conditions simulated here were a cation-conservative environment, we did not add additional fluids as would be expected in an open system environment.

4.2.3 Analytical Methods

Chemical analyses of polished pieces of unaltered synthetic samples were performed using a Cameca SX-100 electron microprobe at the American Museum of Natural History. An accelerating voltage of 15 kV and a nominal beam current of 10 nA were used during all analyses. Chemical and morphological analyses of secondary phases were obtained using a LEO 1550 SFEG scanning electron microscope equipped with an EDAX energy dispersive x-ray spectrometer (EDS). Analyses were performed using an accelerating voltage of 20 kV. The EDS system is capable of quantitative elemental analysis, but only for relatively flat surfaces. All of the energy dispersive analyses discussed here are semi-quantitative because the analyses were performed on samples with variable surface angles. EDS analysis provides the elemental composition of the mineral phase, but does not allow for exact element ratios. With the ratios provided by EDS, a comparison between elements present in the spectra can be done which can be used to constrain the stoichiometry of the phase. Combining the elemental makeup and the morphology of a grain can allow for mineral identification. The other analytical techniques can also be utilized to properly identify phases. The material was characterized by XRD with a Rigaku Ultima-IV diffractometer equipped with Cu K α ($\lambda = 1.5405 \text{ \AA}$) radiation at Stony Brook University. The measurements were within a range of $5^\circ \leq 2\theta \leq 90^\circ$ (counting time: 1°/min; stepsize: 0.02°). X-rays were generated at 40KV and 44mA. The patterns were interpreted using Jade 9 software.

The unaltered synthetic samples were spectrally characterized using MIR and VNIR spectroscopy, while the spectral analysis of the altered samples also included Raman. VNIR (350-2500cm⁻¹) bidirectional reflectance spectra were acquired using an ASD FieldSpec3 Max spectrometer at Stony Brook University. The measurements were collected with incidence and emergence angles of 30° and 0°, respectively, and were performed relative to Spectralon and then corrected for the reflectance properties of Spectralon. VNIR spectra were compared with library

spectra of well-characterized samples available from RELAB (<http://www.planetary.brown.edu/relab/>).

Raman analyses were conducted at Stony Brook University using a WiTEC alpha300R confocal Raman microscope system equipped with a double frequency 532 nm Nd: YAG excitation laser with a nominal laser power of 50 mW at this wavelength. The system is also equipped with multiple object lenses ranging from 4 to 100X magnification, allowing spatial resolutions between several micrometers and 250 nm/pixel. The spectra acquired for this study were in the range of 40-1200 cm^{-1} . Raman spectra were compared with library spectra available from the RRUFF database [Downs, 2006], which are well characterized using XRD and electron microprobe.

MIR emissivity spectra were acquired between 225-2000 cm^{-1} on Stony Brook University's Nicolet 6700 FTIR spectrometer equipped with a CsI beamsplitter and deuterated triglycine sulfate cesium iodide (DTGS CsI) detector. The atmosphere was purged of H₂O and CO₂. Each sample was put into an aluminum sample cup painted with Krylon Ultra Flat Black paint. The unaltered glass samples were heated to 80°C within a chamber and maintained at that temperature for the duration of the ~ 9 minute integration (256 scans).

Because the altered samples were expected to contain sulfate minerals, which could dehydrate upon heating, emission measurements of altered samples were made by cooling the samples well below the detector temperature [Baldrige and Christensen, 2009]. The altered glass samples were cooled outside of the chamber overnight with dry ice. The duration of the measurement was decreased by lowering the number of scans to 50, because the samples were not able to be actively cooled. Five measurements were taken and averaged for each of the altered glass samples.

MIR spectra of altered samples were analyzed using linear least squares analysis [e.g., *Ramsey and Christensen, 1998; Rogers and Aharonson, 2008*] with a library of sulfate, silica, iron oxide and sulfur spectra, over the spectral range between 400-1400 cm^{-1} . Most of the library spectra and samples used in this study are described in [*Lane et al., 2007; Ruff et al., 2011; Lane et al., 2015, Sklute et al. 2015*; see **Appendix Table A4**]. The library also included the spectra of the unaltered samples, so that the altered samples could be modeled as a simple mixture of unaltered material plus alteration products. Last, a quasi-linear slope spectrum was also included to account for slopes present in the altered samples, due to spatial and/or temporal non-isothermality within the sample or sample collection process.

As described briefly in **Section 4.2.2**, the particulate samples were first measured in their post-alteration form, which was a mixture of sand-sized primary material and fine- to coarse-grained alteration material. They were then subsequently analyzed as crushed powders and pressed pellets. Note that, due to the shortage of glassy material, an unaltered glass sample in pellet form was not available. Thus, a pellet made from IRVG-VC-pH4 was used as the “unaltered” sample because little difference was observed between the altered and unaltered particulate sample spectra for this pH.

4.3 Glass Alteration Results

After the reaction period, visible alteration could be observed on the material subjected to pH0 conditions (IRVG-VC-pH0) with the naked eye, but magnification was needed to view the alteration on the pH2 (IRVG-VC-pH2) and pH4 (IRVG-VC-pH4) materials. The secondary phases occur on IRVG-VC-pH0 as a white material that visibly covered the majority of the original basaltic glass and consists of a consolidated white coating partially overlain by a white powder. Evaporation of the residual fluid for IRVG-VC-pH0 resulted in a cemented pellet, instead of the

initial sand-sized grains. No mineral formation was observed until after the evaporation period for the particulate samples. The “glass chunk” altered in a pH of 0 (IRVG-VC-GC-pH0), did not have much visible alteration material at the conclusion of the experiment. An overview of the alteration material observed for the glass Irvine volatile-containing material from the chemical and spectral analyses is displayed in **Figure 4-2**.

4.3.1 Chemical and Mineralogical Analyses

The sample altered in the most acidic environment (pH0) exhibited a variety of secondary mineral phases as detected by SEM, with an assemblage of Mg-Al-, K-Fe-, Fe-Al-, and Mg-sulfates (**Figure 4-3**). **Figure 4-3A** shows the overall alteration of a single grain. Where alteration phases are absent, a cracked, silica-enriched surface is observed by SEM (**Figure 4-3B**). A Mg-Al-sulfate with an acicular form is present with EDS ratios and morphology consistent with pickeringite (**Figure 4-3C**). The chemistry for the rounded phase gives evidence for a K-Fe-sulfate (**Figure 4-3D**), but this phase could not be identified. This sample also exhibits aggregates of acicular Fe-Al-sulfate (**Figure 4-3E**), likely halotrichite based on habit and chemistry. A platy mineral is observed and based on the EDS ratios it is a Mg-sulfate, but the exact phase could not be identified (**Figure 4-3F**). Although the alteration was pervasive on the entire surface of IRVG-VC-pH0, only three distinct spectral signatures were observed using Raman techniques. The three signatures are found in numerous locations on the sample, sometimes in close proximity to each other. Usually the second and/or third spectral signature(s) are found together with the first. The first signature is most consistent with Mn-Al-sulfate (apjohnite), (Zn, Fe⁺², Mn)-Al-sulfate (dietrichite), Fe⁺²-Al-sulfate (halotrichite), and/or Mg-Al-sulfate (pickeringite), which all have similar Raman features. The second spectral signature displays evidence for a combination of two Mg-sulfates (epsomite and hexahydrate). It is not clear whether the mixed hydration states were

formed during alteration, or whether the epsomite formed from partial dehydration of the hexahydrate. The third spectral signature is consistent with Ca-sulfate (gypsum). XRD confirmed the presence of Mg-Al-, Fe⁺²-Al-, Ca-, and Mg-sulfates as observed in the Raman and SEM/EDS analyses for IRVG-VC-pH0. Halite, amorphous material, and Al-, Fe⁺²-, and Fe⁺³-sulfate were also identified by XRD.

The sample altered in the intermediate acidic environment (pH2) had much less alteration material (**Figure 4-4A**). The only secondary phase identified by SEM was a Ca-sulfate (**Figure 4-4B**) in addition to a thin silica-rich surface that was observed in sparse patches. Raman confirms the presence of Ca-sulfate (gypsum), however no alteration material was detected by XRD techniques. Ca-sulfate is also observed by SEM in the sample altered in the least acidic environment (pH4), though the relative abundance is less than that of pH2. The sample altered in pH4 underwent the least alteration, and is characterized as predominantly unaltered basaltic glass by all analytical techniques.

SEM indicated that the interaction of the glass rock chunk with a pH0 solution resulted in a coating rich in sulfur and/or sulfate (**Figure 4-5A square**) with Ca-sulfate crystals (**Figure 4-5A cross**) sparsely distributed on the surface of the coating. The tape used for SEM peeled up part of the coating and revealed fine grained Fe-sulfates under the surface (**Figure 4-5B-C**). The specific phase was not identifiable based on EDS ratios. Only one Raman signature was detected and it was most consistent with Ca-sulfate (anhydrite).

Amorphous secondary phases may be present in all of these samples, but cannot be distinguished from primary glass in XRD. The discrepancies between the assemblages observed by SEM, Raman, and XRD likely reflect the differences between surficial phases and bulk mineralogy. Due to the considerable Fe content of these samples there could be some Fe

fluorescence present in the XRD patterns. This may result in a high intensity background, but the major peaks should still be discernible.

4.3.2 Infrared Spectral Results

4.3.2.1 Visible Near-Infrared

The unaltered glass material, glass samples altered in pH2 and 4, and the glass chunk exhibit very shallow features. The shallow character of these spectra can be attributed to their dark surfaces and lack of alteration material. However, IRVG-VC-pH0 also exhibits features near 0.43, 0.92, 1.47, 1.96, and 2.46 μm , due to H₂O and OH/H₂O vibrational combinations and/or S-O overtones (**Figure 4-6A**). The 1.47 μm feature is likely due to OH stretching overtones or H₂O overtones/combination bands while the feature near 1.96 μm is from H₂O combinations. The 2.46 μm absorption can be attributed to combinations of OH- or H₂O bending, stretching, and rotational fundamentals or S–O bending overtones [*Cloutis et al.*, 2006]. The broad absorption exhibited over near 0.92 μm is likely due to the presence of iron. Although the exact phases are difficult to determine, the IRVG-VC-pH0 sample exhibits the primary and secondary indicators of polyhydrated sulfates (near 1.9, 2.4, and 1.4 μm) [*Lichtenberg et al.*, 2010]. The altered spectrum for IRVG-VC-pH0 is most consistent with Mg-Al-sulfate (pickeringite) (**Figure 4-6B**), but also shares some characteristics with Mg-, Fe⁺²-Al-, and Fe⁺³-sulfate (hexahydrite, halotrichite, and copiapite). Only the library spectrum for pickeringite is shown due to the similarity of the halotrichite features.

4.3.2.2 Mid-Infrared

Here, we first describe the MIR spectral characteristics and modeled abundances of the altered samples in their natural, pressed pellet, and powdered forms. The unaltered glass samples have broad absorptions centered near 1010, 695, and 458 cm^{-1} (**Figure 4-7A**). The glass samples

altered in pH0-2 exhibited variations in emissivity measurements with respect to the unaltered sample. In the spectrum from the most acidic environment, pH0, the original unaltered glass absorptions are lost and the spectrum has additional absorptions near 1115, 1050, 675, and 610 cm^{-1} , consistent with a sulfate-dominated mineral assemblage (**Figure 4-8A**). These models are discussed further in **Section 6.3**.

The spectral character of IRVG-VC-pH0 is dominated by alteration products, including (Mg, Mn)-Al-sulfate with lesser amounts of Ca, Fe^{+2} -Al, Al, Fe^{+2} , (K, H₃O) Fe^{+3} -sulfate and minor amounts of (Na)Mg-sulfate, (Zn, Fe^{+2} ,Mn)-Al-sulfate, and Fe-oxides. Similar to the natural surface, the pressed pellet model of IRVG-VC-pH0 (**Figure 4-8B**) includes a variety of sulfates, with a dominance of Al-bearing sulfates. However, the pressed pellet model also includes ~22% amorphous silica, which could be present in the particulate sample as well. The Fe^{+2} -Al and Mg-sulfate that were modeled in the natural surface were not observed in the pellet model.

The glass subjected to the intermediate acidic environment, pH 2, has retained the original glass absorptions, but the absorption at 1010 cm^{-1} is broadened from the addition of a weak feature near 1085 cm^{-1} and two shallow absorptions near 665 and 605 cm^{-1} (**Figure 4-7A**). However, unaltered material dominates the spectrum and is modeled at 76% (**Figure 4-8C**). The additional absorptions in the IRVG-VC-pH2 spectrum are most consistent with Ca-sulfate; however, the model indicates significant amounts of Fe-oxide with minor amounts of Ca-sulfate. In pellet form, only minor amounts of Fe-oxide, silica, and sulfur are indicated by the model (**Figure 4-8D**), suggesting that the alteration products are volumetrically minor. The glass subjected to the least acidic environment, pH4, retains all of the original glass absorptions and does not show considerable indication of secondary mineral formation spectrally (**Figure 4-8E, F**).

The MIR emission spectra for all of the powders (<63 μ m) have very shallow features and relatively high emissivity (**Figure 4-7C**). These characteristics make it difficult to determine the alteration material of the powder by spectral analysis alone. For the powdered material, negligible spectral difference is observed between samples

The MIR spectral characteristics for the Irvine glass chunk over the 24-week period are shown in **Figure 4-9A**. By the end of the 24-week reaction period, the altered glass rock chunk exhibited spectral features that were modeled as an assemblage of Fe⁺³-sulfate, K-Fe^{+2,+3}-Al-sulfate, amorphous Fe⁺³-sulfate, Fe-oxides, Ca-sulfate, and Mg-sulfate (**Figure 4-9B**). The samples exhibited spectral changes within the 24-week alteration period, with the largest changes in spectral features occurring at weeks 1 and 13 (**Figure 4-9C**). The modeled fits are poor for the rock chunk relative to the sand-sized and pellet material. This could be due to transparency features as a result of thin coating on the surface of the rock chunk or because of residual surface sulfuric acid, which is not present in our spectral library. Despite the poor model fits, many features consistent with sulfates are observed.

The surface of the glass chunk (pH0) was much different from that of the particulate glass sample (pH0), as were the spectral features. Based on variations between the spectral signatures of the particulate material and the rock chunk (after a similar 2-week reaction period as well as the full 24-week reaction period), this is a function of both particle size and reaction period duration. The initial grain size affects the timing of neutralization and deposition of major alteration phases. Increasing the grain size is similar to effect of increasing the fluid to rock ratio, resulting in slower neutralization and later precipitation of alteration phases [Zolotov and Mironenko, 2007].

4.4 Discussion

4.4.1 Effects of pH

In general, the volatile-containing glass samples follow an alteration trend of increasing alteration with decreasing pH, with a significant increase in the amount of alteration for the sample altered under pH0 conditions. Also, a variety of sulfates are observed in the lower pH conditions, but only Ca-sulfates are observed in the high pH conditions (**Figure 4-2**). For the Irvine glass, the overall secondary mineral assemblage, determined by SEM, Raman, and XRD, includes halite, amorphous material, and Fe⁺²-Al-, Mg-Al-, Al-, Fe⁺²-, Fe⁺³-, Ca-, and Mg-sulfates for the most acidic material (pH0). Although clays could form under the conditions implemented here [e.g., *Hynek et al.*, 2013; *Marcucci et al.*, 2013], no evidence for clays or clay precursors were observed through any technique. As described in **Section 4.3.2**, these trends are generally reflected in the IR spectra. Chlorides were only observed in minor abundances by XRD for the glass sample altered under the lowest pH conditions suggesting little influence from HCl. A S:Cl molar ratio of 5:1 was used for the solutions resulting in a relatively larger abundance of sulfates than chlorides. For the sand-sized alteration material was only visible after the evaporation period. It is possible that the secondary phases formed from leaching during the reaction period. However, no mineral formation was observed until after the evaporation period, suggesting that the majority of the alteration material was formed from dissolution and precipitation upon evaporation. Alteration was observed on the rock chunk only after the material was removed from the solution for the first measurements. During the measurements, it is possible that evaporation of the thin film of fluid on the surface resulted in the formation of alteration phases.

The trends described above for the Irvine volatile-containing glass follow trends observed by *Tosca et al.* [2004] for the dissolution of the Pathfinder rock glass (PFSG). In the lower-pH PFSG solutions, dissolution was stoichiometric. In the higher pH solutions, there was a preferential leaching of Na and Ca, resulting in the presence of Ca-sulfates under less acidic conditions. Thus,

our data suggest stoichiometric dissolution in pH0 and preferential release of Ca in pH2 and 4, likely due to the highly mobile nature and abundance of Ca in the starting composition. Based on IR, SEM/EDS, and Raman data, most of the mineral phases observed on the surfaces of IRVG-VC-pH0 contained Al. In typical terrestrial waters (pH5-9), the solubility of Al is low. However, Al solubility increases drastically as pH decreases and Al becomes soluble and mobile [Hurowitz *et al.*, 2006]. There is a relatively smaller amount of pure Mg-sulfate and pure Fe-sulfate than Al-containing sulfates observed for the pH0 sample, despite the higher abundance of FeO_T and equal abundance of MgO in the starting material, indicating the highly soluble nature of Al in this system.

4.4.2 Effects of Volatiles on Glass Spectral Signatures and Chemical Alteration Assemblages

Although the Irvine volatile-containing glasses follow a similar alteration trend (sulfates dominate pH<2) to the Irvine volatile-free glasses, the spectral characteristics of the altered material differs. The unaltered and altered volatile-containing glass exhibited distinct MIR and VNIR features relative to the volatile-free material as well as increased spectral contrast. (**Figure 4-10, 4-11 A-B**). The volatile-free unaltered glass exhibits a broad MIR feature near 1010, and a deep band near 465cm⁻¹. The volatile-containing glass exhibits the same features, but also displays additional features near 888, 790, and 682cm⁻¹ that are absent in the volatile-free signature. The same trend is observed in the unaltered VNIR signatures, with increased spectral contrast observed for the volatile-containing glass relative to the volatile-free glass. For the volatile-containing unaltered sample the feature near 0.99μm is narrower and deeper than that observed for the volatile-free glass. The broad band near 1.32μm in the volatile-free signature is replaced by two distinct bands at 1.26 and 1.32μm. Additionally, there are absorption bands near 1.12, 1.50, 1.62, and a broad feature centered at 2.02μm that are absent in the volatile-free signature. The

differences observed between the spectral signatures for these two compositions require further investigation utilizing a range of volatile contents.

The MIR emission spectral features for the pH0 volatile-free Irvine glass are most consistent with Fe⁺³-sulfate (with influences from silica, Fe-oxides, and Ca-, (Zn, Fe⁺², Mn)-Al-, Mg-, K-Fe^{+2/+3}-Al-sulfates), whereas the pH0 volatile-containing has features most consistent with (Mg, Mn)-Al-sulfate (with lesser amounts of Ca-, Fe⁺²-Al-, Al-, Fe⁺²-, Fe⁺³-, Na-Mg-, and (Zn, Fe⁺², Mn)-Al-sulfate and Fe-oxides). Influences can be observed from Na-Mg-sulfate (blödite), Fe⁺²-sulfate (szomolnokite), and Mg-Al-sulfate (pickeringite) for the IRVG-VF-pH0 reflectance spectrum. However, the VNIR features for IRVG-VC-pH0 are most consistent with Mg-Al-sulfate (pickeringite). Based on the modeled abundances for the volatile-free glass samples altered in pH2-4 there is ~17-20% alteration and the spectral signatures are most consistent with unaltered material with lesser amounts of Fe⁺³-sulfate and Fe-oxides +/- silica. Samples were not altered in pH1 or 3 for the Irvine volatile-containing composition due to a lack of fully glass material. The total alteration abundances are similar for the volatile-containing glass samples altered in pH2-4 (~18-24%) and the spectral signatures are most consistent unaltered material, with lesser amounts of Fe-oxide and Ca-sulfate +/- Fe⁺³-sulfate. The VNIR reflectance spectra for samples altered in pH2-4 conditions from both compositions are most consistent with unaltered material. Although the models indicate some secondary phases in the higher pH conditions, no additional absorptions were observed in the IR. Alteration features were observed spectrally in pH0-2 conditions for the volatile-containing material, but only pH0-1 for the volatile-free material.

The main distinction between the volatile-free and volatile-containing secondary assemblages based on chemical analyses is the presence of Na-Mg-(Fe)-sulfate only in the glass volatile-free samples. This occurrence may be a result of the addition of chlorine. Chlorine complexes with

network modifying elements in the melt [Filiberto and Treiman, 2009] and could be removing more Mg, Na, and Fe from the melt relative to other cations. This would result in less contribution of these cations to the solution chemistry and secondary mineralogy.

4.4.3 Trends in Volatile Containing and Volatile Free Material

Several trends in spectral features and mineral assemblages were observed in both the volatile-containing and volatile-free Irvine samples. (1) Based on the modeled MIR abundances and SEM/EDS, alteration material was dominant over unaltered material on the surface of the glass samples altered in the lowest pH condition. (2) Additional features were observed exclusively in the IR spectra for Irvine samples altered in $\text{pH} \leq 2$ conditions and sulfates dominated the spectra exclusively in conditions with a $\text{pH} = 0$. (3) The most acidic conditions provide a wide variety of sulfate phases with less variety in the higher pH conditions. (4) The VNIR spectral properties of alteration assemblages are difficult to distinguish from one another and tend to be consistent with poly-hydrated sulfates.

The two sets of data also have trends that diverge from one another. For the third trend, the phases observed in the low and high pH alteration assemblages were different. The volatile-containing samples altered in $\text{pH} \leq 1$ solutions had a variety of sulfates phases but lack the Na-Mg-(Fe)-sulfate observed in the volatile-free glass. In volatile-containing samples subjected to the higher pH condition ($\text{pH} 2-4$), Ca-sulfate dominates the alteration assemblages; however, for the volatile-free samples Fe-oxide and Fe^{+3} -sulfate were also present in the glass assemblage. Furthermore, Al-bearing sulfate phases are the most abundant phase modeled for the volatile-containing material altered in lowest pH condition. However, Fe^{+3} -sulfate is the most abundant phase modeled for the volatile-free material altered in low pH conditions ($\text{pH} \leq 1$), instead of Al-bearing sulfates.

4.5 Conclusions

1. Although the volatile-containing materials follow a similar alteration trend (sulfates dominate $\text{pH} < 2$) to the volatile-free glass materials, the spectral characteristics differ for the two compositions in both the MIR and VNIR. Variation can also be observed in the alteration assemblages for the glass material. The spectral characteristics of glass volatile-free and volatile-containing Irvine samples are similar for the unaltered material.
2. The volatile-free glass alteration assemblage includes Na-Mg-(Fe)-sulfates which were absent in the volatile-containing assemblage and Fe-Al-sulfates are observed only in the volatile-containing assemblage.
3. The lack of Na-Mg-(Fe)-sulfate in the volatile-containing glass material may be a result of the addition of chlorine.
4. Fe^{+3} -sulfate is the most abundant phase modeled for glass ($\text{pH} \leq 1$) Irvine volatile free material altered in low pH conditions, instead of Al-bearing sulfates which were the most abundant phase for all of the Irvine volatile containing material altered in low pH (≤ 1) conditions.

4.6 References:

- Baldrige, A.M., P.R. Christensen (2009), Laboratory Technique for Thermal Emission Measurement of Hydrated Minerals: Applied Spectroscopy, v. 63, p. 678-688.
- Carr, M. H., Water on Mars, Oxford, 229 p., 1996.
- Cloutis, E.A., Hawthorne, F.C., Mertzman, S.A., Krenn, K., Craig, M.A., Marcino, D., Methot, M., Strong, J., Mustard, J.F., Blaney, D.L., Bell III, J.F., Vilas, F. (2006), Detection and discrimination of sulfate minerals using reflectance spectroscopy. *Icarus* 184, 121-157. doi:10.1016/j.icarus.2006.04.003

- Dalton, H.A., T.G. Sharp, J.R. Holloway (2007), Investigation of the effects of water on a Martian mantle composition. *Lunar and Planetary Science*, XXXVII: Abstract #2102.
- Dann, J.C., A.H. Holzheid, T.L. Grove, H.Y. McSween (2001), Phase equilibria of the Shergotty meteorite: constraints on pre-eruptive water contents of martian magmas and fractional crystallization under hydrous conditions. *Meteoritics & Planetary Science*, 36 (6), pp. 793–806.
- Downs, R. T. (2006), The RRUFF Project: an integrated study of the chemistry, crystallography, Raman and infrared spectroscopy of minerals. Program and Abstracts of the 19th General Meeting of the International Mineralogical Association in Kobe, Japan. O03-13
- Draper, D.S. (2007), Water-undersaturated near-liquidus phase relations of Yamato 980459. *Lunar and Planetary Science*, XXXVII: Abstract #1447.
- Dreibus G. and H. Wänke (1987), Volatiles on Earth and Mars—a comparison. *Icarus* 71(2):225–240.
- Filiberto, J., and A. H. Treiman (2009), Martian magmas contained abundant chlorine, but little water, *Geology*, 37, 1087–1090.
- Gellert, R., R. Rieder, J. Brückner, B. C. Clark, G. Dreibus, G. Klingelhöfer, G. Lugmair, D. W. Ming, H. Wänke, A. Yen, J. Zipfel, and S. W. Squyres (2006), Alpha Particle X-Ray Spectrometer (APXS): Results from Gusev crater and calibration report, *J. Geophys. Res.*, 111, E02S05.
- Howard, K. T., et al. (2013), Biomass preservation in impact melt ejecta, *Nat. Geosci.*, 6, 1018–1022, doi:10.1038/ngeo1996.
- Hurowitz, J. A., S. M. McLennan, N. J. Tosca, R. E. Arvidson, J. R. Michalski, D. W. Ming, C. Schröder, and S. W. Squyres (2006), In situ and experimental evidence for acidic weathering of rocks and soils on Mars, *J. Geophys. Res.*, 111, E02S19.

- Hynek, B. M., T. M. McCollom, E. C. Marcucci, K. Brugman, and K. L. Rogers (2013), Assessment of environmental controls on acid-sulfate alteration at active volcanoes in Nicaragua: Applications to relic hydrothermal systems on Mars, *J. Geophys. Res. Planets*, 118, 2083–2104, doi:10.1002/jgre.20140.
- Jambon A. (1994), Earth degassing and large-scale geochemical cycling of volatile elements. *Volatiles in Magmas* 30: 479–517.
- Johnson, M.C., M.J. Rutherford, P.C. Hess (1991), Chassigny petrogenesis—melt compositions, intensive parameters, and water contents of martian (questionable) magmas. *Geochimica et Cosmochimica Acta*, 55 (1), pp. 349–366.
- Lane, M.D. (2007), Mid-infrared emission spectroscopy of sulfate and sulfate-bearing minerals. *Am. Mineral.*, 92, pp. 1–18
- Lane, M.D., J.L. Bishop, M.D. Dyar, T.H. Hiroi, S.A. Mertzman, D.L. Bish, P.L. King, and A.D. Rogers (2015), Mid-infrared emission spectroscopy and visible/near-infrared reflectance spectroscopy of Fe-sulfate minerals. *Am. Mineral.*, 100, pp. 66-82.
- Lichtenberg, K. A., R.E. Arvidson, R.V. Morris, S.L. Murchie, J.L. Bishop, D.F. Remolar, T.D. Glotch, E.N. Dobreá, J.F. Mustard, J. Andrews-Hanna, and L.H. Roach (2010), Stratigraphy of hydrated sulfates in the sedimentary deposits of Aram Chaos, Mars, *J. Geophys. Res.*, 115, E00D17.
- Marcucci, E. C., B. M. Hynek, K. S. Kierein-Young, and K. L. Rogers (2013), Visible-near-infrared reflectance spectroscopy of volcanic acid-sulfate alteration in Nicaragua: Analogs for early Mars, *J. Geophys. Res. Planets*, 118, 2213–2233, doi:10.1002/jgre.20159.

- Médard, E., and T. Grove (2008), The effect of H₂O on the olivine liquidus of basaltic melts: Experiments and thermodynamic models: *Contributions to Mineralogy and Petrology*, v. 155, p. 417–432.
- Mysen, B.O., and G.D., Cody (2004), Solubility and solution mechanism of H₂O in alkali silicate melts and glasses at high pressure and temperature: *Geochimica et Cosmochimica Acta*, v. 68, p. 5113–5126.
- Mysen B. O., Fogel M. L., Morrill P. L., and Cody G. D. (2009), Solution behavior of reduced C-O-H volatiles in silicate melts at high pressure and temperature. *Geochimica et Cosmochimica Acta* 73:1696–1710.
- Nekvasil, H., J. Filiberto, F.M. McCubbin, D.H. Lindsley (2007), Alkalic parental magmas for the chassignites? *Meteoritics & Planetary Science*, 42 (6), pp. 979–992.
- Ramsey, M.S., P.R. Christensen (1998), Mineral abundance determination: Quantitative deconvolution of thermal emission spectra. *J. Geophys. Res.* 103 (B1), 577–597.
- Rogers, A.D., Aharonson, O. (2008), Mineralogical composition of sands in Meridiani Planum determined from MER data and comparison to orbital measurements. *J. Geophys. Res. Planets* 113, E06S14.
- Ruff, S. W., J.D. Farmer, W.M. Calvin, K.E. Herkenhoff, J.R. Johnson, R.V. Morris, M.S. Rice, R.E. Arvidson, J.F. Bell III, P.R. Christensen, and S.W. Squyres (2011), Characteristics, distribution, origin, and significance of opaline silica observed by the Spirit rover in Gusev crater, Mars, *J. Geophys. Res.*, 116, E00F23.
- Sklute, E., (2015), On the Subject of Analyzing Iron and Sulfur Bearing Minerals from Three Extreme Environments: Geological Carbon Sequestration, Acid Mine Drainage, and Mars. Ph.D. Dissertation thesis, 433 pp., Stony Brook University, Stony Brook, NY.

- Stebbins, J. F., and Du, L.-S. (2002), Chloride ion sites in silicate and aluminosilicate glasses: a preliminary study by ^{35}Cl solid state NMR. *Am. Mineral.* 87:359–363.
- Tosca, et al., (2004), Acid-sulfate weathering of synthetic Martian basalt: The acid fog model revisited, *J. Geophys. Res.*, 109, E05003.
- Vassamillet, L. F. and Caldwell, V. E. (1969), Electron-probe microanalysis of alkali metals in glasses. *Journal of Applied physics*, 40, 1637-1640.
- Zeng, Q., H., Nekvasil, and C.P. Grey (1999), Proton environments in hydrous aluminosilicate glasses: A H-1 MAS, H-1/Al-27, and H-1/Na- 23 TRAPDOR NMR study: *Journal of Physical Chemistry B*, v. 103, p. 7406–7415.
- Zimova, M., and Webb, S. (2006), The effect of chlorine on the viscosity of Na₂O-Fe₂O₃-Al₂O₃-SiO₂ melts: *American Mineralogist*, v. 91, p. 344–352.
- Zolotov, M. Y., and M. V. Mironenko (2007), Timing of acid weathering on Mars: A kinetic-thermodynamic assessment, *J. Geophys. Res.*, 112, E07006.

Table 4-1. Synthetic Irvine Glass Bulk Compositions for the Volatile-Free and Volatile-Containing material.

Oxide	Component	Irvine VF Average	Irvine VC target	Irvine VC Glass Average (Synthesized Comp.) ^a
SiO ₂	SiO ₂	48.39	46.70	48.99
TiO ₂	TiO ₂	1.08	1.05	1.05
Al ₂ O ₃	Al ₂ O ₃	10.93	10.52	11.09
FeO _r ^b	Fe ₂ O ₃ , Fe Sponge	17.83	19.07	16.77
MnO	MnO	0.39	0.36	0.37
MgO	MgO	10.69	10.52	10.65
CaO	CaSiO ₃	5.87	5.99	5.76
Na ₂ O	Na ₂ Si ₂ O ₅	2.63	2.66	2.32
K ₂ O	K ₂ Si ₂ O ₅	0.67	0.67	0.47
P ₂ O ₅	Ca ₃ (PO ₄) ₂	0.92	0.96	0.99
Cr ₂ O ₃	Cr ₂ O ₃	0.19	0.20	0.22
S	CaSO ₄	0.33	0.30	0.33
Cl	MgCl ₂	0.08	1.00	0.99
Total	-	100.00	100.00	100.00
H ₂ O	Mg(OH) ₂	2.00 ^c	1.00	3.00 ^c

Source: Irvine: *McSween et al.*, 2006 normalized to 100

^aAverage of 20 electron microprobe analyses, normalized to 100.00 wt.%.

^bFe₂O₃ and FeO values have been converted into an 80:20 ratio.

^c2.00 wt. % H₂O from talc dehydration during synthesis.

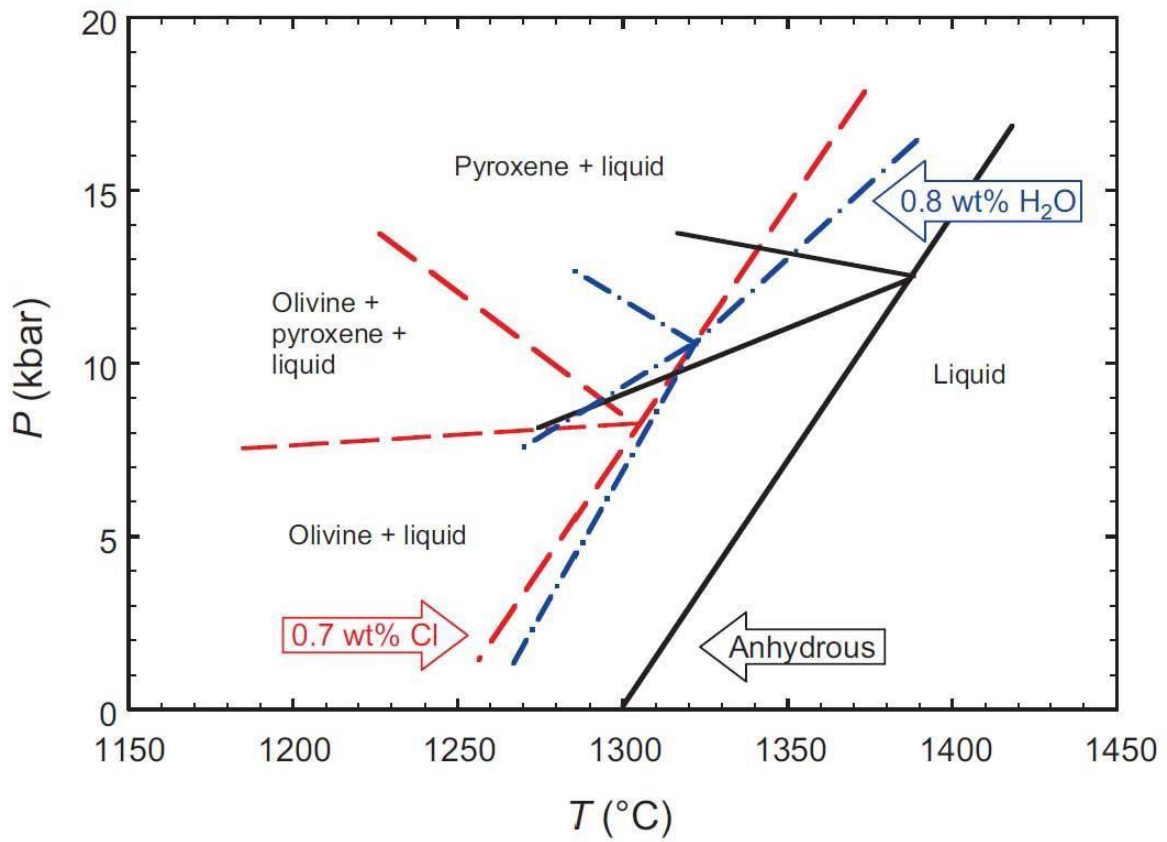

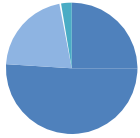
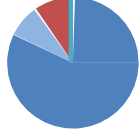
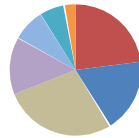






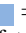
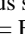
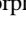

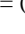
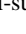
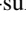
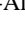



Figure 4-1: Diagram displaying the effects of Cl (0.7 wt. %) and H₂O (0.8 wt. %) on the liquidus of a Humphrey like basalt from *Filiberto and Treiman* [2009].

Irvine Volatile-Containing Glass				
	IRVG-VC-pH0	IRVG-VC-pH2	IRVG-VC-pH4	IRVG-VC-RC-pH0
MIR^A				
VNIR^B	PHS ± silica Slope change	No change	No Change	No Change
SEM/Raman/XRD^C	Al, Ca, Fe ⁺² -Al, Fe ⁺² , Mg, Mg-Al, Fe ⁺³ -sulfate, halite	Ca-sulfate	Ca-sulfate	Ca, Fe-sulfate

^A MIR pie chart color key:  = unaltered material,  = Fe⁺³-sulfate,  = Fe⁺²-sulfate,  = Al-sulfate,  = Ca-sulfate,  = Mg-sulfate,  = Fe-oxides,  = amorphous silica,  = amorphous Fe⁺³-sulfate,  = sulfur,  = (Zn, Fe⁺², Mn)Al-sulfate,  = Na-sulfate,  = Fe⁺²-Al-sulfate,  = (Mg,Mn)Al-sulfate,  = Fe^{+2/+3}-sulfate.

^B PHS = polyhydrated sulfates

^C All XRD measurements indicated amorphous material which could be glass, silica, or other amorphous materials.

Figure 4-2: Overview of alteration material observed for Irvine, Backstay, Pathfinder Soil, and Pathfinder Rock material.

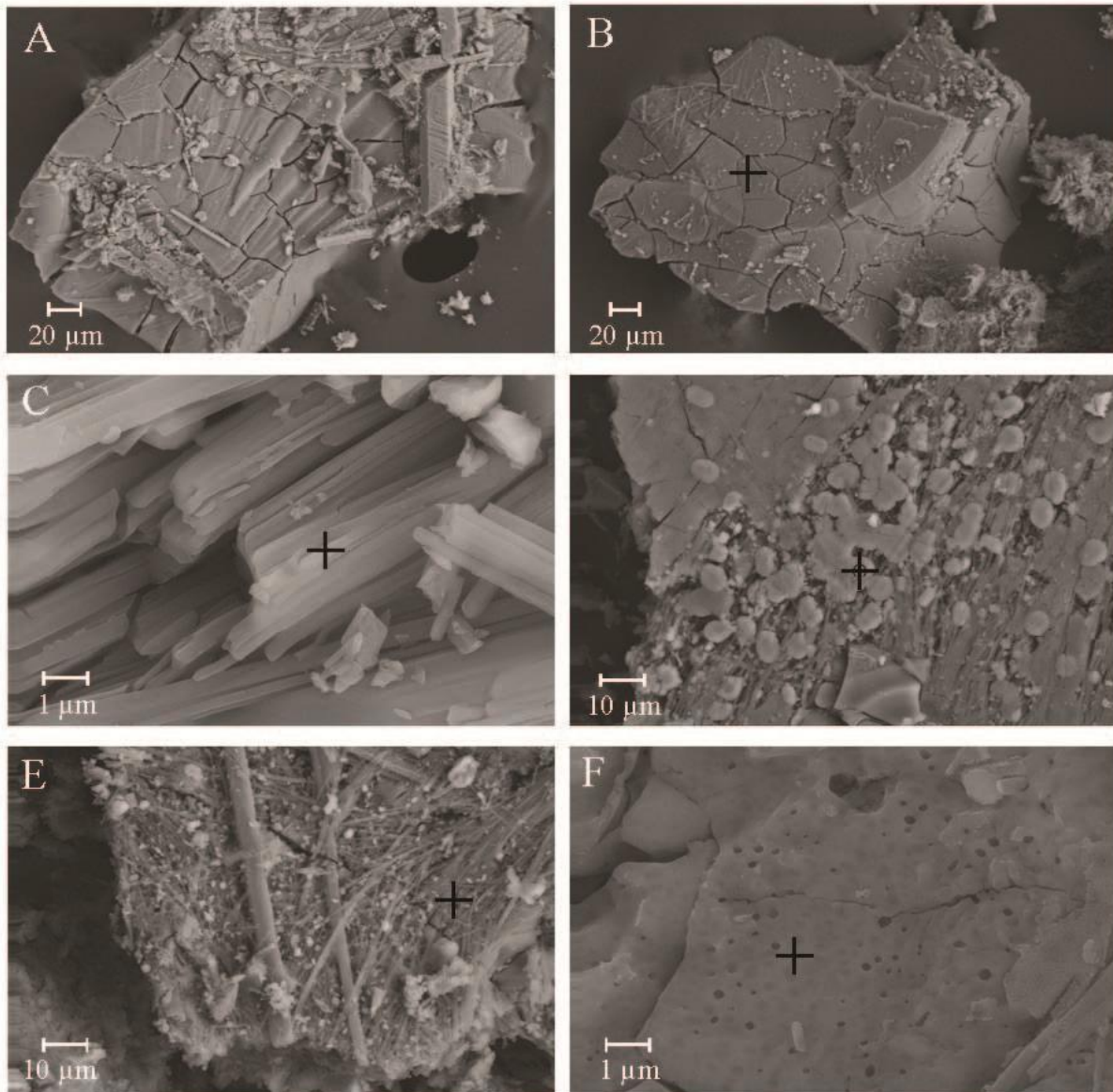


Figure 4-3: Scanning electron micrograph of IRVG-VC-pH0 displaying A) variety of secondary mineral morphologies on a single grain, B) silica rich coating, C) acicular Mg-Al-sulfate, D) round K-Fe-sulfate E) hair-like Fe-Al-sulfate and F) platy Mg-sulfate.

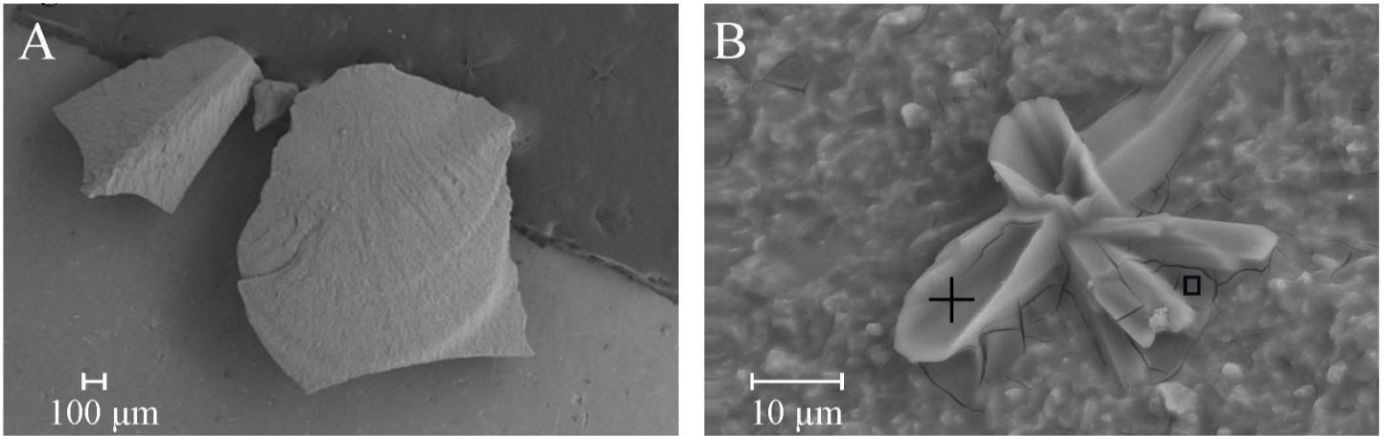


Figure 4-4: Scanning electron micrograph of IRVG-VC-pH2 displaying A) the relatively unaltered grain surface, and B) elongated Ca-sulfate grains and desiccated silica-rich surface.

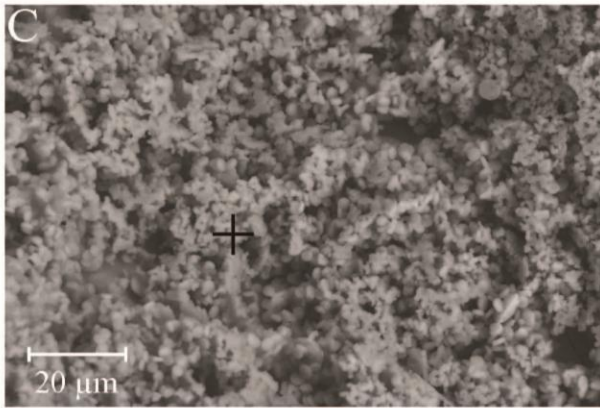
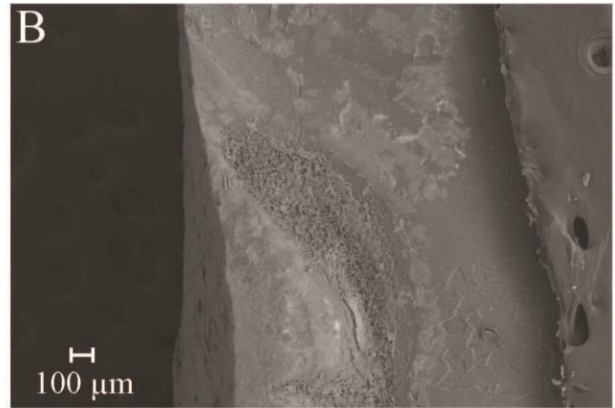
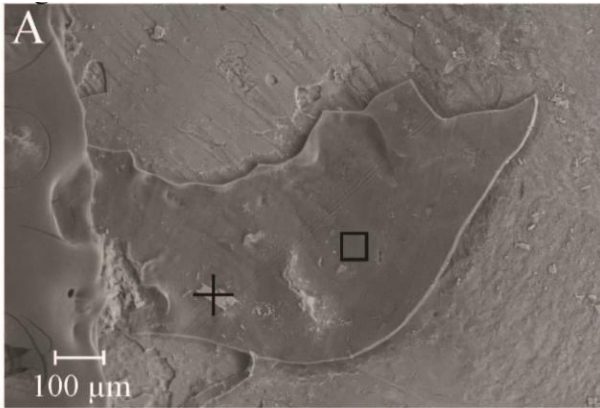


Figure 4-5: Scanning electron micrograph of the glass rock chunk altered in pH 0 (IRVG-VC-RC-pH0) displaying A) sulfur rich peeled off coating (square) and Ca-sulfate forming on top of the coating (cross), B) underlying material of the peeled off piece, and C) closer look at the underlying material, which is most consistent with fine grained Fe-sulfate.

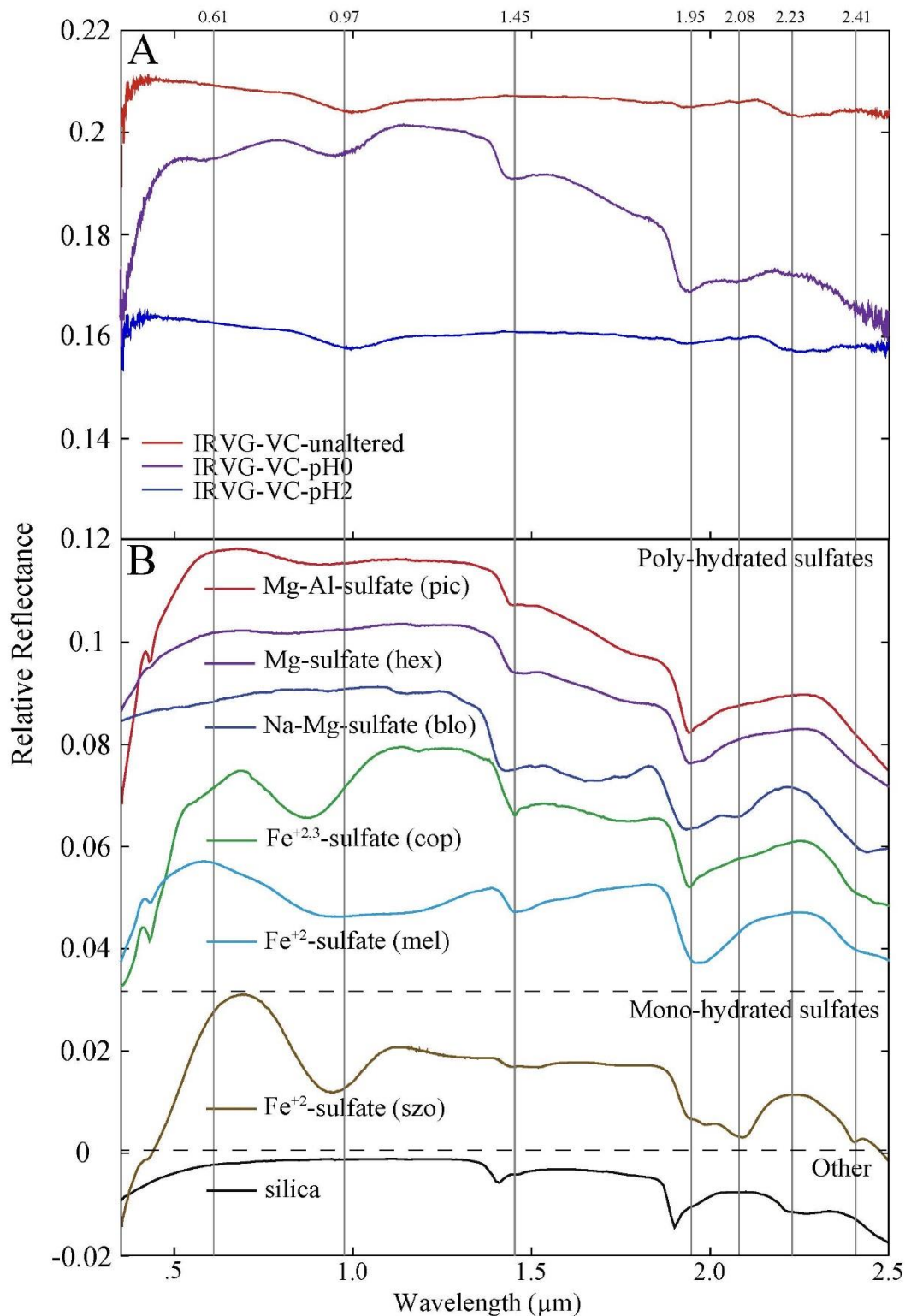


Figure 4-6: A) VNIR reflectance spectra of unaltered and altered (pH0-2) Irvine volatile-containing glass samples plotted with B) the best fit library spectra. Vertical lines indicate features discussed in text. The y-axis has been offset for clarity. Pic = pickeringite, hex = hexahydrite, blo = blödite, cop = copiapite, mel = melanterite, szo = szomolnokite.

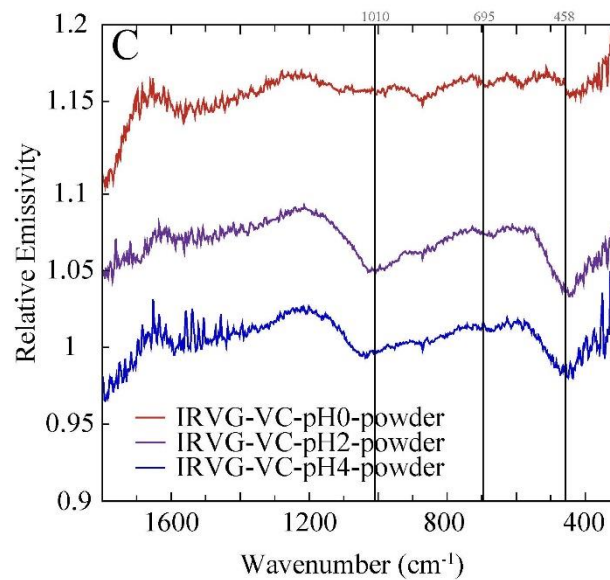
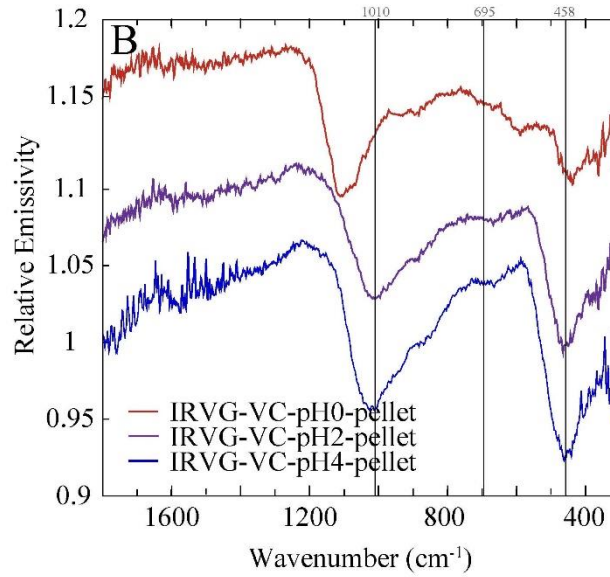
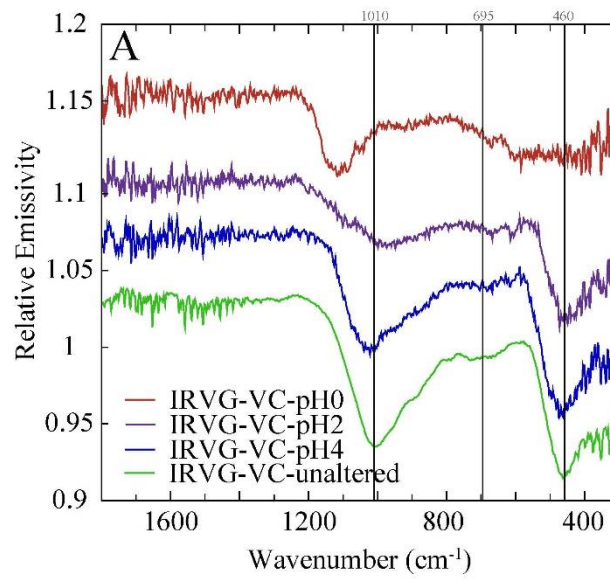


Figure 4-7: Comparison of MIR emission signatures for A) IRVG-VC particulate material, B) IRVG- VC pellet material, and C) IRVG-VC powder material.

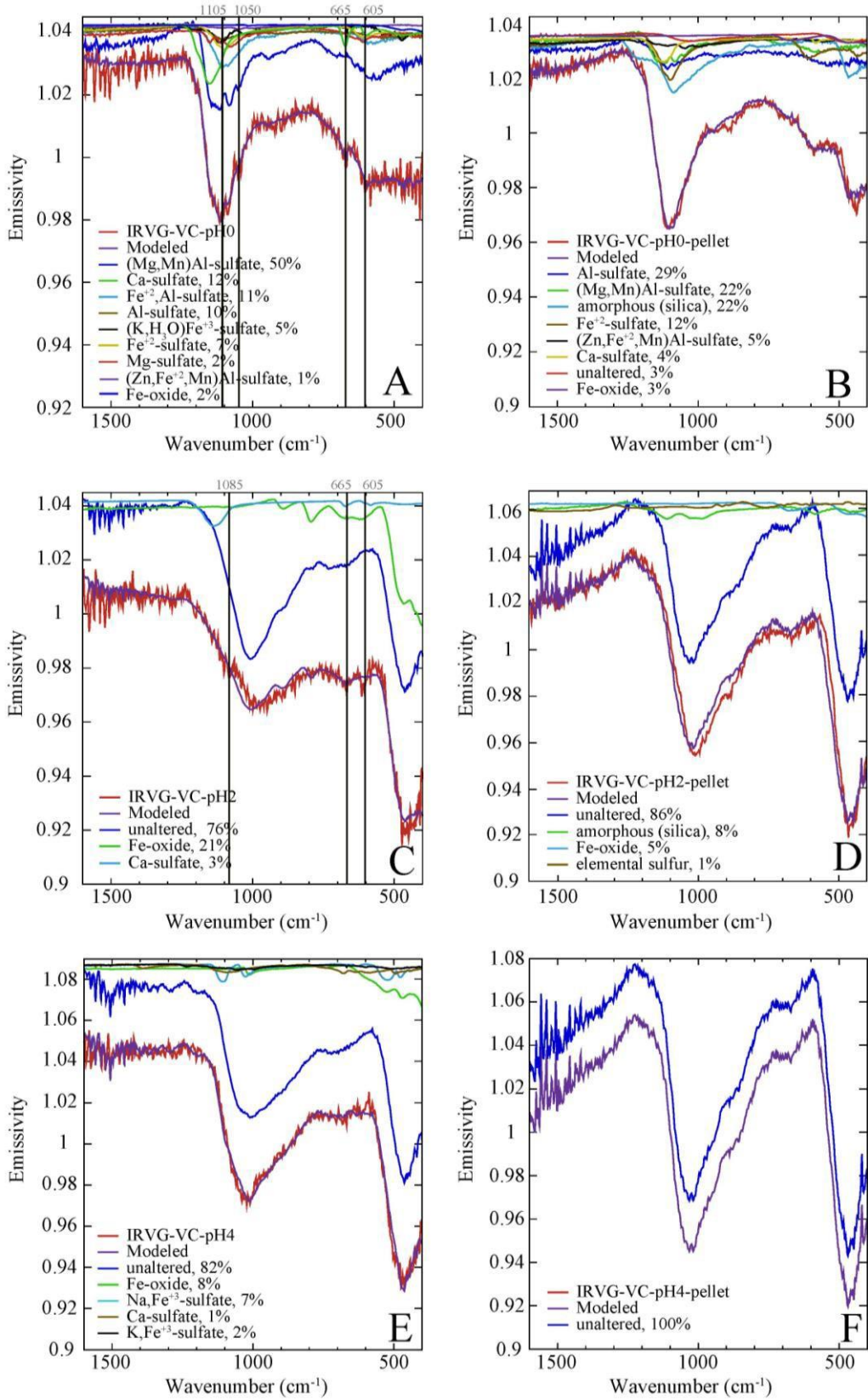


Figure 4-8: Modeled MIR emission spectra of Irvine volatile-containing sand-sized glass samples altered in A) pH0, B) pH2, and C) pH4 and pellet glass samples altered in D) pH0, E) pH2, and F) pH4.

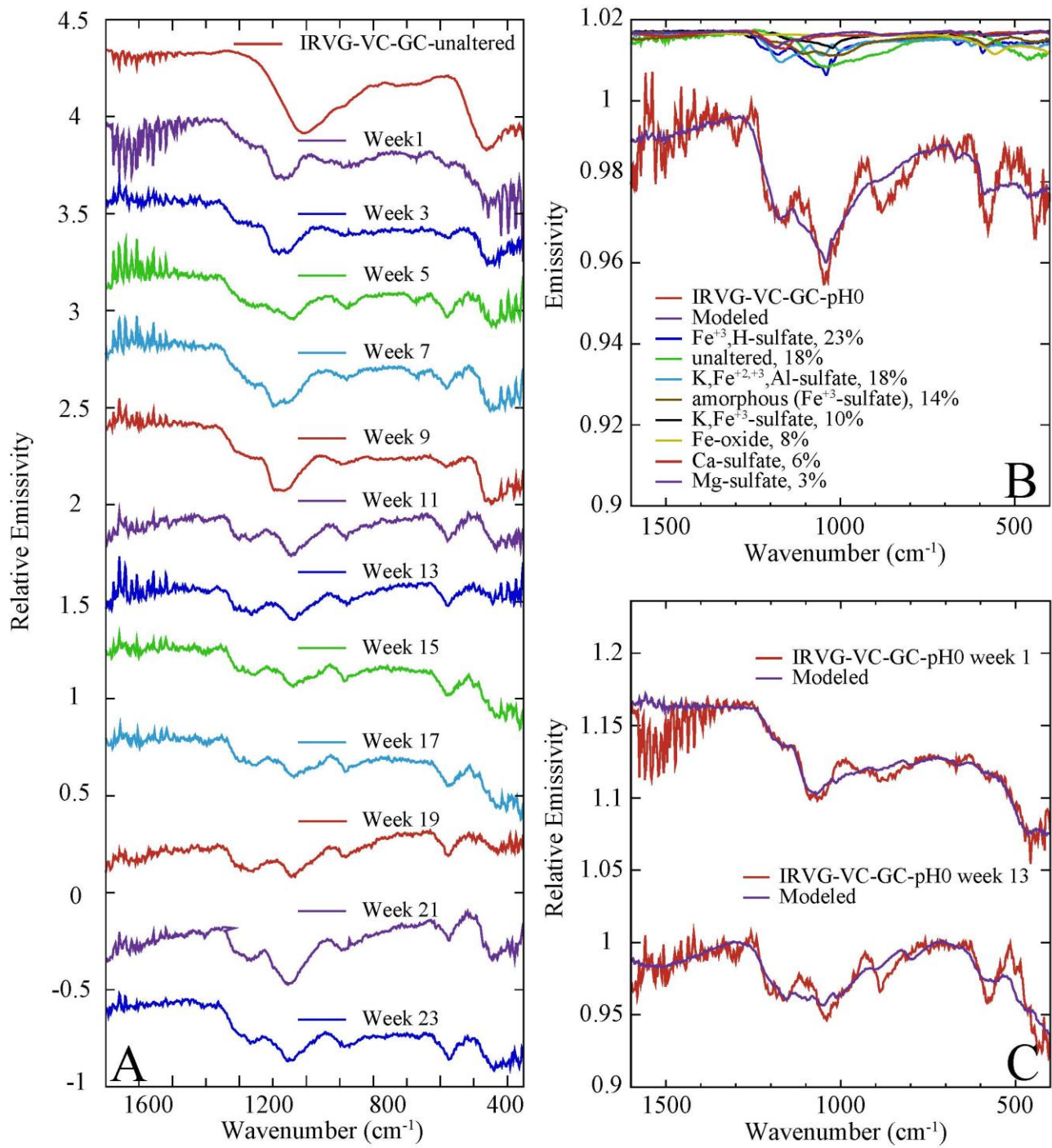


Figure 4-9: Modeled MIR emission spectra of the glass chunk altered in pH 0 (IRVG-VC-GC-pH0) from A) the final week of alteration and B) weeks with a significant change in spectral features, week 1 and week 13.

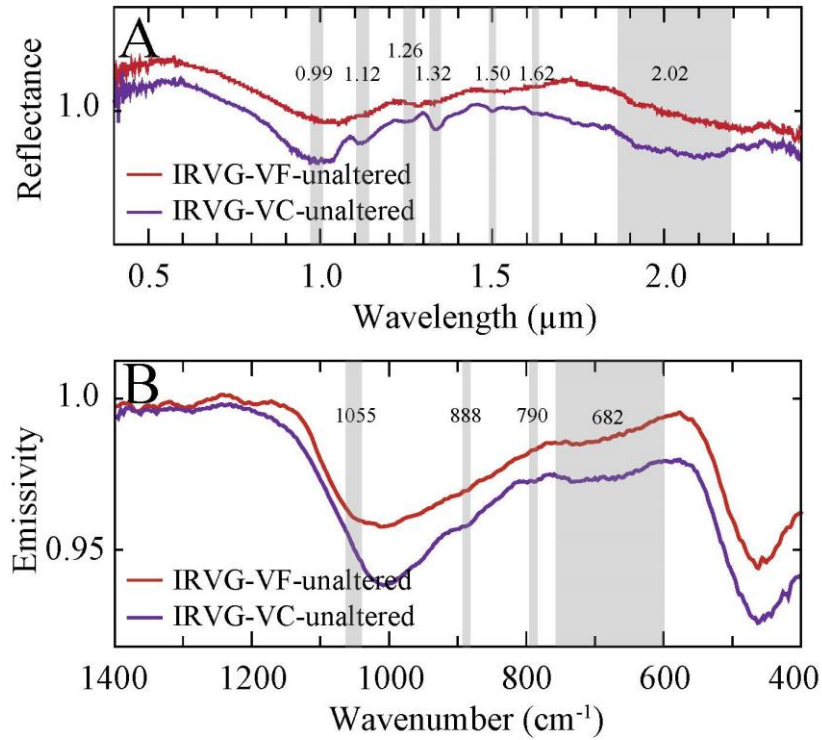


Figure 4-10: Comparison of the A) VNIR reflectance signatures and B) MIR emission signatures for unaltered glass material with Irvine volatile-free (IRVG-VF) and volatile-containing (IRVG-VC) compositions. Gray shading indicates spectral regions that differ between materials. These spectra indicate that volatiles affect the spectral shapes both in the VNIR and MIR.

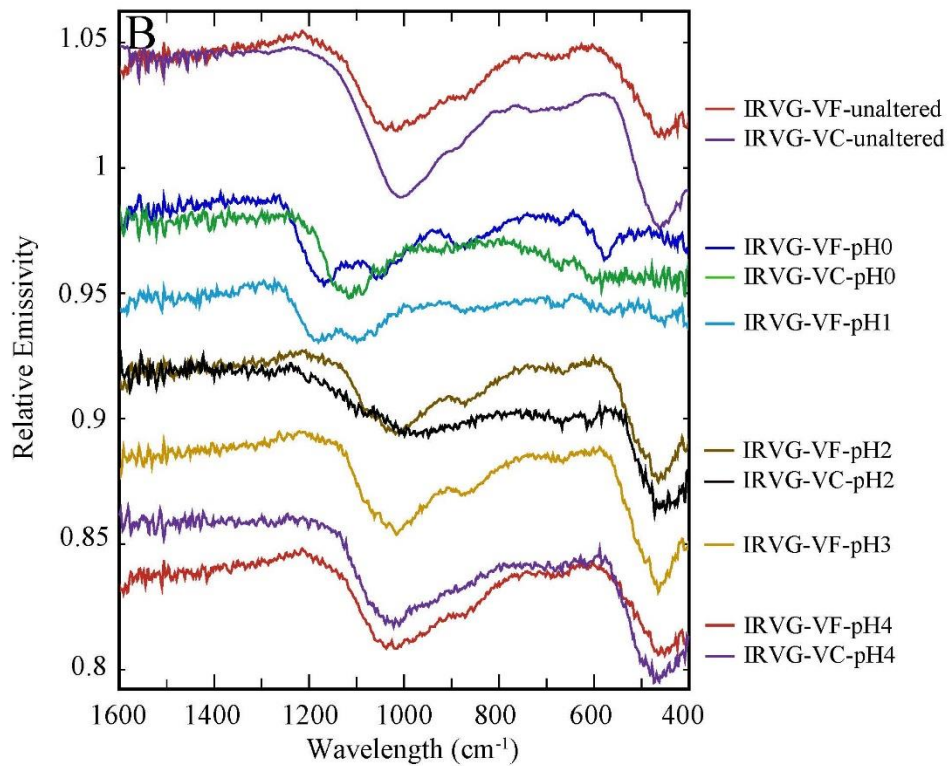
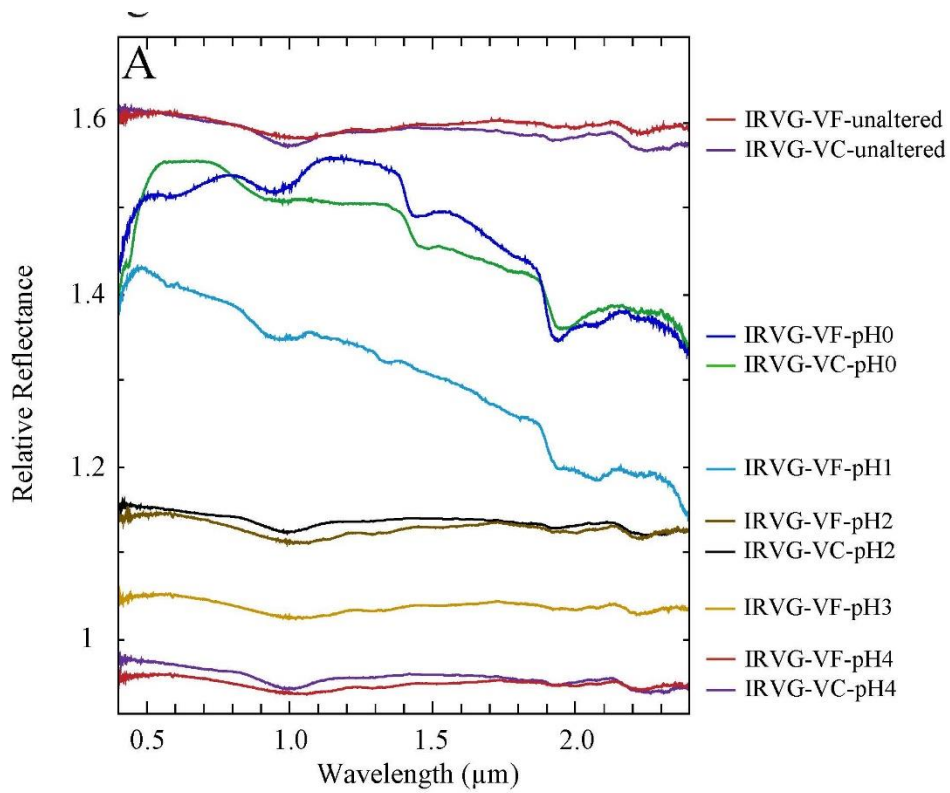


Figure 4-11: Comparison of the A) VNIR reflectance signatures and B) MIR emission signatures for the unaltered and altered material with Irvine volatile-free and volatile-containing compositions.

Chapter 5

Visible, Near-Infrared and Mid-Infrared Spectral Characterization of Hawaiian Fumarolic Alteration near Kilauea's December 1974 Flow: Implications for Spectral Discrimination of Alteration Environments on Mars

This chapter was published in the American Mineralogist Journal

Yant, M., K.E. Young, A. D. Rogers, A.C. McAdam, J.E. Bleacher, J.L. Bishop, and S.A.

Mertzman (2018), Visible, Near-Infrared and Mid-Infrared Spectral Characterization of Hawaiian Fumarolic Alteration near Kilauea's December 1974 Flow: Implications for Spectral Discrimination of Alteration Environments on Mars, *Am. Min.*, 121, doi:10.1002/2015JE004969

5.1 Introduction:

The Martian surface has a complex history that includes volcanic activity and widespread aqueous alteration [e.g., *Bell et al.*, 2008], likely including hydrothermal environments. Hydrothermal environments are of particular interest as they potentially indicate habitable conditions, due to their ability to provide microbial communities with water and energy in an otherwise cold/arid environment [e.g., *Costello et al.*, 2009]. On Earth, fumarolic activity can support microbial life including mat-like photoautotrophic communities (e.g., mosses and liverworts) [*Costello et al.*, 2009], autotrophic communities (e.g., mosses, liverworts, algae, fungi, lichens) [*Halloy*, 1991], and halophilic *Archaea* (single-celled microorganisms) [*Ellis et al.*, 2008]. Thus, detection of fumarolic environments on Mars would suggest a region that could have hosted a habitable environment.

Key constraints on the habitability and astrobiological potential of ancient aqueous environments are provided through detection and interpretation of secondary mineral assemblages,

which vary with alteration conditions (e.g., temperature, pH, fluid-to-rock ratio). Alteration assemblages that were potentially derived from hydrothermal systems have been detected *in situ* on Mars at Gusev Crater and Meridiani Planum [e.g., *Squyres et al.*, 2007; *McCullom and Hynek*, 2005; *Schmidt et al.*, 2008; *Yen et al.*, 2008; *Squyres et al.*, 2012; *Arvidson et al.*, 2014]. The search for hydrothermal systems on Mars has been extended to other locations using orbital measurements of reflectance and emission spectra, which are sensitive to mineral species and abundance. For example, detections of silica from orbit have been used to identify potential fumarolic or near-surface hydrothermal activity [e.g., *Bishop et al.*, 2008; *Milliken et al.*, 2008; *Ehlmann et al.*, 2009; *Skok et al.*, 2010; *Marzo et al.*, 2010; *Wray et al.*, 2011; *Smith and Bandfield*, 2012]. However, orbital spectral interpretations benefit from comparable spectral studies of analog surfaces as demonstrated in **Table 5-1** and of samples altered under controlled conditions in the laboratory [e.g., *Yant et al.*, 2016] because infrared (IR) spectra are also sensitive to other factors, such as particle size, host rock mineral assemblage, and other physical properties. Alteration products often form as a thin coating/fracture fill, or are fine-grained and poorly consolidated, which can lead to challenges in comparing data from different techniques due to non-linear spectral mixing from coating and rind geometry and differences in how the measurements are performed [e.g., *Kraft et al.*, 2003; *Michalski et al.*, 2006; *Kraft et al.*, 2007; *Hamilton et al.*, 2008; *Rampe et al.*, 2009].

Altered ash and tephra sites from the Kilauea region on the big island of Hawaii have been established as Mars analogs due to the physical, chemical, and morphological properties of the Kilauea eruptive products and a range of potentially Mars-relevant environments (e.g., studies in **Table 5-1**). For example, chemically altered Kilauea basaltic materials contain secondary minerals and mineraloids (e.g., hematite, Mg/Fe-sulfates, silica) that have been observed on Mars [e.g.,

Morris et al., 2000a; Morris et al., 2005]. Here, we focus on a hydrothermal solfatara site situated on the Kilauea caldera, directly adjacent to the December 1974 flow on its northwest side, and just above the ash outcrop investigated previously [*Bishop et al., 2005a*]. This area provides samples of hydrothermally-altered basalt and alteration products deposited in and around a passively degassing volcanic vent. These samples provide potential spectral analogs to hydrothermally altered regions on Mars.

Earlier studies have characterized the alteration minerals, pathways of high and low temperature weathering, and hydrothermal activity associated with Hawaiian materials [e.g., *Crisp et al., 1990; Morris et al., 2000a; Morris et al., 2000b; Schiffman et al., 2000; Schiffman et al., 2006; Bishop et al., 2007; Minitti et al., 2007; Hamilton et al., 2008; Chemtob et al., 2010; Seelos et al., 2010; McCanta et al., 2014; Chemtob and Rossman, 2014*] as summarized in **Table 5-1**. Some of these previous studies have also provided spectral analyses of naturally altered volcanic materials [e.g., *Crisp et al., 1990; Morris et al., 2000b; Schiffman et al., 2006; Bishop et al., 2007; Minitti et al., 2007; Hamilton et al., 2008; Seelos et al., 2010*] (**Table 5-1**). The MIR and/or VNIR spectral properties of in situ altered Hawaiian basaltic materials were obtained from widespread locations on samples that included lava flows, tephra, ash, and basalt coatings. Silica was observed in all of these studies, as amorphous silica [*Crisp et al., 1990; Schiffman et al., 2006; Bishop et al., 2007; Seelos et al., 2010*], nanophase silica [*Morris et al., 2000b*], or hydrated silica [*Minitti et al., 2007*]. *Hamilton et al.* [2008] detected silica as a mineral phase, cristobalite. Another common phase among these studies is Fe-oxides, which were identified by all of these works, excluding *Morris et al.* [2000b]. Sulfates (Na-Al, Ca, Fe) were also observed in majority of these previous studies. Phyllosilicates were only exhibited in two of the sample groups [*Bishop et al., 2007; Hamilton et al., 2008*].

A previous study by Seelos *et al.* [2010] included samples and remote measurements from the same fumarole studied here, thus we describe their results in more detail. This particular fumarole is of interest because it is young and well-preserved, and large enough to be analyzed from aerial and orbital observations. Reflectance data of basalts in the Ka'u desert of Hawaii were collected using an Airborne Visible Near Infrared Imaging Spectrometer in order to identify the mineralogic components of relatively young basaltic material. Most of the studied area had spectral signatures consistent with the presence of ferrous and ferric iron in such minerals as pyroxene, olivine, hematite, goethite, and poorly crystalline iron oxides or glass. However, ash duricrusts, coatings on the youngest lava flows, and surfaces downwind of the solfatara vents, exhibited a spectral feature near $2.25\mu\text{m}$, associated with opaline silica. The hydrothermally altered solfatara material was spectrally dominated by sulfur and hydrated silica [Seelos *et al.*, 2010].

The naturally-altered fumarolic materials analyzed here are compared in this study with assemblages formed on laboratory-altered synthetic Martian materials from Yant *et al.* [2016]. These previously studied synthetic basaltic glasses represent one type of environment predicted to be common on Mars, acid sulfate weathering under low fluid-to-rock ratios and nearly isochemical conditions [Burns and Fisher, 1990; Bigham and Nordstrom, 2000; Madden *et al.*, 2004; Golden *et al.*, 2005; Ming *et al.*, 2006]. Results from Hurowitz and Fischer [2014] indicate that the chemistry of soils at Gusev crater and Meridiani Planum and rinds at Gusev crater suggest a water limited environment with chemical alteration dominated by sulfur-rich fluids; this resulted in the formation of secondary phases without physical separation from the primary substrate, also referred to as “cation-conservative” [Niles and Michalski, 2009] conditions. The cation-conservative chemical weathering characteristics displayed by the undisturbed soils from Gusev crater and Meridiani Planum indicate similar weathering processes for the alteration rinds on rocks

and the regolith on Mars [Hurowitz and Fischer, 2014]. Here we investigate how the chemical and spectral properties of naturally-altered Hawaiian fumarolic deposits compare with those of alteration assemblages formed in other Mars-relevant environments.

In this study, we extend the earlier work through visible/near-infrared (VNIR) and mid-infrared (MIR) spectral characterization of the altered glassy basalt surrounding a fumarole vent adjacent to the December 1974 Kilauea flow. This spectral characterization will enhance the understanding of the spectral properties of alteration products found in hydrothermal systems. In addition, analytical measurements including x-ray fluorescence (XRF), x-ray diffraction (XRD), and scanning electron microscopy (SEM) are coordinated with spectral measurements in order to bridge the gap between alteration assemblages and IR signals. Specifically, we address the following questions: 1) What are the VNIR and MIR spectral characteristics of fumarolic alteration from basaltic starting materials? 2) How do the IR spectral signatures relate to chemical and physical variations among samples? 3) How do MIR spectral signatures compare with VNIR signatures? 4) How do the spectral properties of fumarolic deposits compare with those of alteration assemblages formed in other Mars-relevant environments?

5.2 Methods:

5.2.1 Sample Collection:

We collected samples in June 2015 from an active solfatara site, situated directly adjacent to the December 1974 flow at Kilauea caldera (19.362403° N, -155.311090° W), on its northwest side (**Figure 5-1**). This site consisted of hydrothermally altered basalt and alteration products deposited in and around a passively degassing fumarole vent. For the samples with “HI_15_MHY” designations, material was collected within 19.5m of the main volcanic vent with the lowest sample number corresponding with the furthest location. The samples with “HI_15_Solf”

designations were collected from the top and sides of the ridge. The "HI_15" portion of the samples names are not included for labels on figures to cut down on length. The collected material (**Figure 5-1, Table 5-2**) consisted of altered basaltic rocks with variously colored coatings (blue, yellow, white), coatings on friable, wet reddish ash, as well as one lag deposit sample with centimeter sized white and yellow grains. Samples were chosen to reflect the wide variety of different coatings found at this site. Samples were carefully removed from their locations and best efforts were made to preserve the samples in their original form.

5.2.2 Analytical Techniques:

The samples were spectrally characterized using VNIR and MIR spectroscopy; analyses were performed on the sample surfaces as collected (e.g., as solid surfaces instead of powdered samples). VNIR (350-2500nm) bidirectional reflectance spectra were acquired using an ASD FieldSpec3 Max spectrometer at Stony Brook University under ambient laboratory conditions. The samples were purged overnight to remove H₂O and CO₂ from the air and measurements were taken under purged conditions. This was done to remove the spectral effects from adsorbed water on the sample surfaces [e.g., *Anderson and Wickersheim, 1964*]. The purged spectra were compared with previously collected measurements that were performed without an overnight purge. Distinct differences were observed between the two data sets, with adsorbed water broadening the absorption features near 1.4 and 1.9 μ m. The purged spectra provided more diagnostic signatures and these spectra are provided in **Figure 5-2**. The measurements were collected with incidence and emergence angles of 30° and 0°, respectively. The measurements were performed relative to Spectralon and then corrected for the reflectance properties of Spectralon. VNIR spectra were compared with library spectra of well-characterized samples available from RELAB (<http://www.planetary.brown.edu/relab/>).

MIR emissivity spectra were acquired between 225-2000 cm^{-1} on Stony Brook University's Nicolet 6700 FTIR spectrometer equipped with a CsI beamsplitter and deuterated triglycine sulfate cesium iodide (DTGS CsI) detector. The atmosphere was purged of H_2O and CO_2 . Each sample was put into an aluminum sample cup painted with Krylon Ultra Flat Black paint in order to minimize spectral contributions from the sample cups. Measurement of MIR emission spectra requires that the samples be at a different temperature than the detector; typically, samples are heated above ambient temperature to achieve this requirement [e.g., *Ruff and Christensen, 1997*]. However, because our samples were expected to contain sulfate minerals, which could dehydrate upon heating, emission measurements of altered samples were performed by cooling the samples well below the detector temperature [*Baldrige and Christensen, 2009*]. A thermo-electric cooling apparatus was used to actively cool the samples during spectral measurement. The samples were cooled to approximately -15°C within the chamber and maintained at that temperature for the duration of 256 scans (~9 minute integration).

MIR spectra of altered samples were analyzed using linear least squares analysis [e.g., *Ramsey and Christensen, 1998; Rogers and Aharonson, 2008*] with a library of sulfate, silica, Fe-oxide, clay, and sulfur spectra, over the spectral range of 400-1400 cm^{-1} . Most of the library spectra and samples used in this study are described in *Christensen et al. [2000]; Wyatt et al. [2001], Glotch et al. [2004], Lane et al. [2007], Glotch and Kraft [2008], Baldrige [2008], Ruff et al. [2011], Lane et al. [2015], and Sklute [2015] (Appendix Table A5)*. A quasi-linear slope spectrum was also included to account for slopes present in the altered samples, due to spatial and/or temporal non-isothermality within the sample or sample collection process from temperature fluctuations. Although linear spectral mixing cannot be assumed for some of these mixtures, the models allow us to characterize the spectrally dominant phases for descriptive purposes (e.g.,

sulfate- or silica-dominated assemblages), and provides a comparison to what would be observed in models of spectra acquired from Mars.

Chemical and morphological analyses of secondary phases were obtained using a LEO 1550 SFEG scanning electron microscope (SEM) equipped with an EDAX energy dispersive x-ray spectrometer (EDS). SEM analyses were only acquired for the HI_15_MHY samples. Analyses were performed using an accelerating voltage of 20kV. The EDS system is capable of quantitative elemental analysis, but only for relatively flat surfaces. All of the EDS analyses discussed here are semi-quantitative because the analyses were performed on samples with variable surface angles. The EDS analyses do not allow for exact element ratios, but they do provide the elemental composition of the material. With the ratios provided by EDS, a comparison between elements present in the spectra can be done. Combining the elemental makeup and the morphology of a grain can allow for mineral identification. The other analytical techniques (XRF, XRD) can also be utilized to properly identify phases.

X-ray diffraction patterns were determined for a suite of samples using a PANalytical X'Pert PRO x-ray diffractometer equipped with a 15-position sample changer and a ceramic Cu x-ray tube at Franklin and Marshall College. Small aliquots of each sample were hand ground using a ceramic mortar and pestle. Each finely powdered sample was mounted on zero background plates and analyzed sequentially on the same day at 45 kV and 40 mA with the sample holder rotating at 4 revolutions per second while being analyzed to insure sample homogeneity. Scans from 6° to $70^{\circ} 2\theta$ were made for each sample. Routine identification of crystalline materials is made using PANalytical, Inc. Highscore software, which is compatible with the International Center for Diffraction Data (ICDD) Database. Readily visible on each diffractogram is a hump in the

background intensity located between approximately 15° and 35° 2θ that varies in intensity and is related to the amount of amorphous material present in each sample.

Though initially developed for use in industry and mining, the handheld x-ray fluorescence (hXRF) has now been established as a viable and valuable technology for *in situ* geochemical analysis [Young *et al.*, 2015]. Though laboratory XRF instruments will remain the gold standard for detailed chemical analyses, the hXRF permits *in situ* analyses, which are advantageous in this case as they can analyze thin coatings on samples that can be hard to isolate from their underlying bulk rock. As this study seeks to examine thin coatings and veneers in the solfatara region, hXRF technology provides a valuable way to analyze coatings in a large number of locations throughout the study area. Due to the heterogeneous nature of the samples in this study, we focus on measuring the coating materials. Young *et al.* [2011, 2012] demonstrated that the hXRF can provide reasonable constraints on the chemistry of basaltic rocks, and we therefore use this technology in this study. The samples were analyzed using an Olympus Innov-X DELTA Premium Handheld XRF Analyzer. The hXRF calibrations were done using standards (Samples CP-5, HWHL100, BPNTX1, WIME101, and TMGNV5) and the errors on these measurements range from a couple of wt. % to ~10 wt. % depending on the element. All of the calibration curves and methodologies are outlined in Young *et al.* [2016].

5.3 Results:

5.3.1 Infrared Spectroscopy

An overview of the alteration material observed for each sample is shown in **Table 5-2**. The MIR emission spectra were first separated into groups based on variations in spectral properties (**Figure 5-2A-D**). Most of the MIR spectra of our samples appear to be dominated by silica (**Figure 5-2A**), exhibiting features consistent with silica sinter, microporous silica, and/or

amorphous silica [Ruff *et al.*, 2011]. Within the silica dominated group (Group 1), there are 4 sub-groups. The first sub-group (1-1) exhibits deep silica features near 1240, 1100, and 470 cm^{-1} . The second sub-group (1-2) displays a shallowing of these three features, whereas in the third sub-group (1-3) the feature near 1240 cm^{-1} is severely shallowed. The fourth sub-group (1-4) exhibits silica features that are shifted when compared to the previous groups, from 1240 and 1100 cm^{-1} to 1260 and 1115 cm^{-1} , respectively. The remaining 3 groups each only have one associated signature. Group 2 exhibits features near 1145, 675, and 600 cm^{-1} suggesting a Ca-sulfate (gypsum)-dominated [Bishop *et al.*, 2014] assemblage (**Figure 5-2B**). The next group is most consistent with Fe^{+3} -sulfate (coquimbite) with absorptions near 1170, 1095, 525, and 470 cm^{-1} [Lane *et al.*, 2015], but as will be described below, is also consistent with a fine-grained mixture of silica, Ca-sulfate, and Al-sulfate (**Figure 5-2C**). Silica and Fe-oxide (hematite) influence the spectra for the last group with features near 1250, 1105, 655, and 470 cm^{-1} (**Figure 5-2D**).

The VNIR reflectance spectra are divided based on the previous groups established for the MIR emission spectra (**Figure 5-2E-H**). Features consistent with silica ($\text{SiO}_2 \cdot n\text{H}_2\text{O}$) are observed for all of the samples in the VNIR (near 0.98, 1.19, 1.45, 1.93 and/or 2.25 μm [Goryniuk *et al.*, 2004; Rice *et al.*, 2013]), but some samples exhibit additional features influenced by Fe-oxides (features $0.6 < \mu\text{m}$ [e.g., Morris *et al.*, 1985; Bishop and Murad, 1996]) and/or sulfates (1.4-1.5, 1.75-1.85, 1.9-2.0, ~2.2 and/or ~2.4 μm [Bishop *et al.*, 2005b; Lichtenberg *et al.*, 2010; Lane *et al.*, 2015; Cloutis *et al.*, 2006] (**Table 5-2**). Opal-CT and silicic acid are referred to here as hydrated silica as they both represent $\text{SiO}_2 \cdot n\text{H}_2\text{O}$ and SiOH species (Rice *et al.*, 2013). Opal-CT is identified by characteristic features near 1.4-1.41 and 1.91 μm , along with a broader band centered at 2.21 μm with a shoulder extending towards 2.25 μm [e.g., Anderson and Wickersheim, 1964; Milliken *et al.*, 2008; McKeown *et al.*, 2011]. Additionally, silicic acid (synthetic silicon dioxide, a white solid

powder formed by the acidification of silicate salts (e.g., sodium silicate) in aqueous solution) was used to identify hydrated silica with spectral features near 0.98, 1.19, 1.45, 1.93 μm [Rice *et al.*, 2013]. These features are characteristic of H₂O in server minerals, however, based on the shape of the features near 0.98, 1.19, 1.4, and 1.9 μm , these spectral bands may indicate the presence of hydrated silica in our samples.

In general, the features present in the VNIR reflectance spectra are similar within the groups of samples, however there are some variations. In Group 1-1, the spectra exhibited deep silica features in the MIR. Although influence from silica is observed for all five samples in the VNIR, a broad absorption in the 0.92-1.06 μm range is also exhibited, consistent with Fe⁺²-sulfate (melanterite) and/or Fe-oxide (akaganéite), or perhaps an iron impurity within the silica phase or mineral mixing (**Figure 5-2E**). The shoulder near 0.53 μm observed for HI_15_MHY_001 and Solf_002_1 may also indicate influence from Fe-oxides. Overall, MHY_001, Solf_001_1, and Solf_002_1 display shallow features consistent with basaltic glass along with some influence from opal-CT near 1.91 and 2.25 μm ; whereas MHY_002a and MHY_002b exhibit deeper features primarily consistent with opal-CT. Additionally, MHY_001 and Solf_002_1 exhibit negative spectral slopes and a concave nature, possibly due to thin coatings and/or fine grain size [e.g., Fischer and Pieters, 1993] or due to acidic leaching of glass [Horgan and Bell, 2012]. Group 1-2 exhibited shallowed silica features in the MIR. Again, all of the VNIR spectra in this group are consistent with the presence of silica, however all of these samples also exhibit influence from Fe-oxide (akaganéite) and/or trace iron impurity, near 0.44, 0.53 and/or 0.98 μm (**Figure 5-2E**). The feature near 0.44 could also be due to the presence of Fe⁺²-sulfate (melanterite) and/or Fe⁺³-sulfate (copiapite or jarosite). The features observed near 1.45, 1.91, and 2.25 μm for the samples in this group are consistent with opal-CT.

The MIR signatures for Group 1-3 were silica-dominated, but with severe shallowing of the 1240cm^{-1} feature. The VNIR signatures for both samples in this group are influenced by silica, exhibiting features consistent with opal-CT ($1.45, 1.91, 2.25\mu\text{m}$) (**Figure 5-2E**). Both samples included in this group also display features that may be due to the presence of Fe-oxide (akaganéite), near 0.53 and $0.98\mu\text{m}$. The shifted silica features observed for Group 1-4 in the MIR correspond with a VNIR signature dominated by silica and Ca-sulfate (**Figure 5-2E**). The shape of the feature near $1.45\mu\text{m}$ is most consistent with Ca-sulfate (gypsum) along with the absorption near $1.76\mu\text{m}$. The feature near $2.25\mu\text{m}$ is most consistent with opal-CT. Group 2 is Ca-sulfate-dominated in the MIR, and exhibits features dominated by Ca sulfate (gypsum, near $1.45, 1.76, 1.94\mu\text{m}$) with some influence from silica near $2.25\mu\text{m}$ and silicic acid near 0.98 and $1.19\mu\text{m}$ (**Figure 5-2F**). The VNIR reflectance features of the Group 3 spectrum are consistent with Ca-sulfate (gypsum or bassanite, near $1.45, 1.93\mu\text{m}$) in the VNIR with opal likely as well due to the broadness of these bands, lack of $1.76\mu\text{m}$ feature, and the presence of a feature near $2.25\mu\text{m}$ (**Figure 5-2G**). The last group exhibits influence from silica and Fe-oxide in the MIR. The VNIR reflectance signature for Group 4 is also consistent with adsorbed water bands observed for hydrated silica ($1.16, 1.45, 1.76, 1.93\mu\text{m}$) and Fe-oxide (near $0.96\mu\text{m}$). Akaganéite provided the best match from the Fe-oxide library spectra used in this study, as it contains characteristic Fe^{+3} absorptions near $0.44, 0.59$ (shoulder), and $0.92\mu\text{m}$ [Bishop *et al.*, 2015]; however, we did not observe the expected H_2O band near $1.95\text{-}2.0\mu\text{m}$ or OH band near $2.46\mu\text{m}$, so akaganéite cannot be a dominant component. This sample also may display influence from Fe^{+2} -sulfate (melanterite) and/or Fe^{+3} -sulfate (copiapite, jarosite) near $0.44\mu\text{m}$ (**Figure 5-2H**).

Linear least squares analysis was used to model the averaged MIR emission spectra for each group. A full table of the modeling results is available in the Appendix (**Appendix Table**

A5). The phases listed as minor are below the detection limits of this method and may not be present. The MIR Group 1-1 also had a silica-dominated modeled assemblage, but lower amounts of sulfate and minor Fe-oxide were used by the model to improve the fit (**Figure 5-3A**). The shallowed silica features exhibited by MIR Group 1-2 also resulted in a silica-dominated modeled assemblage, but with influence from sulfate, clay, and minor sulfur (**Figure 5-3B**). The relatively poor fits for Groups 1-3 and 1-4 indicate non-linear mixing likely due to small particle sizes, discussed further in **Section 4.1**, and poorly crystalline components. An Fe⁺³-sulfate-Al-sulfate-dominated modeled assemblage (**Figure 5-3C**) was observed for Group 1-3, contrasting the silica-dominated grouping. The shifted silica features observed for MIR Group 1-4 still produced a silica-dominated modeled assemblage, but with influence from Fe-oxide and sulfur (**Figure 5-3D**). The modeled spectrum for MIR Group 2 resulted in a Ca-sulfate-dominated assemblage with influence from silica (**Figure 5-3E**). The Fe⁺³-sulfate-dominated model fit for MIR Group 3 is relatively poor, as with Groups 1-3 and 1-4 and is likely influenced by particle size effects (**Figure 5-3F**). Last, the modeled assemblage for the MIR Group 4 is dominated by silica and Fe-oxide with influence from sulfate (**Figure 5-3G**), consistent with the silica/Fe-oxide-dominated grouping.

5.3.2 Chemical and Mineralogical Analyses

SEM analyses were only acquired for the HI_15_MHY samples and thus only these samples are discussed (no data was collected for Group 1-3 or Group 3) using secondary electron images. The Group 1-1 samples all exhibit similar silica-dominated surfaces (**Figure 5-4A-C**). The surface of HI_15_MHY_001 is characterized by a Si-rich leached coating, overlying a glass with considerable Al, Ca, Mg, and Fe (**Figure 5-4A**). HI_15_MHY_002a is also dominated by a Si-rich coating (**Figure 5-4B**), with some Fe-sulfates and Ca-sulfates observed sparsely. A Si-Ti-Fe-rich surface coating is also observed, but is not as pervasive as the Si-rich surface. A Si-rich

surface is also observed for HI_15_MHY_002b, overlying a glass similar to that observed for HI_15_MHY_001 (**Figure 5-4C**). The samples from Group 1-2 also exhibit a Si-rich coating, but are consistent with other materials (**Figure 5-4D-E**). HI_15_MHY_003 has a Si-rich surface, with Ca-sulfate present in some areas (**Figure 5-4D**). HI_15_MHY_005 has a Si-rich surface with Fe-Ti-oxides and Ca-sulfate deposited on top (**Figure 5-4E**). The surface of the only sample from Group 1-4, HI_15_MHY_007a, is characterized by Si-rich material and Ca-sulfate (**Figure 5-4F**). With Group 2, the surfaces are less dominated by silica compared to Group 1. HI_15_MHY_007b exhibits centimeter sized clasts of Si-rich material (**Figure 5-4G**) and Ca-sulfates (**Figure 5-4H**). For Group 4, the surface of HI_15_MHY_006 is characterized by Si-rich material overlain considerably by Fe-Ti-oxides (**Figure 5-4I**).

The results from the XRD analyses are listed in **Table 5-2**. Generally, amorphous material +/- crystalline silica was observed for all of these samples. The amorphous material could indicate glass, silica, allophane, imogolite, or other amorphous materials which result in a characteristic hump in the XRD pattern. Crystalline silica is referring to crystalline polymorphs of SiO₂ (e. g., tridymite, cristobalite) which have distinct XRD peaks. Small amounts of additional phases were observed for Group 1-2 (bixite, Fe-oxides, zeolites, K-sulfate), Group 1-3 (Fe-oxides), and Group 2 (Ca-sulfate, sulfur). The XRD patterns for all of these samples exhibited broad features consistent with an amorphous material such as amorphous silica, allophane and/or basaltic glass. For three samples, the center position of the broad diffraction hump was shifted to lower 2-theta values (~23 2-theta), indicating material that is more Si rich than pure basaltic glass (**Figure 5-5**). No halite was observed in these samples.

The XRF data has been separated into 3 groups based on chemical similarities determined using a minimum distance clustering algorithm on handheld XRF chemical data for each sample

(**Figure 5-6A**). This independent XRF-based grouping was done in order to compare how/if element-based compositional variability corresponds with spectrally-determined variability. Chemical variations are most strongly driven by abundances of Si, Fe, and lesser by Al and Ca. The abundance of Si is negatively correlated with Fe, Al, and Ca. The XRF Group 1 consists of samples HI_15_Solf_002_3 (MIR Group 1-3) and HI_15_Solf_003_2 (MIR Group 1-2) and displays relatively higher enrichment in Si and lower enrichment in Ca and Fe compared to the other groups. XRF Group 2 exhibits medium enrichment in Si, Fe, Al, and Ca and includes samples from MIR Group 1-1 (HI_15_MHY_001, HI_15_MHY_002a), Group 1-2 (HI_15_MHY_003, HI_15_MHY_005, HI_15_Solf_003_3), Group 1-4 (HI_15_MHY_007a), and Group 4 (HI_15_MHY_006). The XRF Group 3 includes samples from MIR Group 1-1 (HI_15_Solf_001_1, HI_15_Solf_002_1), Group 1-3 (HI_15_Solf_001_2), and Group 3 (HI_15_Solf_002_2) which display relatively low enrichment in Si, and high enrichment in Al, Ca, and Fe. The Al vs. Si and Fe vs. Si plots (**Figure 5-6B-C**) display the negative correlations that were observed by the minimum distance clustering. These plots also indicate that the XRF compositional groupings of samples are not the same as the previous MIR groups, although there are some similarities.

5.4 Discussion

5.4.1 Spectral Detectability

Overall, the surfaces of the hydrothermally altered samples analyzed here are characterized by silica-rich material +/- Fe-oxides and Ca-sulfate, based on chemical and mineralogical analyses (**Table 5-2**). Several XRD patterns exhibited amorphous humps centered near $24\ 2\theta$; this position is consistent with an amorphous material that is more Si rich than basaltic glass (**Figure 5-5**). Silica-rich materials generally have a narrower hump centered at lower positions near $25\ 2\theta$,

whereas basaltic glass generally has a broader hump centered at higher positions, near $31\ 2\theta$, [Morris *et al.*, 2015]. This is consistent with MIR/VNIR data that showed amorphous silica contributed to the spectral shape for all samples. Although both the MIR/VNIR and handheld XRF data are detecting strong enrichments in Si or Si-bearing phases, compositional groupings of samples using each technique are not well correlated. This could be due to the sensitivity of the handheld XRF to chemical changes versus MIR/VNIR spectroscopy which are sensitive to mineral species and abundance. Likewise, minor alteration phases observed on sample surfaces in SEM images are often not exhibited in the XRD data due to the small contribution of the surface material to the bulk sample.

In general, the dominant surface phases are clearly identified in the VNIR and MIR spectral signatures; however, for some samples, the spectral models include large abundances of phases that are absent in SEM data. For example, the surfaces of samples HI_15_MHY_001 and HI_15_MHY_002b (Group 1-1) are both characterized by a silica coating based on SEM analysis (**Figure 5-4A,C**). However, in the MIR additional phases (sulfates and Fe-oxides) are needed in order to provide the best fit to the sample spectra (**Figure 5-3A**). In addition, phyllosilicates (montmorillonite, Fe/Al-smectite) are included in the modeled assemblage for Group 1-2 (**Figure 5-3B**) when none was observed on any of the sample surfaces. This phenomenon, as well as the poor fits to some of the modeled spectra (e.g., MIR Group 3), are likely due to the fine-grained nature of the weathered surfaces. Volume scattering and transmission through small grains or thin coatings can give rise to spectral features that are not well modeled by library spectra of pure, coarse-grained phases.

Differences in grain size also appears to be a major factor in the spectral differences between the samples in the MIR silica-dominated group (Group 1). SEM data was only collected

for the HI_15_MHY samples and thus only these samples are discussed. The samples with the deepest features (Group 1-1; HI_15_MHY_001, 002a, and 002b) all have continuous silica coatings with little to no fine-grained surface material (**Figure 5-4A-C**). However, the samples with shallow silica features (Group 1-2, 1-4; HI_15_MHY_003, 005, 007a) have finer-grained surfaces (**Figure 5-4D-F**), and HI_15_MHY_005 and HI_15_MHY_007a also have numerous cavities. Additionally, the shallow silica features could be due to a relatively low abundance of silica-rich material due the presence of oxides and sulfates.

The variations observed between the subgroups of the silica-dominated MIR emission spectra appear to be correlated with distance from the volcanic vent. The distance was only measured for the HI_15_MHY samples and thus only these are discussed. The purest silica features were exhibited by the material farthest from the vent (Group 1-1, 19.0 – 18.0m) with shallowing of silica features in the intermediate material (Group 1-2, 11.5m – 4.7m), and shifting of features in the material closer to the vent (Group 1-4, 4.5m). The material collected closest to the vent exhibited sulfate-dominated features (Group 2, 4.5m and Group 3, 4.0m). Unfortunately, no fluid or gas measurements were available, and interpretation of the influence of changing gas composition cannot be determined at this time. The presence of sulfates could be due to a greater supply of sulfur near the vent, contributing to the formation of sulfates in the material closest to the vent or due to easier removal of mobile cations farther from the vent. The nature of the sample coating also appears to change with distance from the vent. Materials that exhibit leached surfaces are observed farther away from the vent (Group 1-1, 19.5 – 18.0 m, **Figure 5-1B-C**) and may represent passive silica enrichment from removal of other elements during weathering [e.g., *Morris et al.*, 2008; *Yen et al.*, 2008]. Generally, thicker silica encrustations are observed on samples located closer to the vent (Groups 1-2, 1-3, 1-4, 2, 3, and 4, 11.5 – 4.0 m, **Figure 5-1D-I**) and may

partially result from silica precipitated during low water-to-rock aqueous alteration of the basalts by acidic aerosols supplied by the vent [e.g., *Ruff et al.*, 2011]. Furthermore, the shift of the silica feature from 1115cm^{-1} to 1100cm^{-1} observed in the Group 1-4 MIR spectra could be due to Al-substitution for Si. This could be expected in the samples observed here, as Al (along with Si and Fe^{+3}) has increased solubility under acidic conditions [*Hurowitz et al.*, 2006].

Many of the samples exhibited low abundances of Fe-oxides and sulfates in addition to silica in the chemical analyses (HI_15_MHY_002a, 003, 005, 006, 007a, 007b, HI_15_Solf_003_3, **Table 5-2**). Although these low-abundance materials were not easily identifiable in many of the MIR signatures (**Figure 5-2**) they were commonly distinguished in the VNIR range. The differences observed between the MIR and VNIR signatures are attributed to differences in mineral transparency between these two techniques and the nature of the alteration material. Some samples exhibit powdery surfaces that result in multiple surface scattering and reduced restrahten features in the MIR [*Hunt and Vincent*, 1968; *Salisbury and Wald*, 1992; *Mustard and Hays*, 1997], making it difficult to identify lower abundance phases. In addition, the fine grains and thin coatings that comprise the alteration material permit energy transmission through the grains/coatings [e.g., *Hunt and Logan*, 1972; *Clark and Roush*, 1984]. This effect is enhanced in the VNIR due to the lower absorption coefficients in this range and increased importance of volume scattering [*Salisbury and Wald*, 1992]. This allows small abundance phases to be more easily detected in the VNIR and these may dominate the spectral properties.

The alteration phases observed here provide similar results to the previous works in **Table 5-1**. Here we observed MIR signatures dominated by silica and VNIR signatures influenced by silica, sulfate(s), and Fe-oxide(s). The phyllosilicate phases detected by *Golden et al.* [1993], *Morris et al.* [2000a], *Schiffman et al.* [2000], *Bishop et al.* [2007], and *Hamilton et al.* [2008]

were only observed using linear least squares modeling of the MIR data for Group 1-2 in abundances $\leq 10\%$. Our results agree with the environmental conditions suggested by *Schiffman et al.* [2000] which attribute the development of opaline crusts to acidic conditions (pH <6) and clay mineral formation to more neutral conditions (pH 6.5 – 7.8).

The global abundance and species of chemical alteration products on planetary surfaces are related to the starting composition of unaltered protolith, the style and duration of alteration processes, the fluid composition, the fluid-to-rock ratio [e.g., *Tosca et al.*, 2004; *Golden et al.*, 2005; *Ming et al.*, 2006], and ultimately, to the preservation of those products in rocks and soils. Thus, detection and interpretation of alteration mineral assemblages is critical to deciphering the history of the Mars. However, amorphous material often forms as a product from the alteration of volcanic material and can cause difficulty in identifying additional alteration phases and obtaining quantitative abundances of alteration phases. Amorphous phases are an important component on Mars and have been observed in several occurrences by the Chemistry and Mineralogy Instrument (CheMin) onboard Curiosity [e.g., *Bish et al.*, 2013]. The presence of amorphous material was determined based on the appearance of a broad, diffuse peak rather than the narrow diagnostic peaks of well crystalline phases. This provides a challenge for identification because these phases lack long-range crystallographic order so analyses that depend on crystal structure (e.g., XRD) are non-unique. The fumarolic materials in this study may provide an analog for some of the amorphous phases on Mars, and the distinctive Si-rich features observed show that the addition of MIR/VNIR data helps to distinguish some of those materials.

5.4.2 Hydrothermal Alteration on Mars

MIR and VNIR spectral analyses of hydrothermally altered Hawaiian basalts are presented here in order to enhance the understanding of the IR spectral properties of weathered materials.

The spectral shapes of the signatures acquired in this study can be applied to VNIR and MIR spectral data obtained from Mars in order to better constrain variability of weathering on a global scale. Based on our results, silica detections across both wavelength ranges are common from fumarolic alteration. However, we note that silica deposits are not limited to high-temperature and/or fumarolic processes [e.g., *McLennan, 2003; McAdam et al., 2008*]. For example, silica can form through acid fog weathering of basalt, with low water-to-rock ratios under near isochemical conditions [*Tosca et al., 2004*]. Based on a number of chemical and mineralogical measurements made by landed missions [*Clark, 1993; Haskin et al., 2005; Ming et al., 2006; Clark et al., 2005; Morris et al., 2006*], an acid fog environment has been proposed as a common and persistent alteration setting on the Martian surface [*Hurowitz and McLennan, 2007; Hurowitz and Fischer, 2014*]. Thus, it is useful to compare the spectral properties of silica-bearing samples from this fumarolic environment to those formed in a closed-system acid sulfate environment. Below, we compare the spectral characteristics of our samples to those from a previous study in which basaltic glass was subjected to low-temperature, isochemical weathering under low water-to-rock ratios [*Yant et al., 2016*].

In a previous study, sand-sized synthetic Martian glass particulates were submerged in sulfuric-hydrochloric acidic solutions (pH 0-4) under low fluid-to-rock ratios (1:1) at ambient temperature and pressure [*Yant et al., 2016*]. This system simulates an acid-fog environment which is considered closed due to the very low fluid-to-rock ratios. We use a laboratory environment because of the difficulty in determining how long a natural environment has been closed. In general, acid alteration on particles resulted in sulfate-dominated assemblages in the most acidic solutions (pH \leq 1) that exhibited well-developed sulfate features, in the MIR, and strong 1.45, 1.95, and 2.40 μ m features in the VNIR. Amorphous silica was present based on chemical analyses, but

not as detectable in the MIR/VNIR spectra. The results from *Yant et al.* [2016] contrast significantly with the silica-dominated assemblages observed for the majority of the samples in this study (**Figure 5-7**).

The likely reason for the observed differences relates to open vs. closed system weathering. Sulfates, Fe-oxides, and silica are commonly identified as alteration products in Martian analog studies (**Table 5-1**), and when present on the surface of substrates each contribute uniquely to the visual appearance and MIR/VNIR spectral signatures observed for these materials. In closed system weathering, as simulated by *Yant et al.* [2016], small volumes of acidic fluid react with the surface of the material resulting in a fluid enriched in the most soluble elements. A leached alteration rind, depleted in the most soluble elements, is left behind, and the fluid subsequently undergoes evaporation and deposits alteration minerals. Si^{+4} is relatively insoluble in low pH conditions ($\text{pH} < 2-3$) and basaltic cations are relatively mobile [e.g., *El-Shamy et al.*, 1972; *Minitti et al.*, 2007]. This can result in basalt leaching or dissolution that could form a silica-enriched layer beneath the fluid containing the mobile cations. When the fluid is evaporated, in a closed system, salts containing the more mobile cations can precipitate on top of the silica-enriched layer. The formation of the sulfates overlying the silica layer results in a larger spectral signal from the sulfates relative to the silica. In order to form a sulfate-dominated assemblage, the fluid-to-rock ratio needs to be small enough that the soluble elements are not mobilized and are allowed to precipitate on top of the leached surface in a closed system [*Hurowitz et al.*, 2006]. Additionally, sulfates that are precipitated over a diffuse area can be remobilized by dew and/or rain, whereas silica coatings are less soluble and less likely to be removed.

If the system is open and the fluid can migrate, a silica or Fe-oxide-dominated assemblage can be formed [*Dorn*, 2012; *Chemtob and Rossman*, 2014]. *Chemtob and Rossman* [2014] describe

the formation of silica coatings on glassy basalts from Hawaii through reaction of acidic fluids in an open system using the following model. Fresh rock surfaces are wetted by rainwater or condensed water vapor. The fluid becomes acidified by volcanically derived liquids and reaction with this low pH fluid results in dissolution of the basalt. The basaltic cations are more soluble than the silica and the cations remain dissolved at low pH and the silica is precipitated in place. The fluid is mobilized carrying away the more soluble cations, leaving behind Ti and Fe⁺³, which have lower mobility and are deposited as Fe-Ti-oxides, in addition to the silica. *Chemtob and Rossman* [2014] suggest that this mobilization is facilitated by liquid water, possibly sourced from rainwater and condensed water vapor from nearby plumes. Silica can also be transported to the surface by fluids that penetrate to the interior of the basalt. As alteration continues over a period of years, episodes of dissolution-reprecipitation can result in the thickening of the silica layer and the remobilization of Fe and Ti to the surface, producing silica or Fe-oxide-dominated spectral signatures like those observed here. Additionally, Al behaves in a manner similar to Fe⁺³ and exhibits increased solubility in acidic conditions [Hurowitz *et al.*, 2006] and could be expected to precipitate under the conditions shown here. Negative correlations were observed between Fe vs. Si and Al vs. Si in the XRF data (**Figure 5-6**) supporting the interpretation that Fe and Al are both precipitating on top of the silica layers. The results shown here for the natural Hawaiian samples are in agreement with the model proposed by *Chemtob and Rossman* [2014].

Surfaces showing silica signatures in the VNIR and MIR provide the best candidates for potential fumarolic deposits. For example, hydrated silica has been identified in several locations through VNIR detections from the Compact Reconnaissance Imaging Spectrometer for Mars (CRISM) at Western Hellas [*Bandfield*, 2008], plains near Melas Chasma and Juventae Chasma [*Milliken et al.*, 2008], Isidis Basin [*Ehlmann et al.*, 2009], Northern Syrtis Major [*Ehlmann et al.*,

2009; *Smith and Bandfield*, 2012], Toro Crater [*Marzo et al.*, 2010], Nili Patera [e.g., *Skok et al.*, 2010], Terra Sirenum [*Wray et al.*, 2011], and Noctis Labyrinthus [*Weitz et al.*, 2011]. Hydrated silica has also been identified in MIR data from the Thermal Emission Spectrometer (TES) and Thermal Emission Imaging System (THEMIS) at Western Hellas Basin [*Bandfield*, 2008] and along the dichotomy boundary [*Bandfield and Amador*, 2016]. Hydrothermal processes have been inferred for most of these regions; however, it is difficult to rule out other origins from orbital data alone. Nevertheless, this work provides strong support for those interpretations.

5.5 Implications:

This work provides a unique IR spectral library that includes Martian analog materials that were altered in an active terrestrial solfatara (hydrothermal) setting. Hydrothermal environments are of particular interest as they potentially indicate habitable conditions. Among the techniques to detect potential hydrothermal/habitable conditions on Mars, visible and IR spectroscopic remote sensing provides the greatest coverage at the highest spatial resolution, allowing for assessment of spatial and/or temporal variability in surface conditions. Key constraints on the habitability and astrobiological potential of ancient aqueous environments are provided through detection and interpretation of secondary mineral assemblages; thus, spectral detection of fumarolic alteration assemblages observed from this study on Mars would suggest a region that could have hosted a habitable environment. Alteration assemblages that were potentially derived from hydrothermal systems have been detected *in situ* on Mars at Gusev Crater and Meridiani Planum. *Kraft et al.* [2003] suggest that secondary amorphous silica may account for the spectral signatures observed for ST2, exhibiting the potential widespread nature of this type of alteration. Using the spectral library provided here, the search for hydrothermal systems on Mars can be extended to other

locations using orbital measurements of reflectance and emission spectra, which are sensitive to mineral species and abundance.

5.6 References:

Anderson, J.H. and K.A. Wickersham (1964), Near infrared Characterization of Water and Hydroxyl Groups on Silica Surfaces, *Surface Science*, 2 251-260.

Arvidson, R. E., et al. (2014), Ancient aqueous environments at Endeavour Crater, Mars, *Science*, 343(6169), 1248097, doi:10.1126/science.1248097.

Baldrige, A. M. (2008), Thermal Infrared Spectral Studies of Sulfates and Chlorides; Applications to Salts on the Martian Surface, Ph.D. Dissertation thesis, 204 pp., Arizona State University, Tempe, AZ.

Baldrige, A.M., P.R. Christensen (2009), Laboratory Technique for Thermal Emission Measurement of Hydrated Minerals: *Applied Spectroscopy*, v. 63, p. 678-688.

Bandfield, J.L. (2008), High-silica deposits of an aqueous origin in western Hellas Basin, Mars. *Geophysical Research Letters*, 35, 142–147. <http://dx.doi.org/10.1029/2008GL033807>.

Bandfield, J. L. and E. S. Amador (2016), Extensive aqueous deposits at the base of the dichotomy boundary in Nilosyrtis Mensae, Mars, *Icarus*, 275, 29–44.

Bell, J III (2008), *The Martian Surface—Composition, Mineralogy, and Physical Properties*. New York: Cambridge University Press.

Bigham, J. M., and D. K. Nordstrom (2000), Iron and aluminum hydroxysulfates from acid sulfate waters, in *Sulfate Minerals: Crystallography, Geochemistry and Environmental Significance*, edited by C. N. Alpers, J. L. Jambor, and D. K. Nordstrom, pp. 351 – 403, Mineral. Soc. Of Am., Washington, D. C.

- Bish, D. L., et al. (2013), X-ray diffraction results from Mars Science Laboratory: Mineralogy of Rocknest at Gale Crater, *Science*, 341.
- Bishop, J. L., and E. Murad (1996), Schwertmannite on Mars? Spectroscopic analyses of schwertmannite, its relationship to other ferric minerals, and its possible presence in the surface material on Mars, in *Mineral Spectroscopy: A Tribute to Roger G. Burns*, edited by M. D. Dyar et al., *Spec. Publ. Geochem. Soc.*, 5, 337–358.
- Bishop, J.L., Schiffman P., Lane M.D., and Dyar M.D. (2005a) Sulfatation alteration in Hawaii as a mechanism for formation of the sulfates observed on Mars by OMEGA and the MER instruments. Lunar and Planetary Science Conference, XXVI, LPI, Houston, Abstract #1456.
- Bishop, J.L., Dyar M.D., Lane M.D., and Bandfield J.F. (2005b), Spectral identification of hydrated sulfates on Mars and comparison with acidic environments on Earth. *International Journal of Astrobiology*, 3, 275-285.
- Bishop, J.L., P. Schiffman, E. Murad, M.D. Dyar, A. Drief, M.D.
- Bishop, J.L., P. Schiffman, E. Murad, M.D. Dyar, A. Drief, M.D. Lane (2007), Characterization of alteration products in tephra from Haleakala, Maui: a visible-infrared spectroscopy, Mössbauer spectroscopy, XRD, EMPA and TEM study *Clay Clay Miner.*, 55 (1), pp. 1-17.
- Bishop, J.L., Noe Dobrea E.Z., McKeown N.K., Parente M., Ehlmann B.L., Michalski J.R., Milliken R.E., Poulet F., Swayze G.A., Mustard J.F., Murchie S.L., and Bibring J.-., P. (2008) Phyllosilicate diversity and past aqueous activity revealed at Mawrth Vallis, Mars. *Science*, 321, 830-833.
- Bishop, J.L., Lane M.D., Dyar M.D., King S.J., Brown A.J., and Swayze G. (2014), Spectral properties of Ca-sulfates: Gypsum, bassanite and anhydrite. *American Mineralogist*, 99, 2105-2115.

- Bishop, J. L., E. Murad, and M. D. Dyar (2015), Akaganéite and schwertmannite: Spectral properties and geochemical implications of their possible presence on Mars, *American Mineralogist*, 100(4), 738–746.
- Burns R.D., D.S. Fisher (1990), Iron–sulfur mineralogy of Mars: magmatic evolution and chemical weathering products, *J. Geophys. Res.*, 95 pp., 14415–14421.
- Chemtob, S.M, G.R. Rossman (2014), Timescales and mechanisms of formation of amorphous silica coatings on fresh basalts at Kīlauea Volcano, Hawai'i, *Journal of Volcanology and Geothermal Research*, Volume 286, 1 October 2014, Pages 41-54, ISSN 0377-0273.
- Chemtob, S.M., Jolliff, B.L., Rossman, G.R., Eiler, J.M., Arvidson, R.E., (2010), Silica coatings in the Ka'u Desert, Hawaii, a Mars analog terrain: a micromorphological, spectral, chemical, and isotopic study. *Journal of Geophysical Research*, 115, E04001.
- Christensen, P.R., J. L. Bandfield, R. N. Clark, K. S. Edgett, V. E. Hamilton, T. Hoefen, H. H. Kieffer, R. O. Kuzmin, M. D. Lane, M. C. Malin, R. V. Morris, J. C. Pearl, R. Pearson, T. L. Roush, S. W. Ruff, and M. D. Smith (2000), Detection of crystalline hematite mineralization on Mars by the Thermal Emission Spectrometer: Evidence for near-surface water. *Journal of Geophysical Research*, 105:9623–9642.
- Clark, B. C. (1993), Geochemical components in Martian soil. *Geochimica et Cosmochimica Acta*, 57, 4575–4581.
- Clark, B.C., R.V. Morris, S.M. McLennan, R. Gellert, B. Jolliff, A.H. Knoll, S.W. Squyres, T.K. Lowenstein, D.W. Ming, N.J. Tosca, A. Yen, P.R. Christensen, S.P. Gorevan, J. Brückner, W.M. Calvin, G. Dreibus, W.H. Farrand, G. Klingelhöfer, H. Waenke, J. Zipfel, J.F. Bell III, J.P. Grotzinger, H.Y. McSween Jr., R. Rieder (2005), Chemistry and mineralogy of outcrops at Meridiani Planum, *Earth and Planetary Science Letters*. 240, 73-94.

- Clark, R. N., and T. L. Roush (1984), Reflectance spectroscopy: Quantitative analysis techniques for remote sensing applications, *Journal of Geophysical Research*, 89(B7), 6329–6340, doi:10.1029/JB089iB07p06329.
- Cloutis, E.A., Hawthorne, F.C., Mertzman, S.A., Krenn, K., Craig, M.A., Marcino, D., Methot, M., Strong, J., Mustard, J.F., Blaney, D.L., Bell III, J.F., Vilas, F. (2006), Detection and discrimination of sulfate minerals using reflectance spectroscopy. *Icarus* 184, 121-157. doi:10.1016/j.icarus.2006.04.003
- Costello E.K. Halloy S.R.P. Reed S.C. Sowell P. Schmidt S.K. (2009), Fumarole-supported islands of biodiversity within a hyperarid, high-elevation landscape on Socompa Volcano, Puna de Atacama, Andes. *Applied Environmental Microbiology*, 2009; 75:735–747.
- Crisp, J., Kahle, A.B., Abbott, E.A. (1990), Thermal infrared spectral character of Hawaiian basaltic glasses. *Journal of Geophysical Research*, 95, 21657 – 21669.
- Dorn, R.I. (2012), Formation of silica glaze rock coatings through water vapor interactions. *Physical Geography*, 33 (1), 21–31.
- Ehlmann, B. L., et al. (2009), Identification of hydrated silicate minerals on Mars using MRO-CRISM: Geologic context near Nili Fossae and implications for aqueous alteration, *Journal of Geophysical Research*, 114, E00D08, doi:10.1029/2009JE003339.
- Ellis D.G., Bizzoco R.W., Kelley S.T. (2008), Halophilic Archaea determined from geothermal steam vent aerosols. *Environmental Microbiology*, 10:1582–1590.
- El-Shamy, T. M., J. Lewins, and R. W. Douglas (1972), The dependence of the pH on the decomposition of glasses by aqueous solutions, *Journal of the Society of Glass Technology*, 13(3), 81 – 87.

- Fischer, E.M., Pieters, C.M. (1993), The continuum slope of Mars: bidirectional reflectance investigations and applications to Olympus Mons. *Icarus* 102, 185–202.
- Glotch, T.D., R.V. Morris, P.R. Christensen, T.G. Sharp (2004), Effect of precursor mineralogy on the thermal infrared emission spectra of hematite: application to Martian hematite mineralization. *Journal of Geophysical Research*, 109.
- Glotch, T. D., and M. D. Kraft (2008), Thermal transformations of akaganéite and lepidocrocite to hematite: Assessment of possible precursors to Martian crystalline hematite, *Physics and Chemistry of Minerals*, 35, 569-581.
- Golden et al. (1993), Mineralogy of three slightly palagonitized basaltic tephra samples from the summit of Mauna Kea, Hawaii. *JGR* 98, 3401-3411.
- Golden, D. C., D. W. Ming, R. V. Morris, and S. A. Mertzman (2005), Laboratory-simulated acid-sulfate weathering of basaltic materials: Implications for formation of sulfates at Meridiani Planum and Gusev crater, Mars, *J. Geophys. Res.*, 110, E12S07.
- Goryniuk, M.C., Rivard, B.A., Jones, B. (2004), The reflectance spectra of opal-A (0.5-25 μm) from the Taupo Volcanic Zone: Spectra that may identify hydrothermal systems on planetary surfaces. *Geophys. Res. Lett.* 31, n/a-n/a. doi:10.1029/2004GL021481
- Halloy S. (1991), Islands of life at 6000 m altitude—the environment of the highest autotrophic communities on Earth (Socompa Volcano, Andes) *Arctic and Alpine Research.*;23:247–262.
- Horgan, B., and J. F. Bell III (2012), Widespread weathered glass on the surface of Mars, *Geology*, 40(5), 391–394.
- Hamilton, V. E., R. V. Morris, J. E. Gruener, and S. A. Mertzman (2008), Visible, near-infrared, and middle infrared spectroscopy of altered basaltic tephra: Spectral signatures of

- phyllosilicates, sulfates, and other aqueous alteration products with application to the mineralogy of the Columbia Hills of Gusev Crater, Mars: *Journal of Geophysical Research-Planets*, v. 113, p. E12S43.
- Haskin L.A., et al. (2005), Water alteration of rocks and soils on Mars at the Spirit rover site in Gusev crater. *Nature*, 436, 66-69.
- Hunt, G. R. and L. M. Logan (1972), Variation of Single Particle Mid-Infrared Emission Spectrum with Particle Size, *Appl. Opt.* 11, 142-147.
- Hunt, G. R., and R. K. Vincent (1968), The behavior of spectral features in the infrared emission from particulate surfaces of various grain sizes, *Journal of Geophysical Research*, 73(18), 6039–6046, doi:10.1029/JB073i018p06039.
- Hurowitz, J. A., and W. W. Fischer (2014), Contrasting styles of water–rock interaction 862 at the Mars Exploration Rover landing sites, *Geochimica et Cosmochimica Acta*, 127, 863 25-38.
- Hurowitz, J. A., S. M. McLennan, N. J. Tosca, R. E. Arvidson, J. R. Michalski, D. W. Ming, C. Schröder, and S. W. Squyres (2006), In situ and experimental evidence for acidic weathering of rocks and soils on Mars, *Journal of Geophysical Research*, 111, E02S19.
- Hurowitz, J.A and S.M. McLennan (2007), A ~ 3.5 Ga record of water-limited, acidic weathering conditions on Mars, *Earth and Planetary Science Letters*, Volume 260, Issues 3–4, 30 August 2007, Pages 432-443, ISSN 0012-821X.
- Kraft et al. (2003), Effects of pure silica coatings on thermal emission spectra of basaltic rocks: Considerations for Martian surface mineralogy, *GRL* 30, 2288.

- Kraft, M. D., T. G. Sharp, J. R. Michalski, and E. B. Rampe (2007), Combined Thermal and Near Infrared Spectra of Hydrous Silica Coatings: Implications for Surface Type 2 Mineralogy and Recent Liquid Water on Mars: *Lunar Planet. Sci.* XXXVIII.
- Lane, M.D. (2007), Mid-infrared emission spectroscopy of sulfate and sulfate-bearing minerals. *American Mineralogist*, 92, pp. 1–18.
- Lane, M.D., J.L. Bishop, M.D. Dyar, T.H. Hiroi, S.A. Mertzman, D.L. Bish, P.L. King, and A.D. Rogers (2015), Mid-infrared emission spectroscopy and visible/near-infrared reflectance spectroscopy of Fe-sulfate minerals. *American Mineralogist*, 100, pp. 66-82.
- Lichtenberg, K. A., R.E. Arvidson, R.V. Morris, S.L. Murchie, J.L. Bishop, D.F. Remolar, T.D. Glotch, E.N. Dobra, J.F. Mustard, J. Andrews-Hanna, and L.H. Roach (2010), Stratigraphy of hydrated sulfates in the sedimentary deposits of Aram Chaos, Mars, *Journal of Geophysical Research*, 115, E00D17.
- Madden M. E., R. J. Bodnar and J. D. Rimstidt (2004), Jarosite as an indicator of water-limited chemical weathering on Mars. *Nature* 431, 821–823.
- Marzo, G.A. et al. (2010), Evidence for Hesperian impact-induced hydrothermalism on Mars. *Icarus*, 208, 667–683.
- McAdam, A. C., M. Y. Zolotov, M. V. Mironenko, and T. G. Sharp (2008), Formation of silica by low-temperature acid alteration of Martian rocks: Physical-chemical constraints, *Journal of Geophysical Research*, 113, E08003, doi:10.1029/2007JE003056.
- McCanta, M.C., M.D. Dyar, and A.H. Treiman (2014), Alteration of Hawaiian basalts under sulfur-rich conditions: Applications to understanding surface–atmosphere interactions on Mars and Venus. *American Mineralogist*, 99, pp. 291–302.

- McCollom, T. M., and B. M. Hynek (2005), A volcanic environment for bedrock diagenesis at Meridiani Planum, Mars, *Nature*, 438, 1129-1131.
- McKeown, N.K., J.L. Bishop, J. Cuadros, S. Hillier, E. Amador, H.D. Makarewicz, M. Parente, and E.A. Silver (2011), Interpretation of reflectance spectra of clay mineral-silica mixtures; implications for Martian clay mineralogy at Mawrth Vallis, *Clays and Clay Minerals*, v. 59, p. 400-415, doi: 10.1346/CCMN.2011.0590404.
- McLennan, S. M. (2003), Sedimentary silica on Mars, *Geology*, 31(4), 315 – 318, doi:10.1130/0091-7613(2003)0312.0.CO;2.
- Michalski, J. R., M. D. Kraft, T. G. Sharp, and P. R. Christensen (2006), Effects of chemical weathering on infrared spectra of Columbia River Basalt and spectral interpretations of martian alteration: *Earth and Planetary Science Letters*, v. 248, p. 822-829.
- Milliken, R.E. et al. (2008), Opaline silica in young deposits on Mars. *Geology*, 36, 847– 850. <http://dx.doi.org/10.1130/G24967A.1>.
- Ming D. W., D. W. Mittlefehldt, R. V. Morris, D. C. Golden, R. Gellert, A. Yen, B.C. Clark, S. W. Squyres, W. H. Farrand, S. W. Ruff, R. E. Arvidson, G. Klingelhöfer, H. Y. McSween, D. S. Rodionov, C. Schröder, P. A. de Souza, and A. Wang (2006), Geochemical and mineralogical indicators for aqueous processes in the Columbia Hills of Gusev crater, Mars. *Journal of Geophysical Research*, 111, E02S12.
- Minitti, M. E., C. M. Weitz, M. D. Lane, and J. L. Bishop (2007), Morphology, chemistry, and spectral properties of Hawaiian rock coatings and implications for Mars, *Journal of Geophysical Research*, 112, E05015, doi:10.1029/2006JE002839.
- Morris, R. V., H. V. Lauer Jr., C. A. Lawson, E. K. Gibson Jr., G. A. Nace, and C. Stewart (1985), Spectral and other physicochemical properties of submicron powders of

- hematite (α -Fe₂O₃), maghemite (γ -Fe₂O₃), magnetite (Fe₃O₄), goethite (α -FeOOH), and lepidocrocite (γ -FeOOH), *J. Geophys. Res.*, 90, 3126–3144.
- Morris, R. V., et al. (2006), Mössbauer mineralogy of rock, soil, and dust at Gusev crater, Mars: Spirit's journey through weakly altered olivine basalt on the plains and pervasively altered basalt in the Columbia Hills, *Journal of Geophysical Research*, 111, E02S13.
- Morris, R. V., D.C. Golden, J.F. Bell III, T.D. Shelfer, A.C. Scheinost, N.W. Hinman, G. Furniss, S.A. Mertzman, J.L. Bishop, D.W. Ming, C.C. Allen, D.T. Britt (2000a), Mineralogy, composition and alteration of Mars Pathfinder rocks and soils: Evidence from multispectral, elemental and magnetic data on terrestrial analogue, SNC meteorite and Pathfinder samples, *Journal of Geophysical Research*, 105, 1757– 1817.
- Morris, R. V., T. Graff, M. D. Lane, D. C. Golden, C. S. Schwandt, D.W. Ming, T.D. Shelfer, S. A. Mertzman, J. F. Bell, J. Crisp, and P. R. Christensen (2000b), Acid sulfate alteration products of a tholeiitic basalt: Implications for interpretation of Martian thermal emission spectra, *Lunar and Planetary Science Conference*, XXXI, Abs. 2014.
- Morris, R.V., et al. (2005), Hematite spherules in basaltic tephra altered under aqueous, acid-sulfate conditions on Mauna Kea volcano, Hawaii: Possible clues for the occurrence of hematite-rich spherules in the Burns formation at Meridiani Planum, Mars, *Earth and Planetary Science Letters*, 240, 168-178.
- Morris, R. V. et al. (2008), The hydrothermal system at Home Plate in Gusev crater, Mars: Formation of high silica material by acid-sulfate alteration of basalt. *Lunar and Planetary Science Conference*, XXIX, Abs. 2208.

- Morris, R.V., E.B. Rampe, T.G. Graff, et al. (2015) Transmission X-ray diffraction (XRD) patterns relevant to the MSL CheMin amorphous component: sulfates and silicates. Lunar and Planetary Science Conference, XXVI, Abs. #2434.
- Mustard, J. F., and J. E. Hayes (1997), Effects of hyperfine particles on reflectance spectra from 0.3 to 25 μm , *Icarus*, 125, 145–163.
- Niles P. B. and Michalski J. (2009), Meridiani Planum sediments on Mars formed through weathering in massive ice deposits. *Nat. Geosci.* 2, 215–220.
- Rampe, E. B., M. D. Kraft, and T. G. Sharp (2009), Chemical Weathering Trends from TIR Spectral Models: Implications for Deriving Weathering Trends From Martian Spectral Data, LPSC XL, Abs. 2132.
- Ramsey, M.S., P.R. Christensen (1998), Mineral abundance determination: Quantitative deconvolution of thermal emission spectra. *Journal of Geophysical Research*, 103 (B1), 577–597.
- Rice, M. S., E. A. Cloutis, J. F. Bell III, D. L. Bish, B. H. Horgan, S. A. Mertzman, M. A. Craig, R. W. Renaut, B. Gautason, and B. Mountain (2013), Reflectance spectra diversity of silica-rich materials: Sensitivity to environment and implications for detections on Mars, *Icarus*, 223(1), 499–533, doi:10.1016/j.icarus.2012.09.021.
- Rogers, A.D., Aharonson, O. (2008), Mineralogical composition of sands in Meridiani Planum determined from MER data and comparison to orbital measurements. *Journal of Geophysical Research – Planets*, 113, E06S14.
- Ruff, S. W., P. R. Christensen, P. W. Barbera, and D. L. Anderson (1997), Quantitative thermal emission spectroscopy of minerals: A laboratory technique for measurement and calibration, *Journal of Geophysical Research* 102, 14899–14913, doi:10.1029/97JB00593.

- Ruff, S. W., J.D. Farmer, W.M. Calvin, K.E. Herkenhoff, J.R. Johnson, R.V. Morris, M.S. Rice, R.E. Arvidson, J.F. Bell III, P.R. Christensen, and S.W. Squyres (2011), Characteristics, distribution, origin, and significance of opaline silica observed by the Spirit rover in Gusev crater, Mars, *J. Geophys. Res.*, 116, E00F23.
- Salisbury, J. W., and A. Wald (1992), The role of volume scattering in reducing spectral contrast of Reststrahlen bands in spectra of powdered minerals, *Icarus*, 96, 121-128.
- Schiffman, P., Spero, H.J., Southard, R.J., Swanson, D.A., (2000), Controls on palagonitization versus pedogenic weathering of basaltic tephra: Evidence from the consolidation and geochemistry of the Keanakako'i Ash Member, Kilauea Volcano. *Geochemistry, Geophysics, Geosystems*, 1, 1040.
- Schiffman, P., Zierenberg, R., Marks, N., Bishop, J.L., Dyar, M.D., (2006), Acid-fog deposition at Kilauea volcano: A possible mechanism for the formation of siliceous-sulfate rock coatings on Mars. *Geology* 34, 921-924.
- Schmidt, M.E. et al., (2008), Hydrothermal origin of halogens at Home Plate, Gusev Crater. *Journal of Geophysical Research*, 113, E06S12.
- Seelos, K. D., R. E. Arvidson, B. L. Jolliff, S. M. Chemtob, R. V. Morris, D. W. Ming, and G. A. Swayze (2010), Silica in a Mars analog environment: Ka'u Desert, Kilauea Volcano, Hawaii, *Journal of Geophysical Research* ,115, E00D15, doi:10.1029/2009JE003347.
- Sklute, E., (2015), On the Subject of Analyzing Iron and Sulfur Bearing Minerals from Three Extreme Environments: Geological Carbon Sequestration, Acid Mine Drainage, and Mars. Ph.D. Dissertation thesis, 433 pp., Stony Brook University, Stony Brook, NY.

- Skok, J. R., J. F. Mustard, B. L. Ehlmann, R. E. Milliken, and S. L. Murchie (2010), Silica deposits in the Nili Patera caldera on the Syrtis Major volcanic complex on Mars, *Nature Geoscience*, 3(12), 838–841.
- Smith, M. R., and J. L. Bandfield (2012), Geology of quartz and hydrated silica-bearing deposits near Antoniadi Crater, Mars, *J. Geophys. Res.*, 117, E06007, doi:10.1029/2011JE004038
- Squyres, S. et al., (2007), Pyroclastic activity at Home Plate in Gusev Crater, Mars. *Science*, 316, 738-742.
- Squyres, S. W., et al. (2012), Ancient impact and aqueous processes and Endeavour Crater, Mars, *Science*, 336, 570–576, doi:10.1126/science.1220476.
- Tosca, et al., (2004), Acid-sulfate weathering of synthetic Martian basalt: The acid fog model revisited, *Journal of Geophysical Research*, 109, E05003.
- Weitz, C.M., Bishop, J.L., Thollot, P., Mangold, N., Roach, L.H. (2011), Diverse mineralogies in two troughs of Noctis Labyrinthus. *Geology* 39, 899–902, doi: 10.1130/G32045.1.
- Wray, J.J. et al., (2011), Columbus crater and other possible groundwater-fed paleolakes of Terra Sirenum, Mars. *Journal of Geophysical Research*, 116, E01001, doi: 10.1029/2010JE003694.
- Wyatt, M. B., V. E. Hamilton, H. Y. McSween Jr., P. R. Christensen, and L. A. Taylor (2001), Analysis of terrestrial and Martian volcanic compositions using thermal emission spectroscopy: 1. Determination of mineralogy, chemistry, and classification strategies, *Journal of Geophysical Research*, 106(E7), 14711–14732.
- Yant, M., A. D. Rogers, H. Nekvasil, Y.-Y. S. Zhao, and T. Bristow (2016), Spectral characterization of acid weathering products on Martian basaltic glass, *Journal of Geophysical Research - Planets*, 121, doi:10.1002/2015JE004969.

- Yen, A. S., et al. (2008), Hydrothermal processes at Gusev Crater: An evaluation of Paso Robles class soils, *J. Geophys. Res. Journal of Geophysical Research*, 113, E06S10, doi:10.1029/2007JE002978.
- Young, K. E., C. A. Evans, and K. V. Hodges (2011), Laboratory Tests of a Handheld X-Ray Fluorescence Spectrometer: A Tool for Planetary Exploration, American Geophysical Union, Fall Meeting, Abstract P43B-1672.
- Young, K. E., C. A. Evans, and K. V. Hodges (2012), Evaluating Handheld X-Ray Fluorescence (XRF) Technology in Planetary Exploration: Demonstrating Instrument Stability and Understanding Analytical Constraints and Limits for Basaltic Rocks, Lunar and Planetary Science Conference, XLIII, Abstract 2628.
- Young, K. E., J. E. Bleacher, C. A. Evans, A. D. Rogers, G. Ito, Z. Arzoumanian, and K. Gendreau (2015), Examining Volcanic Terrains Using In Situ Geochemical Technologies: Implications for Planetary Field Geology, Lunar and Planetary Science Conference, XLVI, Abstract 1658.
- Young, K. E., Evans, C. A., Hodges, K. V., Bleacher, J. E., & Graff, T. G. (2016). A review of the handheld X-ray fluorescence spectrometer as a tool for field geologic investigations on Earth and in planetary surface exploration. *Applied Geochemistry*, 72, 77-87. DOI: 10.1016/j.apgeochem.2016.07.003.

Table 5-1. Previous studies of Hawaiian basalt and tephra in situ alteration from a planetary perspective.

	Hawaiian Material	Conditions	Analytical techniques^A	Secondary phases
<i>Bishop et al., 2005a</i>	Solfataric alteration of ash under 1974 flow in Halemaumau crater	In situ, hydrothermal alteration	VNIR, MIR, SEM, EMP, XRD, MB	Opal-A, gypsum, jarosite, phyllosilicates
<i>Crisp et al., 1990</i>	Basalt lava flows, Mauna Loa and Kilauea Volcano	In situ, acid alteration	MIR, EMP	Amorphous silica, Fe-Ti-oxides
<i>Golden et al., 1993</i>	Palagonitized basaltic tephra, Summit of Mauna Kea	In situ, hydrothermal alteration	Diffuse reflectance, FIR, XRD, MB, EMP	Fe-Ti-oxides, erionite, smectite, np-Ox, Ti-hematite
<i>Morris et al., 2000a</i>	unaltered, palagonitic, and sulfatetic tephra from Mauna Kea Volcano, steam vent material from Kilauea Volcano	In situ, hydrolytic and acid-sulfate alteration	Diffuse reflectance, XRD, MB, XRF	Nanophase-oxides, glass, silica, Fe-sulfate, Al-sulfate, smectite, Fe-oxides
<i>Morris et al., 2000b</i>	Tholeiitic basalt from Sulfur Bank	In situ, acidic alteration (pH~4-5)	XRD, MIR	Anatase, nanophase silica, Na-Al-sulfate, Ca-sulfate
<i>Schiffman et al., 2000</i>	Keanakako'I Ash, Kilauea Volcano	In situ, acidic (pH<6) to neutral (pH6.5-7.8)	XRD, SEM	Kaolinite, allophane, imogolite, smectite, opal, palagonitized glass
<i>Schiffman et al., 2006</i>	Siliceous-sulfate basalt coatings, Ka'u Desert	In situ, low pH alteration	XRD, SEM, VNIR, EMP, MB	Amorphous silica, jarosite, hydrated iron oxides
<i>Bishop et al., 2007</i>	Basaltic tephra, Halekala, Maui	In situ, hydrothermal alteration	XRD, EMP, SEM, TEM, MB, VNIR, TrIR, MIR	Fe-oxides, phyllosilicates, sulfates, amorphous Al-Si-material
<i>Minitti et al., 2007</i>	Glass-rich basalts	In situ, low pH alteration	EMP, VNIR, MIR	Hydrated silica with minor Fe, Ti, and S-bearing materials, ferric oxides/oxyhydroxides
<i>Hamilton et al., 2008</i>	Basaltic tephra, Mauna Kea Volcano	In situ, low – neutral-high pH, ambient – high temperature	XRD, VNIR, MIR	Phyllosilicates, Fe-oxides, kaolinite, smectite, cristobalite, palagonite, Na-(Fe,Al)-sulfate
<i>Chemtob et al., 2010</i>	Surface coatings in Ka'u Desert	In situ, low pH alteration	Raman, TrIR, EMP, NanoSIMS, SEM	Altered glass, anatase, rutile, jarosite
<i>Seelos et al., 2010</i>	Lava, ash, and solfatara deposits, Ka'u Desert	In situ, low pH alteration	VNIR, Raman, EMP	Amorphous silica, sulfur, Fe-oxides
<i>McCanta et al., 2014</i>	Solfatara deposits, Halemaumau crater	In situ, low pH (<<2) alteration	SEM, MB, XRD	Amorphous silica overlain by sulfates (Ca, Na-Al, Na-Fe)
<i>Chemtob and Rossman., 2014</i>	Surface coatings on basalts, Kilauea Volcano	In situ, low pH alteration	SEM, EMP, Raman	Amorphous silica, Fe-Ti-oxides

^AXRD = x-ray diffraction, MB = Mossbauer, XRF= x-ray fluorescence, MIR = mid-infrared, SEM = scanning electron microscopy, VNIR = visible/near-infrared, EMP = electron microprobe, TrIR = transmission infrared, TEM = transmission electron microscopy, FIR =

Table 5-2: Overview of alteration material observed for all of the samples analyzed in this study.

Sample	Vent distance	Sample description	MIR	VNIR ^A	SEM ^B	XRD ^C
HI_15_MHY_001	19.5m	Blue surface coating on basalt	Group 1-1 silica-dominated	silica +/- Fe-oxides	Si-Ti-rich coating	Am
HI_15_MHY_002a	18.0m	White alteration coating on basalt	Group 1-1 silica-dominated	silica, Fe ^{+2/+3} -sulfate	Si-Fe-Ti-rich coating, Fe-, Ca-sulfates	Am
HI_15_MHY_002b	18.0m	Yellow alteration coating on basalt	Group 1-1 silica-dominated	silica, Fe ^{+2/+3} -sulfate	Si-rich coating	Am, xtl silica
HI_15_Solf_001_1	n/a	Brown basalt	Group 1-1 silica-dominated	silica, Fe-oxides +/- Fe ^{+2/+3} -sulfate	n/a	Am
HI_15_Solf_002_1	n/a	Reddish soil	Group 1-1 silica-dominated	silica, Fe-oxides +/- Fe ^{+2/+3} -sulfate	n/a	Am
HI_15_MHY_003	11.5m	White alteration coating on basalt	Group 1-2 silica-dominated	silica, Fe-oxides	Si-rich coating, Ca-sulfate	Am, Blix
HI_15_MHY_005	4.7m	White encrusted coating on soft red material	Group 1-2 silica-dominated	silica, Fe-oxides	Fe-Ti-oxides, Ca-sulfate, Si-rich coating	Am, Fe-ox
HI_15_Solf_003_2	n/a	White coating on basalt	Group 1-2 silica-dominated	silica, Fe-oxides	n/a	Am
HI_15_Solf_003_3	n/a	Reddish soil	Group 1-2 silica-dominated	silica, Fe-oxides	n/a	Am, Fe-ox, Zeo, K-sulfate
HI_15_Solf_001_2	n/a	White encrusted material on soft red material	Group 1-3 silica-dominated	silica	n/a	Am, Fe-ox
HI_15_Solf_002_3	n/a	White globular crust	Group 1-3 silica-dominated	silica	n/a	Am
HI_15_MHY_007a	4.5m	Yellow/white coating on soft red material	Group 1-4 silica-dominated	silica, Ca-sulfate	Si-rich coating, Ca-sulfate	Am
HI_15_MHY_007b	4.5m	Mm-sized yellow and white grains	Group 2 Ca-sulfate-dominated	silica, Ca-sulfate	Si-rich coating, Ca-sulfate	Am, Ca-sulfate, sulfur
HI_15_Solf_002_2	n/a	White and yellow coating filling topographic lows	Group 3 Fe/Al-sulfate-dominated	silica, Ca-sulfate	n/a	Am
HI_15_MHY_006	4.0m	Yellow/ white encrusted coating on soft red material	Group 4 silica-Fe-oxide-dominated	silica, Fe-oxides +/- Fe ^{+2/+3} -sulfate	Fe-Ti-oxides, Si-rich coating	Am, xtl silica

^ASilica indicates opal-CT and/or silicic acid (SiO₂·nH₂O)

^BSEM analysis was only performed on the HI_15_MHY samples.

^CAmorphous material could indicate glass, silica, or other amorphous materials which result in a characteristic hump in the XRD pattern.

Xtl silica indicates a crystalline silica phase that produced distinct peaks in the XRD pattern. Am = amorphous material, Blix = blixite, Fe-ox = Fe-oxides, Zeo = zeolite. Fe-oxides could be primary or secondary material.

Table 5-3: Quantitative elemental abundances as determined by hXRF.

Sample	Mg	Al	Si	P	K	Ca	Ti	Mn	Fe
HI_15_MHY_001	0.38	6.80	73.46	0.40	0.28	4.62	2.02	0.23	13.98
HI_15_MHY_002a	0.32	9.18	73.75	0.56	0.34	1.51	1.95	0.13	12.28
HI_15_Solf_001_1	3.88	13.48	54.61	0.30	0.32	7.27	1.97	0.43	17.75
HI_15_Solf_002_1	0.61	11.96	59.24	0.42	0.38	5.88	2.11	0.26	19.15
HI_15_MHY_003	1.19	9.32	70.48	0.57	0.20	2.38	2.18	0.12	13.57
HI_15_MHY_005	9.67	7.30	62.67	0.63	0.12	0.00	2.72	0.05	17.36
HI_15_Solf_003_2	0.00	10.22	84.39	0.64	0.45	0.18	2.05	0.08	3.86
HI_15_Solf_003_3	0.00	9.41	80.00	0.76	0.04	0.76	2.38	0.07	14.67
HI_15_Solf_001_2	3.53	11.63	58.59	0.46	0.30	7.58	2.33	0.24	15.34
HI_15_Solf_002_3	3.16	6.37	87.44	0.56	0.10	0.00	1.84	0.05	0.94
HI_15_MHY_007a	8.38	6.91	72.55	0.61	0.20	0.03	2.40	0.07	8.86
HI_15_Solf_002_2	7.61	12.58	53.00	0.22	0.29	8.20	1.92	0.26	15.92



Figure 5-1: A) Image of the volcanic vent from which the samples were collected, B-I) close-up images of the samples in situ, J-P) laboratory images of the HI_15_MHY samples, and Q-W) laboratory images of the HI_15_Solf samples. See text for a description of the sample labels.

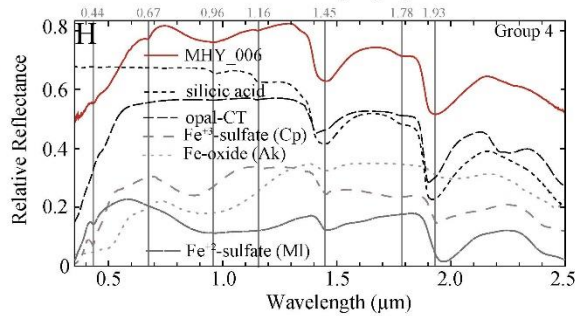
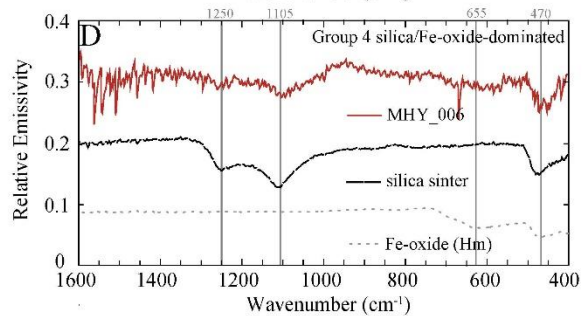
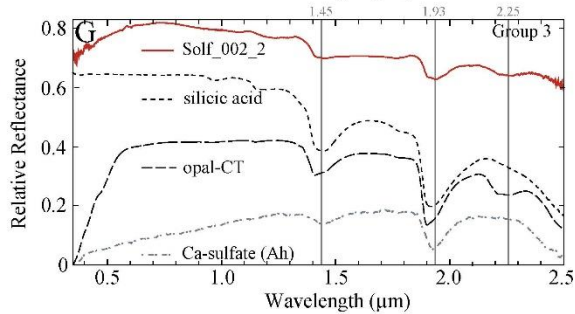
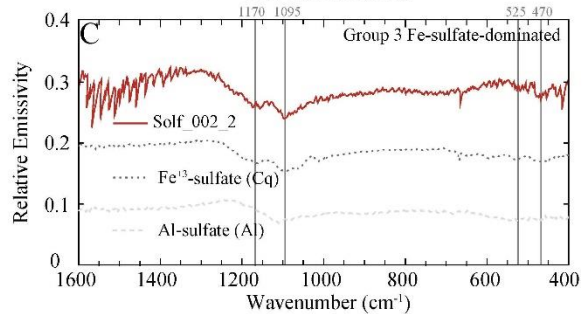
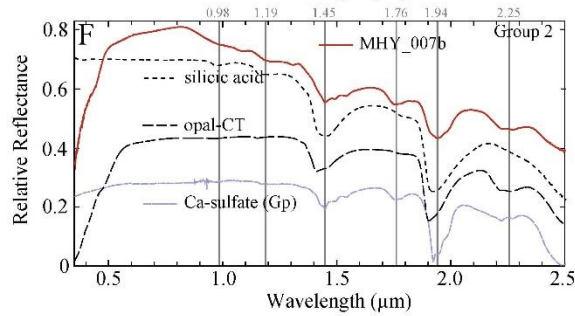
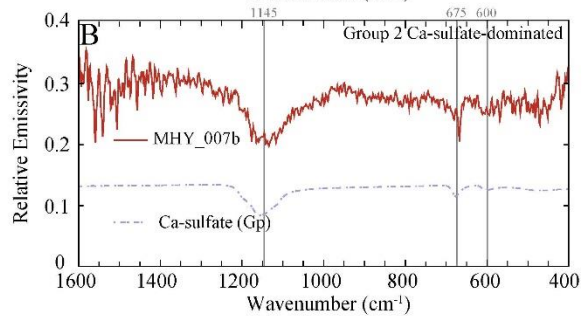
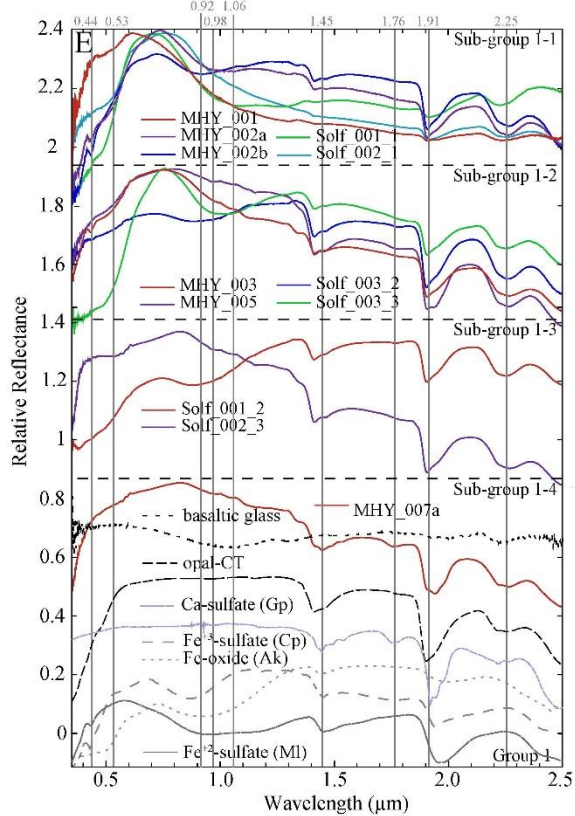
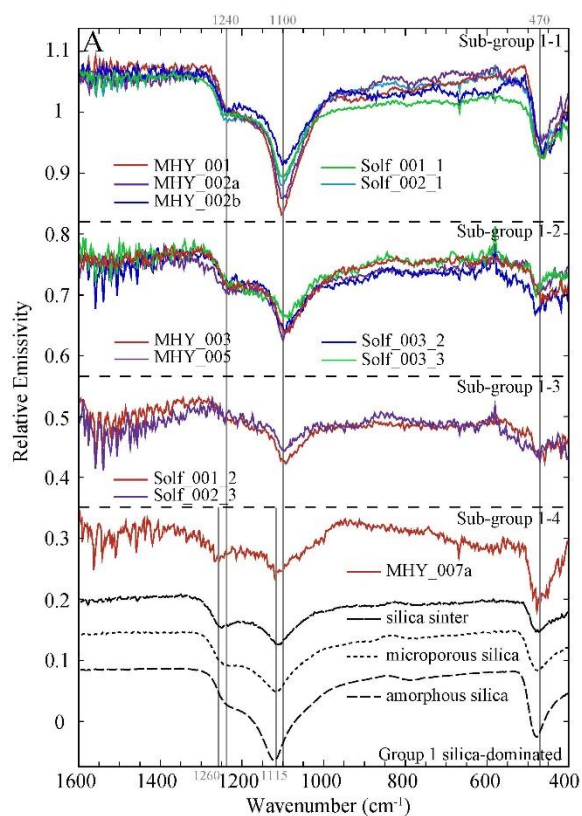


Figure 5-2: MIR emission signatures of the collected samples grouped based on similarities of dominant spectral features into **A)** Group 1, silica-dominated, **B)** Group 2, Ca-sulfate-dominated, **C)** Group 3, Fe-sulfate-dominated, and **D)** Group 4 (silica/Fe-oxide-dominated). The VNIR reflectance spectra are separated into groups based on the MIR groups established in panels A-D, **E)** Group 1, **F)** Group 2, **G)** Group 3, and **H)** Group 4. Vertical lines indicate features discussed in text. The spectra have been offset along the y-axis for clarity. Gp = gypsum, Ah = anhydrite, Ak = akaganéite, MI = melanterite, Al = alunogen, Cq = coquimbite, Hm = hematite. The library spectra used here were not measured in this study and include silica sinter, microporous silica, amorphous silica [Ruff *et al.*, 2011], gypsum [Lane *et al.*, 2007], coquimbite [Lane *et al.*, 2015] alunogen [Lane *unpublished*], and hematite [Christensen *et al.*, 2000] for the MIR. In the VNIR, the library spectra include basaltic glass (Yant *et al.*, 2016), silicic acid, opal-CT [Rice *et al.*, 2013], gypsum (RELAB ID: C1JB557), akaganéite (RELAB ID: 397F212D), melanterite (RELAB ID: CASF44), copiapite (RELAB ID: C1JBA51), and anhydrite (RELAB ID: C1JB641A).

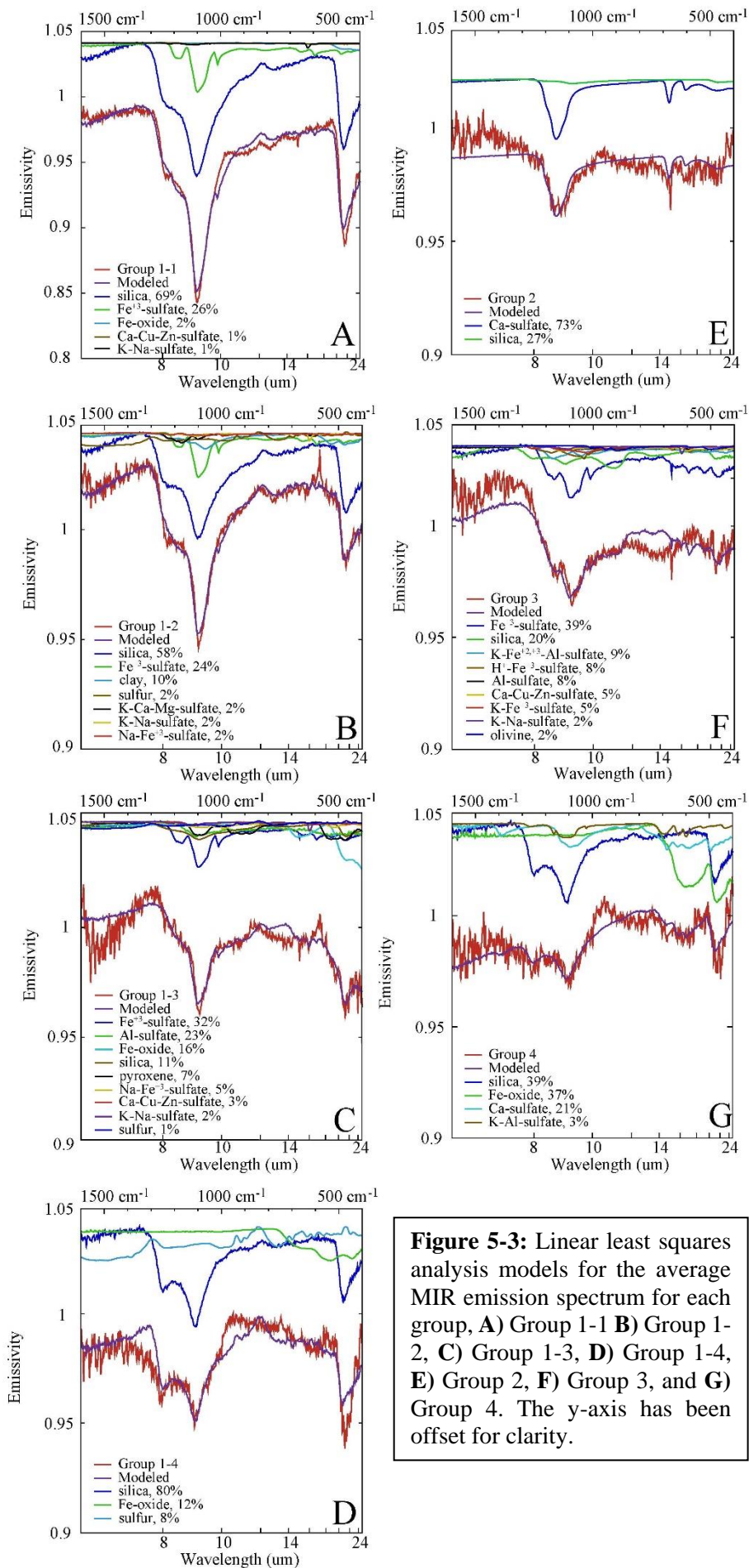


Figure 5-3: Linear least squares analysis models for the average MIR emission spectrum for each group, **A)** Group 1-1 **B)** Group 1-2, **C)** Group 1-3, **D)** Group 1-4, **E)** Group 2, **F)** Group 3, and **G)** Group 4. The y-axis has been offset for clarity.

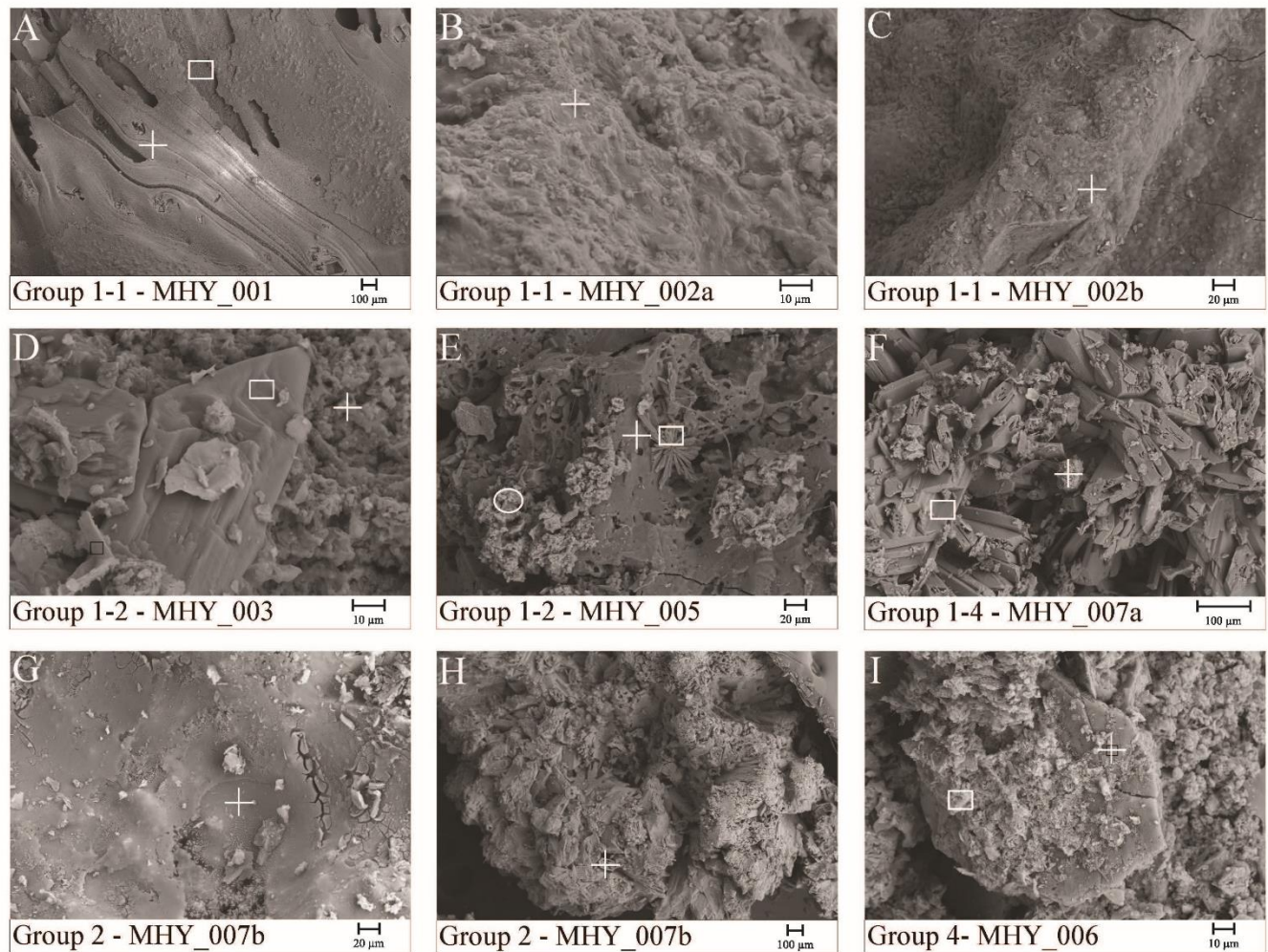


Figure 5-4: Secondary electron images of HI_15_MHY samples: Group 1-1: **A)** HI_15_MHY_001 exhibiting a Si-rich coating (cross) overlying a Al, Ca, Mg, Fe-rich glass (square), **B)** HI_15_MHY_002a exhibiting a Si-rich surface (cross), and **C)** HI_15_MHY_002b exhibiting a Si-rich coating (cross); Group 1-2: **D)** HI_15_MHY_003 exhibiting Si-rich material (cross) and Ca-sulfate (square) and **E)** HI_15_MHY_005 exhibiting Si-rich surface (cross), Ca-sulfate (square), Fe-Ti-oxide (circle); Group 1-4: **F)** HI_15_MHY_007a exhibiting Si-rich material (cross) and Ca-sulfate (square); Group 2: HI_15_MHY_007b exhibiting **G)** Si-rich clast and **H)** Ca-sulfate rich clast; and Group 3: **I)** HI_15_MHY_006 exhibiting Si-rich material (cross) and Fe-Ti-oxide (square).

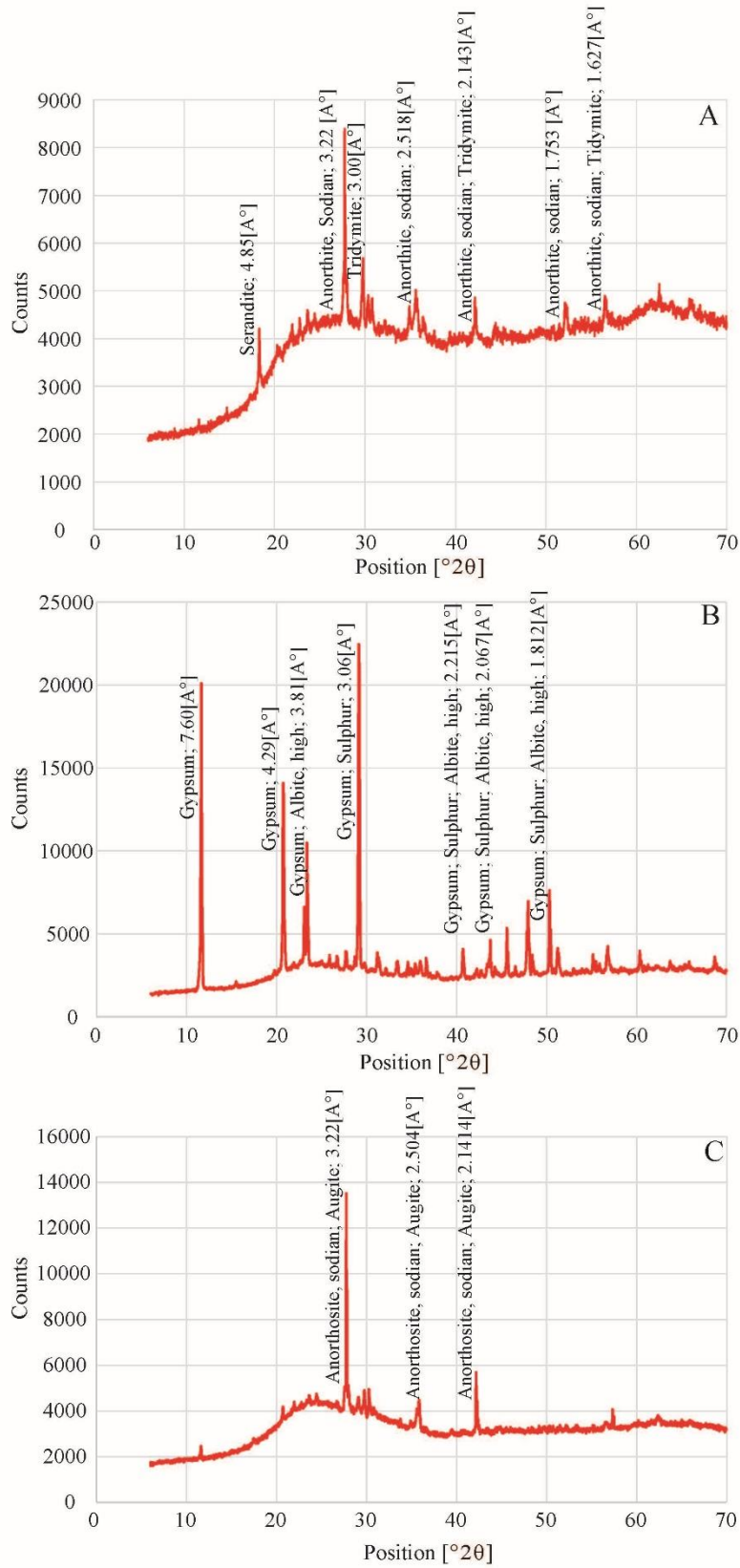


Figure 5-5: XRD patterns for the three samples that exhibited amorphous humps consistent with more Si-rich material than basaltic glass, **A)** HI_15_MHY_002b, **B)** HI_15_MHY_007b, and **C)** HI_15_Solf_002_2.

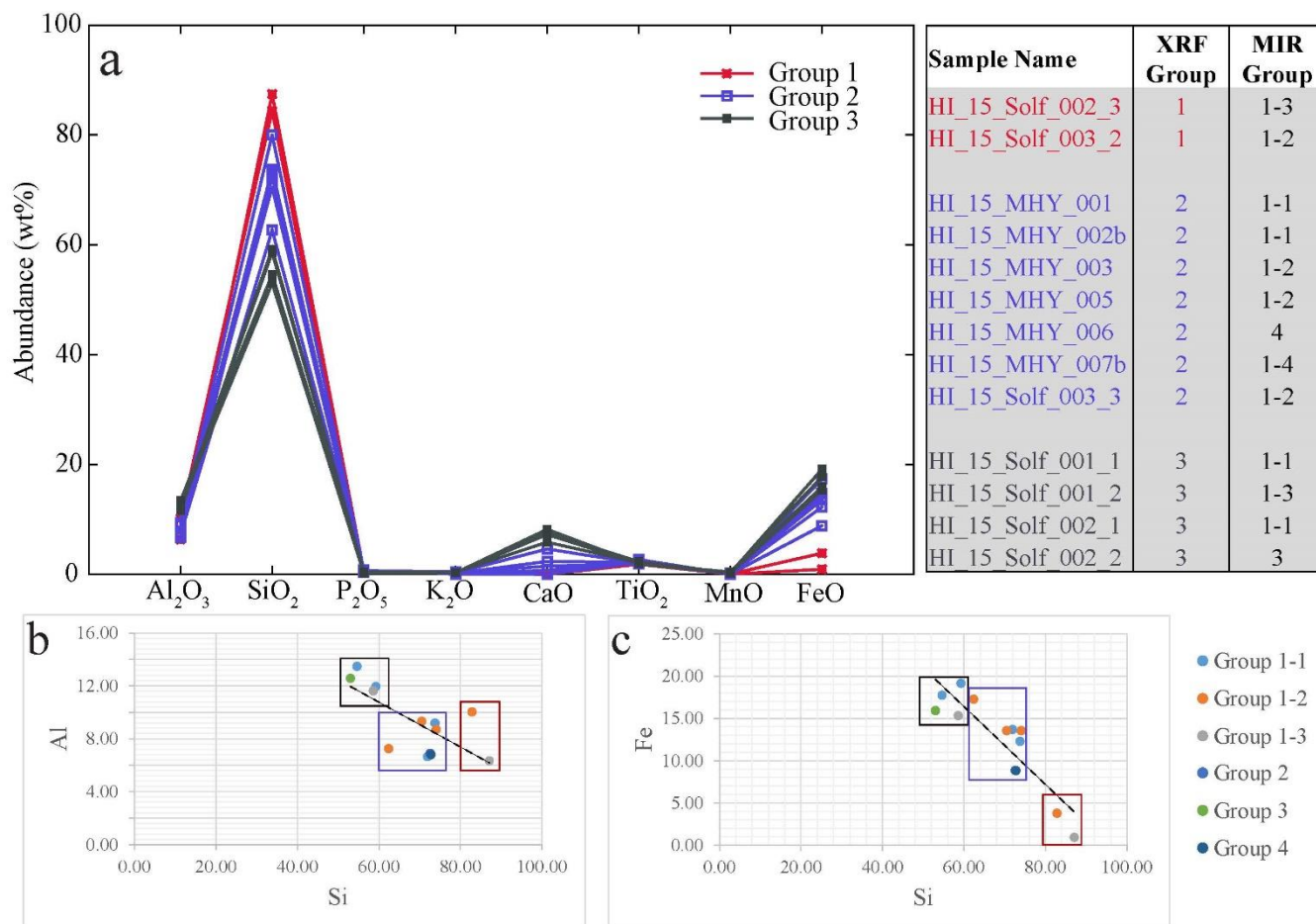


Figure 5-6: A) Handheld XRF data separated into groups determined using a minimum distance clustering algorithm on chemical data for each sample. Plots of B) Al vs. Si contents and C) Fe vs. Si contents for the natural fumarolic materials. The outlined boxes represent the XRF groupings and the color of the points represent the MIR groupings.

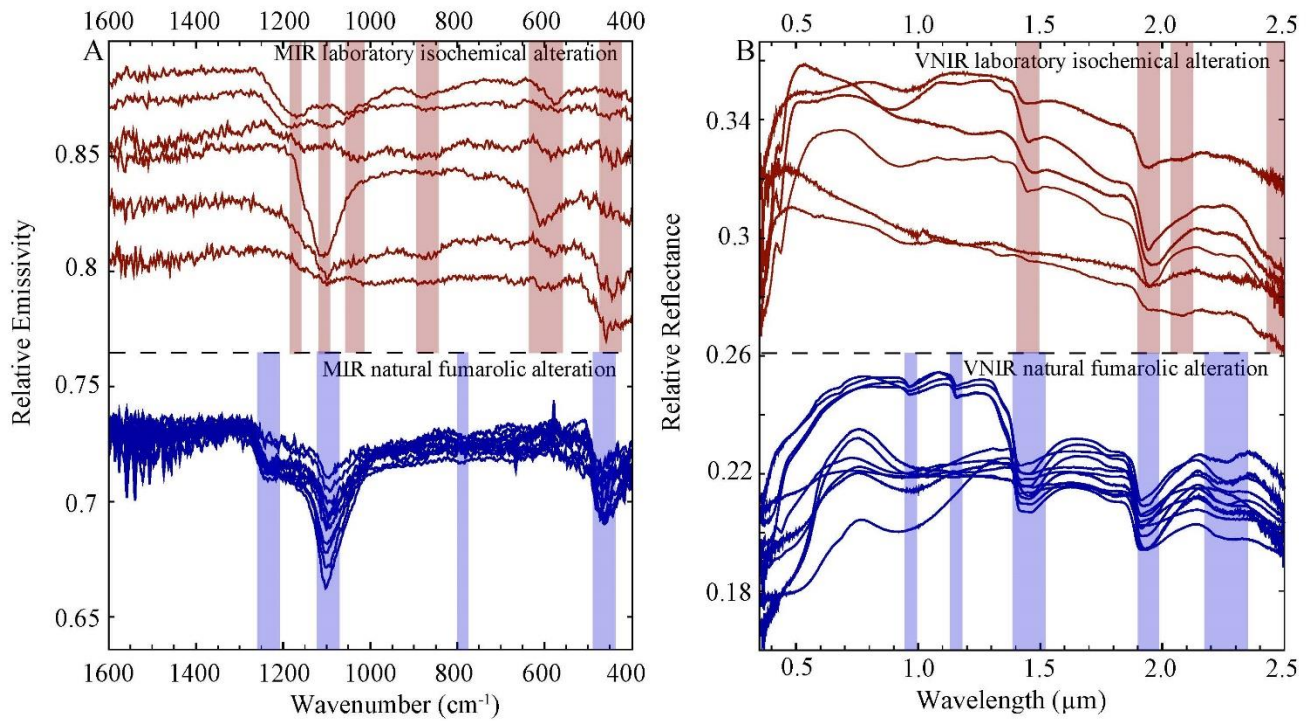


Figure 5-7: Comparison of the spectral signatures for the laboratory isochemically altered materials (sulfate-dominated) with the natural fumarolic altered materials (silica-dominated) in both the **A)** MIR and **B)** VNIR wavelength ranges. Red shaded areas correspond to sulfate-related features and blue shaded areas correspond to silica-related features.

Chapter 6

Aqueous Alteration of Glass on the Martian Surface: A Comparison of Remotely-Acquired and Experimental Data Sets

This chapter is being prepared for submission to the Journal of Geophysical Research – Planets

Yant, M., A. D. Rogers, and B.H. Horgan

6.1 Introduction

Chemical and mineralogical analyses of Martian rocks and soils by instruments on the Pathfinder [*Foley et al.*, 2003], Spirit [*Morris et al.*, 2006], Opportunity [*Clark et al.*, 2005], and Curiosity [*Vaniman et al.*, 2014] landers/rovers have suggested that acid sulfate weathering under cation-conservative conditions has been common on Mars [*Burns and Fisher*, 1990; *Bigham and Nordstrom*, 2000; *Madden et al.*, 2004; *Golden et al.*, 2005; *Ming et al.*, 2006]. Based on the presence of Ca- and Mg-sulfates and the formation of coatings/rinds on Gusev rocks, *Golden et al.* [2005] suggests that the Gusev crater surface materials were derived from acid sulfate alteration of an originally basaltic composition under low fluid-to-rock ratios and/or nearly isochemical conditions. The presence of ferric sulfates, which form exclusively under low-pH conditions, combined with the absence of Al-phyllsilicates in altered materials also suggests an acidic and low fluid-to-rock ratio weathering environment [*Ming et al.*, 2006]. These parameters can be extended to other areas of Mars including the Opportunity, Pathfinder, and Viking 1 landing sites because the elemental measurements and soil chemistry are consistent with low pH and fluid-limited conditions [*Hurowitz et al.*, 2006]. The alteration of basaltic materials under low fluid-to-rock ratios, acidic, and isochemical conditions should result in a coating of salts (chlorides and/or sulfates) and amorphous products (e.g., silica), which is observed on numerous sites on Mars by rover rock analysis [*Clark*, 1993; *Haskin et al.*, 2005; *Ming et al.*, 2006; *Clark et al.*, 2005; *Morris*

et al., 2006]. *Hurowitz and McLennan* [2007] suggest that this low fluid to rock ratio and low pH alteration environment has been dominant since approximately 3.5 Ga.

From orbit, however, evidence of widespread surface alteration is lacking. The visible/near infrared (VNIR) spectrometers, Observatoire pour la Minéralogie, l'Eau, les Glaces et l'Activité (OMEGA) [e.g., *Gendrin et al.*, 2005; *Carter et al.*, 2013] and Compact Reconnaissance Imaging Spectrometer for Mars (CRISM) [e.g., *Bishop et al.*, 2008; *Mustard et al.*, 2008; *Ehlmann et al.*, 2011], have observed and mapped secondary minerals (sulfates, chlorides, carbonates, oxides, phyllosilicates, and zeolites) in numerous, but dispersed and isolated locations [e.g., *Bibring et al.*, 2005; *Gendrin et al.*, 2005; *Langevin et al.*, 2005; *Poulet et al.*, 2005; *Ehlmann et al.*, 2011; *Ehlmann and Edwards*, 2014]. Detections of secondary minerals with the mid-infrared (MIR) spectrometers, Thermal Emission Spectrometer (TES) [*Christensen et al.*, 2000] and Thermal Emission Imaging System (THEMIS) [*Milam et al.*, 2010; *Viviano and Moersch*, 2012; *Smith et al.*, 2013], have been sparse. Spectrally, much of the Martian surface is consistent with unaltered or minimally-altered material [e.g., *Christensen et al.*, 2008; *Ody et al.*, 2012]. Thus, there is a difference in the picture of Martian surface materials provided by the lander/rover and orbiter data.

In this work, we investigated the hypothesis that the lack of widespread orbital signatures of alteration could be due to a lack of appropriate spectral endmembers for comparison. As described by *Yant et al.* [2016], spectral searches for evidence of chemical alteration have mostly relied on spectral libraries that include only pure minerals, sometimes of a restricted grain size. The spectral properties and detectability of alteration materials depends greatly on the presence of mixtures, particle size, and areal coverage within the field of view [e.g., *Michalski et al.*, 2006]. Weathering products often form as a thin coating/fracture fill, or are fine-grained and poorly consolidated. As a consequence of the complex coatings and rind geometries formed by

weathering processes, non-linear IR spectral mixing may arise. Fine grains can result in multiple surface scattering and reduced reststrahlen features in the MIR [Hunt and Vincent, 1968; Salisbury and Wald, 1992; Mustard and Hays, 1997], making it difficult to identify alteration abundance phases [e.g., Michalski et al., 2006; Kraft et al., 2007] and obtain quantitative abundances [Kraft et al., 2003; Michalski et al., 2006; Hamilton et al., 2008; Rampe et al., 2009] of alteration phases. In addition, the fine grains and thin coatings that comprise the alteration material permit energy transmission through the grains/coatings [e.g., Hunt and Logan, 1972; Clark and Roush, 1984]; this effect is enhanced in the VNIR due to the lower absorption coefficients in this range. Due to the complications of translating alteration assemblage mineral abundances measured through in-situ chemical and Mossbauer measurements (or from laboratory alteration experiments) into infrared spectral signatures, it has been difficult to project the influence of alteration products on the spectral characteristics measured from orbit. Direct spectral measurements of experimentally altered materials provide a means to assess expected spectral signatures of altered materials [Yant et al., 2016; Horgan et al., 2017; Smith et al., 2017].

In this work, we compare laboratory acquired IR spectral signatures of experimentally altered synthetic Martian basaltic glasses [Yant et al., 2016] and natural terrestrial analog basaltic glasses [Horgan et al., 2017] (**Figures 6-1, 6-2; Section 6-2**) with TES and OMEGA data. These data sets provide global coverage of the Martian surface across two complementary wavelength ranges. The laboratory-acquired signatures include basaltic glasses with Martian surface compositions that were altered under controlled, cation-conservative, acid-sulfate conditions [Yant et al., 2016]. These experiments provided constraints on how IR spectral features vary as a function of alteration conditions, such as pH and composition for Martian surface material. The terrestrial analog glass alteration experiments were performed under controlled, open-system, acid-sulfate

conditions [Horgan *et al.*, 2017]. Combined, these data sets provide a spectral library that includes mixtures of unaltered and altered material, poorly crystalline phases, combinations of various grain sizes, and alteration coatings that are difficult to capture with a standard mineral library. In this work, we address the following questions: to what degree do Martian surface materials exhibit spectral signatures consistent with alteration via open-system and/or cation-conservative weathering processes? Are there locations spectrally consistent with acidic, low fluid-to-rock ratios, and cation-conservative weathering beyond the rover-investigated sites? What alteration conditions are represented on Mars currently (at landing sites and globally)?

6.2 Spectral Library Description

We expand a previous spectral library from *Koeppen and Hamilton* [2008] and *Rogers and Hamilton* [2015] to include altered and unaltered basaltic glasses from previous analog work [*Yant et al.*, 2016; *Horgan et al.*, 2017] (**Table 6-1**). This provides a novel library with unaltered and cation-conservative altered synthetic glass endmembers with measured Martian compositions [*Yant et al.*, 2016] (**Section 6.2.1**) as well as unaltered and open-system altered natural glass endmembers for terrestrial analogs [*Horgan et al.*, 2017], allowing for improved global mapping.

6.2.1 Synthetic Analog Materials

Previous work by *Tosca et al.* [2004] and *Yant et al.* [2016] simulated acid-sulfate weathering of synthetic Martian basaltic glasses under nearly isochemical conditions; all samples were then spectrally measured using VNIR reflectance spectroscopy and TIR emission spectroscopy by *Yant et al.* [2016]. Four different compositions were used, Irvine (tholeiitic basaltic), Backstay (alkalic basaltic), Pathfinder soil (basaltic andesitic, lower silica), and Pathfinder rock (basaltic andesitic, higher silica) compositions (**Table 6-2**). The synthesis, alteration, and chemical analysis of the Pathfinder samples were done by *Tosca et al.* [2004],

whereas the Irvine and Backstay samples were done by *Yant et al.* [2016]. Sand-sized material from all compositions were altered in various acidic solutions (pH ~0-4) under low fluid-to-rock ratios (1:1, 10:1) for 14 days at ambient temperature and pressure. Reaction of the samples and subsequent evaporation lead to the formation of secondary minerals that varied with changes in pH and composition. The alteration assemblages included various sulfates, Fe-oxides, and amorphous material.

Spectral differences in the VNIR and MIR between the alteration products from each starting material were present, reflecting changes in the secondary mineral assemblage. The Irvine, Backstay, and Pathfinder soil materials altered in $\text{pH} \leq 1$ conditions exhibited strong 1.4, 1.9, and 2.4 μm features (indicative of poly-hydrated sulfates) along with negative spectral slopes in the VNIR (**Figure 6-1A**) and well-developed sulfate features in the MIR (**Figure 6-1B**). Little to no alteration was observed for the composition with the highest silica content, Pathfinder rock.

Three of the laboratory MIR signatures from *Yant et al.* [2016] exhibited absorption features with decreased spectral contrast: IRVG-pH1, BKSG-pH1, and PFSG-A (pH0) (**Figure 6-1B**). This phenomenon is likely due to the fine-grained nature of the weathered surfaces for these particular samples. Fine particles can lead to a reduction in spectral contrast of the reststrahlen features due to an increase in porosity and volumetric scattering [*Lyon, 1965; Hunt and Vincent, 1968; Salisbury and Wald, 1992; Salisbury, 1993; Moersch and Christensen, 1995*]. As grain size decreases more surfaces are created; this increases the opportunity for multiple surface reflections before the photon exits the material [*Henderson et al., 1992; Moersch and Christensen, 1995*], subsequently increasing the amount of energy received by the detector, increasing emissivity and decreasing spectral contrast. Additionally, the pores associated with smaller grain sizes can act as blackbody cavities which can decrease the spectral contrast. Typically, spectra of mineral mixtures

in the MIR wavelength range are approximately equivalent to the linear sum of their mineral constituents in proportion to their abundance over a range of particle sizes; but the assumption of linear mixing is not valid for smaller particle sizes ($< \sim 63 \mu\text{m}$) [e.g., *Ramsey and Christensen, 1998*].

The shallow spectral contrast associated with these fine-grained surfaces cannot be avoided, as they are a consequence of the cation-conservative, acidic weathering conditions utilized for these samples and could be present on the Martian surface. However, we exclude them from our library because their flat, featureless shapes are interchangeable with blackbody in the linear least squares model and allows their abundances to be potentially overestimated. Maps created using libraries that include these shallow spectra are provided in the supplemental material (**Appendix Figures A1, A2, A3**).

Last, only the materials altered in $\text{pH} \leq 1$ conditions exhibited spectral signatures consistent with alteration in the MIR and VNIR wavelengths (*Yant et al. [2016]*). It is difficult to distinguish between glasses exposed to pH 2-4 fluids and unaltered materials. Therefore, we also remove the glasses altered in $\text{pH} \geq 2$ conditions from the spectral libraries in order to eliminate redundancy.

6.2.2 Terrestrial Analog Materials

We also include materials from open system experiments that provide spectra representative of surfaces that have undergone removal of secondary alteration products (e.g., sulfates) by subsequent aqueous activity or physical abrasion [*Horgan et al., 2017*]. These materials result in silica-dominated IR spectra and produce similar negative spectral slopes to the cation-conservative materials in the VNIR.

Two glass compositions were used, including a Hawaiian glassy basalt from a subaerial flow (BAS101) and Hawaiian basaltic glass sand (BSB101) that was produced during explosive

quenching of a lava flow entering the ocean and concentrated on a black sand beach (**Table 6-2**). These two analogs are most comparable to the synthetic Backstay composition. BAS101 and BSB101 share similar Si, Al, and Mg contents with Backstay. However, the terrestrial analogs have decreased Fe contents and increased Ca relative to all of the synthetic glasses. This material was altered under acidic conditions in a simulated open-system environment. Glass sand-sized material from these two compositions were altered by repeatedly rinsing and submerging the samples in ~pH1 and ~pH3 sulfate solutions for 220 days. Reaction of the samples and subsequent rinsing lead to the formation of silica-rich leached rinds under the lowest pH condition [*Horgan et al.*, 2017].

These results are comparable to the IR spectral signatures from Yant *et al.* [2016], because alteration rinds were only observed in the VNIR and MIR spectra from the glass materials altered in the most acidic solution, pH1. Little to no alteration was observed for the materials subjected to pH3 conditions, and thus these were excluded from our library to avoid redundancy with the unaltered glass samples. In the VNIR, the pH1 BAS101 and BSB101 samples both exhibit spectra consistent with a leached rind, hydrated silica coating, and loss of oxides (**Figure 6-2A**). Negative spectral slopes are observed for both of these samples, but appears stronger for BSB101. In the MIR, spectral signatures closely resemble that of opal-A for both pH1 glass materials [*Horgan et al.*, 2017] (**Figure 6-2B**).

6.3 Data and Methods

6.3.1 General Approach

Previous global mineral mapping efforts using OMEGA data have shown that spectral signatures consistent with sulfate and/or altered glass (strong negative spectral slopes) are not widespread across the surface, but rather restricted to certain regions of the planet [e.g., *Poulet et*

al., 2005; *Horgan et al.*, 2012]. Here we first determine the extent to which MIR spectral measurements correspond with previous sulfate and altered glass detections with OMEGA, by creating global abundance maps of the altered glass materials from models of binned TES surface emissivity spectra. Next, we highlight regions of interest where both datasets are spectrally consistent with acid altered materials, and directly compare TES and OMEGA spectra with our experimentally obtained altered spectra.

6.3.2 Thermal Emission Spectrometer (TES)

Global abundance maps of the altered glass materials were created using linear least squares modeling [e.g., *Ramsey and Christensen*, 1998] of TES spectra binned at a resolution of 1 pixel per degree (ppd). Binned TES emissivity maps were the same as those used by *Rogers et al.* [2007]. A spectral library including potential surface components (**Section 6.2, Table 6-1**), atmospheric components [*Bandfield et al.*, 2000b], and a blackbody [*Hamilton et al.*, 1997] is used to obtain a linear least squares fit to binned TES emissivity spectra. The fit coefficients are normalized for blackbody and atmospheric concentration and represent the areal contribution of each component to the spatial footprint of the detector. The areal fractions correspond to volume percentages of each phase, if the surface materials are homogeneously mixed throughout the depth of penetration (tens of microns). The maps were also masked to discard bins with total modeled surface concentrations less than 0.5. This removed bins with low-spectral contrast, which is associated with small particles sizes and can result in nonlinear spectral mixing [e.g., *Ramsey and Christensen*, 1998].

The modeled fits depend on the spectral library used; the better the library represents Martian phases, the better the model fit will represent the surface mineralogy. Six libraries were created, each utilizing only one of the laboratory compositions (**Table 6-1**). Additionally, MIR spectra of

pixels that overlap OMEGA sulfate features in particular regions were modeled using linear least squares analysis [e.g., *Ramsey and Christensen, 1998; Rogers and Aharonson, 2008*]. These pixels were chosen based on location, relatively high concentration, and relatively low RMS error. To show areas that were better modeled with inclusion of any given altered glass composition, the TES emissivity data sets were modeled using the both the original library from *Rogers and Hamilton [2015]* and the expanded library described above. RMS error maps for the *Rogers and Hamilton [2015]* library were compared with those of our expanded libraries, by taking the difference between the RMS errors with and without the addition of the experimentally altered materials. Regions with the largest reduction in RMS error appear red in the difference maps. Finally, the RMS error difference maps were also masked to discard bins with total modeled surface concentrations less than 0.5 as described above.

6.3.3 Observatoire pour la Minéralogie, l'Eau, les Glaces et l'Activité (OMEGA)

OMEGA spectral images were used to ascertain the VNIR characteristics of regions of interest. OMEGA data was calibrated to I/F and then atmospherically corrected using the volcano scan method [e.g., *Bibring et al., 2005*]. For the cation-conservative altered laboratory materials, we focus on identifying sulfate detections because of the alteration material observed in the laboratory experiments [*Yant et al., 2016*]. Poly-hydrated sulfates exhibit spectral signatures in the VNIR with features near 1.40, 1.90, and 2.40 μm , whereas monohydrated sulfates have indicator features near 2.10 and 2.40 μm [*Lichtenburg et al., 2010*]. Absorption bands near 1.40 μm are likely due to OH stretching overtones or H₂O overtones/composition bands while the features in the 1.90 μm region are likely from H₂O combinations. Absorption bands in the 2.0-2.7 μm regions can be attributed to combinations of OH or H₂O bending, stretching, and rotational fundamentals or S–O bending overtones [*Cloutis et al., 2006*]. In order to locate sulfate features, we test for the presence

of diagnostic absorption bands using spectral parameters from *Carter et al.* [2013]. Although negative spectral slopes are also characteristic of the alteration materials, we did not map these because the slopes are not unique indicators of particular alteration phases [*Viviano-Beck et al.*, 2014]. The parameters utilized in this study are listed in **Table 6-3** and analysis was done via the following equation:

$$SC = 1 - \frac{\langle r \rangle_{\lambda_{band}}}{\langle r \rangle_{\lambda_{continuum}}}$$

Where SC is the spectral channel, r is the reflectance and λ_{band} and $\lambda_{continuum}$ are each a range of spectral channels for which the median value $\langle r \rangle$ of the reflectance spectrum is calculated. Once potential sulfate signatures were detected, the spectra were ratioed with neutral surfaces from within the same image, in order to avoid imposing detector-dependent noise into the ratios [e.g., *Ehlmann et al.*, 2009].

6.4 Results

Global TES abundance/RMS error maps were generated using two libraries that include 1) all of the unaltered compositions from *Yant et al.* [2016] and *Horgan et al.* [2017] (**Figure 6-3A,B**) and 2) all of the altered compositions that exhibited new features (Irvine pH0, Backstay pH0, Pathfinder Soil pH1, BAS101 pH1, BSB101 pH1) (**Figure 6-3C,D**). The unaltered materials are scattered in low densities across the surface of Mars, with a higher spatial concentration in Acidalia Planitia. The altered materials have a similar scattered distribution compared to the unaltered materials, but are more prevalent and widespread with a higher spatial concentration in the northern plains. Additionally, global TES abundance maps displaying sulfate (**Figure 6-3E**) and glass (**Figure 6-3F**) were generated using the original library from *Rogers and Hamilton* [2015]. The distribution of the sulfates is pervasive across the entire surface of Mars, but the abundance is

generally lower than that of the *Yant et al.* [2016] and *Horgan et al.* [2017] altered compositions. The glass from the original library is not well modeled relative to our synthetic and terrestrial unaltered samples, only displaying lower abundances in the northern plains.

Each of the six compositions, were also modeled using individual libraries as discussed below. The altered Irvine composition is modeled at significant abundances globally, but the pixels with high abundances are spatially scattered and show no clear regional concentration. In contrast, the Backstay and Pathfinder Soil compositions are modeled at significant abundances in the northern lowlands and are spatially concentrated (**Figure 6-4A-C**). The composition with the highest silica content, Pathfinder Rock, is modeled at lower abundances and is primarily concentrated in the northern plains (**Figure 6-4D**).

The global TES abundance maps for the open-system, acid-sulfate weathered glasses (BAS101, BSB101) are shown in **Figure 6-5**. The BAS101 glass provides a similar distribution to the cation-conservative composition altered Pathfinder Rock, providing a few good modeled fits in the northern plains and sparsely contributing to the TES assemblages in the southern regions (**Figure 6-5A**). However, the BSB101 composition is a significant component of the modeled assemblages for TES pixels throughout the northern lowlands, with some concentrated areas in the southern highlands (**Figure 6-5B**). The distribution of the BSB101 map is similar to that of the synthetic composition Backstay.

The TES-derived maps (**Figures 6-4, 6-5**) show a strong concentration of altered glass signatures in Acidalia Planitia; this observation agrees with previous VNIR data sets which indicate signatures consistent with acid-sulfate leaching of glass [*Horgan and Bell, 2012*]. Thus, we provide further detailed analysis of Acidalia Planitia in **Section 6.5.2** below. However, the maps also suggest numerous potential spectral matches in other low-dust regions, particularly for

the Irvine composition. Detailed analysis of these potential matches is beyond the scope of this paper, thus we selected additional regions of interest for detailed spectral analysis primarily by focusing on areas where sulfate minerals have been previously detected in VNIR data sets. Because the laboratory VNIR spectra from the cation-conservative altered samples show sulfate-dominated signatures, selecting TES-based potential detections from known sulfate-bearing surfaces provides the best locations to evaluate the overall spectral properties and compare with our altered samples. These sulfate-bearing regions of interest include Terra Meridiani, Valles Marineris, Mawrth Vallis, and Terra Sirenum [e.g., *Murchie et al.*, 2009; *Milliken et al.*, 2010; *Ackiss and Wray*, 2012; *Carter et al.*, 2013; *Elhmann and Edwards*, 2014] as described below. The particular TES pixels modeled for each region were determined based on overlap with sulfate detections in the OMEGA data. TES data were only modeled for pixels that provided a better RMS error using our expanded library (**Section 6.3.1**).

6.4.1 Acidalia Planitia

Acidalia Planitia is an extensive, relatively flat region located in the northern lowlands with a distinctive MIR and VNIR spectral signature compared to other low-dust regions [*Bandfield et al.*, 2000a; *Poulet et al.*, 2005]. Previous work has shown that best-fit models of TES spectra in this region must include a component that spectrally resembles obsidian, at abundances of ~40% [*Bandfield et al.*, 2000a; *Rogers and Christensen*, 2007]. A number of materials are spectrally similar to obsidian glass in the MIR, including zeolites [*Ruff et al.*, 2004], oxidized basalts [*Salvatore et al.*, 2014], and leached basaltic glass [*Horgan et al.*, 2017, **Figure 6-2**]. Thus, as expected, the open-system weathered glass samples show high concentrations in the Acidalia region (**Figure 6-5**). However, the cation-conservative compositions are also well modeled here

(the dominant component varies regionally within Acidalia), with the altered Backstay composition generally showing the highest concentrations (**Figure 6-4**).

In the VNIR, sulfate signatures are lacking in Acidalia Planitia. Instead, most signatures in this region are consistent with a negatively sloping, shallow spectrum as observed in OMEGA stamps 0311_4 and 0905_3 (**Figure 6-6**). The Irvine, Backstay, and Pathfinder Soil glasses altered in $\text{pH} \leq 1$ cation-conservative conditions exhibited similar negative slopes, but also contain weak hydration features that are absent in the OMEGA spectrum. Negative slopes were observed for both glass samples altered under $\text{pH} \leq 1$ open-system conditions, BAS101 and BSB101. The slope is more apparent in the BSB101 glass and this spectrum has shallow features comparable with the OMEGA signature observed in this region (**Figure 6-6**).

Linear least squares models were performed for each of the six compositions for TES pixels that overlap negative sloping signatures in the OMEGA data. As expected from **Figure 6-4**, the altered Backstay composition provides the highest modeled abundance (**Figure 6-4B**) indicating approximately 22 - 28% $\text{pH} 0$ material (**Figure 6-7A, C**) for the pixels outlined in **Figure 6-6B, D**. A strong absorption minimum near 1110cm^{-1} was generally observed for TES pixels that allowed for good model fits with Backstay. This feature will be discussed further in **Section 6.5.2**.

6.4.2 Terra Meridiani

Sulfates have been observed by OMEGA in Terra Meridiani over large areas in the etched units, including kieserite and poly-hydrated sulfates (e.g., epsomite, copiapite, halotrichite) [Gendrin *et al.*, 2005; Arvidson *et al.*, 2005; Griffes *et al.*, 2007]. The presence of copiapite and halotrichite can be associated with an acidic weathering environment [Joeckel *et al.*, 2007], similar to the experimental parameters implemented by Yant *et al.* [2016]. The TES pixels in the Terra Meridiani region are consistent with the altered Irvine glass composition suggesting cation-

conservative weathering of a tholeiitic basaltic glass (**Figure 6-4A**). Due to the number of well modeled TES pixels in this region, we only show the linear least squared fit for one TES pixel, with the lowest RMS error, that overlaps sulfate detections in the OMEGA data (**Figure 6-8A**, discussed below). TES data for each of the compositions was modeled and the Irvine glass composition provided the highest modeled abundances with this specific region. For the area enclosed by OMEGA stamp 0518_2 (**Figure 6-8A**), the outlined pixel indicated Irvine glass as the highest contributing component at approximately 26% (pH0) (**Figure 6-8B**).

Terra Meridiani areas consistent with sulfate signatures in the OMEGA data are indicated in green for stamp 0518_2 (**Figure 6-8A**). The reflectance signature for this region exhibits features near 1.45, 1.93, and 2.06 μm , consistent with mono-hydrated and poly-hydrated sulfates (**Figure 6-6**). The feature near 1.45 μm is weak which could be due to mixing and/or coating by more opaque Fe-bearing oxides [e.g., *Swayze et al.*, 2002, 2003]. The absorptions located near 2.06 μm and the lack (or weakening) of the 1.4 μm absorption for this signature is most consistent with the altered Irvine glass material. Consequently, Irvine provided the best model fits in the TES data in Terra Meridiani.

6.4.3 Mawrth Vallis

The Mawrth Vallis region on Mars is one of the oldest outflow channels [*Scott and Tanaka*, 1986; *Edgett and Parker*, 1997] and contains plains with extensive clay deposits [*Poulet et al.*, 2005; *McKeown*, 2009; *Michalski and Noe Dobrea*, 2007; *Bishop et al.*, 2008; *Loizeau et al.*, 2010; *Noe Dobrea et al.*, 2010]. Mawrth Vallis exhibits spectral signatures consistent with nontronite, montmorillonite, kaolinite, saponite, other smectite clay minerals, as well as amorphous silica, volcanic glass, and sulfate minerals. Among the sulfate phases observed are jarosite and copiapite which are indicators of acid-sulfate processes [e.g., *Farrand et al.*, 2009; *Farrand et al.*, 2014].

The patchy occurrences of these sulfate phases suggest limited interaction with low pH solutions in a potentially low fluid-to-rock environment. Additionally, kaolinite group minerals can be associated with acid leaching [Gaudin *et al.*, 2011]. Although Mawrth Vallis exhibits spectra consistent with large exposures of clay, volcanic glass may also be contributing to these spectral signatures, up to ~50% [McKeown *et al.*, 2011].

The Mawrth Vallis region contains some TES pixels that are well modeled by Irvine (**Figure 6-4A**). The Backstay, Pathfinder Soil, and Pathfinder Rock compositions fit little to no pixels in this area (**Figure 6-4B-D**). Irvine is modeled using a TES pixel outlined in white, near the top of OMEGA stamp (0353_3) (**Figure 6-8C**). This pixel was chosen as it had a lower RMS error and overlapped with sulfate features in the VNIR. Irvine glass was modeled as the highest contributing component to the MIR assemblage at approximately 28% (pH0) in this region (**Figure 6-8D**). The sulfate detections in OMEGA stamp 0353_3 are scattered throughout the stamp (**Figure 6-8C**). These regions exhibit absorptions near 1.44, 1.92, and 2.48 μm , suggesting the presence of poly-hydrated sulfates (**Figure 6-6**). These features are most consistent with the Irvine glass material altered under pH0 conditions.

6.4.4 Valles Marineris

The interior layered deposits of Valles Marineris have been interpreted as flood basalts [McEwen *et al.*, 1999] or lavas interbedded with sediments [Malin and Edgett, 2000]. Spectral signatures acquired by CRISM have indicated the presence of hydrated silicate glass [Swayze *et al.*, 2007; Murchie *et al.*, 2009], opaline silica, and altered glass [Milliken *et al.*, 2008] in layered deposits in this region. A variety of sulfates, including Fe-sulfates (jarosite), Mg-sulfates, and other hydrated sulfates [Gendrin *et al.*, 2005; Bibring *et al.*, 2007; Mangold *et al.*, 2008; Milliken *et al.*, 2008; Murchie *et al.*, 2009], have also been identified in association with the layered deposits. The

detection of jarosite is consistent with low-temperature acidic alteration of this region during the Late Hesperian and potentially the Amazonian [Milliken *et al.*, 2008]. Sulfates have also been observed by CRISM in the dune fields of this region which are hypothesized to be derived from a local source [Chojnacki *et al.*, 2014]. Additionally, the sequence of opaline silica stratigraphically below layers enriched in sulfates in the Juventae Chasma region is consistent with low fluid-to-rock ratio, acid-sulfate weathering of basaltic materials [Tosca *et al.*, 2004; Hurowitz *et al.*, 2005; Yant *et al.*, 2016].

In the Valles Marineris region, the altered Irvine composition again provides the best model fits and abundances (**Figure 6-4A**). For the area outlined by the OMEGA stamp in this area (0581_3), the TES pixels consistent with Irvine do not overlap the sulfate features observed in the VNIR (**Figure 6-8E**). Since the two data sets do not overlap a linear least squared model is not shown for this region. The sulfate signatures observed in the VNIR for OMEGA stamp 0485_3 are concentrated near the top of the stamp as well as centered near the left border (**Figure 6-8E**). The reflectance signature for this region exhibits features near 1.97 and 2.06 μm , most consistent with the altered Irvine material and may indicate the presence of mono-hydrated sulfate (**Figure 6-6**).

6.4.5 Terra Sirenum

The Terra Sirenum region of Mars is located in the cratered southern highlands, situated southwest of the Tharsis rise. Several sulfate phases have been observed in the VNIR wavelength ranges including, alunite, jarosite, gypsum, and Mg/Fe sulfates [e.g., Wray *et al.*, 2009; Murchie *et al.*, 2009; Wray *et al.*, 2011]. These phases are observed in a ring around the wall of Columbus crater as well as on the crater floor possibly beneath lava flows. The detection of jarosite and alunite is consistent with low pH alteration of this region. Gusev crater, situated just north of Terra

Sirenum, was the source for the synthetic glass compositions used for preparing samples for the Irvine and Backstay laboratory spectra in this study [Yant *et al.*, 2016]. In the Terra Sirenum region, TES data are broadly consistent with the Irvine, Backstay, and Pathfinder Soil compositions (**Figure 6-4A-C**). Although the synthetic analogs allow for good TES fits in Terra Sirenum (**Figure 6-4A**), no sulfate signatures were observed in the OMEGA data for this region. Instead, VNIR signatures are consistent with unaltered basalt (**Figure 6-6**).

6.5 Discussion

6.5.1 Isochemical Acid Alteration on the Martian Surface

Evidence for cation-conservative, low-pH (pH0-1) weathering is observed by overlapping TES and OMEGA data in small locations from Mawrth Vallis and Terra Meridiani (**Figure 6-8A, 6-8C**). Because lander/rover measurements have observed isochemically altered, acid-sulfate weathering at disparate locations, the lack of orbital detections is seemingly in conflict with the rover data. If acidic conditions, involving alteration fluids of initial $\text{pH} \leq 1$ in a closed-system, persisted regionally into more recent times, sulfate-dominated signatures in TES and OMEGA spectra would be expected to be more common at larger scales because sulfates produced in more recent times may be less likely to be reworked and diluted by unaltered material. Sulfate signatures were preserved in the laboratory spectra even when reworked and consolidated, though it was weakened [Yant *et al.*, 2016]. Repeated mixing events could result in MIR spectral signatures dominated by unaltered material, as observed here. TES models do suggest low levels of sulfate in Martian soils [e.g., Cooper and Mustard, 2001; Bandfield, 2002; Cooper and Mustard, 2002; Gendrin and Mustard, 2004; Rogers and Christensen, 2007] and our models indicate up to ~44% (areal percentage) sulfate material (**Figure 6-4**), but in isolated regions. Thus, perhaps these sulfates were produced in more ancient times in large amounts on regional scales but have since

been redistributed throughout Martian soils and diluted by other materials. This would suggest that acid-sulfate weathering has not resulted in abundant sulfates being formed in more recent times over regions large enough to be detected (with the possible exception of Acidalia Planitia, discussed in **Sections 6.5.3 and 6.5.4**). In Terra Meridiani and Mawrth Vallis, sulfate minerals may have formed on small grains (rather than rock surfaces), which were then deposited and lithified. This would result in a more pervasive (volumetrically abundant) sulfate abundance that would persist after billions of years of impact/erosion. Sulfates could be potentially present at smaller spatial scales that are not detected due to the poor spatial resolution of some instruments. However, even with CRISM targeted resolution (18 m/pixel), sulfates are rarely observed. Small amounts of acid sulfate alteration could be widespread in recent times but not intense enough in any specific large location to result in a concentration of sulfates high enough to be detectable with IR techniques (e.g., minor interactions with acid aerosols). Additionally, small scale and subsurface alteration via brines [e.g., *Chevrier and Altheide, 2008; Tosca et al., 2008*] or seasonal water frost [*Niles and Michalski, 2009*] could persist into recent times and lead to large amounts of sulfates but on local scales difficult to observe with orbital spectral observations.

6.5.2 Spectral Detectability in the MIR and VNIR

In this work, the location and spatial density of associated sulfate features vary between the MIR and VNIR datasets. The differences observed between these two wavelength ranges could be due to a number of factors that likely include 1) non-linear mixing in the VNIR, 2) the obscuration of hydration features by dust in certain regions and/or 3) the incorporation of sulfate phases in TES models when they are actually not present. In the VNIR range, non-linear mixing is expected to occur for intimate mixtures [*Lyon, 1964; Nash and Conel, 1974; Mustard and Pieters, 1989*]. This can make it difficult to detect minerals that are not the spectrally dominant

phase. Highly absorbing, or dark, materials can have a larger impact on the spectral features, masking more weakly absorbing materials [*Nash and Conel, 1974; Clark, 1983*]. For example, *Giuranna et al. [2011]* observed that the presence of glass and opaques can obscure OH and H₂O features and electronic transitions in the VNIR. However, these phases would not spectrally obscure sulfates in the MIR range. Non-linear mixing could result in discrepancies that indicate a lack of acid-sulfate weathering products in the VNIR, while appearing present in the MIR.

IR spectral identifications of Martian surfaces can also be obscured by thin coatings (10-100 μ m) of atmospherically deposited dust [e.g., *Fischer and Pieters, 1993; Mustard and Hays, 1997; Johnson et al., 2002*]. These coatings can cause difficulty in discriminating spectral features attributable to fine-particle coatings from those of the rock surface. Although dust can mask the spectral signature of the underlying material in both the VNIR and MIR, a greater amount of masking is expected in the VNIR range because the penetration depth of light is generally lower at shorter wavelengths. This could lead to the detection of regions through the dust at some wavelengths, while the subsurface is effectively masked at others.

The spectral signatures of sulfate phases generally exhibit relatively simple features in the MIR, near 1150 cm^{-1} . The locations of these features overlap with silicate absorptions, allowing the possibility for sulfates to be products in the TES linear least squares models even when they are not present on the surface [*Bandfield, 2002*]. This phenomenon would result in discrepancies that indicate the presence of sulfates in the MIR data sets, while appearing absent in the VNIR.

6.5.3 On the Possible Sulfate Detection in Acidalia Planitia

In the TIR, Acidalia is the type locality for “TES Surface Type 2”, a global spectral endmember that exhibits a broad absorption near 1070 cm^{-1} , and near 465 cm^{-1} [*Bandfield et al., 2000a*]. a large region where acidic alteration signatures have been observed using

CRISM/OMEGA data. However, isolated locations within Acidalia have been previously noted to exhibit an absorption minimum near 1110cm^{-1} [Bandfield, 2002]. This feature was previously attributed to a highly polymerized component [Michalski *et al.*, 2005], which is consistent with the interpretation from Horgan *et al.* [2017]. Horgan *et al.* [2017] suggests that an acid-leached basaltic glass (~pH1) could be contributing to the high-silica component of TES Surface Type 2 which is supported by the strong concave-up visible/near-infrared spectral shape of the northern plains. However, here we show that the absorption minimum could be due to the presence of sulfate (**Figure 6-9**). From the linear deconvolution models, Backstay provided the best model fits in Acidalia with the pH0 material contributing up to 28%. The Backstay glass altered under pH0 conditions produced a strong absorption near 1110cm^{-1} (**Figure 6-9**) which could be contributing to the TES signatures.

Sulfate signatures in the VNIR range are lacking for Acidalia, however. Instead, the spectra exhibit shallow features with negative spectral slopes. The Backstay materials altered in pH0-1 conditions exhibit similar spectral slopes, however, the sulfate hydration features at ~ 1.4 and ~ 1.9 μm observed in the laboratory materials are absent in the OMEGA data [**Figure 6-6**]. The open-system materials altered in pH1 exhibited shallow features along with negative spectral slopes that are more comparable with the Acidalia OMEGA signatures. The combined analysis of TIR and VNIR would suggest that the 1110cm^{-1} feature is more likely due to acid-leached glass, where the sulfate weathering products have been removed via subsequent aqueous activity or physical abrasion, as suggested by Horgan *et al.*, [2017].

However, it is possible that sulfates are present, but are masked in VNIR by opaques or dust, as described above (**Section 6.5.2**). Alternately, if the sulfate phases are poorly crystalline or amorphous, they could have weakened hydration bands that would be more challenging to detect

[*Sklute et al.*, 2015]. Elevated sulfur and hydrogen signatures in the Acidalia region of the northern lowlands, measured from Mars Odyssey Gamma Ray Spectrometer (GRS) data [*Karunatillake et al.*, 2016], provides support for this suggestion.

6.5.4 Evidence for Geologically Recent Acid Weathering in the Northern Plains

Regardless of whether the spectral signatures represent open- or closed-system acid weathering, both data sets indicate that the materials in the northern lowlands have experienced very low pH conditions. The northern lowlands provide the only areally extensive region where these spectral signatures are observed. The detection of signatures consistent with acid alteration in both the MIR and VNIR wavelength ranges over such an expansive region suggests a more recent, active and regional process for weathering in Acidalia. Additional evidence for a recent process is that the alteration signatures lack association with outcrops (which would suggest preserved, ancient alteration); rather, they are distributed across the plains, which are dominated by clasts and soils. One potential mechanism for recent alteration is melting of seasonal water frost [*Niles and Michalski*, 2009; *Kite et al.*, 2013] or snow [*Soare et al.*, 2015]. Globally, seasonal water frost is most common in the northern lowlands [*Bapst et al.*, 2015], where signatures of altered glass are most concentrated (**Figures 6-3, 6-4**). Additionally, geomorphological traits (e.g., polygons, thermokarst landforms) are present in this region that are consistent with periglacial processes [*Soare et al.*, 2015]. Water frost or snow deposited on the surface could occasionally melt and wet surficial materials for short periods of time. This would lead to weathering that occurs in thin films affecting the surface/near-surface materials. Melting can occur via localized magmatic processes, impacts, seasonal/obliquity changes, and/or radiant heating. Liquid water can also exist at temperatures below freezing in porous rock surfaces [*Anderson et al.*, 1967]. Additionally, the presence of salts can reduce the pressure and temperature requirements for melting of liquid water.

Sulfur and chlorine can react with the melted water to form acidic fluids. Sulfur and chlorine could be sourced from the initial bulk composition of the rock (e.g., sulfides, phosphates) or from previously outgassed aerosols or dust that are trapped within the frost. This type of weathering could be active under current Martian conditions near the poles as suggested by *Niles and Michalski* [2009] and could be responsible for the spectral signatures observed in the Acidalia region.

6.6 Conclusions:

From our work, we can make the following conclusions:

1. In the TES data, there are widespread signatures consistent with the laboratory data on a global scale and in the OMEGA data the signatures are still widespread, but on a much smaller scale. If acidic conditions, involving alteration fluids of initial $\text{pH} \leq 1$, persisted regionally into more recent times, sulfate-dominated signatures in TES and OMEGA spectra would be expected to be more common on a larger scale. Thus, perhaps these sulfates were produced in more ancient times in large amounts on regional scales but have since been redistributed throughout Martian soils and diluted by other materials.
2. In both the cation-conservative and open-system samples, only the materials altered under the most acidic conditions ($\text{pH} \leq 1$) produced alteration features in the IR. For regions where sulfates have been previously observed using CRISM data, the altered Irvine composition provided the best modeled fits in the TES and OMEGA data.
3. Acidalia provides an areally extensive region that exhibits signatures consistent with acidic alteration in both the MIR and VNIR. This suggests a more recent active process for weathering in this region and could be related to melting of seasonal water frost or snow.

6.7 References:

- Ackiss S, Wray J. (2012), Hydrated sulfates in the southern high latitudes of Mars. *Lunar Planet. Sci. Conf. Abstr.* 43:2434.
- Anderson D. M., Gaffney E. S., and Low P. E (1967) Frost phenomena on Mars. *Science*, 155, 319-322.
- Arvidson RE, Poulet F, Bibring J-P, Wolff M, Gendrin A, et al. 2005. Spectral reflectance and morphologic correlations in eastern Terra Meridiani, Mars. *Science* 307:1591–94.
- Bandfield, J. L., V. E. Hamilton, and P. R. Christensen (2000a), A global view of Martian surface compositions from MGS-TES, *Science*, 287, 1626– 1630.
- Bandfield, J. L., P. R. Christensen, and M. D. Smith (2000b), Spectral data set factor analysis and end-member recovery: Application to analysis of Martian atmospheric particulates, *J. Geophys. Res.*, 105, 9573–9587, doi:10.1029/1999JE001094.
- Bandfield, J. L. (2002), Global mineral distributions on Mars, *J. Geophys. Res.*, 107(E6), 5042, doi:10.1029/2001JE001510.
- Bapst, J, J.L. Bandfield, and S.E. Wood (2015) Hemispheric asymmetry in martian seasonal surface water ice from MGS TES. *Icarus*, 260, 396–408.
- Bibring, J.-P., Y. Langevin, A. Gendrin, et al., (2005), Mars surface diversity as revealed by the OMEGA/Mars Express observations, *Science* 307, 1576–81.
- Bibring J-P, Langevin Y, Mustard JF, Poulet F, Arvidson R, et al. (2006), Global mineralogical and aqueous Mars history derived from OMEGA/Mars Express data. *Science* 312:400–4.
- Bibring J-P, Arvidson RE, Gendrin A, Gondet B, Langevin Y, et al. (2007), Coupled ferric oxides and sulfates on the martian surface. *Science* 317:1206–10.
- Bigham, J. M., and D. K. Nordstrom (2000), Iron and aluminum hydroxysulfates from acid sulfate waters, in *Sulfate Minerals: Crystallography, Geochemistry and Environmental Significance*,

- edited by C. N. Alpers, J. L. Jambor, and D. K. Nordstrom, pp. 351 – 403, Mineral. Soc. Of Am., Washington, D. C.
- Bishop et al., (2008), Phyllosilicate diversity and past aqueous activity revealed at Mawrth Vallis, Mars. Science 321:830–833.
- Burns R.D., D.S. Fisher (1990), Iron–sulfur mineralogy of Mars: magmatic evolution and chemical weathering products, J. Geophys. Res., 95 pp., 14415–14421.
- Carter et al., (2013), Hydrous minerals on Mars as seen by the CRISM and OMEGA imaging spectrometers: Updated global view. JGR, 118:831–858.
- Chevrier, V. F., and T. S. Altheide (2008), Low temperature aqueous ferric sulfate solutions on the surface of Mars, Geophys. Res. Lett., 35, L22101, doi:10.1029/2008GL035489.
- Chojnacki, M., D. M. Burr, J. E. Moersch, and J. J. Wray (2014), Valles Marineris dune sediment provenance and pathways, Icarus, 232, 187–219, doi:10.1016/j.icarus.2014.01.011.
- Christensen, et al., (2000), Detection of crystalline hematite mineralization on Mars by the Thermal Emission Spectrometer: Evidence for near-surface water. JGR, 105:9623–9642.
- Christensen PR, Jakosky BM, Kieffer HH, Malin MC, McSween HY Jr, et al. (2004), The Thermal Emission Imaging System (THEMIS) for the Mars 2001 Odyssey mission. Space Sci. Rev. 110:85–130.
- Clark, R. N. (1983), Spectral properties of mixtures of montmorillonite and dark carbon grains: Implications for remote sensing minerals containing chemically and physically adsorbed water, J. Geophys. Res., 88, 10635–10644.
- Clark, R.N., King, T.V.V., Klejwa, M., Swayze, G.A., (1990), High spectral resolution reflectance spectroscopy of minerals. J. Geophys. Res. 95, 12653–12680.

- Clark, B. C. (1993), Geochemical components in Martian soil. *Geochim. Cosmochim. Acta* 57, 4575–4581.
- Clark, et al. (2005), Chemistry and mineralogy of outcrops at Meridiani Planum, *EPSL*. 240, 73-94.
- Cloutis, E.A., Asher, P.M., Mertzman, S.A. (2002), Spectral reflectance properties of zeolites and remote sensing doi:10.1029/2000JE001467.
- Cloutis, E. A., F.C. Hawthorne, S.A. Mertzman, K. Krenn, M.A. Craig, D. Marcino, M. Methot, J. Strong, J.F. Mustard, D.L. Blaney, J.F. Bell III, and F. Vilas (2006), Detection and discrimination of sulfate minerals using reflectance spectroscopy, *Icarus*, 184, 121 – 157.
- Cooper, C.D., Mustard, J.F. (1999), Effects of very fine particle size on reflectance spectra of smectite and palagonitic soil. *Icarus* 142, 557–570.
- Cooper, C. D. and J. F. Mustard (2001), TES observations of the global distribution of sulfate on Mars, *Lunar Planet. Sci.* XXXII, Abs# 2048.
- Cooper, C. D. and J. F. Mustard (2002), Sulfates on Mars: Comparing TES and ISM Results, *Lunar Planet. Sci.* XXXIII, Abs# 1997.
- Declercq, T. Diedrich, M. Perrot, S.R. Gislason, E.H. Oelkers (2012), Experimental determination of rhyolitic glass dissolution rates at 40–200 °C and $2 < \text{pH} < 10.1$. *Geochim. Cosmochim. Acta*, 100, pp. 251–263.
- Dehouck, E., V. Chevrier, A. Gaudin, N. Mangold, P.-E. Mathé, and P. Rochette (2012), Evaluating the role of sulfide-weathering in the formation of sulfates and carbonates on Mars, *Geochim. Cosmochim. Acta*, 90, 47-63.

- Edgett, K. S., and T. J. Parker (1997), Water on early Mars: Possible subaqueous sedimentary deposits covering ancient cratered terrain in western Arabia and Sinus Meridiani, *Geophys. Res. Lett.*, **24**, 2897–2900.
- Ehlmann, B.L. and Edwards, C.S. (2014), Mineralogy of the martian surface. *Annual Reviews of Earth and Planetary Sciences*, **42**, 291–315.
- Ehlmann BL, Mustard JF, Swayze GA, Clark RN, Bishop JL, et al. (2009), Identification of hydrated silicate minerals on Mars using MRO-CRISM: geologic context near Nili Fossae and implications for aqueous alteration. *J. Geophys. Res.* 114:E00D08.
- Ehlmann B.L. et al., (2011), Subsurface water and clay mineral formation during the early history of Mars. *Nature*. 479, 53.
- Farrand, W.H., Glotch, T.D., Rice, J.W., Hurowitz, J.A., Swayze, G.A. (2009), Discovery of jarosite within the Mawrth Vallis region of Mars: Implications for the geologic history of the region. *Icarus* 204, 478–488. doi:10.1016/j.icarus.2009.07.014.
- Farrand, W., T. Glotch, and B. Horgan (2014), Detection of copiapite in the northern Mawrth Vallis Region of Mars: Evidence of acid-sulfate alteration. *Icarus*, 241 (2014), pp. 346–357.
- Fischer, E.M., Pieters, C.M., 1993. The continuum slope of Mars: bidirectional reflectance investigations and applications to Olympus Mons. *Icarus* 102, 185–202.
- Foley, C. N., T. Economou, and R. N. Clayton (2003), Final chemical results from the Mars Pathfinder alpha proton X-ray spectrometer, *JGR.*, 108, 8096, E12.
- Gaudin A., Dehouck E. and Mangold N. (2011), Evidence for weathering on early Mars from a comparison with terrestrial weathering profiles. *Icarus* 216, 257–268.
- Gendrin, A. and J.F. Mustard (2004), Sulfate-cemented soils detected in TES data through the application of an automatic band detection algorithm. *LPSC XXXV*, Abs #1205.

- Gendrin, A., N. Mangold, J.-P. Bibring, et al., (2005), Sulfates in Martian layered terrains: the OMEGA/Mars Express view, *Science* 307, 1587–91.
- Giuranna, M. et al. (2011), Compositional interpretation of PFS/MEx and TES/MGS thermal infrared spectra of Phobos. *Planet. Space Sci.* 59, 1308–1325.
- Golden, D. C., D. W. Ming, R. V. Morris, and S. A. Mertzman (2005), Laboratory-simulated acid-sulfate weathering of basaltic materials: Implications for formation of sulfates at Meridiani Planum and Gusev crater, Mars, *J. Geophys. Res.*, 110, E12S07.
- Hamilton, V. E., P. R. Christensen, and H. Y. McSween Jr. (1997), Determination of Martian meteorite lithologies and mineralogies using vibrational spectroscopy, *J. Geophys. Res.*, 102, 25,593–26,603.
- Hamilton, V. E., et al., (2001), Analysis of terrestrial and Martian volcanic compositions using thermal emission spectroscopy: II. Application to Martian surface spectra from MGS TES, *JGR.*, 106, 14,733–14,746.
- Hamilton, V. E., R. V. Morris, J. E. Gruener, and S. A. Mertzman (2008), Visible, near-infrared, and middle infrared spectroscopy of altered basaltic tephras: Spectral signatures of phyllosilicates, sulfates, and other aqueous alteration products with application to the mineralogy of the Columbia Hills of Gusev Crater, Mars: *Journal of Geophysical Research-Planets*, v. 113, p. E12S43.
- Haskin, L.A., A. Wang, B.L. Jolliff, et al. (2005), Water alteration of rocks and soils from the Spirit rover site, Gusev crater, Mars, *Nature* 436, 66-9.
- Horgan, B., and J. F. Bell III (2012), Widespread weathered glass on the surface of Mars, *Geology*, 40(5), 391–394.

- Horgan, B. H. N., R. J. Smith, E. A. Cloutis, P. Mann, and P. R. Christensen (2017), Acidic weathering of basalt and basaltic glass: 1. Near-infrared spectra, thermal infrared spectra, and implications for Mars, *J. Geophys. Res. Planets*, 122, 172–202, doi:10.1002/2016JE005111.
- Hurowitz, J.A., and S.M. McLennan (2007), A ~3.5 Ga record of water-limited, acidic weathering conditions on Mars: *Earth and Planetary Science Letters*, v. 260, p. 432-443.
- Hurowitz, J. A., S. M. McLennan, D. H. Lindsley, and M. A. A. Schoonen (2005), Experimental epithermal alteration of synthetic Los Angeles meteorite: Implications for the origin of Martian soils and identification of hydrothermal sites on Mars, *J. Geophys. Res.*, 110, E07002.
- Hurowitz, J. A., S. M. McLennan, N. J. Tosca, R. E. Arvidson, J. R. Michalski, D. W. Ming, C. Schröder, and S. W. Squyres (2006), In situ and experimental evidence for acidic weathering of rocks and soils on Mars, *J. Geophys. Res.*, 111, E02S19.
- Hynek, B. M., R. E. Arvidson, and R. J. Phillips (2002), Geologic setting and origin of Terra Meridiani hematite deposit on Mars, *J. Geophys. Res.*, 107(E10), 5088, doi:10.1029/2002JE001891.
- Joeckel, R. M., Wally, K. D., Fischbein, S. A., and Hanson, P. R. (2007), Sulfate mineral paragenesis in Pennsylvanian rocks and the occurrence of slavikite in Nebraska: *Great Plains Research*, v. 17, p. 17–33.
- Johnson, J. R., P. R. Christensen, and P. G. Lucey (2002), Dust coatings on basaltic rocks and implications for thermal infrared spectroscopy of Mars, *J. Geophys. Res.*, 107(E6), 5035.
- Karunatillake, S., et al. (2006), Composition of northern low-albedo regions of Mars: Insights from the Mars Odyssey Gamma Ray Spectrometer, *J. Geophys. Res.*, 111, E03S05, doi:10.1029/2006JE002675.

- Kite, E.S., Halevy, I., Kahre, M.A., Wolff, M.J., and Manga, M. (2013), Seasonal melting and the formation of sedimentary rocks on Mars, with predictions for the Gale Crater mound: *Icarus*, v. 223, p. 181–210, doi:10.1016/j.icarus.2012.11.034.
- Koeppen, W. C., and V. E. Hamilton (2008), Global distribution, composition, and abundance of olivine on the surface of Mars from thermal infrared data, *J. Geophys. Res.*, 113, E05001, doi:10.1029/2007JE002984.
- Kraft, M.D., Michalski, J.R., Sharp, T.G. (2003), Effects of pure silica coatings on thermal emission spectra of basaltic rocks: considerations for martian surface mineralogy. *Geophys. Res. Lett.* 30 (24). <http://dx.doi.org/10.1029/2003GL018848>.
- Kraft, M. D., T. G. Sharp, J. R. Michalski, and E. B. Rampe (2007), Combined Thermal and Near Infrared Spectra of Hydrous Silica Coatings: Implications for Surface Type 2 Mineralogy and Recent Liquid Water on Mars: *Lunar Planet. Sci.* XXXVIII.
- Kruse, F.A., Lefkoff, A.B., Boardman, J.B., Heidebrecht, K.B., Shapiro, A.T., Barloon, P.J., Goetz, A.F.H. (1993), The spectral image processing system (SIPS)—interactive visualization and analysis of imaging spectrometer data. *Remote Sensing Environ.* 44, 145–163.
- Langevin, Y., F. Poulet, J.-P. Bibring, and B. Gondet (2005), Sulfates in the North Polar region of Mars detected by OMEGA/Mars Express, *Science* 307, 1584–6.
- Lichtenberg, K. A., R.E. Arvidson, R.V. Morris, S.L. Murchie, J.L. Bishop, D.F. Remolar, T.D. Glotch, E.N. Dobreá, J.F. Mustard, J. Andrews-Hanna, and L.H. Roach (2010), Stratigraphy of hydrated sulfates in the sedimentary deposits of Aram Chaos, Mars, *J. Geophys. Res.*, 115, E00D17.
- Loizeau, D., Mangold, N., Poulet, F., Ansan, V., Hauber, E., Bibring, J.-P., Gondet, B., Langevin, Y., Masson, P., Neukum, G. (2010), Stratigraphy in the Mawrth Vallis region through

- OMEGA, HRSC color imagery and DTM. *Icarus* 205 (2), 396–418, <http://dx.doi.org/10.1016/j.icarus.2009.04.018>.
- Lyon, R. J. P. (1964), Evaluation of infrared spectrophotometry for compositional analysis of lunar and planetary soils, 2, Rough and powdered surfaces, NASA Contract. Rep. CR-100.
- Madden M. E., R. J. Bodnar and J. D. Rimstidt (2004), Jarosite as an indicator of water-limited chemical weathering on Mars. *Nature* 431, 821–823.
- Malin, M.C. and K.S. Edgett (2000), Sedimentary rocks of early Mars. *Science*, 290 (5498) pp. 1927–1937.
- Mangold, N., V. Ansan, P. Masson, C. Quantin, and G. Neukum (2008), Geomorphic study of fluvial landforms of northern Valles Marineris plateau, Mars, using HRSC/MEX images and topography, *J. Geophys. Res.*, 113, E08009, doi:10.1029/2007JE002985.
- McCullom, T. M. and B. M. Hynek (2005), A volcanic environment for bedrock diagenesis at Meridiani Planum on Mars, *Nature* 438, 1129–31.
- McKeown, N.K., Bishop, J.L., Cuadros, J., Hillier, S., Amador, E., Makarewicz, H.D., Parente, M., Silver, E. (2011), Interpretation of reflectance spectra of clay mineral–silica mixtures: implications for Martian clay mineralogy at Mawrth Vallis. *Clays and Clay Mineral* 59, 400–415.
- McKeown, N. K., J. L. Bishop, E. Z. Noe Dobrea, B. L. Ehlmann, M. Parente, J. F. Mustard, S. L. Murchie, G. A. Swayze, J.-P. Bibring, and E. A. Silver (2009), Characterization of phyllosilicates observed in the central Mawrth Vallis region, Mars, their potential formational processes, and implications for past climate, *J. Geophys. Res.*, 114, E00D10.
- Michalski, J. R., and E. Z. Noe Dobrea (2007), Ancient clay-bearing sedimentary rocks in the Mawrth Vallis region, Mars, *Geology*, 35, 951–954, doi:10.1130/G23854A.1.

- Michalski J.R., et al., (2005), Mineralogical constraints on the high-silica martian surface component observed by TES. *Icarus* 174: 161-177.
- Michalski, J. R., et al., (2006), Effects of chemical weathering on infrared spectra of Columbia River Basalt and spectral interpretations of martian alteration: *EPSL*, v. 248, p. 822-829.
- Milam et al., (2010), Distribution and variation of plagioclase compositions on Mars. *JGR*, 115, E09004.
- Milliken, R.E., Swayze, G.A., Arvidson, R.E., Bishop, J.L., Clark, R.N., Ehlmann, B.L., Green, R.O., Grotzinger, J., Morris, R.V., Murchie, S.L., Mustard, J.F., Weitz, C.M. (2008), Opaline silica in young deposits on Mars. *Geology* 36, 847–850, <http://dx.doi.org/10.1130/G24967A.1>.
- Milliken, R.E., Grotzinger, J.P., Thomson, B.J. (2010), Paleoclimate of Mars as captured by the stratigraphic record in Gale Crater. *Geophys. Res. Lett.* 37, L04201. doi:10.1029/2009GL041870.
- Ming D. W., D. W. Mittlefehldt, R. V. Morris, D. C. Golden, R. Gellert, A. Yen, B.C. Clark, S. W. Squyres, W. H. Farrand, S. W. Ruff, R. E. Arvidson, G. Klingelhöfer, H. Y. McSween, D. S. Rodionov, C. Schröder, P. A. de Souza, and A. Wang (2006), Geochemical and mineralogical indicators for aqueous processes in the Columbia Hills of Gusev crater, Mars. *J. Geophys. Res.* 111, E02S12.
- Minitti, M.E., Hamilton, V.E. (2010), A search for basaltic-to-intermediate glasses on Mars: assessing martian crustal mineralogy. *Icarus* 210, 135–149.
- Minitti, M. E., et al., (2007), Morphology, chemistry, and spectral properties of Hawaiian rock coatings and implications for Mars, *JGR.*, 112, E05015.

- Morris, R.V., Graff, T.G., Mertzman, S.A., Lane, M.D., Christensen, P.R. (2003), Palagonitic (not andesitic) Mars: evidence from the thermal emission and VNIR spectra of palagonitic alteration rinds on basaltic rocks. In: Proceeding from the International Conference on Mars, vol. 6, abstract 3211.
- Morris, R. V., et al. (2006), Mössbauer mineralogy of rock, soil, and dust at Gusev crater, Mars: Spirit's journey through weakly altered olivine basalt on the plains and pervasively altered basalt in the Columbia Hills, JGR., 111, E02S13.
- Morris, R.V., Hamilton, V.E., Gruener, J.E., Ming, D.W., Mertzman, S. (2008), Visible and near-IR spectra for aqueous alteration products (palagonite, phyllosilicates, sulfates) of basaltic tephra on Mauna Kea volcano, Hawaii. In: Proceedings from the Workshop on Martian Phyllosilicates: Recorders of Aqueous Processes, abstract 1441.
- Murchie, S.L., Mustard, J.F., Ehlmann, B.L., Milliken, R.E., Bishop, J.L., McKeown, N.K., Noe Dobra, E.Z., Seelos, F.P., Buczkowski, D.L., Wiseman, S.M., Arvidson, R.E., Wray, J.J., Swayze, G.A., Clark, R.N., Des Marais, D.J., McEwen, A.S., Bibring, J.P. (2009), A synthesis of Martian aqueous mineralogy after 1 Mars year of observations from the Mars Reconnaissance Orbiter. *Journal of Geophysical Research* 114, <http://dx.doi.org/10.1029/2009JE003342>.
- Mustard, J. F. and C. M. Pieters (1989), Photometric phase functions of common geologic minerals and application to quantitative analysis of mineral mixture reflectance spectra, *J. Geophys. Res.*, 94, 13619–13634.
- Mustard, J.F., Hays, J.E., 1997. Effects of hyperfine-particles on reflectance spectra from 0.3 to 25 μ m. *Icarus* 125, 145–163.

- Mustard, J.F., et al. (2008), Hydrated silicate minerals on Mars observed by the CRISM instrument on MRO. *Nature* 454:305–309.
- Nash, D. B., and J. E. Conel (1974), Spectral reflectance systematics for mixtures of powdered hypersthene, labradorite, and ilmenite, *J. Geophys. Res.*, 79(11), 1615–1621, doi:10.1029/JB079i011p01615.
- Niles P. B. and Michalski J. (2009), Meridiani Planum sediments on Mars formed through weathering in massive ice deposits. *Nat. Geosci.* 2, 215–220.
- Noe Dobrea, E.Z., Bishop, J.L., McKeown, N.K., Fu, R., Rossi, C.M., Michalski, J.R., Heinlein, C., Hanus, V., Poulet, F., Arvidson, R., Mustard, J.F., Ehlmann, B.L., Murchie, S., McEwen, A.S., Swayze, G., Bibring, J.-P., Malaret, J.F.E., Hash, C. (2010), Mineralogy and Stratigraphy of Phyllosilicate-bearing and dark mantling units in the greater Mawrth Vallis/west Arabia Terra area: constraints on geological origin. *Journal of Geophysical Research* 115, <http://dx.doi.org/10.1029/2009JE003351>.
- Ody, A., et al., (2012), Global maps of anhydrous minerals at the surface of Mars from OMEGA/MEx, *JGR.*, 117, E00J14.
- Pelkey, S.M., Mustard, J.F., Murchie, S., Clancy, R.T., Wolff, M., Smith, M., Milliken, R.E., Bibring, J.-P., Gendrin, A., Poulet, F., Langevin, Y., Gondet, B. (2007), CRISM multispectral summary products: parameterizing mineral diversity on Mars from reflectance. *Journal of Geophysical Research* 112, <http://dx.doi.org/10.1029/2006JE002831>.
- Perret, J.L. Crovisier, P. Stille, G. Shields, U. Mäder, T. Advocat, K. Schenk, M. Chardonnens (2003), Thermodynamic stability of waste glasses compared to leaching behavior. *Appl. Geochem.*, 18, pp. 1165–1184.

- Poulet, F., J.-P. Bibring, J. F. Mustard, et al., (2005), Phyllosilicates on Mars and implications for early martian climate, *Nature* 438, 623–7.
- Poulet, F., R.E. Arvidson, C. Gomez, R.V. Morris, J.-P. Bibring, Y. Langevin, B. Gondet, and J. Griffes (2008), Mineralogy of Terra Meridiani and western Arabia Terra from OMEGA/MEx and implications for their formation, *Icarus*, 195(1), 106 – 130, 10.1016/j.icarus.2007.11.031.
- Rampe, E. B., M. D. Kraft, and T. G. Sharp (2009), Chemical Weathering Trends From TIR Spectral Models: Implications For Deriving Weathering Trends From Martian Spectral Data, LPSC XL, Abs. 2132.
- Ramsey, M.S., P.R. Christensen (1998), Mineral abundance determination: Quantitative deconvolution of thermal emission spectra. *J. Geophys. Res.* 103 (B1), 577–597.
- Rogers, A.D., Aharonson, O. (2008), Mineralogical composition of sands in Meridiani Planum determined from MER data and comparison to orbital measurements. *JGR*, 113, E06S14.
- Rogers A.D. and P.R. Christensen, (2007), Surface mineralogy of Martian low-albedo regions from MGS-TES data: Implications for upper crustal evolution and surface alteration, *JGR.*, 112, E01003.
- Rogers, A. D., and V. E. Hamilton (2015), Compositional provinces of Mars from statistical analyses of TES, GRS, OMEGA and CRISM data, *J. Geophys. Res. Planets*, 120, 62–91, doi:10.1002/2014JE004690.
- Ruff, S.W. (2004), Spectral evidence for zeolite in the dust on Mars. *Icarus* 168, 131–143.
- Ruff, S. W., P. R. Christensen, D. L. Blaney, W. H. Farrand, J. R. Johnson, J. R. Michalski, J. E. Moersch, S. P. Wright, and S. W. Squyres (2006), The rocks of Gusev Crater as viewed by the Mini-TES instrument, *J. Geophys. Res.*, 111, E12S18, doi:10.1029/2006JE002747.

- Salisbury, J. W., and A. Wald (1992), The role of volume scattering in reducing spectral contrast of Reststrahlen bands in spectra of powdered minerals, *Icarus*, 96, 121-128.
- Salvatore, M. R., J. F. Mustard, J. W. Head, R. F. Cooper, D. R. Marchant, and M. B. Wyatt (2013), Development of alteration rinds by oxidative weathering processes in Beacon Valley, Antarctica, and implications for Mars, *Geochim. Cosmochim. Acta*, 115, 137–161, doi:10.1016/j.gca.2013.04.002.
- Salvatore, M.R., et al., (2014), The dominance of cold and dry alteration processes on recent Mars, as revealed through pan-spectral orbital analyses. *EPSL.*, 404 (2014), pp. 261-272.
- Scott, D. H., and K. L. Tanaka (1986), Geologic map of the western equatorial region of Mars, 1:15,000,000.
- Settle, M. (1979), Formation and deposition of volcanic sulfate aerosols on Mars, *J. Geophys. Res.*, 84, 8343–8354.
- Skulte, E., (2015), On the Subject of Analyzing Iron and Sulfur Bearing Minerals from Three Extreme Environments: Geological Carbon Sequestration, Acid Mine Drainage, and Mars. Ph.D. Dissertation thesis, 433 pp., Stony Brook University, Stony Brook, NY.
- Soare, R. J., B. Horgan, S. J. Conway, C. Souness, and M. R. El Maarry (2015), Volcanic terrain and the possible periglacial formation of “excess ice” at the mid-latitudes of Utopia Planitia, Mars, 423(C), 182–192, doi:10.1016/j.epsl.2015.04.033.
- Smith, M.R., J.L. Bandfield, E.A. Cloutis, M.S. Rice (2013), Hydrated silica on Mars: Combined analysis with near-infrared and thermal-infrared spectroscopy, In *Icarus*, Volume 223, Issue 2, Pages 633-648, ISSN 0019-1035, <https://doi.org/10.1016/j.icarus.2013.01.024>.

- Swayze, G.A., et al. (2007), Spectral evidence for hydrated volcanic and/or impact glass on Mars with MRO CRISM. In Seventh International Conference on Mars, July 9–13, Pasadena, California, Lunar and Planetary Institute, Contribution No. 3384.
- Swayze, G. A., et al. (2002), Mineral mapping Mauna Kea and Mauna Loa shield volcanoes on Hawaii using AVIRIS data and the USGS Tetracorder spectral identification system: Lessons applicable to the search for relict Martian hydrothermal systems, JPL Publ., 03 – 4, 373 – 387.
- Swayze, G. A., R. N. Clark, A. F. H. Goetz, T. G. Chrien, and N. S. Gorelick (2003), Effects of spectrometer band pass, sampling, and signal-to-noise ratio on spectral identification using the Tetracorder algorithm, J. Geophys. Res., 108(E9), 5105, doi:10.1029/2002JE001975.
- Tosca, N.J., S. M. McLennan, D. H. Lindsley, and M. A. A. Schoonen (2004), Acid-sulfate weathering of synthetic Martian basalt: The acid fog model revisited, JGR., 109, E05003.
- Tosca, N.J., S. M. McLennan, B. C. Clark, J. P. Grotzinger, J. A. Hurowitz, A. H. Knoll, C. Schroder, and S. W. Squyres (2005), Geochemical modeling of evaporation processes on mars: Insight from the sedimentary record at meridiani planum. EPSL, 240(1):122–148.
- Tosca, N.J., A.H. Knoll, and S.M. McLennan (2008), Water activity and the challenge for life on early Mars: Science, v. 320, p. 1204–1207, doi: 10.1126/science.1155432.
- Vaniman, D. T., et al., (2014), Mineralogy of a mudstone on Mars, Science, 343.
- Viviano and Moersch (2012), A technique for mapping Fe/Mg-rich phyllosilicates on Mars using THEMIS multispectral thermal infrared images. JGR, 117:E07007.
- Viviano-Beck, C. E., F.P. Seelos, S.L. Murchie, E.G. Kahn, K.D. Seelos, H.W. Taylor, K. Taylor, B.L. Ehlmann, S.M. Wiseman, J.F. Mustard, M.F. Morgan (2014), Revised CRISM spectral parameters and summary products based on the currently detected mineral diversity on Mars, J. Geophys. Res. Planets, 119, 1403–1431, doi:10.1002/2014JE004627.

- Wolff-Boenisch D., S. R. Gislason, E. H. Oelkers, and C. V. Putnis (2004), The dissolution rates of natural glasses as a function of their composition at pH 4 and 10.6, and temperatures from 35 to 74C, *Geochim. Cosmochim. Acta*, 68, 4843-4858.
- Wray, J.J., Murchie, S.L., Squyres, S.W., Seelos, F.P., Tornabene, L.L. (2009), Diverse aqueous environments on ancient Mars revealed in the southern highlands. *Geology* 39, 1043–1046.
- Wray, J.J., et al. (2011), Columbus crater and other possible groundwater-fed paleolakes of Terra Sirenum, Mars. *Journal of Geophysical Research*, 116, E01001, doi:10.1029/2010JE003694.
- Wyatt, M. B., and H. Y. McSween (2002), Spectral evidence for weathered basalt as an alternative to andesite in the northern lowlands of Mars. *Nature*, 417, 263– 266.
- Wyatt, M. B., V. E. Hamilton, H. Y. McSween Jr., P. R. Christensen, and L. A. Taylor (2001), Analysis of terrestrial and Martian volcanic compositions using thermal emission spectroscopy: 1. Determination of mineralogy, chemistry, and classification strategies, *J. Geophys. Res.*, 106(E7), 14711–14732.
- Yant, M., A. D. Rogers, H. Nekvasil, Y.-Y. S. Zhao, and T. Bristow (2016), Spectral characterization of acid weathering products on Martian basaltic glass, *J. Geophys. Res. Planets*, 121, doi:10.1002/2015JE004969.
- Yant, M. H., et al., (2015), Spectral Characterization and Effects of Volatiles on Synthetic Irvine Basalt and Glass, *LPSC.*, XLVI, abstract 1230.

Table 6-1. Library spectra.

Library phase	Group	Library phase	Group
1 ol_fo91	olivine	22 kieserite	sulfate
2 ol_fo68	olivine	23 anhydrite	sulfate
3 ol_fo53	olivine	24 quartz	quartz
4 ol_fo39	olivine	25 krichglass	high-silica phase
5 ol_fo18	olivine	26 silicaglass	high-silica phase
6 ol_fo1	olivine	27 serpentine	high-silica phase
7 albite	feldspar	28 illite	high-silica phase
8 oligoclase	feldspar	29 camont	high-silica phase
9 andesine	feldspar	30 saponite	high-silica phase
10 labradorite	feldspar	31 heulandite	high-silica phase
11 bytownite	feldspar	32 stilbite	high-silica phase
12 anorthite	feldspar	33 calcite	carbonate
13 diopside	high-Ca pyroxene	34 dolomite	carbonate
14 augite_nmnh9780	high-Ca pyroxene	35 hematite	hematite
15 augite_nmmh122302	high-Ca pyroxene	37-1 Irvine pH0	Irvine synthetic glass
16 hedenbergite	high-Ca pyroxene	37-2 Backstay pH0	Backstay synthetic glass
17 pigeonite	low-Ca pyroxene	37-3 Pathfinder soil pH1	Pathfinder soil synthetic glass
18 enstatite	low-Ca pyroxene	37-4 BAS101 pH1	Hawaiian glassy basalt
19 bronzite	low-Ca pyroxene	37-5 BSB101 pH1	Hawaiian basaltic glass sand
20 alh84001	low-Ca pyroxene	37-6 Pathfinder rock pH0	Pathfinder rock synthetic glass
21 gypsum	sulfate		

Table 6-2. Synthetic Pathfinder, Irvine, Backstay and terrestrial Bas101, Bsb101 glass bulk compositions.

Oxide	PFR Average	PFS Average	Irvine Average	Backstay Average	Bas 101	Bsb 101
SiO₂	57.87	48.68	47.91	49.78	50.96	50.84
TiO₂	0.51	1.16	1.04	0.96	3.21	2.21
Al₂O₃	10.36	10.29	10.99	13.69	13.19	13.04
FeO_T^b	13.73	19.23	17.83	14.81	11.64	11.53
MnO	0.46	0.49	0.39	0.23	0.18	0.17
MgO	2.47	7.66	10.89	8.32	6.42	9.77
CaO	8.68	7.07	5.98	5.96	10.78	10.02
Na₂O	4.28	3.56	2.74	3.65	3.07	2.04
K₂O	1.11	0.67	0.68	0.77	0.54	0.37
P₂O₅	0.54	1.19	0.94	1.35	0.00	0.00
Cr₂O₃	0.00	0.00	0.19	0.14	0.00	0.00
S	0.00	0.00	0.33	0.33	0.00	0.00
Cl	0.00	0.00	0.09	0.01	0.00	0.00
Total	100.01	100.00	100.00	100.00	100.00	100.00

Source: Irvine and Backstay: Yant *et al.*, 2016, PFR and PFS: Tosca *et al.*, 2004, Bas101 and Bsb101: Horgan *et al.*, 2016. All values are listed as wt.% and have been normalized to 100.

Table 6-3. Spectral parameters utilized for the detection of sulfates

Band	λ_{band}	$\lambda_{\text{continuum}}$	Target mineral
BD 1.90	1.91-1.94	1.73-1.85, 2.10, 2.16	Most hydrated minerals
BD 2.10	2.06-2.16	1.85-1.95, 2.20-2.24	Mono-hydrated sulfates
BD 2.45	2.43-2.50	2.28-2.35	Zeolites, Sulfates

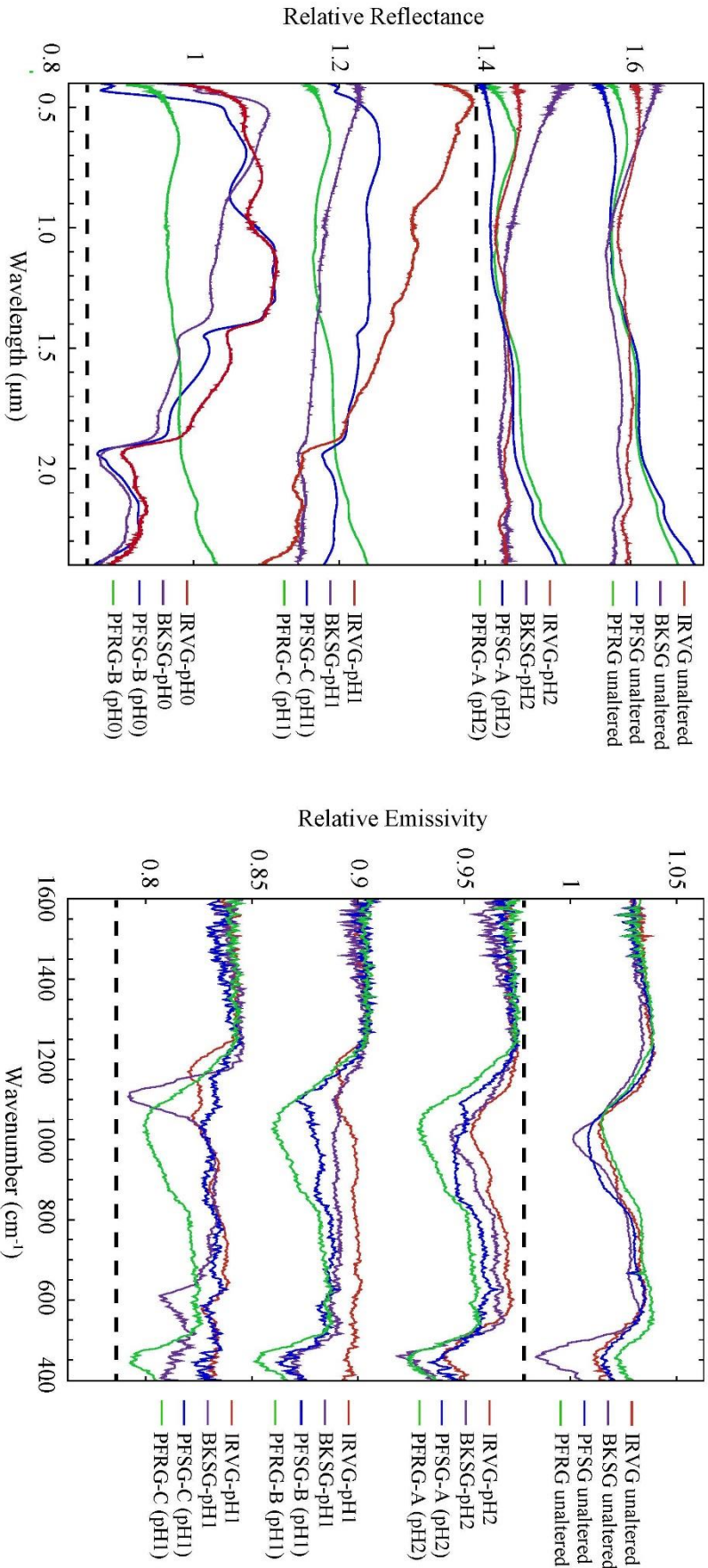


Figure 6-1: Overview of the A) reflectance signatures and B) thermal emission signatures of the unaltered and altered (pH0-2) material from the four Yant *et al.* [2016] compositions; Irvine (IRVG, red), Backstay (BKSG, blue), Pathfinder soil (PFSG, purple), and Pathfinder rock (PFRG, green). The dotted lines outline the spectra that exhibit alteration features, (VNIR – pH0-1, MIR – pH0-2).

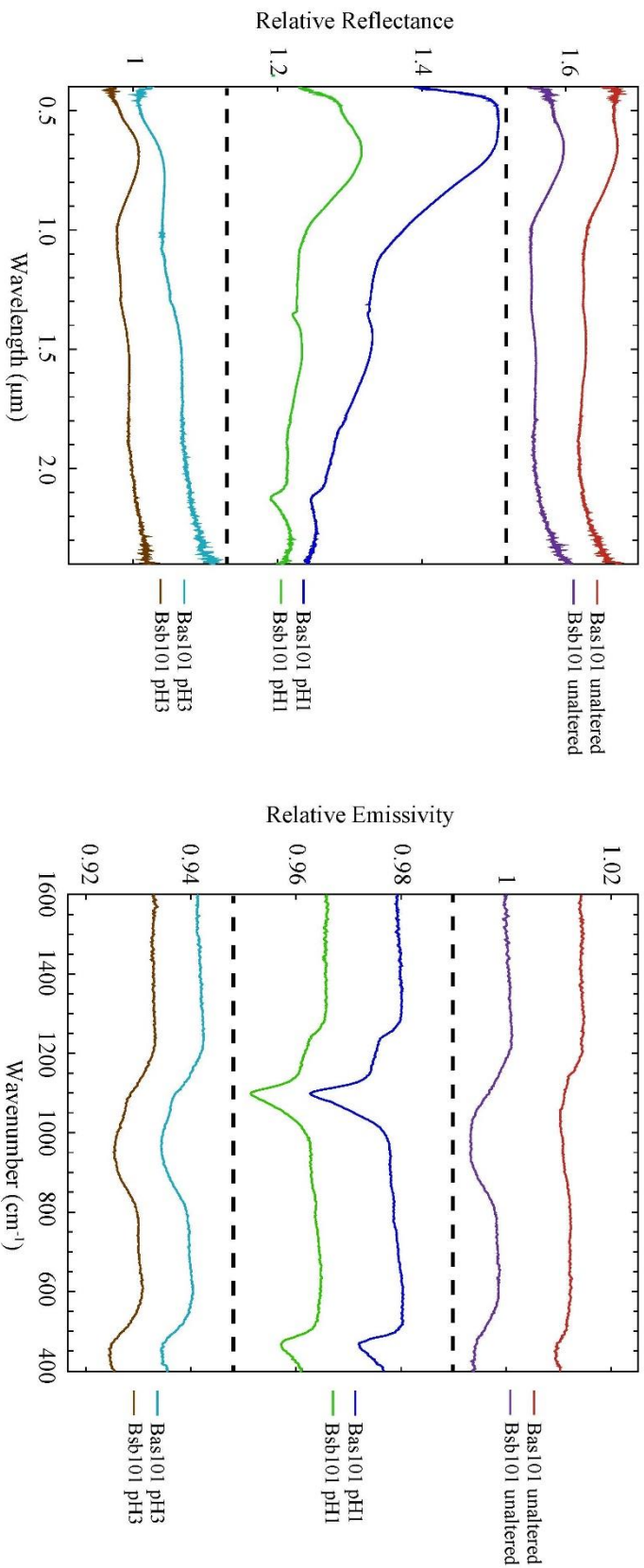


Figure 6-2: Overview of the A) reflectance signatures and B) thermal emission signatures of the unaltered and altered material from the two Horgan *et al.* [2017] compositions; the dotted lines outline the spectra that exhibit alteration features, (VNIR, MIR – pH1).

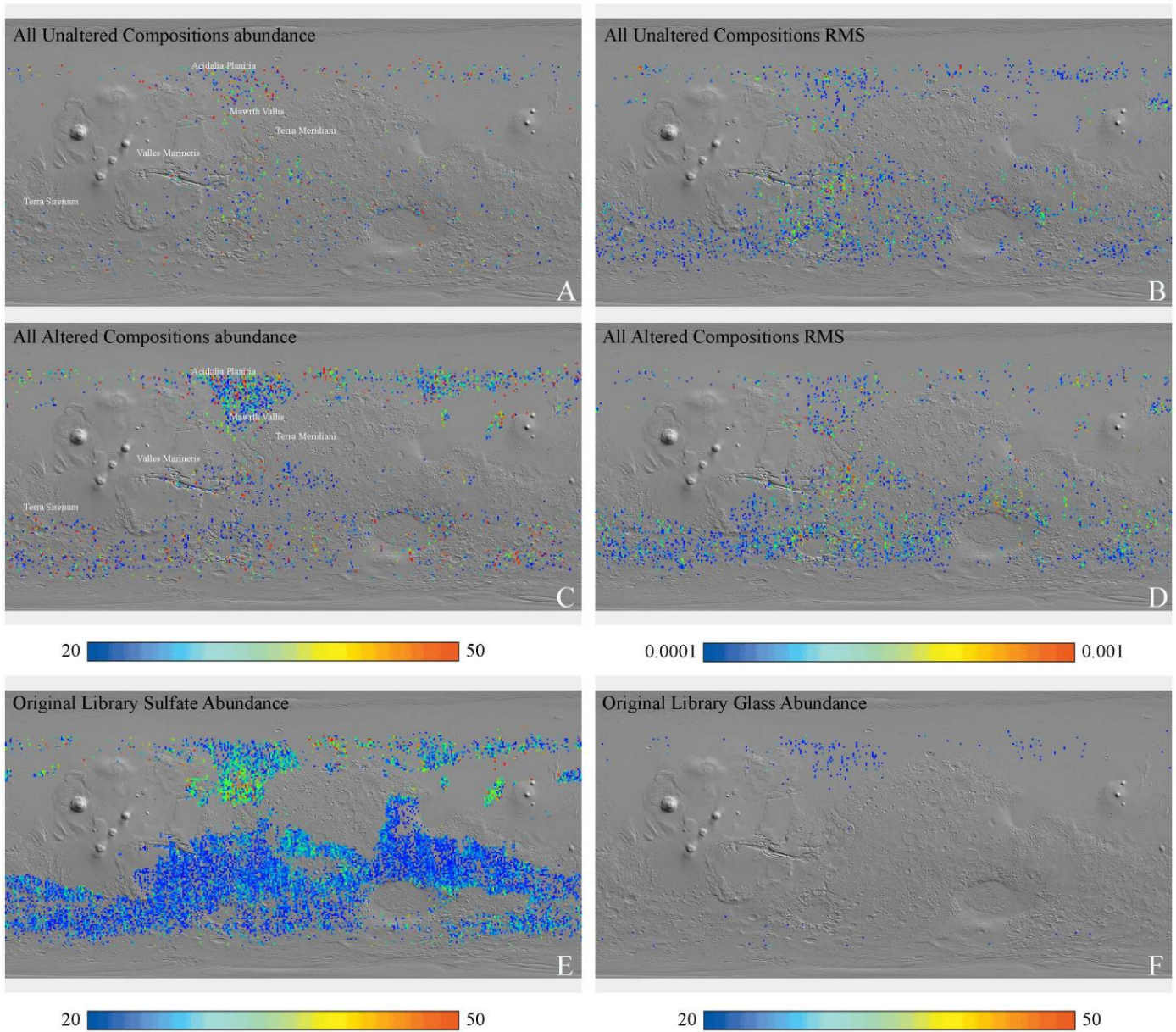


Figure 6-3: One pixel per degree binned global TES maps showing combined abundances and RMS differences for A, B) all unaltered compositions and C, D) all altered compositions (Irvine pH0, Backstay pH0, Pathfinder Soil pH1, BAS101 pH 1, BSB101 pH1). The scale ranges from blue (abundance = 20) to red (abundance = 50). RMS difference maps are shown for pixels where our expanded library provides better fits than the previous library. Global TES abundance maps using the original library from *Rogers and Hamilton* [2015] are shown for E) sulfates and F) glass.

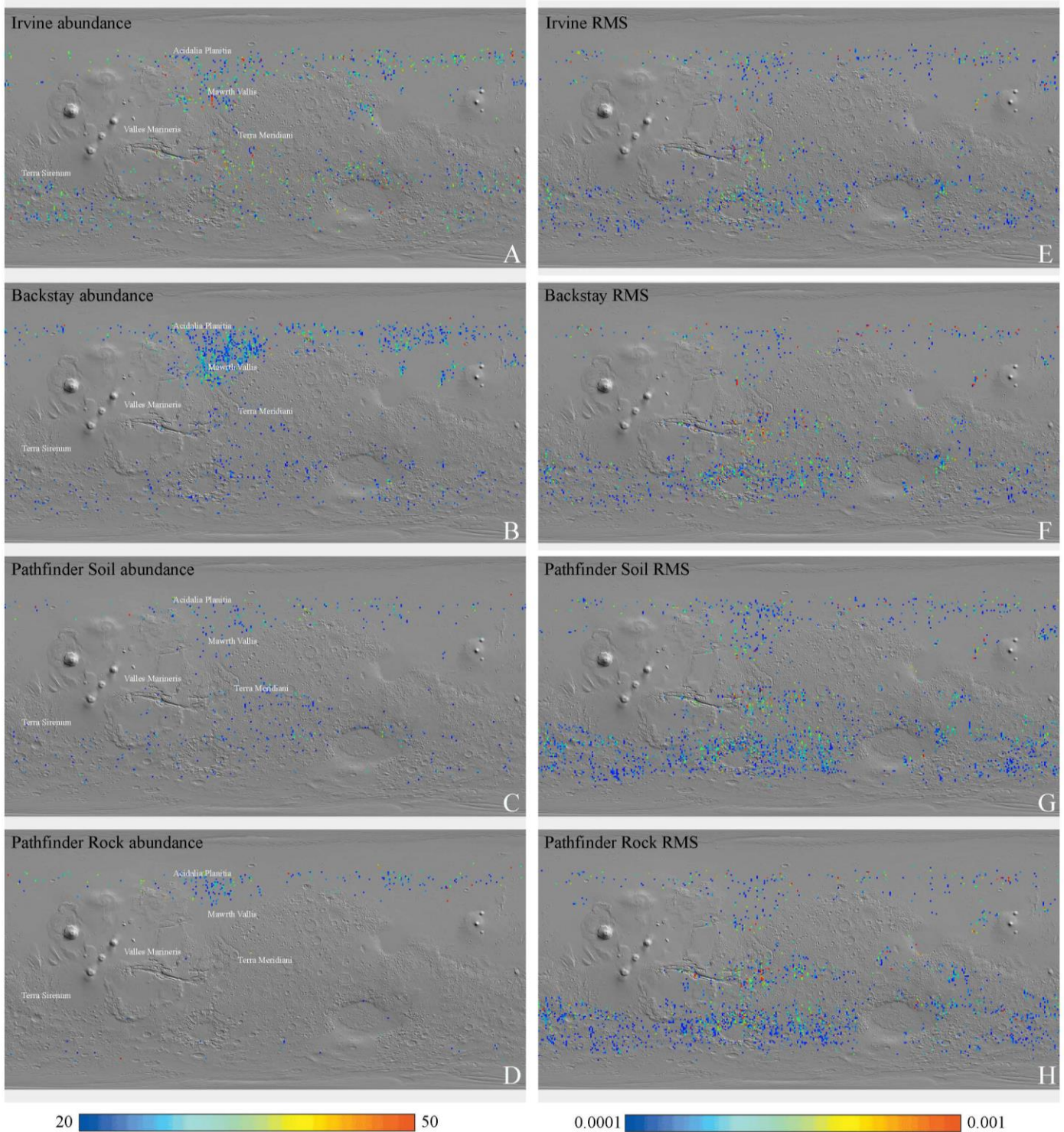


Figure 6-4: One pixel per degree binned global TES map showing the abundances ranging from 20-50% for A) Irvine (pH0), B) Backstay (pH0), C) Pathfinder Soil (pH1), and D) Pathfinder Rock (pH0-4). The scale ranges from blue (abundance = 20) to red (abundance = 50). RMS difference maps showing pixels where our expanded library provides better fits than the previous library for E) Irvine, F) Backstay, G) Pathfinder Soil, and H) Pathfinder Rock.

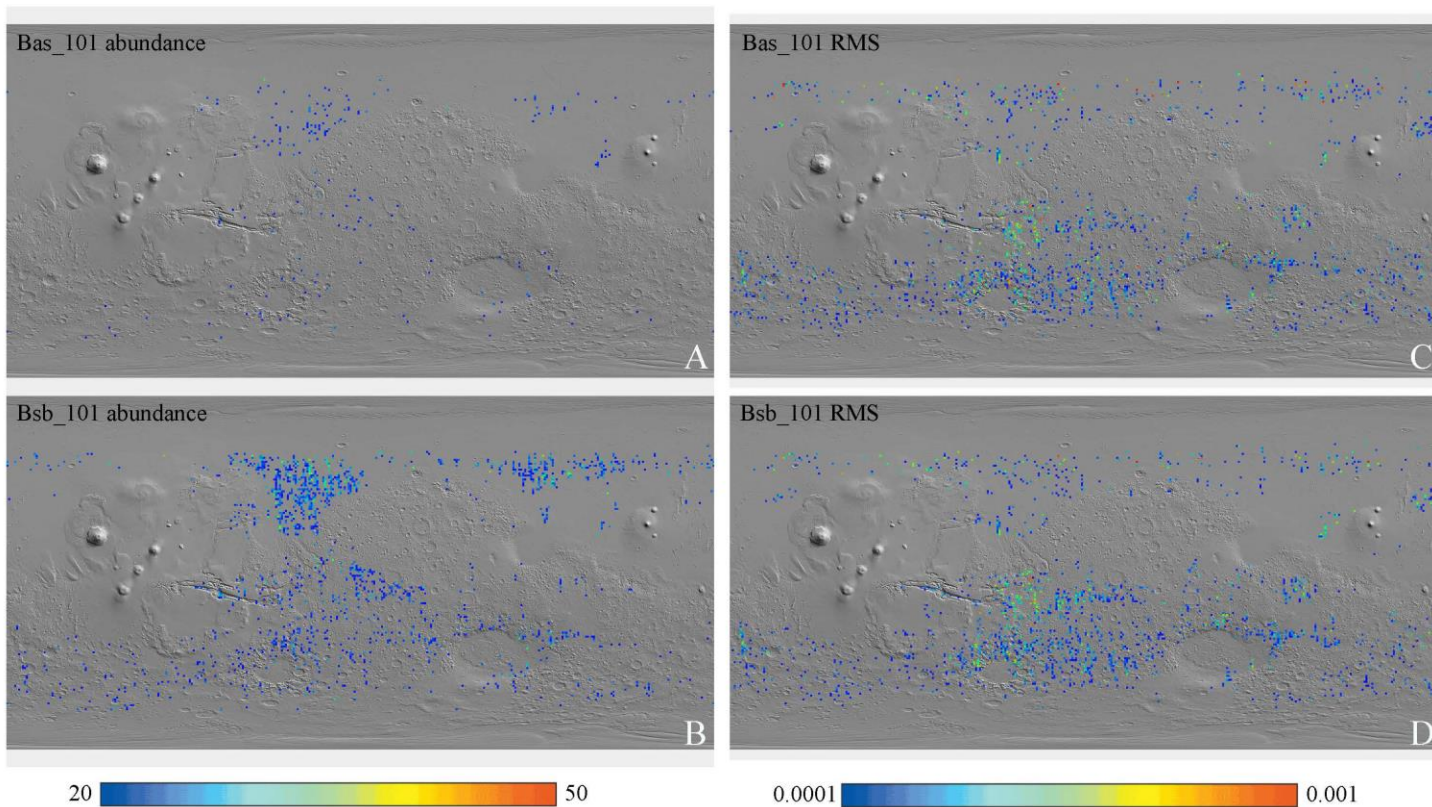


Figure 6-5: One pixel per degree binned global TES map showing the abundances ranging from 20-50% for A) Bas_101 (pH1) and B) Bsb_101 (pH1). The scale ranges from blue (abundance = 20) to red (abundance = 50). RMS difference maps showing pixels where our expanded library provides better fits than the previous library for C) Bas_101 and D) Bsb_101.

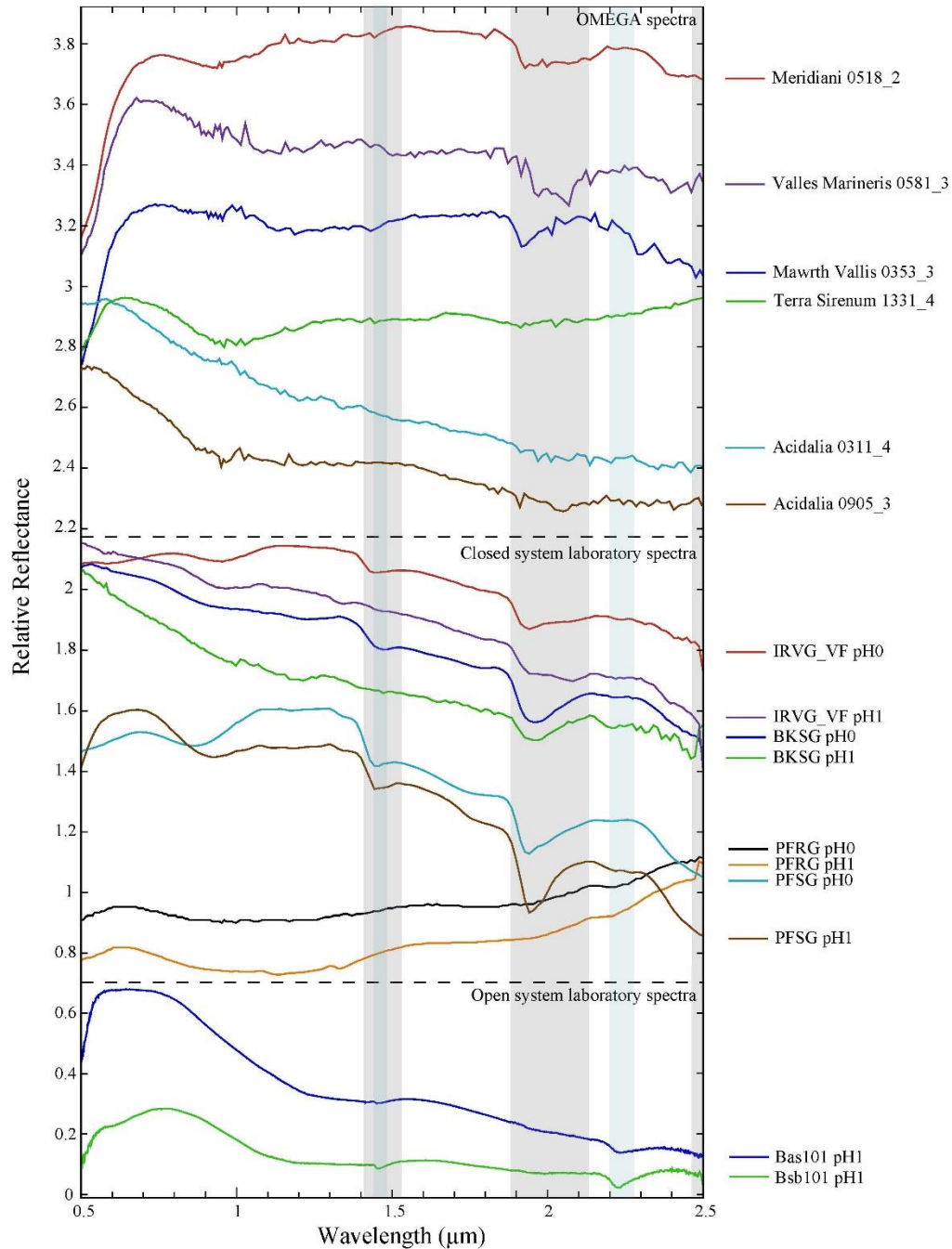


Figure 6-6: Reflectance spectra for each of the regions of interest from the green areas shown in Figure 6-8. For comparison, the spectral signatures for the Irvine, Backstay, Pathfinder Soil, and Pathfinder Rock glasses altered in pH0-1 are plotted along with the spectral signatures for the Bas101 and Bsb101 glasses altered in pH1. BKSG-pH1 is scaled by a factor of 5. Gray shaded areas indicate regions consistent with sulfate features. Blue shaded areas indicate regions consistent with silica features. The y-axis has been offset for clarity.

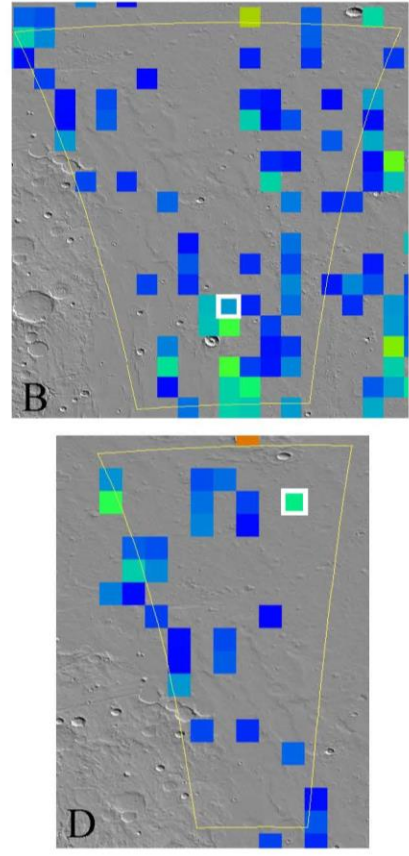
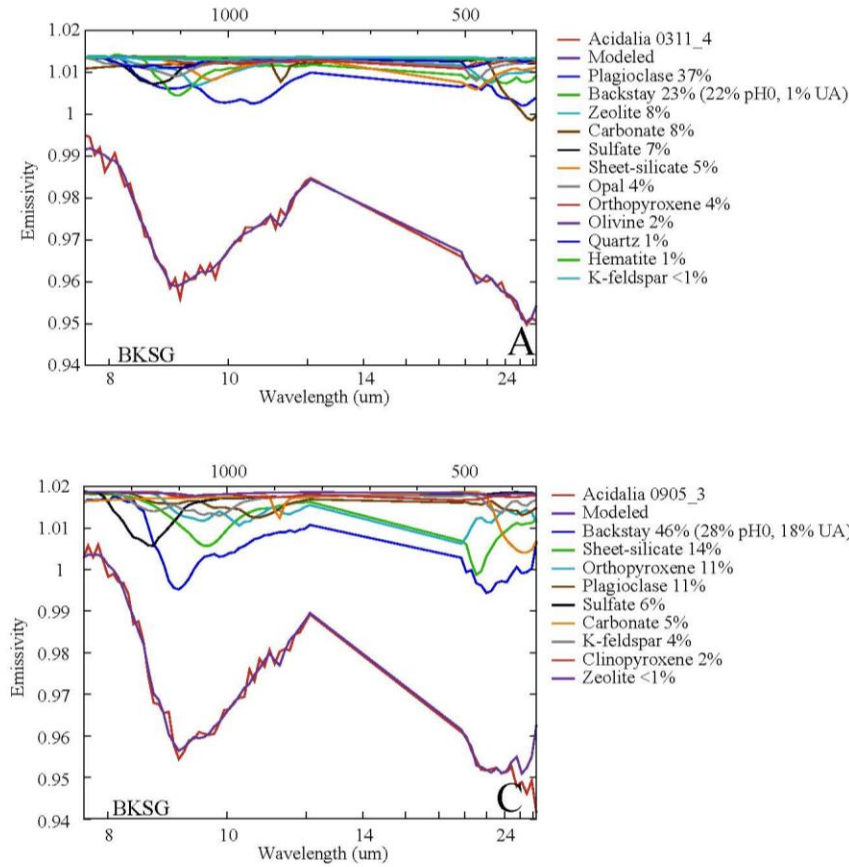


Figure 6-7: A, C) Linear least squares models using the Backstay library for TES pixels that overlap with OMEGA sulfate detections in Acidalia. The modeled pixels are outlined in white in panels B and D.

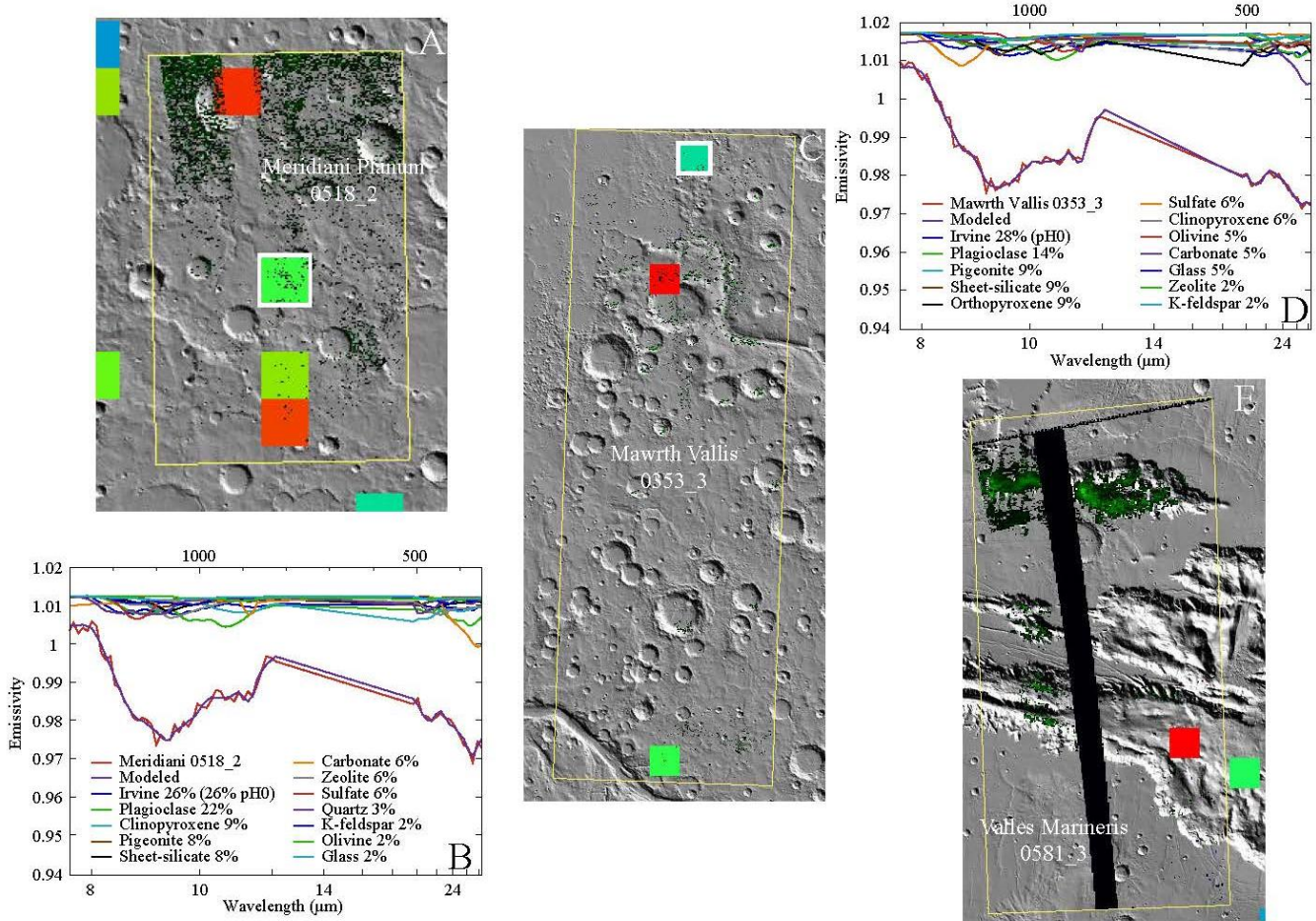


Figure 6-8: Images of stamps showing the overlap of Irvine TES pixels (squares) with OMEGA sulfate features (green areas) for A) Meridiani Planum, C) Mawrth Vallis, and E) Valles Marineris. White outlined boxes indicate the pixels used for linear least squares modeling in panels B and D.

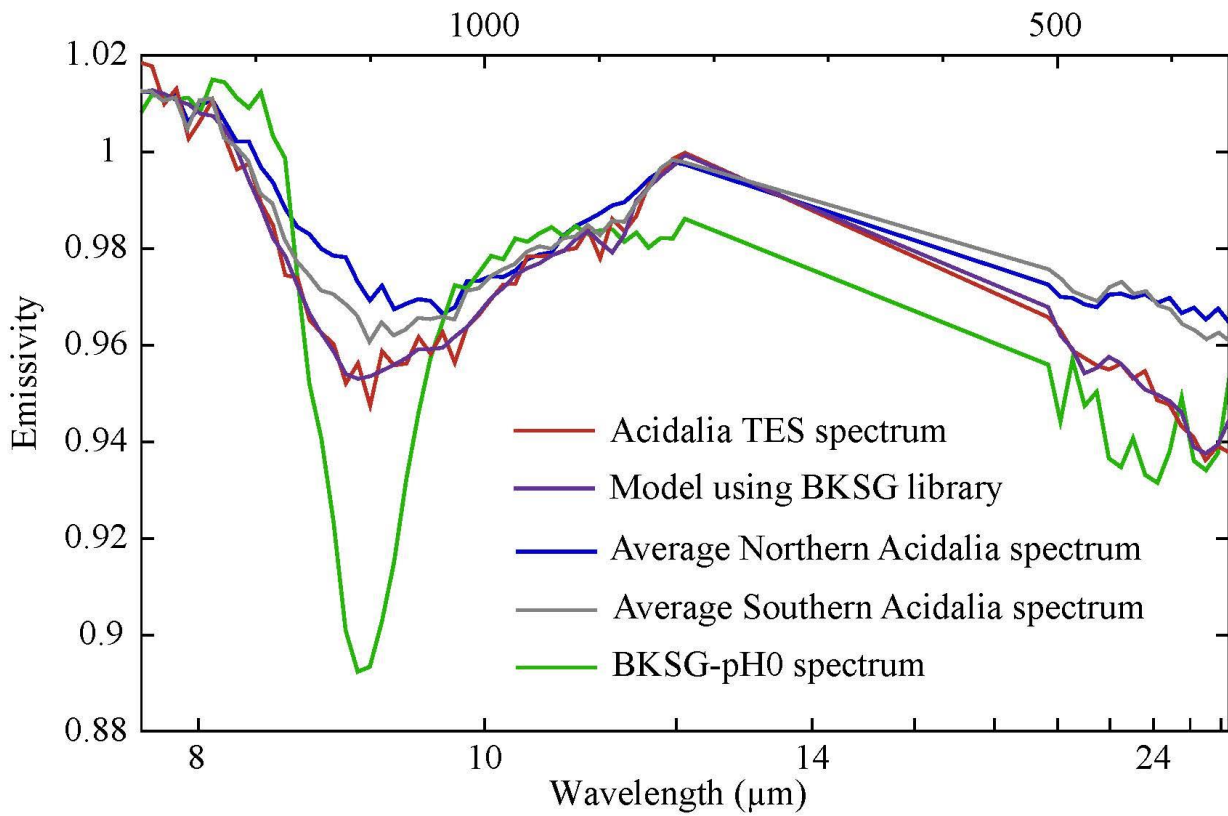


Figure 6-9: TES signature from Acidalia (red) plotted along with model using Backstay Library (purple). Shown for comparison are the spectra for average northern (blue) and southern (gray) Acidalia signatures along with the Backstay material altered under pH0 (green).

Chapter 7: Concluding Remarks

The spectral and chemical analysis of unaltered/cation-conservative altered synthetic glass endmembers with measured Martian compositions [Yant *et al.*, 2016] as well as unaltered/open-system altered natural glass endmembers for terrestrial analogs [Horgan *et al.*, 2017; Yant *et al.*, 2018] provided a novel library that allows insight into the aqueous alteration history of the surface of Mars. The results from the synthetic and terrestrial laboratory glass experiments indicated that only solutions with a starting pH less than or equal to one, yielded alteration-dominated spectral signatures. For the cation-conservative synthetic glasses, sulfate-dominated signatures were observed in the infrared [Yant *et al.*, 2016], whereas silica-dominated signatures were observed for the open-system terrestrial glasses [Horgan *et al.*, 2017]. Additionally, strong negative slopes were observed in the VNIR for both the synthetic and terrestrial $\text{pH} \leq 1$ materials. These results are similar to spectral signatures observed for Hawaiian glassy basalts altered in an active solfatara environment [Yant *et al.*, 2018]. Primarily silica-dominated spectral signatures were observed in the MIR and the VNIR signatures are consistent with silica, Fe-oxides, and sulfates (Ca, Fe). The silica-dominated signatures exhibited by the open system materials are distinct from the sulfate-dominated signatures exhibited by cation-conservative altered samples. This likely reflects a difference in open vs. closed system weathering, where mobile cations are removed from the altered surfaces in the fumarolic setting.

In order to assess the prevalence of acid-weathered surfaces on Mars, the libraries created here for laboratory altered materials were applied to TES and OMEGA data sets between 70°N and 70°S latitude. Both TES and OMEGA data sets exhibit strong evidence for acid weathered glass in the northern lowlands of Mars, with additional potential detections in Terra Meridiani, Vallis Marineris, and Mawrth Vallis. Acidalia provides a large region where acidic alteration

signatures have been observed using CRISM/OMEGA data. Acidalia TES spectral signatures often exhibit an absorption minima near 1110cm^{-1} . This feature was previously attributed to a highly polymerized component [Michalski *et al.*, 2005], which is consistent with the interpretation from Horgan *et al.* [2017]. Horgan *et al.* [2017] suggests that an acid-leached basaltic glass ($\sim\text{pH}1$) could be contributing to the high-silica component of TES Surface Type 2 which supported by the strong concave-up visible/near-infrared spectral shape of the northern plains. However, the Backstay glass altered under $\text{pH}0$ conditions produced a strong absorption near 1110cm^{-1} which could be contributing to the TES signatures.

Sulfate signatures in the VNIR range are lacking for Acidalia, instead the spectra exhibit shallow features with negative spectral slopes. The open-system materials altered in $\text{pH}1$ exhibited shallow features along with negative spectral slopes that are more comparable with the Acidalia OMEGA signatures than the Backstay signatures. The combined analysis of TIR and VNIR would suggest that the 1110 cm^{-1} feature is more likely due to acid-leached glass, where the sulfate weathering products have been removed via subsequent aqueous activity or physical abrasion, as suggested by Horgan *et al.*, [2017]. However, it is possible that sulfates are present, but are masked in VNIR by opaques or dust, which is supported by elevated sulfur and hydrogen signatures in the Acidalia region. Regardless of whether the spectral signatures represent open- or closed-system acid weathering, both data sets indicate that the materials in the northern lowlands have experienced very low pH conditions. The detection of signatures consistent with acid alteration in both the MIR and VNIR wavelength ranges over such an expansive region suggests a more recent, active and regional process for weathering in Acidalia.

Future work will be aimed at addressing the spectral characteristics of other planetary bodies. This work has shown that starting composition, pH , volatile content, and particle size all

affect the spectral properties of Martian analog materials which suggests that these are important parameters for analyzing the surfaces of other planetary bodies as well. Additionally, further investigation is required with volatile contents (e.g., volatile species, wt.% ranges) to fully understand their effects on spectral signatures.

References:

- Michalski J.R., M.D. Kraft, T.G. Sharp, L.B. Williams, and P.R. Christensen (2005), Mineralogical constraints on the high-silica martian surface component observed by TES. *Icarus* 174: 161-177.
- Horgan, B. H. N., R. J. Smith, E. A. Cloutis, P. Mann, and P. R. Christensen (2017), Acidic weathering of basalt and basaltic glass: 1. Near-infrared spectra, thermal infrared spectra, and implications for Mars, *J. Geophys. Res. Planets*, 122, 172–202, doi:10.1002/2016JE005111.
- Yant, M., A. D. Rogers, H. Nekvasil, Y.-Y. S. Zhao, and T. Bristow (2016), Spectral characterization of acid weathering products on Martian basaltic glass, *Journal of Geophysical Research - Planets*, 121, doi:10.1002/2015JE004969.
- Yant, M., K.E. Young, A. D. Rogers, A.C. McAdam, J.E. Bleacher, J.L. Bishop, and S.A. Mertzman (2018), Visible, Near-Infrared and Mid-Infrared Spectral Characterization of Hawaiian Fumarolic Alteration near Kilauea's December 1974 Flow: Implications for Spectral Discrimination of Alteration Environments on Mars, *Am. Min.*, 121, doi:10.1002/2015JE0049

Table A1: Modeled abundances for Irvine and Backstay glass thermal infrared spectra from *Chapter 3*.

Library Endmember	Quality	Irvine Glass					Backstay Glass				
		IRVG-pH0	IRVG-pH1	IRVG-pH2	IRVG-pH3	IRVG-pH4	BKSG-pH0	BKSG-pH1	BKSG-pH2	BKSG-pH3	BKSG-pH4
¹ Unaltered	wc	18.67	6.90	81.53	82.57	79.99	-	69.55	83.55	77.40	84.53
² Thenardite	wc	-	-	-	-	-	-	-	-	-	-
² Aphthitalite	wc	-	-	-	-	-	2.80	-	-	-	-
² Glauberite	wc	-	-	-	-	-	-	-	-	-	-
² Anhydrite	wc	-	1.56	-	-	-	-	-	-	-	-
² Barite	wc	-	-	-	-	-	-	-	-	-	-
² Celestite	wc	-	-	-	-	-	-	-	-	-	-
^{2a} Anglesite	wc	-	-	-	-	-	-	-	-	-	-
² Antlerite	wc	-	-	-	-	-	-	-	-	-	-
² Alunite	wc	-	-	-	-	-	1.84	-	-	-	-
^{2b} Minamiite	wc	-	-	-	-	-	-	-	-	-	-
² Sulfohalite	wc	-	-	-	-	-	-	-	-	-	-
² Hanksite	wc	-	-	-	-	-	-	-	-	-	-
² Szomolnokite	wc	-	-	-	-	-	-	-	-	-	-
² Bloedite	wc	-	-	-	-	-	-	-	-	-	-
² Polyhalite	wc	-	-	-	-	-	-	-	-	-	-
² Bassanite	wc	6.27	11.59	-	-	-	-	-	-	-	-
² Gypsum	wc	-	-	-	-	-	-	-	-	-	-
² Zincobotryogen	wc	-	-	-	-	-	-	-	-	-	-
^{2c} Coquimbite/Paracoquimbite	wc	-	21.69	-	-	-	2.00	2.96	-	-	-
³ Römerite	wc	-	-	-	-	-	-	-	-	-	-
³ Botryogen-Zn	wc	-	-	-	-	-	-	-	-	-	-
^{3d} Copiapite	wc	-	-	-	-	-	-	-	-	-	-
³ Amaranite	wc	-	-	-	-	-	-	-	-	-	-
^{3e} Butlerite	wc	-	-	-	-	-	-	-	-	-	-
³ Parabutlerite	wc	-	-	-	-	-	-	-	-	-	-
^{3f} Jarosite	wc	-	-	0.34	-	-	-	-	-	-	-
³ Hydronium jarosite	wc	-	-	-	-	-	-	-	-	-	-

³	Goldichite	wc	-	-	-	-	-	-	-	-	-	-
³	Rhomboclase	wc	19.34	1.05	-	-	-	-	-	-	-	-
³	Kornelite	wc	-	-	-	-	-	-	-	-	-	-
³	Voltaite	wc	4.44	-	-	-	-	-	-	-	-	-
^{3g}	Beaverite	wc	-	-	-	-	-	-	-	-	-	-
³	Mg-copiapite	wc	-	-	-	-	1.39	-	-	-	-	-
³	Natrojarosite	wc	-	-	6.14	5.76	-	-	-	-	-	-
^{3h}	Sideronatrite	wc	-	-	-	-	-	-	-	-	-	-
³	Slavikite	wc	-	-	-	-	-	-	-	-	-	-
³	Yavapaiite	wc	4.57	-	-	-	7.26	-	-	-	-	-
¹	K-jarosite powder	wc	-	-	-	-	-	-	-	-	-	-
⁴	Anhydrite	wc	-	-	-	-	-	-	-	-	-	-
⁴	Anhydrous Magnesium Sulfate	wc	2.16	-	-	-	-	-	-	-	-	-
⁴	Bassanite	wc	-	-	-	-	-	-	3.56	2.54	1.06	1.66
⁴	Epsomite	wc	-	-	-	-	-	5.03	-	-	-	-
⁴	Gypsum	wc	10.79	-	-	-	-	16.76	7.36	-	-	-
⁴	Kieserite	wc	9.08	9.24	-	-	-	-	-	-	-	-
⁴	Pentahydrate	wc	-	-	-	-	-	-	-	-	-	-
⁴	Sanderite	wc	-	-	-	-	-	-	-	-	-	-
⁴	Starkeyite	wc	-	-	-	-	-	-	-	-	-	-
⁵	Halotrichite pellet	nc	-	-	-	-	-	0.90	-	-	-	-
⁵	Dietrichite pellet	nc	13.19	-	-	-	-	-	-	6.50	17.11	9.55
⁵	Leonite pellet	nc	-	-	-	-	-	-	-	-	-	-
⁶	Mikasaite	wc	-	-	-	-	-	-	-	-	-	-
⁶	Rozenite	wc	-	-	-	-	-	-	-	-	-	-
⁶	Amorphous ferrous sulfate	wc	-	-	-	-	-	-	-	-	-	-
⁶	MV amorphous	wc	-	-	-	-	-	-	-	-	-	-
⁶	LV amorphous	wc	-	-	-	-	8.30	-	-	-	-	-
⁶	MH amorphous	wc	-	-	-	-	3.06	-	-	-	-	-
⁶	LH amorphous	wc	7.34	-	-	-	-	-	-	-	-	-

6	Acros (lausenite)	wc	-	-	-	-	-	-	-	-	-	-
6	Melanterite	wc	-	-	-	-	70.28	4.31	-	-	-	-
6	Szomolnokite	wc	-	8.07	-	-	-	-	-	-	-	-
7	Al-Opal	wc	-	20.37	-	-	-	9.12	2.14	0.38	-	-
8	K-rich Glass	wc	-	-	-	-	-	-	-	-	-	-
8	SiO2 Glass	wc	-	-	-	-	-	-	-	-	-	-
9	elemental sulfur	wc	-	0.31	-	-	0.04	0.89	4.51	4.05	4.26	-
10	Goethite Powder GTS2	wc	-	2.69	6.50	5.39	-	2.25	0.76	-	-	-
11	Akaganeite akg1	wc	-	0.98	2.21	2.88	-	-	-	-	-	-
11	Lepidocrocite lps2	wc	-	-	2.01	1.81	-	-	-	-	-	-
12i	Hematite BUR-2600	wc	-	-	-	-	-	-	-	-	-	-
10	Hematite gtsh2-300	wc	-	-	1.27	1.59	-	-	-	-	-	-
10	Magnetite mts4	wc	4.15	-	-	-	-	-	-	-	-	-
10	Magnetite mts5	wc	-	-	-	-	-	-	-	-	-	-
2j	Pickeringite	wc	-	-	-	-	-	-	-	-	-	-
2k	Apjohnite	wc	-	-	-	-	-	-	-	-	-	-
2	Thaumasite	wc	-	-	-	-	0.35	-	-	-	-	-
2	Serpierite	wc	-	-	-	-	-	-	-	-	-	-
5	Alunogen	nc	-	15.55	-	-	-	-	-	-	-	-
13	jf_sinter12b (silica sinter)	nc	-	-	-	-	-	-	-	-	-	-
13	jf_sinter12_63-500f	nc	-	-	-	-	-	-	-	-	-	-
13	jf_sinter12_L63f2	nc	-	-	-	-	-	-	-	-	-	-
13	frit203flat (synthetic amorphous silica)	wc	-	-	-	-	-	-	-	-	-	-
13	frit203_G63	wc	-	-	-	-	-	-	-	-	-	-
13	frit203_L63	wc	-	-	-	-	-	-	-	-	-	-
13	fqtz_disc (synthetic microporous silica)	wc	-	-	-	-	-	-	-	-	-	-
13	fqtz_G63f	wc	-	-	-	-	-	-	-	-	-	-
13	fqtz_L63f	wc	-	-	-	-	-	-	-	-	-	-
Total			100	100	100	100	100	100	100	100	100	100

Table A2: Linear least squares modeled abundances for Pathfinder Soil and Rock glass thermal infrared spectra from *Chapter 3*.

Library Endmember	Quality	Pathfinder Soil Glass					Pathfinder Rock Glass				
		PFSG-A	PFSG-B	PFSG-C	PFSG-D	PFSG-E	PFRG-A	PFRG-B	PFRG-C	PFRG-D	PFRG-E
¹ Unaltered	wc	22.63	46.45	70.91	80.88	78.23	89.43	89.92	89.96	88.29	90.82
² Thenardite	wc	-	-	-	-	-	-	-	-	-	-
² Aphthitalite	wc	-	-	-	-	-	-	-	-	-	-
² Glauberite	wc	-	-	-	-	-	-	-	-	-	-
² Anhydrite	wc	-	-	-	-	-	-	-	-	-	-
² Barite	wc	-	-	-	-	-	-	-	-	-	-
² Celestite	wc	-	-	-	-	-	-	-	-	-	-
^{2a} Anglesite	wc	-	-	-	-	-	-	-	-	-	-
² Antlerite	wc	-	-	-	-	-	-	-	-	-	-
² Alunite	wc	-	-	-	-	-	-	-	-	-	-
^{2b} Minamiite	wc	-	-	-	-	-	-	-	-	-	-
² Sulfohalite	wc	-	-	-	-	-	-	-	-	-	-
² Hanksite	wc	-	-	-	-	-	-	-	-	-	-
² Szomolnokite	wc	-	-	-	-	-	-	-	-	-	-
² Bloedite	wc	-	-	-	-	-	-	-	-	-	-
² Polyhalite	wc	-	-	-	-	-	-	-	-	-	-
² Bassanite	wc	-	-	-	-	-	-	-	-	-	-
² Gypsum	wc	-	-	-	-	-	-	-	-	-	-
² Zincobotryogen	wc	-	-	-	-	-	-	-	-	-	-
^{2c} Coquimbite/Paracoquimbite	wc	-	4.27	10.75	2.23	-	-	0.32	-	-	-
³ Römerite	wc	-	-	-	-	-	-	-	-	-	-
³ Botryogen-Zn	wc	-	-	-	-	-	-	-	-	-	-
^{3d} Copiapite	wc	-	-	-	-	-	-	-	-	-	-
³ Amarantite	wc	-	-	-	-	-	-	-	-	-	-
^{3e} Butlerite	wc	-	-	-	-	-	-	-	-	-	-
³ Parabutlerite	wc	-	-	-	-	-	-	-	-	-	-
^{3f} Jarosite	wc	-	-	1.55	0.76	-	1.10	0.81	-	0.08	-
³ Hydronium jarosite	wc	-	-	-	-	-	-	-	-	-	-

³	Goldichite	wc	-	-	-	-	-	-	-	-	-	-
³	Rhomboclase	wc	-	-	-	-	-	-	-	-	-	-
³	Kornelite	wc	-	-	-	-	-	-	-	-	-	-
³	Voltaite	wc	-	-	-	-	-	-	-	-	-	-
^{3g}	Beaverite	wc	-	-	-	-	-	-	-	-	-	-
³	Mg-copiapite	wc	-	-	-	-	-	-	-	-	-	-
³	Natrojarosite	wc	-	1.80	-	-	0.48	-	-	-	-	-
^{3h}	Sideronatrite	wc	-	-	-	-	-	-	-	-	-	-
³	Slavikite	wc	-	-	-	-	-	-	-	-	-	-
³	Yavapaiite	wc	-	-	-	-	-	-	-	-	-	-
¹	K-jarosite powder	wc	2.67	-	-	-	-	-	1.10	-	1.05	1.14
⁴	Anhydrite	wc	-	-	-	-	-	-	-	-	-	-
⁴	Anhydrous Magnesium Sulfate	wc	-	0.31	-	-	-	-	-	-	-	-
⁴	Bassanite	wc	-	-	-	-	-	-	-	-	-	-
⁴	Epsomite	wc	-	-	-	-	-	-	-	-	-	-
⁴	Gypsum	wc	-	5.77	2.07	-	-	-	0.07	-	-	-
⁴	Kieserite	wc	-	-	-	-	-	-	-	-	-	-
⁴	Pentahydrate	wc	-	-	-	-	-	-	-	-	-	-
⁴	Sanderite	wc	-	-	-	-	-	-	-	-	-	-
⁴	Starkeyite	wc	-	-	-	-	-	-	-	-	-	-
⁵	Halotrichite pellet	nc	-	2.59	-	-	-	-	-	-	-	-
⁵	Dietrichite pellet	nc	10.31	-	-	-	-	-	-	-	-	0.83
⁵	Leonite pellet	nc	-	-	-	-	-	-	-	-	-	-
⁶	Mikasaite	wc	-	-	-	-	-	-	-	-	-	-
⁶	Rozenite	wc	-	-	-	-	-	-	-	-	-	-
⁶	Amorphous ferrous sulfate	wc	-	-	-	-	-	-	-	-	-	-
⁶	MV amorphous	wc	-	-	-	-	-	-	-	-	-	-
⁶	LV amorphous	wc	-	-	-	-	-	-	-	-	-	-
⁶	MH amorphous	wc	-	-	-	-	-	-	-	-	-	-
⁶	LH amorphous	wc	-	-	-	-	-	-	-	-	-	-

6	Acros (lausenite)	wc	-	0.34	-	-	-	-	-	-	-	-
6	Melanterite	wc	-	0.06	-	-	-	-	-	-	-	-
6	Szomolnokite	wc	-	-	-	-	-	-	-	-	-	-
7	Al-Opal	wc	-	9.67	-	-	-	-	-	-	-	-
8	K-rich Glass	wc	-	-	-	-	-	-	-	-	-	-
8	SiO2 Glass	wc	-	-	-	-	-	-	-	-	-	-
9	elemental sulfur	wc	1.05	-	-	-	0.49	-	0.04	-	-	0.06
10	Goethite Powder GTS2	wc	-	0.23	5.46	1.19	-	-	-	-	-	-
11	Akaganeite akg1	wc	-	3.52	0.04	1.10	2.38	5.50	5.73	5.77	5.76	4.24
11	Lepidocrocite lps2	wc	-	1.85	-	1.92	1.37	-	-	-	-	-
12i	Hematite BUR-2600	wc	-	-	-	-	-	-	-	-	-	-
10	Hematite gtsh2-300	wc	-	-	-	-	-	0.07	-	-	0.03	0.26
10	Magnetite mts4	wc	0.67	-	-	-	1.73	-	-	-	-	-
10	Magnetite mts5	wc	1.36	-	-	-	-	-	-	-	-	-
2j	Pickeringite	wc	-	-	-	-	-	-	-	-	-	-
2k	Apjohnite	wc	-	-	-	-	-	-	-	-	-	-
2	Thaumasite	wc	0.36	-	-	-	1.01	0.96	0.89	4.27	0.77	2.65
2	Serpierite	wc	-	-	-	-	-	-	-	-	-	-
5	Alunogen	nc	60.95	23.14	9.22	11.92	14.31	2.94	1.12	-	4.02	-
13	jf_sinter12b (silica sinter)	nc	-	-	-	-	-	-	-	-	-	-
13	jf_sinter12_63-500f	nc	-	-	-	-	-	-	-	-	-	-
13	jf_sinter12_L63f2	nc	-	-	-	-	-	-	-	-	-	-
13	frit203flat (synthetic amorphous silica)	wc	-	-	-	-	-	-	-	-	-	-
13	frit203_G63	wc	-	-	-	-	-	-	-	-	-	-
13	frit203_L63	wc	-	-	-	-	-	-	-	-	-	-
13	fqtz_disc (synthetic microporous silica)	wc	-	-	-	-	-	-	-	-	-	-
13	fqtz_G63f	wc	-	-	-	-	-	-	-	-	-	-
13	fqtz_L63f	wc	-	-	-	-	-	-	-	-	-	-
Total			100	100	100	100	100	100	100	100	100	100

Table A3: Linear least squares modeled abundances for pressed pellet Irvine and Backstay glass thermal infrared spectra from *Chapter 3*.

Library Endmember	Quality	Irvine Glass Pellet					Backstay Glass Pellet				
		IRVG-pH0	IRVG-pH1	IRVG-pH2	IRVG-pH3	IRVG-pH4	BKSG-pH0	BKSG-pH1	BKSG-pH2	BKSG-pH3	BKSG-pH4
¹ Unaltered	wc	-	39.96	82.52	91.48	95.39	41.17	84.60	82.71	86.17	86.48
² Thenardite	wc	-	-	-	-	-	-	-	-	-	-
² Aphthitalite	wc	0.02	0.62	-	-	-	-	-	-	-	-
² Glauberite	wc	-	-	-	-	-	-	-	-	-	-
² Anhydrite	wc	-	-	-	-	-	-	-	-	-	-
² Barite	wc	-	-	-	-	-	-	-	-	-	-
² Celestite	wc	-	-	-	-	-	-	-	-	-	-
^{2a} Anglesite	wc	-	-	-	-	-	-	-	-	-	-
² Antlerite	wc	-	-	-	-	-	-	-	-	-	-
² Alunite	wc	0.19	-	-	-	-	-	-	-	-	-
^{2b} Minamiite	wc	-	-	-	-	-	-	-	-	-	-
² Sulfohalite	wc	-	1.23	-	-	-	0.16	-	-	-	-
² Hanksite	wc	-	-	-	-	-	-	-	-	-	-
² Szomolnokite	wc	-	-	-	-	-	-	-	-	-	-
² Bloedite	wc	-	-	-	-	-	-	-	-	-	-
² Polyhalite	wc	-	-	-	-	-	-	-	-	-	-
² Bassanite	wc	-	0.39	-	-	-	2.40	-	-	-	-
² Gypsum	wc	-	-	-	-	-	-	-	-	-	-
² Zincobotryogen	wc	-	-	-	-	-	-	-	-	-	-
^{2c} Coquimbite/Paracoquimbite	wc	-	1.04	-	-	-	8.40	-	-	-	-
³ Römerite	wc	-	-	-	-	-	-	-	-	-	-
³ Botryogen-Zn	wc	-	-	-	-	-	-	-	-	-	-
^{3d} Copiapite	wc	-	-	-	-	-	-	-	-	-	-
³ Amarantite	wc	-	-	-	-	-	-	-	-	-	-
^{3e} Butlerite	wc	-	-	-	-	-	-	2.60	-	-	-
³ Parabutlerite	wc	-	-	-	-	-	-	-	-	-	-
^{3f} Jarosite	wc	-	-	-	-	-	-	-	-	-	-
³ Hydronium jarosite	wc	-	-	-	-	-	-	-	-	-	-

³	Goldichite	wc	2.02	-	1.80	-	-	4.95	-	-	-	-
³	Rhomboclase	wc	-	-	-	-	-	-	-	-	-	-
³	Kornelite	wc	-	-	-	-	-	-	-	-	-	-
³	Voltaite	wc	-	-	-	-	-	-	-	-	-	-
^{3g}	Beaverite	wc	-	-	-	-	-	-	-	0.62	-	0.58
³	Mg-copiapite	wc	-	-	-	-	-	-	-	-	-	-
³	Natrojarosite	wc	-	-	-	-	0.97	-	-	-	-	-
^{3h}	Sideronatrite	wc	-	-	-	-	-	-	-	4.30	-	6.40
³	Slavikite	wc	-	-	0.47	-	-	-	-	-	-	-
³	Yavapaiite	wc	1.15	-	-	-	1.05	-	-	6.74	3.58	-
¹	K-jarosite powder	wc	-	-	-	-	-	-	-	-	-	-
⁴	Anhydrite	wc	-	-	-	-	-	-	-	-	-	-
⁴	Anhydrous Magnesium Sulfate	wc	-	-	-	-	-	-	-	-	-	-
⁴	Bassanite	wc	-	-	-	-	-	-	-	-	-	-
⁴	Epsomite	wc	-	-	-	-	-	-	-	-	-	-
⁴	Gypsum	wc	5.44	-	-	-	-	0.44	-	-	-	-
⁴	Kieserite	wc	-	-	-	-	-	-	-	-	-	-
⁴	Pentahydrate	wc	-	-	-	-	-	-	-	-	-	-
⁴	Sanderite	wc	-	-	-	-	-	-	-	-	-	-
⁴	Starkeyite	wc	-	-	-	-	-	3.77	-	-	-	-
⁵	Halotrichite pellet	nc	18.55	-	-	-	-	-	-	-	-	-
⁵	Dietrichite pellet	nc	-	-	-	-	-	-	-	5.54	10.25	-
⁵	Leonite pellet	nc	-	-	-	-	-	-	-	-	-	-
⁶	Mikasaite	wc	-	-	-	-	-	-	-	-	-	-
⁶	Rozenite	wc	-	-	-	-	-	-	-	-	-	-
⁶	Amorphous ferrous sulfate	wc	-	-	-	-	-	-	-	-	-	-
⁶	MV amorphous	wc	-	-	-	-	-	-	-	-	-	5.62
⁶	LV amorphous	wc	-	-	-	-	-	-	-	-	-	-
⁶	MH amorphous	wc	1.07	7.31	-	-	-	9.01	-	-	-	-
⁶	LH amorphous	wc	-	-	-	-	-	-	-	-	-	-

6	Acros (lausenite)	wc	-	-	-	-	-	-	-	-	-	-
6	Melanterite	wc	17.43	-	-	-	-	-	-	-	-	-
6	Szomolnokite	wc	-	-	-	-	-	-	-	-	-	-
7	Al-Opal	wc	13.03	9.74	-	-	-	1.44	-	-	-	-
8	K-rich Glass	wc	-	-	-	-	-	-	-	-	-	-
8	SiO2 Glass	wc	-	-	-	-	-	-	-	-	-	-
9	elemental sulfur	wc	-	-	-	-	2.05	-	-	0.09	-	0.92
10	Goethite Powder GTS2	wc	-	6.58	0.56	7.14	-	3.23	1.36	-	-	-
11	Akaganeite akg1	wc	0.27	4.23	2.20	-	-	4.82	0.64	-	-	-
11	Lepidocrocite lps2	wc	-	-	-	-	0.54	-	-	-	-	-
12i	Hematite BUR-2600	wc	-	-	-	-	-	-	1.61	-	-	-
10	Hematite gtsh2-300	wc	-	-	-	1.38	-	-	-	-	-	-
10	Magnetite mts4	wc	-	-	0.08	-	-	-	-	-	-	-
10	Magnetite mts5	wc	-	-	-	-	-	-	-	-	-	-
2j	Pickeringite	wc	-	-	-	-	-	-	-	-	-	-
2k	Apjohnite	wc	25.01	-	-	-	-	-	-	-	-	-
2	Thaumasite	wc	-	-	-	-	-	-	5.17	-	-	-
2	Serpierite	wc	-	-	-	-	-	-	-	-	-	-
5	Alunogen	nc	15.82	28.9	12.37	-	-	20.21	4.02	-	-	-
13	jf_sinter12b (silica sinter)	nc	-	-	-	-	-	-	-	-	-	-
13	jf_sinter12_63-500f	nc	-	-	-	-	-	-	-	-	-	-
13	jf_sinter12_L63f2	nc	-	-	-	-	-	-	-	-	-	-
13	frit203flat (synthetic amorphous silica)	wc	-	-	-	-	-	-	-	-	-	-
13	frit203_G63	wc	-	-	-	-	-	-	-	-	-	-
13	frit203_L63	wc	-	-	-	-	-	-	-	-	-	-
13	fqtz_disc (synthetic microporous silica)	wc	-	-	-	-	-	-	-	-	-	-
13	fqtz_G63f	wc	-	-	-	-	-	-	-	-	-	-
13	fqtz_L63f	wc	-	-	-	-	-	-	-	-	-	-
Total			100	100	100	100	100	100	100	100	100	100

Table A4: Linear least squares modeled abundances for Irvine volatile-containing glass particulate thermal infrared spectra from *Chapter 4*.

		Irvine Glass Particulate			
Library Endmember	Quality	IRVG- VC-pH0	IRVG- VC-pH2	IRVG- VC-pH4	
¹ Unaltered	wc	-	75.77	82.26	
² Thenardite	wc	-	-	-	
² Aphthitalite	wc	-	-	-	
² Glauberite	wc	-	-	-	
² Anhydrite	wc	-	-	-	
² Barite	wc	-	-	-	
² Celestite	wc	-	-	-	
^{2a} Anglesite	wc	-	-	-	
² Antlerite	wc	-	-	-	
² Alunite	wc	0.8	-	-	
^{2b} Minamiite	wc	-	-	-	
² Sulfohalite	wc	-	-	-	
² Hanksite	wc	-	-	-	
² Szomolnokite	wc	-	-	-	
² Bloedite	wc	0.64	-	-	
² Polyhalite	wc	-	-	-	
² Bassanite	wc	-	-	-	
² Gypsum	wc	1.01	1.24	-	
² Zincobotryogen	wc	-	-	-	
^{2c} Coquimbite/Paracoquimbite	wc	-	-	-	
³ Römerite	wc	-	-	-	
³ Botryogen-Zn	wc	-	-	-	
^{3d} Copiapite	wc	-	-	-	
³ Amaranтите	wc	-	-	-	
^{3e} Butlerite	wc	0.52	-	-	
³ Parabutlerite	wc	-	-	-	
^{3f} Jarosite	wc	-	-	-	
³ Hydronium jarosite	wc	4.00	-	-	

³	Goldichite	wc	-	-	-
³	Rhomboclase	wc	-	-	-
³	Kornelite	wc	-	-	-
³	Voltaite	wc	-	-	-
^{3g}	Beaverite	wc	-	-	-
³	Mg-copiapite	wc	-	-	-
³	Natrojarosite	wc	-	-	6.59
^{3h}	Sideronatrite	wc	-	-	-
³	Slavikite	wc	-	-	-
³	Yavapaiite	wc	0.63	-	1.66
¹	K-jarosite powder	wc	-	-	-
⁴	Anhydrite	wc		-	-
⁴	Anhydrous Magnesium Sulfate	wc	0.08	-	-
⁴	Bassanite	wc		-	-
⁴	Epsomite	wc	1.31	-	-
⁴	Gypsum	wc	2.65	1.91	-
⁴	Kieserite	wc	-	-	-
⁴	Pentahydrate	wc	-	-	-
⁴	Sanderite	wc	-	-	-
⁴	Starkeyite	wc	-	-	-
⁵	Halotrichite pellet	nc	10.99	-	-
⁵	Dietrichite pellet	nc	0.72	-	-
⁵	Leonite pellet	nc	-	-	-
⁶	Mikasaite	wc	-	-	-
⁶	Rozenite	wc	-	-	-
⁶	Amorphous ferrious sulfate	wc	-	-	-
⁶	MV amorphous	wc	-	-	-
⁶	LV amorphous	wc	-	-	-
⁶	MH amorphous	wc	-	-	-
⁶	LH amorphous	wc	-	-	-

6	Acros (lausenite)	wc	-	-	-
6	Melanterite	wc	7.06	-	-
6	Szomolnokite	wc	-	-	-
7	Al-Opal	wc	-	-	-
8	K-rich Glass	wc	-	-	-
8	SiO2 Glass	wc	-	-	-
9	elemental sulfur	wc	-	-	1.33
10	Goethite Powder GTS2	wc	0.1	14.04	0.48
11	Akaganeite akg1	wc	-	7.04	0.03
11	Lepidocrocite lps2	wc	1.34	-	5.37
12i	Hematite BUR-2600	wc	-	-	-
10	Hematite gtsh2-300	wc	0.11	-	1.69
10	Magnetite mts4	wc	0.71	-	-
10	Magnetite mts5	wc	-	-	-
2j	Pickeringite	wc	-	-	-
2k	Apjohnite	wc	49.17	-	-
2	Thaumasite	wc	8.71	-	0.59
2	Serpierite	wc	-	-	-
5	Alunogen	nc	9.45	-	-
13	jf_sinter12b (silica sinter)	nc	-	-	-
13	jf_sinter12_63-500f	nc	-	-	-
13	jf_sinter12_L63f2	nc	-	-	-
13	frit203flat (synthetic amorphous silica)	wc	-	-	-
13	frit203_G63	wc	-	-	-
13	frit203_L63	wc	-	-	-
13	fqtz_disc (synthetic microporous silica)	wc	-	-	-
13	fqtz_G63f	wc	-	-	-
13	fqtz_L63f	wc	-	-	-
Total			100	100	100

Table A5: Linear least squares modeled abundances for the averaged thermal emission spectra for each group of Hawaiian material from *Chapter 5*.

	Library Endmember	Quality	Group 1-1	Group 1-2	Group 1-3	Group 1-4	Group 2	Group 3	Group 4
¹	Amorphous silica (whole rock)	wc	-	-	-	-	-	-	-
¹	Amorphous silica (>63μm)	wc	-	-	-	-	-	-	-
¹	Amorphous silica (<63μm)	wc	0.43	2.72	1.32	-	-	18.58	-
¹	Microporous silica (whole rock)	wc	-	-	-	4.51	-	-	-
¹	Microporous silica (>63μm)	wc	-	-	-	-	-	-	-
¹	Microporous silica (<63μm)	wc	-	-	-	-	-	-	-
¹	Silica sinter (whole rock)	wc	15.75	26.10	-	75.23	-	-	39.77
¹	Silica sinter (>63μm)	wc	26.82	-	-	-	-	-	-
¹	Silica sinter (<63μm)	wc	-	-	5.87	-	-	0.93	-
²	Thenardite	wc	-	-	-	-	-	-	-
²	Aphthitalite	wc	1.11	1.72	2.46	-	-	2.36	-
²	Glauberite	wc	-	-	-	-	-	-	-
²	Anhydrite	wc	-	-	-	-	-	-	-
²	Barite	wc	-	-	-	-	-	-	-
²	Celestite	wc	-	-	-	-	-	-	-
^{2a}	Anglesite	wc	-	-	-	-	-	-	-
²	Antlerite	wc	-	-	-	-	-	-	-
²	Alunite	wc	-	-	-	-	-	-	2.22
^{2b}	Minamiite	wc	-	-	-	-	-	-	-
²	Sulfohalite	wc	-	-	-	-	-	-	-
²	Hanksite	wc	-	-	-	-	-	-	-
²	Szomolnokite	wc	-	-	-	-	-	-	-
²	Bloedite	wc	-	-	-	-	-	-	-
²	Polyhalite	wc	-	1.77	-	-	-	-	-
²	Bassanite	wc	-	-	-	-	-	-	-
²	Gypsum	wc	0.48	-	-	-	72.94	-	-
²	Zincobotryogen	wc	-	-	-	-	-	-	-
^{2c}	Coquimbite/Paracoquimbite	wc	26.25	24.26	23.54	-	-	23.80	0.58
³	Römerite	wc	-	-	-	-	-	-	-

³	Botryogen-Zn	wc	-	-	-	-	-	-	-
^{3d}	Copiapite	wc	-	-	-	-	-	-	-
³	Amarantite	wc	-	-	6.13	-	-	15.55	-
^{3e}	Butlerite	wc	-	-	-	-	-	-	-
³	Parabutlerite	wc	-	-	-	-	-	-	-
^{3f}	Jarosite	wc	-	-	-	-	-	-	-
³	Hydronium jarosite	wc	-	-	-	-	-	-	-
³	Goldichite	wc	-	-	-	-	-	-	-
³	Rhomboclase	wc	-	-	1.78	-	-	8.32	-
³	Kornelite	wc	-	-	-	-	-	-	-
³	Voltaite	wc	-	-	-	-	-	9.34	-
^{3g}	Beaverite	wc	-	-	-	-	-	-	-
³	Mg-copiapite	wc	-	-	-	-	-	-	-
³	Natrojarosite	wc	-	-	0.73	-	-	-	-
^{3h}	Sideronatrite	wc	-	1.58	4.20	-	-	-	-
³	Slavikite	wc	-	-	-	-	-	-	-
³	Yavapaiite	wc	-	-	-	-	-	5.22	-
¹	K-jarosite powder	wc	-	-	-	-	-	-	-
⁴	Anhydrite	wc	-	-	-	-	-	-	-
⁴	Anhydrous Magnesium Sulfate	wc	-	-	-	-	-	-	-
⁴	Bassanite	wc	-	-	-	-	-	0.32	-
⁴	Epsomite	wc	-	-	-	-	-	-	-
⁴	Gypsum	wc	-	-	-	-	-	-	-
⁴	Kieserite	wc	-	-	-	-	-	-	-
⁴	Pentahydrate	wc	-	-	-	-	-	-	-
⁴	Sanderite	wc	-	-	-	-	-	-	-
⁴	Starkeyite	wc	-	-	-	-	-	-	-
⁵	Halotrichite pellet	nc	-	-	-	-	-	-	-
⁵	Dietrichite pellet	nc	-	-	-	-	-	-	-
⁵	Leonite pellet	nc	-	-	-	-	-	-	-

6	Mikasaite	wc	-	-	-	-	-	-	-
6	Rozenite	wc	-	-	-	-	-	-	-
6	Amorphous ferrious sulfate	wc	-	-	-	-	-	-	-
6	MV amorphous	wc	-	-	-	-	-	-	-
6	LV amorphous	wc	-	-	-	-	-	-	-
6	MH amorphous	wc	-	-	-	-	-	-	-
6	LH amorphous	wc	-	-	-	-	-	-	-
6	Acros (lausenite)	wc	-	-	-	-	-	-	-
6	Melanterite	wc	-	-	-	-	-	-	-
6	Szomolnokite	wc	-	-	-	-	-	-	-
7	Al-Opal	wc	17.50	29.04	-	-	27.06	-	-
8	K-rich Glass	wc	8.62	-	3.71	-	-	-	-
8	SiO2 Glass	wc	-	-	-	-	-	-	-
9	elemental sulfur	wc	-	1.86	1.16	7.98	-	-	-
10	Goethite Powder GTS2	wc	1.14	-	4.52	-	-	-	-
11	Akaganeite akg1	wc	0.60	0.50	11.65	-	-	-	14.78
11	Lepidocrocite lps2	wc	-	-	-	-	-	-	-
12i	Hematite BUR-2600	wc	-	-	-	-	-	-	20.91
10	Hematite gts2-300	wc	-	-	-	-	-	-	-
10	Magnetite mts4	wc	-	-	-	-	-	-	-
10	Magnetite mts5	wc	-	-	-	-	-	-	-
2j	Pickeringite	wc	-	-	-	-	-	-	-
2k	Apjohnite	wc	-	-	-	-	-	-	-
2	Thaumasite	wc	-	-	-	-	-	-	21.74
2	Serpierite	wc	1.30	-	2.85	-	-	5.36	-
5	Alunogen	nc	-	-	23.01	-	-	7.87	-
5	Kaolinite	wc	-	-	-	-	-	-	-
5	Montmorillonite	wc	-	2.80	-	-	-	-	-
5	Montmorillonite (Ca)	wc	-	-	-	-	-	-	-
5	Montmorillonite (Na)	wc	-	-	-	-	-	-	-

5	Clinochlore	wc	-	-	-	-	-	-	-
5	Muscovite	wc	-	-	-	-	-	-	-
5	Nontronite	wc	-	-	-	-	-	-	-
5	Palygorskite	wc	-	-	-	-	-	-	-
5	Serpentine	wc	-	-	-	-	-	-	-
5	Smectite	wc	-	7.51	-	-	-	-	-
5	Dickite	wc	-	-	-	-	-	-	-
5	Talc	wc	-	-	-	-	-	-	-
9	Augite	wc	-	0.14	7.07	-	-	-	-
9	Ilmenite	wc	-	-	-	12.28	-	-	-
9	Fayalite	wc	-	-	-	-	-	2.35	-
9	Forsterite	wc	-	-	-	-	-	-	-
9	Albite	wc	-	-	-	-	-	-	-
9	Andesine	wc	-	-	-	-	-	-	-
9	Anorthite	wc	-	-	-	-	-	-	-
9	Bytownite	wc	-	-	-	-	-	-	-
9	Diopside	wc	-	-	-	-	-	-	-
9	Enstatite	wc	-	-	-	-	-	-	-
9	Magnetite	wc	-	-	-	-	-	-	-
9	Oligoclase	wc	-	-	-	-	-	-	-
9	Labradorite	wc	-	-	-	-	-	-	-
Total			100	100	100	100	100	100	100

wc = well characterized / nc= not characterized

^acontains minor celestine

^b90% minamiite, 8% alunite, 2% other

^cequal amounts of coquimbite and paracoquimbite

^d25% ferricopiapite

^e5% pararbutlerite

^ftrace amount of unknown phase

^gminor impurity ~5-7% anglesite

^hminor impurity of unknown phase

ⁱminor impurities

^jKalinite/Apjohnite/Halotrichite

^kcontains minor kalinite/halotrichite,pickeringite

¹Ruff et al., 2011

²Lane 2007

³Lane et al., 2015

⁴Baldrige 2008

⁵Lane unpublished

⁶Sklute 2015

⁷M.D. Kraft Personal Communication

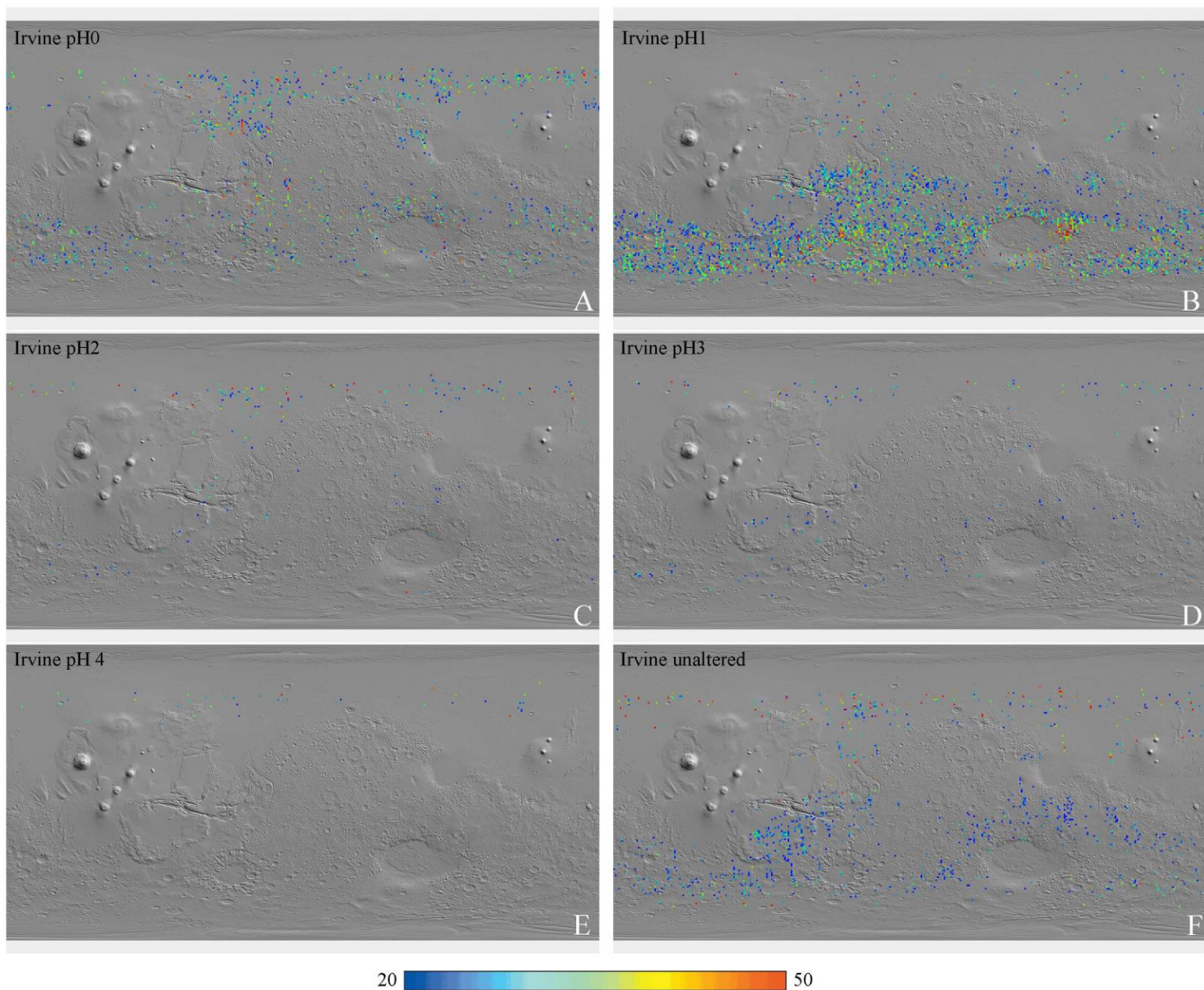
⁸Wyatt et al., 2001

⁹A.D. Rogers Personal Collection

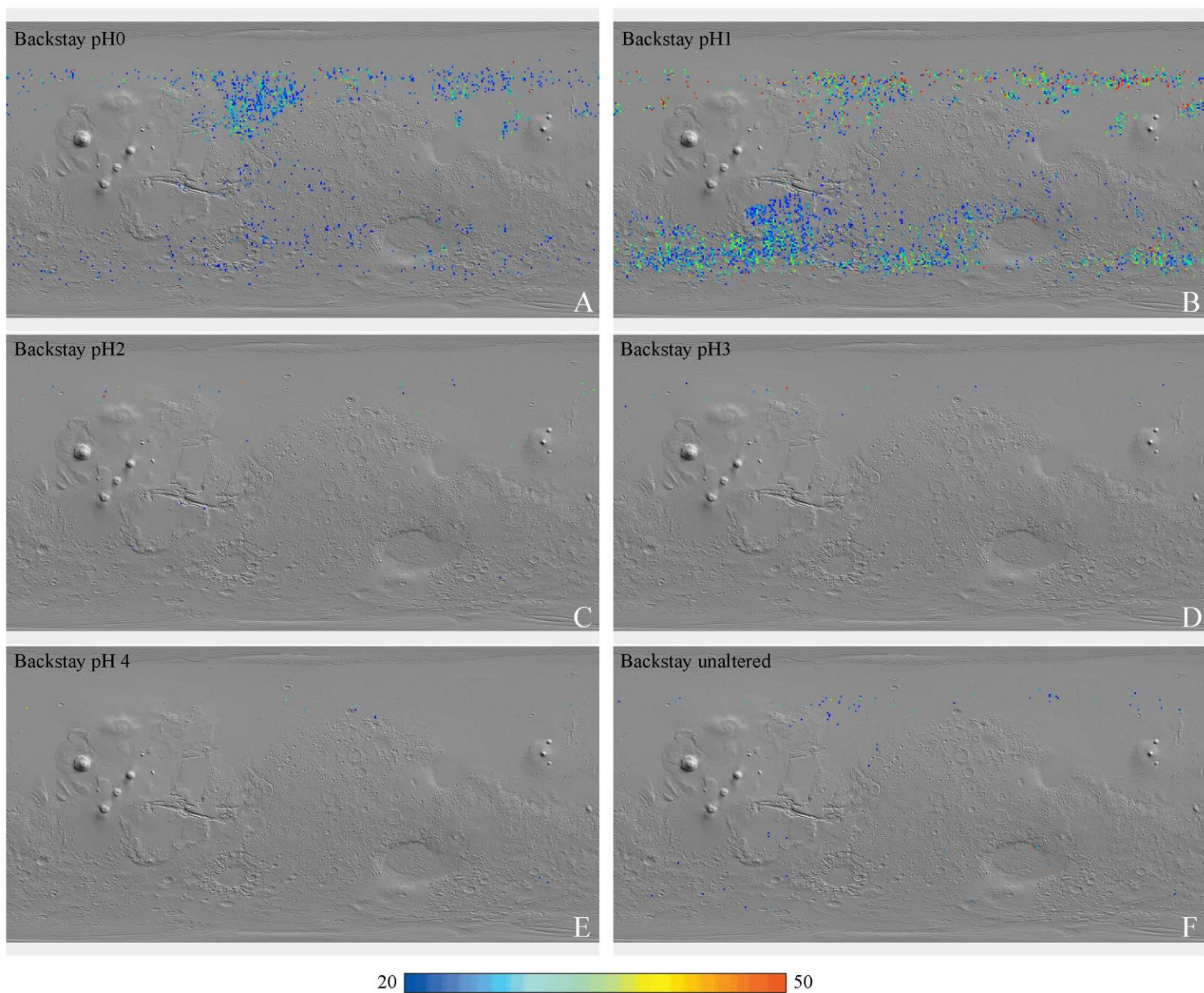
¹⁰Glotch et al., 2004

¹¹Glotch and Kraft 2008

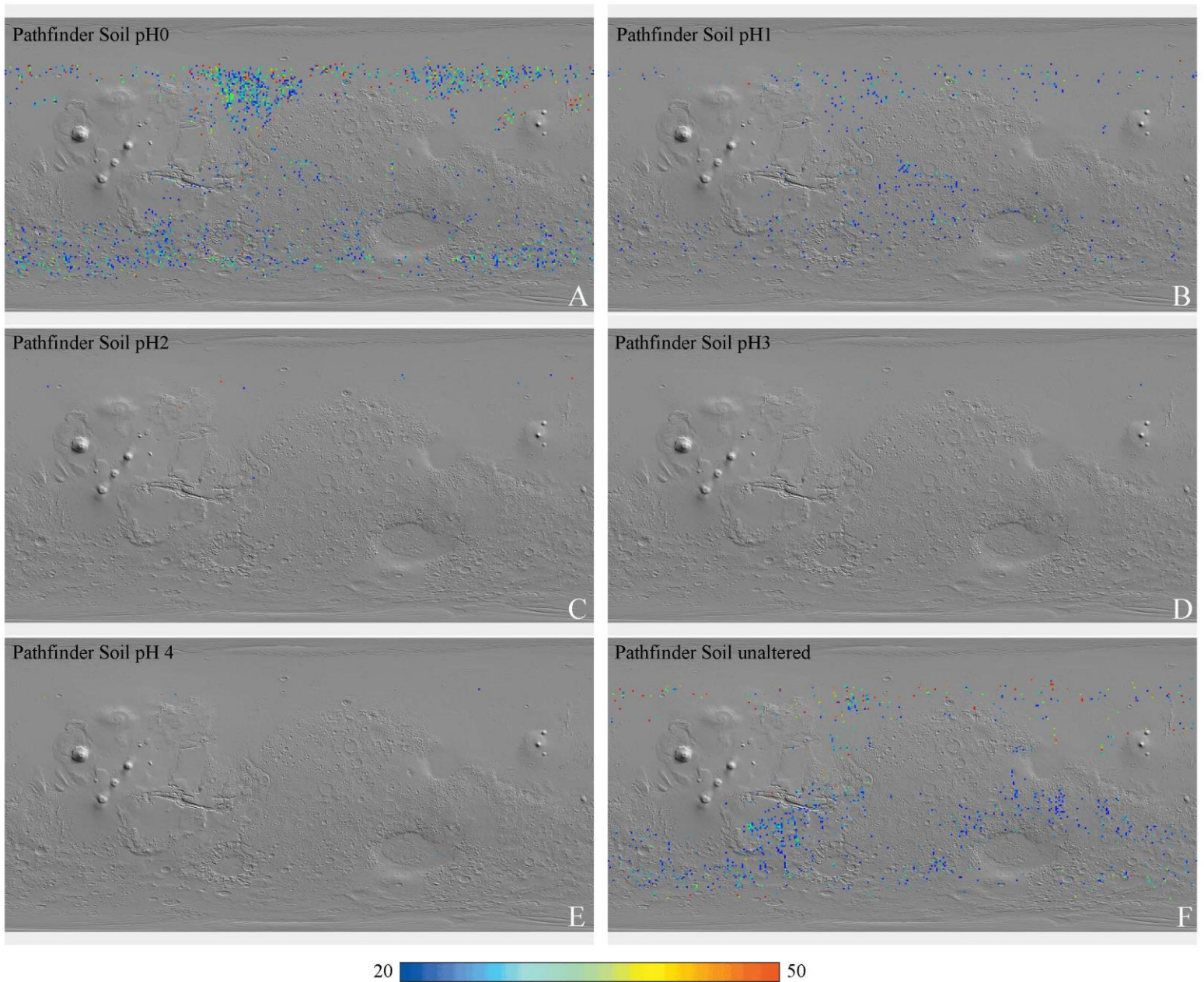
¹²Christensen et al., 2000



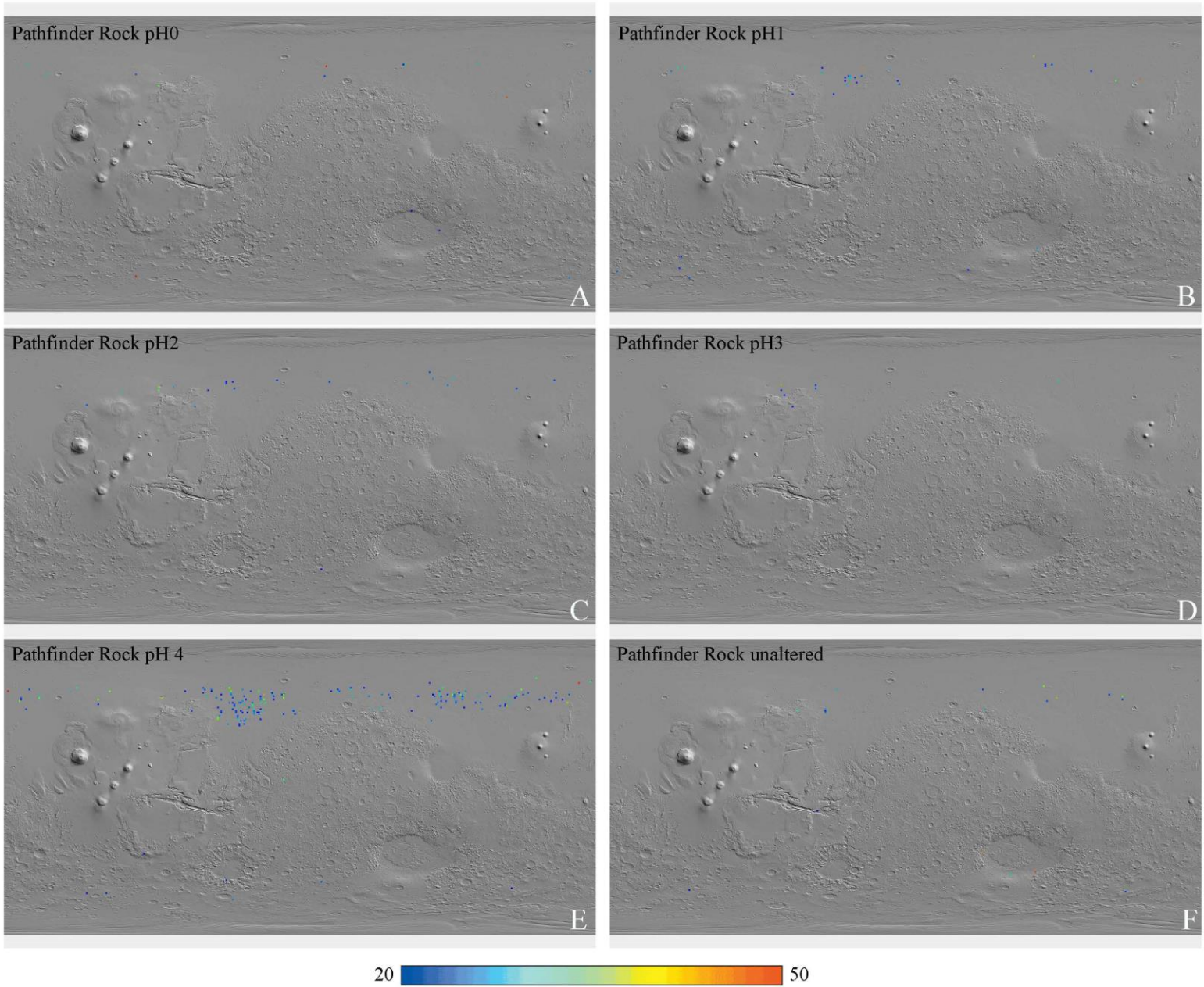
Appendix Figure A1: One pixel per degree binned global TES map showing the abundances ranging from 20-50% for the Irvine material altered in A) pH0, B) pH1, C) pH2, D) pH3, and E) pH4. The global TES map for the unaltered material is shown in panel F.



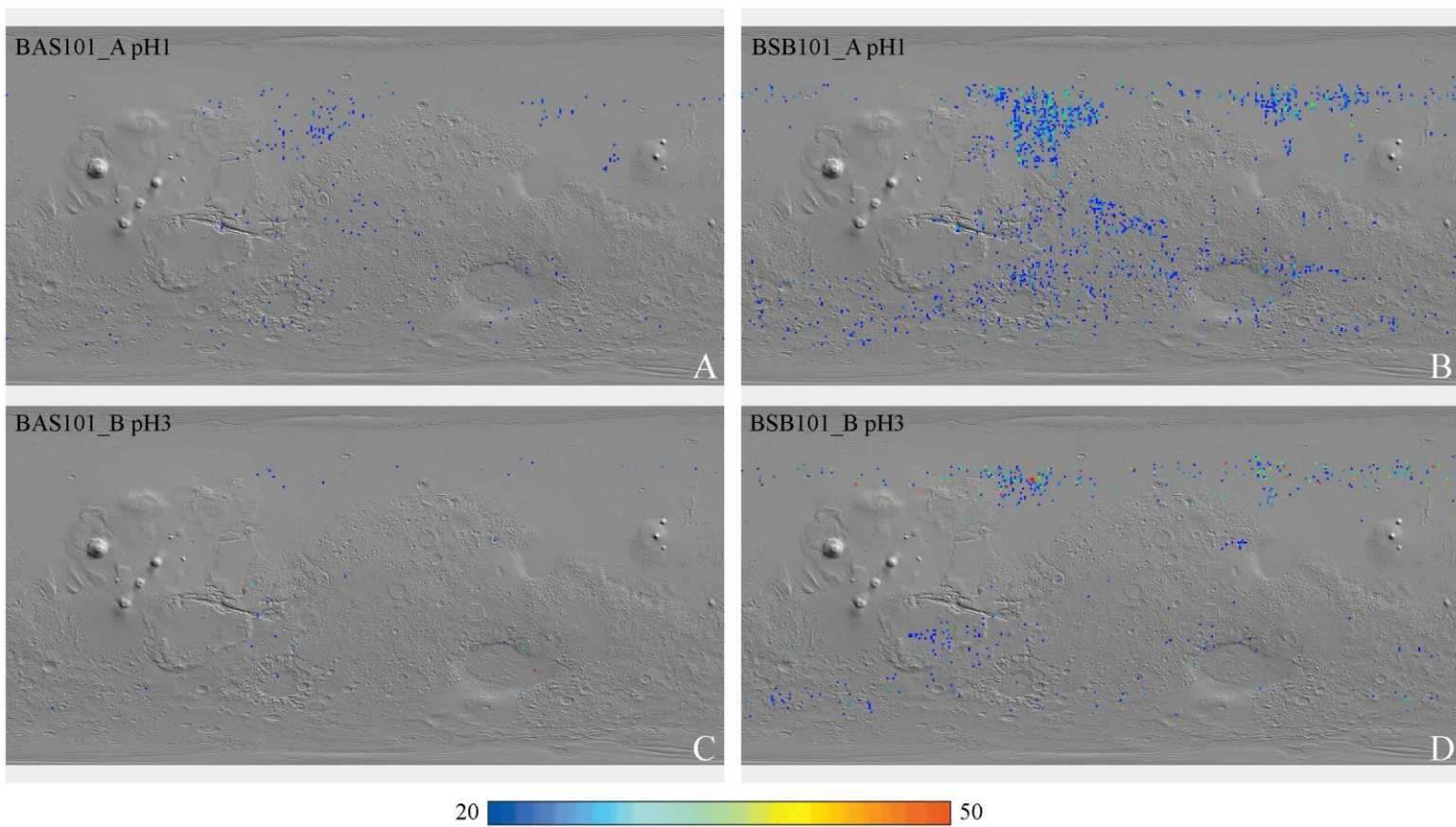
Appendix Figure A2: One pixel per degree binned global TES map showing the abundances ranging from 20-50% for the Backstay material altered in A) pH0, B) pH1, C) pH2, D) pH3, and E) pH4. The global TES map for the unaltered material is shown in panel F.



Appendix Figure A3: One pixel per degree binned global TES map showing the abundances ranging from 20-50% for the Pathfinder Soil material altered in A) pH0, B) pH1, C) pH2, D) pH3, and E) pH4. The global TES map for the unaltered material is shown in panel F.



Appendix Figure A4: One pixel per degree binned global TES map showing the abundances ranging from 20-50% for the Pathfinder Rock material altered in A) pH0, B) pH1, C) pH2, D) pH3, and E) pH4. The global TES map for the unaltered material is shown in panel F.



Appendix Figure A5: One pixel per degree binned global TES map showing the abundances ranging from 20-50% for the terrestrial analog materials A) BAS101_A (pH1), B) BAS101_B (pH3), C) BSB101_A (pH1), D) BAS101_B (pH3).